Stellingen
behorende bij het proefschrift
"DERIVATION, IMPLEMENTATION, AND VALIDATION
OF COMPUTER SIMULATION MODELS
FOR GAS-SOLID FLUIDIZED BEDS"
van Berend van Wachem.

1. De uitdrukking "two-fluid" model voor een Euleriaans-Euleriaans gas-deeltjes model is om fysische redenen foutief.
   Hoofdstuk 3 van dit proefschrift

2. Het tweedimensionale Euleriaanse-Lagrangiaanse gas-deeltjes model vertoont realistisch gedrag maar is als kwantitatief model onbruikbaar.
   Hoofdstuk 6 van dit proefschrift

3. Het is onterecht dat Xu en Yu de drukval over een deeltje in een gasstroom verwaarlozen bij de berekening van de kracht op dat deeltje.
   B.H. Xu and A.B. Yu, Numerical simulation of the gas-solid flow in a fluidized bed by combining discrete particle method with computational fluid dynamics, Chem. Eng. Sci., 52:2785-2809 (1997)

4. De juiste coefficienten voor een derde orde nauwkeurige benadering van een eerste afgeleide op de rand waar de roosterpunten verschoven liggen ten opzichte van de rand, zijn onjuist geponeerd door Laney en moeten zijn $\left(-\frac{1}{24}, \frac{9}{8}, -\frac{9}{8}, \frac{1}{24}\right)$
   C.B. Laney, Computational Gasdynamics, first edition, Cambridge University Press, UK (1998), pagina 437

5. Het vertonen van video's met daarin een grote hoeveelheid kleuren die meet- of simulatieresultaten representeren heeft een grote emotionele maar weinig wetenschappelijke overtuigingskracht.

6. Bij het maken van de keuze tussen het compressibel en incompressibel berekenen van een gasstroom, spelen niet alleen de gassnelheid en de temperatuurgradient een rol, maar zijn ook de verschillen in grootte van brontermen belangrijk.

7. De oorsprong van de jazz muziek ligt in Duitsland en niet in Amerika.
   L. van Beethoven, Piano Sonata 32, opus 111, deel 2: Arietta (1820)

8. De kans op vervloeiing van grond die optreedt als gevolg van een aarbeving neemt af met een toenemende graad van consolidatie. In de praktijk is er echter nooit sprake van "onderconsolidatie", zoals beweerd door Zijne Koninklijke Hoogheid.
W.-A. van Oranje-Nassau, redevoering, Japan, Mei 2000

9. Als het Westen eerlijk handel zou voeren met tweede- en derdewereldlanden, is het doneren van geld in het kader van ontwikkelingshulp overbodig.

10. In het heterogene regime van een slurry-kolom zijn de krachten op de deeltjes als gevolg van vloeistofconvectie veel groter dan de krachten op de deeltjes als gevolg van de interactie tussen de gas-vloeistof grenslaag en het hydrofiel of hydrofoob zijn van het deeltje; in het homogene regime is dit echter niet het geval. Het meten van een hold-up toe- of afname in het homogene regime door het toevoegen van deeltjes is daarom niet karakteristiek voor het gehele regime van een slurry- kolom.

11. Het voor grote bedragen veilen van GSM en UMTS licenties leidt niet tot een effectief vollere staatkas, maar tot een vergroting van de inflatie.

12. Bloed- en orgaandonoren zouden bij gebruik van donormateriaal voor moeten gaan bij mensen die kiezen om niet te doneren maar dat wel zouden kunnen of hebben gekund.

13. Het is een verarming voor de roeisport dat de categorie zware-heren-twee-met-stuurman geen Olympische status meer heeft.

14. Milieubescherming en economische groei zijn onverenigbaar.

15. Als bij een zeehondencreche de aaibaarheidsfactor van de zeehonden een grotere rol speelt dan het behoud van de kwaliteit van de totale zeehondenpopulatie, is het voortbestaan van deze zeehondencreche niet gerechtvaardigd.

16. De vraag naar promovendi bij de Nederlandse universiteiten en de vraag naar gepromoveerden bij Nederlandse bedrijven en instellingen zijn niet aan elkaar gerelateerd.

Propositions

complementing the dissertation

"DERIVATION, IMPLEMENTATION, AND VALIDATION OF COMPUTER SIMULATION MODELS FOR GAS-SOLID FLUIDIZED BEDS"

of Berend van Wachem.

1. The expression "two-fluid" model for the Eulerian-Eulerian gas-solid model is incorrect for physical reasons.
   Chapter 3 of this dissertation.

2. The two-dimensional Eulerian-Lagrangian gas-solid model shows qualitatively realistic behaviour, but is unusable as a quantitative model.
   Chapter 6 of this dissertation.

3. It is incorrect that Xu and Yu neglect the pressure drop over a particle in a gas flow in calculating the force on that particle.
   B.H. Xu and A.B. Yu, Numerical simulation of the gas-solid flow in a fluidized bed by combining discrete particle method with computational fluid dynamics, Chem. Eng. Sci., 52:2785-2809 (1997)

4. The correct coefficients for a third order accurate approximation of the first derivative on the edge, where the grid points lie staggered with respect to the edge, have been incorrectly given by Laney and should be $\left(-\frac{1}{24}, \frac{9}{8}, -\frac{9}{8}, \frac{1}{24}\right)$
   C.B. Laney, Computational Gasdynamics, first edition, Cambridge University Press, UK (1998), page 437

5. Showing videos with a large amount of colors representing measurement or simulation data has a large emotional but little scientific cogency.

6. Not only the gas velocity and the temperature gradient, but also the differences in sizes of source terms are important in choosing to calculate a gas flow compressible or incompressible.

7. The origin of jazz music lies in Germany and not in the United States.
   L. van Beethoven, Piano Sonata 32, opus 111, part 2: Arietta (1820)

8. The chance on liquefaction of soil as a result of an earthquake decreases with an increasing degree of consolidation. In practice, however, soil is never "underconsolidated" as claimed by His Royal Highness.
   W.-A. van Oranje-Nassau, oration, Japan, May 2000

9. Donation of money in the framework of development aid is redundant if the Western countries would trade fairly with second and third world countries.

10. In the heterogeneous flow regime of a slurry column, the forces on a particle as a result of fluid convection are much larger than the forces on a particle as a result of the interaction of the gas-liquid interface and the wettability of a particle; in the homogeneous regime, however, this is not the case. Therefore, measuring a hold-up increase or decrease in the homogeneous regime with the addition of particles is not characteristic for the behaviour of the complete regime of a slurry column.

11. Auctioning GSM and UMTS licenses does not lead to an increase of public money, but to an increase of inflation.

12. Blood and organ donors should precede in the usage of donor material compared to people who choose not to donate but could have done so.

13. It is an impoverishment for the sport of rowing that the category heavy weight coxed pair is no longer an Olympic one.

14. Environmental protection is incompatible to economic growth.

15. If the cuddliness of sea lions is more important than the quality of the sea lion population for a refuge for sea lions, the existence of this refuge is no longer justifiable.

16. The demand of PhD students at Dutch universities is not related to the demand of PhD's at Dutch companies and institutions.

Derivation, Implementation, and Validation of Computer Simulation Models for Gas-Solid Fluidized Beds

Berend van Wachem

Derivation, Implementation, and Validation of Computer Simulation Models for Gas-Solid Fluidized Beds

PROEFSCHRIFT

ter verkrijging van de graad van doctor
aan de Technische Universiteit Delft,
op gezag van de Rector Magnificus prof. ir. K.F. Wakker,
voorzitter van het College voor Promoties,
in het openbaar te verdedigen
op maandag 18 september 2000 te 16:00 uur

door

Berend Gerardus Michiel VAN WACHEM
natuurkundig ingenieur

geboren op 5 juni 1972 te Amsterdam

Dit proefschrift is goedgekeurd door de promotoren:
Prof.ir. C.M. van den Bleek
Prof.dr. R. Krishna
Prof.dr.ir. J.C. Schouten

Samenstelling promotiecomissie:

Rector Magnificus,	voorzitter
Prof.ir. C.M. van den Bleek,	Technische Universiteit Delft, promotor
Prof.dr. R. Krishna,	Universiteit van Amsterdam, promotor
Prof.dr.ir. J.C. Schouten,	Technische Universiteit Eindhoven, promotor
Prof.dr. J.L. Sinclair,	Purdue University (Verenigde Staten van Amerika)
Prof.dr. S.W. de Leeuw,	Technische Universiteit Delft
Prof.dr.ir. P. Wesseling,	Technische Universiteit Delft
Dr.ir. H.C.J. Hoefsloot,	Universiteit van Amsterdam

Wachem, Berend Gerardus Michiel van
Derivation, Implementation, and Validation of Computer Simulation Models for Gas-Solid Fluidized Beds / by Berend Gerardus Michiel van Wachem
Dissertation at Delft University of Technology. - With ref.- With summary in Dutch
ISBN 90-9013931-1
NUGI 812/813
Subject headings: Computer simulations / Gas-solid fluidized beds / Eulerian-Eulerian / Eulerian-Lagrangian / Granular kinetic theory

Cover: F.A. van Wachem.

The work described in this thesis was financially supported by SON/NWO, the National Dutch Science Foundation for Chemistry, and Delft University of Technology.

Contents

Summary xi

Samenvatting (Summary in Dutch) xiii

1 Introduction 1
- 1.1 Fluidization . . . 2
- 1.2 Hydrodynamic modeling of fluidized beds . . . 4
- 1.3 Research objectives . . . 5
- 1.4 Outline . . . 6

2 Kinetic theory of granular flow 9
- 2.1 Introduction . . . 10
- 2.2 Probability density function . . . 10
- 2.3 The Boltzmann equation . . . 11
- 2.4 Change of particle properties . . . 12
- 2.5 Flow of particle properties . . . 15
- 2.6 Particle collisions . . . 16
- 2.7 Solving Boltzmann's equation . . . 20
- 2.8 Boltzmann's equation in steady, ideal state . . . 21
- 2.9 Expressing $f_{(2)}$ in f . . . 23
- 2.10 Solving the PDF for the non-ideal state: Enskog approach . . . 24
  - 2.10.1 The second approximation to f for a slightly inelastic granular material . . . 25
- 2.11 Solving the PDF with Grad's method . . . 29
- 2.12 Solving f for a bimodal particle distribution . . . 30
- 2.13 Conclusions . . . 31

3 Comparison of CFD models for Dense Gas-Solid Flows 35
- 3.1 Introduction . . . 36
- 3.2 Governing equations . . . 37
  - 3.2.1 Comparing the Ishii and Jackson governing equations . 42
- 3.3 Closure relations . . . 44

3.3.1 Kinetic theory 44
3.3.2 Solid-phase stress tensor 45
3.3.3 Conductivity of granular energy 48
3.3.4 Dissipation and generation of granular energy 50
3.3.5 Radial distribution function 50
3.3.6 Frictional stress 51
3.3.7 Interphase transfer coefficient 53
3.4 Simulations 57
3.4.1 Boundary conditions 57
3.4.2 Initial conditions 58
3.5 Test cases 59
3.5.1 Freely bubbling fluidized beds 59
3.5.2 Slugging fluidized beds 62
3.5.3 Bubble injection in fluidized beds 63
3.6 Results and Discussion 63
3.6.1 Governing equations 63
3.6.2 Solids stress models 63
3.6.3 Drag models 64
3.6.4 Frictional stress 66
3.6.5 Granular energy balance 68
3.7 Conclusions 69

4 Eulerian Simulations of Gas-Solid Fluidized Beds 75
A. Steady State Results from Simulations 76
4.A.1 Introduction 76
4.A.2 Gas-solid multiphase model 78
4.A.3 Simulations 83
4.A.4 Classical bubble size and velocity relations 86
4.A.5 CFD simulation results 89
4.A.6 Conclusions 91
B. Dynamic behavior of fluidized beds 95
4.B.1 Introduction 95
4.B.2 Gas-solid CFD models 96
4.B.3 Model validation and dynamic simulation results 97
4.B.4 (**A**) Velocity of pressure and voidage waves in fluidized beds 101
4.B.5 (**B**) Power of pressure and voidage waves in fluidized beds 104
4.B.6 (**C**) Reorientation effect in fluidized beds 107
4.B.7 (**D**) Chaotic behaviour of fluidized beds 109
4.B.8 Conclusions 110

5 Modeling of Fluidized Beds with Bimodal Particle Distribution 115
5.1 Introduction . . . 116
5.2 Governing equations . . . 118
5.3 Kinetic Theory for a Bimodal Particle Mixture . . . 119
5.4 Frictional stress . . . 125
5.5 Simulations . . . 126
5.5.1 *Boundary conditions* . . . 129
5.6 Results and Discussion . . . 129
5.6.1 Bimodal mixture Case 1 . . . 129
5.6.2 Bimodal Mixture Case 2 . . . 131
5.7 Conclusions . . . 133
5.8 Nomenclature . . . 135
5.A Appendix . . . 138

6 Experimental validation of Lagrangian Simulations 139
6.1 *Introduction* . . . 140
6.2 Particle phase . . . 141
6.2.1 Motion of particles . . . 141
6.2.2 Collision of particles . . . 142
6.2.3 From two dimensions to three dimensions . . . 144
6.3 Gas phase . . . 145
6.4 Solution method . . . 147
6.5 Experiments and simulations . . . 148
6.5.1 Experimental set-up . . . 148
6.5.2 Measurements . . . 149
6.5.3 Simulations . . . 150
6.5.4 Comparison . . . 151
6.6 Results and discussion . . . 151
6.7 Conclusions . . . 158

7 Conclusions and Outlook 163
7.1 Developments since 1967 . . . 163
7.2 Aim and scope of this work . . . 164
7.3 Comparing governing equations . . . 164
7.4 Interphase momentum transfer . . . 165
7.5 Validation . . . 165
7.6 Granular theory for a bimodal particle mixture . . . 166
7.7 Lagrangian-Eulerian fluidized bed simulations . . . 166
7.8 Conclusion . . . 167
7.9 Two- versus three-dimensions . . . 167
7.10 Outlook . . . 167

A The software manual **169**
A.1 PartGas: Lagrangian code with Eulerian coupling 171
A.1.1 Introduction 171
A.1.2 Structure of the solving method 171
A.1.3 Structure of the code 172
A.1.4 Running the code 173
A.1.5 Makefile 174
A.1.6 info.hpp 174
A.1.7 infile 178
A.1.8 Output 179
A.2 Eulerian-Eulerian gas-solid codes 181
A.2.1 Introduction 181
A.2.2 FORTRAN and CFX 181
A.2.3 equilib 182
A.2.4 fullgran 183
A.2.5 bimodal 185
A.2.6 Pre- and Postprocessing 187
A.3 Animations of simulations 189

Bibliography **191**

Nawoord, Epilogue **199**

About the Author **201**

Summary

This work focuses on the computer modeling of an important application in dense gas-solid flows: gas-solid fluidized beds. Fluidized beds are commonly encountered in the chemical, petroleum, pharmaceutical, agricultural, food, and power generation industries. This thesis describes both the Euler-Euler and the Lagrange-Euler approach to model dense gas-solid flow.

The Euler-Euler approach is currently considered as being the highest possible level of continuum modeling, as it allows for dynamic interaction between the two phases by writing a separate set of mass and momentum equations for each of the phases. There is still a considerable debate regarding the correct formulation of the Euler-Euler governing equations and especially about the closure relations, such as the interphase momentum transfer and the particle-particle interactions. In this work the different forms of the governing equations and the closure relations are discussed and validated.

Different forms of the interphase momentum transfer have been proposed in the literature, but all of them are (semi) empirical and determined on a large scale at liquid-solid conditions. The different correlations predicting the interphase momentum transfer have been compared in simulations of fluidized beds to experiments described in the literature and it has been found that the Wen and Yu (1966) correlation is preferred above the others. The fact that the momentum transfer between the gas and the solids phase is empirical and determined under liquid-solid conditions on a fairly large scale is, however, still a weak chain in the model; the clustering behavior of particles is a local scale effect and is obviously different in gas-solid and in gas-liquid flow.

The particle-particle interactions are described as binary collisions, hence strongly resembling the gas kinetic theory. An important difference between two colliding particles and two colliding gas molecules is the occurrence of non-ideal behaviour described by the coefficient of restitution; momentum is lost during a collision due to local compression of the particle. Taking into account this non-ideal behaviour, a granular kinetic theory can be derived, describing the particle-particle interactions due to collisional and kinetic (streaming) effects. The granular kinetic theory described in this work does not account for the fact that the gas phase behavior influences the particle-particle collision, as is important in a liquid-solid or a dilute gas-solid flow. Some correlations proposed in the literature describing the gas phase fluctuating velocity and the particle phase fluctuating velocity have been applied in simulations, but have a negligible effect in the case of dense gas-solid fluidized beds.

Extensive validation of both the steady-state as well as the dynamic behav-

ior of gas-solid fluidized bed simulations with data from the literature and from experiments show that the predicting capability of the Euler-Euler approach is fairly well. Moreover, most experimental studies only predict the average steady-state or average dynamic behavior of these reactors, whereas CFD simulations predict the complete, time-dependent behavior of fluidized beds. The large drawback in applying CFD to dense gas-solid flows, however, is the enormous amount of computational costs.

In the 1980's a gas kinetic theory was developed by Lopez de Haro *et al.* for gases consisting of multiple different types of ideal molecules. The granular theory for two species of non-ideal particles has been implemented, verified and validated in this work. Although the computational effort required to get results are enormous, an order of magnitude larger than the monodispersed granular theory, simulation results show the model is capable of successfully predicting segregation, mixing and inversion of gas-solid fluidized beds with a bimodal particle size distribution.

The Lagrange-Euler approach describes the behavior of the solids phase at particle level and describes the behavior of the gas phase at a continuum level. Most often, the solution of the gas phase is determined on a larger scale than a single particle. Hence, again an empirical correlation is required to describe the gas-solids interphase momentum transfer. Moreover, in the two-dimensional Lagrange approach, particles are modeled as disks, which introduces problems in translating the two-dimensional properties of the disks to the pseudo three-dimensional solution of the gas phase. Different strategies for this translation have been studied and validated. Extensive steady-state and dynamic validation of the Lagrange-Euler approach with detailed small-scale experiments show this model is not as promising as claimed by many authors.

Samenvatting (Summary in Dutch)

Dit proefschrift beschrijft wiskundige modellen voor een zeer belangrijke toepassing in gas stromingen met een zeer hoge volume fractie deeltjes: gas-vaste wervelbedden. Wervelbedden komen veelvuldig voor in de chemische, olie, farmaceutische, voedings, en energie industrie. Dit proefschrift behandelt zowel Euler-Euler modellen als Lagrange-Euler modellen in het beschrijven van stromingsverschijnselen waarin veel deeltjes voorkomen.

Het Euler-Euler model beschrijft zowel de gasfase als de deeltjesfase als een continuüm waarbij het dynamische gedrag van beide fases wordt beschreven door de massa- en impulsbehoudswetten voor elke individuele fase te beschouwen. Zogenaamde sluitingsrelaties worden gebruikt om de eigenschappen van beide individuele fases en de dynamische interactie tussen de fases te beschrijven. In de literatuur is een veelvuldige discussie omtrent de correcte formulering van de individuele massa- en impulsbehoudswetten en met name omtrent de sluitingsrelaties is geen overeenstemming. Dit werk zet de behoudswetten en sluitingsrelaties gedetailleerd uiteen en de uitkomsten van simulaties met de verschillende behoudswetten en sluitingsrelaties worden met elkaar en met experimenteel werk vergeleken.

Verschillende vormen van de impulsoverdrachtsrelatie tussen de gasfase en de deeltjesfase zijn in de literatuur voorgesteld, maar allen van deze zijn (deels) empirisch en zijn bepaald uit metingen over een grote lengte- en tijdschaal in vloeistof condities. Simulaties met verschillende vormen van de impulsoverdrachtsrelatie zijn vergeleken met experimenten, waarbij de Wen en Yu (1966) relatie het beste bevonden is. Het feit dat de impulsoverdrachtsrelatie op een grote lengte- en tijdschaal en in vloeistof condities is afgeleid, maakt deze relatie een zwakke schakel in het Euler-Euler model. Hierdoor wordt het dynamische "samenklont" gedrag van deeltjes op zeer kleine schaal niet goed beschreven.

De deeltjes-deeltjes interacties worden beschouwd als binaire botsingen, en lijken daardoor sterk op de theorie van de kinetische gas theorie. Een belangrijk verschil tussen twee botsende deeltjes en twee botsende gas moleculen is het niet ideale botsgedrag bij deeltjes, beschreven door de restitutie coefficient. De restitutie coefficient is gedefinieerd als de verhouding van de totale loodrechte impuls voor de botsing en de totale loodrechte impuls erna. Een granulaire kinetische theorie kan worden afgeleid op basis van dit niet ideale gedrag, waarin zowel de deeltje botsingen als de deeltjes bewegingen worden beschouwd. De granulaire theorie beschreven in dit werk verwaarloost de invloed van de gasfase op deeltjes-deeltjes botsingen. Het is te verwachten dat deze invloed wel belangrijk is bij vloeistof-deeltjes stromingen

of gas stromingen met weinig deeltjes. In de literatuur worden vergelijkingen voorgesteld waarin de correlatie tussen de gasfase snelheidsfluctuaties en de deeltjesfase snelheidsfluctuaties wordt beschreven. Deze vergelijkingen zijn toegepast in de simulaties maar blijken een te verwaarlozen rol te spelen.

Een uitgebreide experimentele validatie van zowel het stationaire als het dynamische gedrag van gas-vaste wervelbedden met simulaties van het Euler-Euler model laat zien dat dit model een redelijk goede voorspelling geeft van het stationaire en dynamische gedrag van wervelbedden. Waar experimenten beschreven in de literatuur slechts het gemiddelde stationaire gedrag en het gemiddelde dynamische gedrag beschrijven, voorspelt het Euler-Euler model het gehele, tijdsafhankelijke gedrag van gas-vaste wervelbedden. Het grote nadeel van van deze computermodellen is de enorme rekentijd die vereist is om een complete voorspelling te verkrijgen van een reële geometrie.

In de jaren 80 is een kinetische theorie ontwikkeld door Lopez de Haro en anderen voor gassen bestaande uit verschillende soorten moleculen. De granulaire theorie voor twee verschillende, niet ideale deeltjes is geïmplementeerd en gevalideerd in dit werk. Hoewel de rekentijd voor dit model enorm is, laten simulatieresultaten zien dat dit model in de realiteit in wervelbedden voorkomende fysische effecten, zoals segregatie, mengen, en inversie van deeltjeslagen, goed kan beschrijven.

Het Lagrange-Euler model beschrijft het gedrag van de vaste fase als individuele deeltjes en beschrijft de gasfase als continuüm. Meestal wordt de oplossing van de gasfase op een grotere lengteschaal bepaald dan de grootte van een enkel deeltje. Hierdoor zijn wederom (deels) empirische correlaties vereist om de impulsoverdracht tussen de gasfase en de vaste fase te beschrijven. Nog een nadeel van het tweedimensionale Lagrange-Euler model komt voort uit de vertaling van de tweedimensionale porositeit van de deeltjes fase naar een driedimensionale porositeit vereist voor de pseudo driedimensionale gasfase. Verschillende strategieën voor deze vertaalslag zijn in dit werk beschreven en gevalideerd. Een uitgebreide stationaire en dynamische validatie van het Lagrange-Euler model met zelf uitgevoerde gedetailleerde experimenten van een vergelijkbare geometrie laten zien dat dit model niet zo veel belovend is als door veel auteurs wordt geclaimd.

Chapter 1

Introduction

Abstract

A fluidized bed is widely used in many operations in the chemical, petroleum, pharmaceutical, agricultural, biochemical, food, and power generation industries. The hydrodynamic behavior of fluidized systems is non-linear and therefore very complex. Especially, scale-up from lab-scale to industrial scale is a major problem. A short introduction into fluidization is given and the issues in modeling fluidized beds are pointed out. Finally, the research objectives and outline of this thesis are presented.

1.1 Fluidization

A collection of particles in a column, tube or container is called a bed of particles. When a fluid is blown from below into the column, tube or container, this flow exerts a (drag) force on each individual particle. In fluidization, the gravity force acting on the particles is (over) compensated by the drag forces exerted on the particles by the local flow of fluid. This local flow of the fluid is different for every particle, making the exact behavior of each particle unique. Gas-solid fluidization probably constitutes the most important industrial application involving gas-solid flows (Kunii and Levenspiel, 1991), because of its excellent heat transfer characteristics and easy solids handling due to solids mobility. n fluidization different regimes exist, each inhabiting different overall gas- and solids-flow patterns and thus different heat- and mass-transfer properties. Some examples of fluidization regimes are shown in Figure 1.1. When the gravity force is counter balanced by the average drag force result-

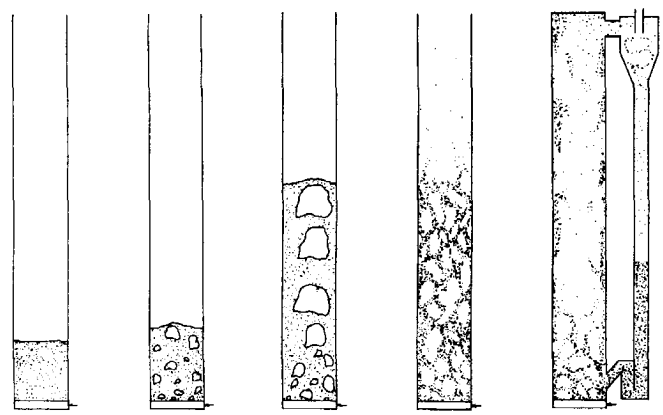

Figure 1.1: *Different fluidization regimes with increasing gas velocity. (Grace, 1990)*

ing from the gas flow, the state of fluidization is called minimum fluidization. Most industrial fluidized systems are operated at a gas flow well above the so-called minimum fluidization velocity, because then the fluidized solids behave somewhat like a fluid, with a highly improved mass and heat transfer. Depending on the size of the individual particles, bubbles form at a gas flow somewhere above this minimum fluidization velocity. With so called Geldart B particles (see Figure 1.2), gas bubbling occurs just beyond the state of minimum fluidization. With finer particles, denoted by Geldart A particles, there is

a fluidization regime called "delayed bubbling" between the state of minimum fluidization and the fluidization state in which bubbles form. The gas velocity at which gas bubbles start occurring is called the minimum bubbling velocity. Gas bubbles determine the behavior of the fluidized system to a large extent, and are responsible for solids agitation. This work focusses on bubbling and

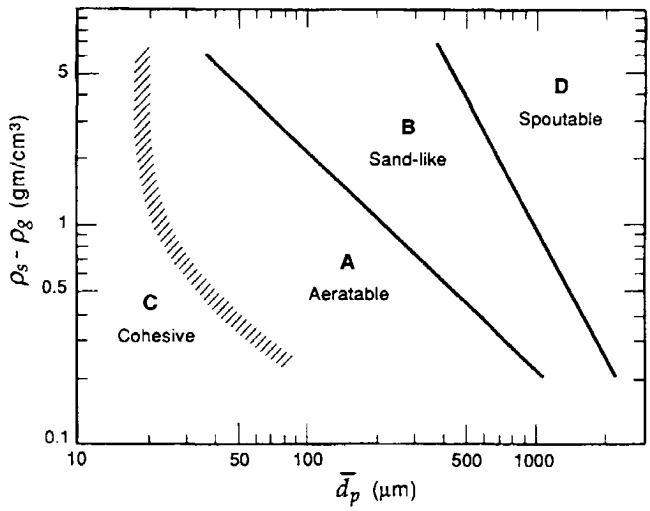

Figure 1.2: *The Geldart particle size classification, from very fine particles (C) to very coarse particles (D) (Geldart, 1973).*

slugging fluidized beds (see Figure 1.1). Such fluidized beds typical operate in the dense flow regime, characterized by a solids volume fraction ranging from 0.4 to 0.6. Bubbling fluidized beds possess several advantages:

- The liquid-like flow of the bed allows easy handling of the particles.
- The solids are rapidly mixed, leading to almost isothermal conditions.
- It is possible to continuously operate the bed for both the gas and solid phases.
- The heat and mass transfer rates between the particles are high.
- The circulation of particles makes it possible to add or remove vast quantities of heat.
- The bed is suitable for large-scale operations.

However, fluidized beds inhabit major disadvantages, such as:

- The hydrodynamics of the fluidized bed are very complex.

- The fluidized bed is difficult to scale-up due to its non-linear behavior.
- The erosion rate of the reactor and internals can be very high.
- In some processes, agglomeration and sintering of fine particles can occur which can considerably change the fluidization behavior of the bed.
- The rapid solids mixing induces a significant back-mixing of the gas phase, which spreads the gas residence time, thus effecting the selectivity and conversion of the chemical reactions involved.

The success of fluidized beds in industrial operations has shown that the advantages can outweigh the disadvantages.

The ability to improve existing fluidized beds and to design optimal future processes strongly depends on the possibility to develop a better understanding of the hydrodynamics of these systems. The difficulty in design consists mainly of the scale-up problem; many equations describing the behavior of fluidized beds are empirical and determined under laboratory conditions, giving too little confidence that these equations scale-up properly to predict the correct behavior of industrial size fluidized beds.

It has been shown that fluidized beds are deterministic chaotic systems (Daw and Halow, 1991; Van den Bleek and Schouten, 1993). By accepting this dynamic characterization of the fluidized bed, the hydrodynamics may be quantified through non-linear methods. Non-linear analysis techniques determining the unpredictability of the system through means of the Kolmogorov entropy can possibly determine the type of hydrodynamic behavior of the fluidized bed. Scale-up laws based on these quantities have been proposed in literature (Van der Stappen, 1996; Schouten *et al.* 1996).

A step further is not only to accept the chaotic behavior of the fluidized bed, but also to exploit this. It is well-known that applying a small perturbation to a chaotic system can lead to a different behavior in time. This may well be possible with fluidized bed reactors. First, however, detailed knowledge of the hydrodynamics of fluidized beds must be known to understand how, when, and where to apply a perturbation.

1.2 Hydrodynamic modeling of fluidized beds

Computational fluid dynamics (CFD) is an emerging technique for predicting the flow behavior of many systems, necessary for scale-up, design or optimization. Although single-phase CFD tools are widely available and in most cases successfully applied (Hirsch, 1988, Anderson, 1995), multiphase flow

remains difficult due to the complex mathematics and the difficulty in the physical description.

CFD models for gas-solid flow can be divided into two groups, Lagrangian models and Eulerian models. Lagrangian models, or discrete particle models, calculate the path of each individual particle with the second law of Newton. The interaction between the particles can be described by a potential force, by collision dynamics, or this interaction may be neglected. The drawbacks of the Lagrangian technique are the large memory requirements and the long calculation time. Moreover, the description of the drag force from the gas phase acting on each particle is difficult to model accurately, and is in practice based on experimental correlations.

Eulerian models treat the particle phase as a continuum and average out motion on the scale of individual particles. Computations by this method can predict the behavior of dense-phase flows on a realistic geometry. The drawback of this method, however, is that one requires complex statistics to translate the behavior of many particles into one continuum. For this purpose, often granular kinetic theory is employed. This is becoming a typical approach for performing Eulerian simulations.

With nowadays granular kinetic theory, Eulerian simulations should predict very similar results as Lagrangian simulations, as the assumptions and underlying equations applied in both methods are the same. A difference between the methods arises when the length scale of the averaging in the kinetic theory exceeds the length scale of physical phenomena influencing the behavior. For instance, clusters of particles can play a role in the stress behavior of the solids phase. When the length scale of averaging is taken to be larger than the size of the smallest clusters, a discrepancy between the actual physics and averaged kinetic theory can occur. This is the key issue for the failure of correctly describing very fine powders (Geldart A type) with kinetic theory; the mesh size should be taken only a few particle diameters to obtain sensible results and this has not been done up to now.

1.3 Research objectives

The key issue of this thesis is to model the hydrodynamics of the fluidized bed, and verify the outcome of the models with experimental data and existing empirical correlations. Detailed modeling of the Eulerian model and the Lagrangian model is undertaken. The goals of this thesis are to:

- determine the correct governing equations of the Eulerian-Eulerian model for describing gas-solid flows, and compare the impact of applying differ-

ent governing equations by performing simulations with different governing equations and compare the outcome of these simulations with data from the literature.

- make an inventory of the closure models describing the solids phase in the Eulerian-Eulerian model, and compare the impact of each of the closure relations on simulations. The outcome of the different simulations is compared with data and empirical correlations from the literature.
- validate the Eulerian-Eulerian CFD model with the well known experimental steady-state data from Hilligardt and Werther (1986) and Darton *et al.* (1977) and propose values based on performed simulations for empirical parameters present in the model proposed by Hilligardt and Werther (1986).
- validate the dynamic predictions from the Eulerian-Eulerian CFD model by comparing the unpredictability of the fluidized bed expressed by the Kolmogorov entropy with experimental values, by comparing the most dominant frequency in the pressure and voidage fluctuations with the equation proposed by Baskakov *et al.* (1986), and by comparing the power spectral density from the fluctuations with the power spectral densities determined through experiments.
- develop a Eulerian-Eulerian CFD model describing a mixture containing two particle species and verify the trends predicted by simulations obtained by employing this model with trends put forward by De Groot (1967), Grace and Sun (1991), Wu and Baeyens (1998) and Rasul *et al.* (1999).
- validate the outcome of Lagrangian-Eulerian simulations with experiments described in this thesis.

Results of all performed simulations are validated with experimental work as much as possible. Obtaining the detailed description of what the experimentalist has exactly measured, and the spread and error in the measurements are some of the key problems in comparing the abundance of data obtained form the simulations with the experimentalists' work. The final step would be to use the simulations to predict new empirical correlations, which predict values and variation on these values for all types of fluidized bed parameters.

1.4 Outline

In Chapter **2**, a detailed derivation of the granular kinetic theory is presented. All the assumptions and equations are shown. It can be seen that the Eulerian model inhabits the same physics as the Lagrangian model.

In Chapter 3, a detailed derivation of the governing equations of gas-solid flows is made. One of the most important conclusions of Chapter 3 is that many researchers are using incorrect governing equations. Also, the influence of differing granular kinetic theories and interphase drag correlations is presented. Finally, the impact of all the differences in CFD models are illustrated by simulations of three types of fluidized beds.

Chapter 4 presents detailed information regarding simulations of steady state and the dynamic behavior of fluidized beds, and compares these to generally accepted measurements of (semi)-empirical correlations from the literature. New correlation values are presented for existing correlations describing the bubble rise velocity in fluidized beds. Finally, it is shown that present gas/solid CFD models can correctly capture the dynamics of fluidized beds.

Chapter 5 presents the development of the kinetic theory for a bimodal mixture of spherical, nearly elastic, spheres. This kinetic theory is implemented in an Eulerian-Eulerian CFD model. The CFD model is used to demonstrate some of the key features of binary mixture fluidization, and outcome of the simulations are compared to trends described in literature.

In Chapter 6, the Lagrangian-Eulerian model for gas-solid flow is outlined. Some of the features and assumptions of this model are described and discussed. This chapter also describes a small laboratory-scale experiment of which the results are directly compared to results of the Lagrangian-Eulerian simulations employing the same geometry. Conclusions are drawn upon the basis of the comparison between the simulations and the experiments.

In Chapter 7 the main conclusions of this chapter are put forward in the framework of earlier research in simulations describing gas-solid flow. Finally a short outlook of the future is presented in this chapter.

Appendix A describes the software and animations present on the CD accompanying this thesis. With the software, you can reproduce some of the simulations described in this thesis, or expand to your own wishes. The animations give some idea of the features of the software.

Chapter 2

Kinetic theory of granular flow

In this chapter, the derivation of the granular kinetic theory is presented from first principles. This work is an overview based on the work of Chapman and Cowling (1970), Jenkins and Richman (1983), Grad (1963), and Lun *et al.* (1984).

Abstract

In this chapter, the Boltzmann equation and the physical principles of the kinetic theory for granular flow are put forward and the resulting Enskog equation is derived. It is shown how to derive the flow of any particle property, and how to incorporate inelastic collisions into the Boltzmann or Enskog equation. One analytical method is presented that solves the steady-state form of the Enskog equation assuming fully elastic conditions, leading to the Maxwellian velocity distribution, and two analytical methods are presented that approximate the full transient Enskog equation. The results of these approximations are shown for granular flow with frictionless, inelastic collisions. Finally the method to incorporate a bimodal particle size or weight distribution is outlined.

2.1 Introduction

The purpose of this chapter, is to elucidate the observed properties of particle suspensions, and capture these properties in so-called closure relations. These closure relations can be employed to describe the continuum behavior of the particle suspension in the Eulerian-Eulerian framework. The method described is the kinetic theory of granular flow. We consider an idealized system of identically shaped, spherical particles, because the individual behavior of these particles is well-known. In an ordinary description of particle systems, usually mechanics (second law of Newton) are used to determine the behavior of the complete system. In mechanics, the aim is usually to precisely determine the events that follow from prescribed initial conditions. However, we seldom know the detailed initial conditions of the particles, that is, the situation and the state of motion of every particle at a prescribed initial instant. Furthermore, the power of nowadays computers, and even computers in the next decennia, are quite insufficient to follow all the subsequent motions and locations of every particle of any practical application. Hence, for practical applications, we do not elucidate the behavior of the individual particles, but focus ourselves only on the statistical properties, such as the mean number or velocity of particles, averaged over a short time interval, or the average distribution of linear velocities or other motions among these particles.

The restriction we imply ourselves is not only *necessary*, for the feasibility, it is also physically *adequate*, because experiments and simulations of particulate systems in nearly all cases produce only such 'average' properties. Thus, the aim of the kinetic theory of granular flow is to find out, for example, how the distribution of the *averaged* motion of the particles will vary with time; or again, how a mixture of two sets of particles of different kinds will vary, by the process known as diffusion or segregation. In this attempt, we consider both the dynamics of the particle-particle collisions as well as the statistics of the collisions. In this, we must use probability assumptions, for example, that the particles are generally distributed throughout a very small volume.

To start the derivation of the kinetic theory, we will first introduce the averaging through probabilities.

2.2 Probability density function

The distribution of velocities among a large number of particles in a volume element $d\mathbf{r}$ can be represented by the distribution of their velocity points $\mathbf{c}$ in the velocity space. The number density of this volume element will generally be a function of the location in space, $\mathbf{r}$, of the time, t, as well of the velocity $\mathbf{c}$. Therefore, the number density of the particles at volume $\mathbf{r}$ with velocity

$\mathbf{c}$ at time t is denoted by $f(\mathbf{c}, \mathbf{r}, t)$. This definition implies that the probable number of particles which at time t are situated in the volume element $(\mathbf{r}, \mathbf{r} + d\mathbf{r})$, and have velocities lying in the range $(\mathbf{c}, \mathbf{c} + d\mathbf{c})$ is $f(\mathbf{c}, \mathbf{r}, t)d\mathbf{c}d\mathbf{r}$, where f is called the *probability density function*. This does not mean that the given volume element actually contains this number of particles having velocities in the range $(\mathbf{c}, \mathbf{c} + d\mathbf{c})$ at the time t. This is the average number of such particles when the fluctuations which occur in a short time dt are smoothed out. This definition involves a probability concept; the form in which function f appears will be a result of the probable, or average, behavior of the particles.
The whole number of particles in the space at time t, is obtained by integrating f over all possible velocities and locations at this time. The number density is thus defined as,

$$n(\mathbf{r}, t) = \int f(\mathbf{c}, \mathbf{r}, t)d\mathbf{c} \tag{2.1}$$

The function f can never be negative, must tend to zero as $\mathbf{c}$ becomes infinite, and is assumed to be finite and continuous for all values of t.

When the behavior or number of the particles also depends upon the temperature, T, or the differing mass of the particle, m, the definition of the probability density function can be extended to

$$f(\mathbf{c}, \mathbf{r}, T, m, t)d\mathbf{c}d\mathbf{r}dTdm$$

indicating the number of particles at time t, in volume element $(\mathbf{r}, \mathbf{r}+d\mathbf{r})$, with velocities in the range $(\mathbf{c}, \mathbf{c} + d\mathbf{c})$, temperatures in the range $(T, T + dT)$, and masses in the range $(m, m + dm)$. The resulting equations from this probability density function can be derived analogously. In most cases in this work, however, this extension is not necessary.

2.3 The Boltzmann equation

We consider the situation in which each particle is subject to an external force with acceleration $\mathbf{a}$. Between times t and $t + dt$ the velocity $\mathbf{c}$ of any particle that does not collide with another particle will change to $\mathbf{c} + \mathbf{a}dt$, and its position vector $\mathbf{r}$ will change to $\mathbf{r} + \mathbf{c}dt$. The number of particles $f(\mathbf{c}, \mathbf{r}, t)d\mathbf{c}d\mathbf{r}$ at time t is equal to the number of particles $f(\mathbf{c} + \mathbf{a}dt, \mathbf{r} + \mathbf{c}dt, t + dt)d\mathbf{c}d\mathbf{r}$ at time $t + dt$ if collisions between particles are neglected. The change in f over dt is caused only by collisions of particles:

$$\{f(\mathbf{c} + \mathbf{a}dt, \mathbf{r} + \mathbf{c}dt, t + dt) - f(\mathbf{c}, \mathbf{r}, t)\}d\mathbf{c}d\mathbf{r} = \frac{\partial_c f}{\partial t}d\mathbf{c}d\mathbf{r}dt \tag{2.2}$$

where $\frac{\partial_e f}{\partial t}$ is the rate of change of f at a fixed point due to particle collisions. By dividing by dcdrdt and making dt tend to zero, Boltzmann's equation for f is obtained:

$$\frac{\partial f}{\partial t} + \mathbf{c} \cdot \nabla f + \mathbf{a} \cdot \frac{\partial f}{\partial \mathbf{c}} = \frac{\partial_e f}{\partial t} \tag{2.3}$$

or

$$\mathfrak{D} f = \frac{\partial_e f}{\partial t} \tag{2.4}$$

where $\mathfrak{D} f$ denotes the left-hand side of Equation 2.3.

2.4 Change of particle properties

This section describes the effect of influences which are able to change specific particle properties; these particle properties can be, for instance, mass, momentum, or energy. Let ϕ be any particle property. If the Boltzmann equation is multiplied by $\phi d\mathbf{c}$ and integrated over the velocity-space, the equation of change of particle properties is obtained:

$$\int \phi \mathfrak{D} f d\mathbf{c} = n\mathbb{C}(\phi) \tag{2.5}$$

in which the right-hand term denotes the influence of binary, instantaneous collisions, so it is the integrated form of $\frac{\partial_e f}{\partial t}$. For convenience, the peculiar velocity C is used as an independent variable instead of c:

$$\mathbf{C} \equiv \mathbf{c} - \langle \mathbf{c} \rangle \tag{2.6}$$

The dependency of f on c should also be changed to C, for example for $\frac{\partial f(\mathbf{C})}{\partial t}$

$$\frac{\partial f(\mathbf{c} - \langle \mathbf{c} \rangle)}{\partial t} = \frac{\partial f}{\partial \mathbf{C}} \frac{\partial \mathbf{C}}{\partial t} = \frac{\partial f}{\partial \mathbf{C}} \frac{\partial (\mathbf{c} - \langle \mathbf{c} \rangle)}{\partial t} = -\frac{\partial \langle \mathbf{c} \rangle}{\partial t} \frac{\partial f}{\partial \mathbf{C}} + \frac{\partial f}{\partial t} \frac{\partial \mathbf{c}}{\partial \mathbf{C}} \tag{2.7}$$

Hence, $\frac{\partial f}{\partial t}$ and $\frac{\partial f}{\partial \mathbf{r}}$ have to be replaced by respectively

$$\frac{\partial f}{\partial t} - \frac{\partial \langle \mathbf{c} \rangle}{\partial t} \cdot \frac{\partial f}{\partial \mathbf{C}} \quad \text{and} \quad \frac{\partial f}{\partial \mathbf{r}} - \frac{\partial \langle \mathbf{c} \rangle}{\partial \mathbf{r}} \frac{\partial f}{\partial \mathbf{C}}$$

in order to take account of the dependence of f on t and r through the dependence of C on c. Hence, the expression for $\mathfrak{D} f$ becomes

$$\frac{\partial f}{\partial t} - \frac{\partial \langle \mathbf{c} \rangle}{\partial t} \cdot \frac{\partial f}{\partial \mathbf{C}} + (\langle \mathbf{c} \rangle + \mathbf{C}) \left(\frac{\partial f}{\partial \mathbf{r}} - \frac{\partial \langle \mathbf{c} \rangle}{\partial \mathbf{r}} \frac{\partial f}{\partial \mathbf{C}} \right) + \mathbf{a} \frac{\partial f}{\partial \mathbf{C}} \tag{2.8}$$

Now the 'mobile operator' or 'time-derivative following the motion' is introduced as is common in hydrodynamics:

$$\frac{D}{Dt} = \frac{\partial}{\partial t} + <\mathbf{c}> \cdot \frac{\partial}{\partial \mathbf{r}}$$

This is the time derivative following the mean flow. Then

$$\mathfrak{D}f = \frac{Df}{Dt} + \mathbf{C} \cdot \frac{\partial f}{\partial \mathbf{r}} + <\mathbf{a} \cdot \frac{\partial f}{\partial \mathbf{C}}> - \frac{D <\mathbf{c}>}{Dt} \cdot \frac{\partial f}{\partial \mathbf{C}} - \frac{\partial f}{\partial \mathbf{C}} \mathbf{C} : \frac{\partial <\mathbf{c}>}{\partial \mathbf{r}} \tag{2.9}$$

With this, Equation 2.5 can be rewritten into

$$\int \phi \left(\frac{Df}{Dt} + \mathbf{C} \cdot \frac{\partial f}{\partial \mathbf{r}} + <\mathbf{a} \cdot \frac{\partial f}{\partial \mathbf{C}}> - \frac{D <\mathbf{c}>}{Dt} \cdot \frac{\partial f}{\partial \mathbf{C}} - \frac{\partial f}{\partial \mathbf{C}} \mathbf{C} : \frac{\partial <\mathbf{c}>}{\partial \mathbf{r}} \right) = n\mathbb{C}(\phi) \tag{2.10}$$

For further derivation of this equation, the following integrals are used for the transformation:

$$\int \phi \frac{Df}{Dt} d\mathbf{C} = \frac{D}{Dt} \int \phi f d\mathbf{C} - \int \frac{D\phi}{Dt} f d\mathbf{C} = \frac{D(n <\phi>)}{Dt} - n <\frac{D\phi}{Dt}> \tag{2.11}$$

$$\int \phi \frac{\partial f}{\partial \mathbf{r}} d\mathbf{C} = \frac{\partial}{\partial \mathbf{r}} \cdot \int \phi \mathbf{C} f d\mathbf{C} - \int \frac{\partial \phi}{\partial \mathbf{r}} \cdot \mathbf{C} f d\mathbf{C} = \frac{\partial n <\phi \mathbf{C}>}{\partial \mathbf{r}} - n <\mathbf{C} \cdot \frac{\partial \phi}{\partial \mathbf{r}}> \tag{2.12}$$

$$\int \phi \frac{\partial f}{\partial \mathbf{C}} = \left[\phi f \right]_{u,v,w=-\infty}^{u,v,w=\infty} - \int \frac{\partial \phi}{\partial \mathbf{C}} f d\mathbf{C} = -n <\frac{\partial \phi}{\partial \mathbf{C}}> \tag{2.13}$$

in which $\phi f \to 0$ as any velocity component approaches $\pm\infty$. By the same argument

$$\int \phi \frac{\partial f}{\partial \mathbf{C}} \mathbf{C} d\mathbf{C} = -n <\frac{\partial \phi \mathbf{C}}{\partial \mathbf{C}}> = -n <\phi> - n <\frac{\partial \phi}{\partial \mathbf{C}} \mathbf{C}> \tag{2.14}$$

Using these results, we obtain the Enskog equation, which is a generalization of Maxwell's equation:

$$\begin{aligned} n\mathbb{C}(\phi) = & \frac{Dn <\phi>}{Dt} + n <\phi> \frac{\partial <\mathbf{c}>}{\partial \mathbf{r}} + \frac{\partial n <\phi \mathbf{C}>}{\partial \mathbf{r}} \\ & - n \left[<\frac{D\phi}{Dt}> + <\mathbf{C} \frac{\partial \phi}{\partial \mathbf{r}}> + <\mathbf{a} \cdot \frac{\partial \phi}{\partial \mathbf{C}}> - \frac{D <\mathbf{c}>}{Dt} \cdot <\frac{\partial \phi}{\partial \mathbf{C}}> - \right. \\ & \left. <\frac{\partial \phi}{\partial \mathbf{C}} \mathbf{C}> : \frac{\partial <\mathbf{c}>}{\partial \mathbf{r}} \right] \end{aligned} \tag{2.15}$$

Setting $\phi = 1$, the mass balance can be obtained:

$$\frac{Dn}{Dt} + n \frac{\partial <\mathbf{c}>}{\partial \mathbf{r}} = 0 \tag{2.16}$$

This equation is also called the equation of continuity, expressing the conservation of the number of particles in the suspension. Inserting the equation of continuity into the Enskog equation (Equation 2.15), simplifies the Enskog equation to

$$n\mathbb{C}(\phi) = n\frac{D<\phi>}{Dt} + \frac{\partial n<\phi\mathbf{C}>}{\partial \mathbf{r}} - n\left[<\frac{D\phi}{Dt}> + <\mathbf{C}\frac{\partial\phi}{\partial \mathbf{r}}> + <\mathbf{a}\cdot\frac{\partial\phi}{\partial \mathbf{C}}> - \frac{D<\mathbf{c}>}{Dt}\cdot<\frac{\partial\phi}{\partial \mathbf{C}}> - <\frac{\partial\phi}{\partial \mathbf{C}}\mathbf{C}>:\frac{\partial<\mathbf{c}>}{\partial \mathbf{r}}\right] \tag{2.17}$$

With $\phi = \mathbf{C}$, this simplified Enskog equation corresponds to the balance of linear momentum:

$$n\frac{D<\mathbf{c}>}{Dt} + \frac{\partial n<\mathbf{CC}>}{\partial \mathbf{r}} = n<\mathbf{a}> + n\mathbb{C}(\mathbf{C}) \tag{2.18}$$

because $<\mathbf{C}> = 0$. The first term denotes the change, following the motion, of momentum. The second term denotes the stress tensor due to particle movement. The first term on the right-hand side represents the external body-forces, as fluid influences and gravity. The last term on the right-hand side denotes the momentum change due to collisions. The momentum equation and the continuity equation are identical with the equations of continuity and momentum derived for a continuous fluid in hydrodynamics. This provides a justification for the hydrodynamical treatment of a particle suspension.

With $\phi = \mathbf{CC}$ the mean of the second moment of velocity fluctuation is obtained from the simplified Enskog equation:

$$n\frac{D\mathbf{CC}}{Dt} + \frac{\partial n<\mathbf{CCC}>}{\partial \mathbf{r}} = -2n<\mathbf{CC}>:\frac{\partial<\mathbf{c}>}{\partial \mathbf{r}} + 2n<\mathbf{aC}> + n\mathbb{C}(\mathbf{CC}) \tag{2.19}$$

The first term denotes the change of the second moment of velocity fluctuation. The second term represents the third moment of velocity fluctuation. The first term on the right-hand side represents the transport of the second moment of velocity fluctuation due to the average velocity of the particles. The second term on the right-hand side represents the influence of the external forces. It can be readily seen, that if the force does not depend on $\mathbf{C}$, this term vanishes. The last term represents the influences of collisions on the second moment of velocity fluctuation. The balance of third moment of velocity fluctuation is obtained by inserting $\phi = \mathbf{CCC}$:

$$n\frac{D\mathbf{CCC}}{Dt} + \frac{\partial n<\mathbf{CCCC}>}{\partial \mathbf{r}} = -3n<\mathbf{CCC}>:\frac{\partial<\mathbf{c}>}{\partial \mathbf{r}} + 3n<\mathbf{aCC}> + 3n<\mathbf{CC}><\mathbf{c}>\frac{\partial<\mathbf{c}>}{\partial \mathbf{r}} + n\mathbb{C}(\mathbf{CC}) \tag{2.20}$$

Balances of higher order momenta are fairly easily generated. However, most methods concerned with solving these equations only consider up to second order.

2.5 Flow of particle properties

This section describes the influence of the flow of particles upon the particle properties. Consider the flow of particles across a small element of surface dS, moving in the system with a velocity c', as depicted in Figure 2.1. Let n be a unit vector drawn normal to the surface dS. The passage of a particle across dS is regarded as positive or negative according as the particle crosses dS in the direction of n. The velocity of the particle is C' relative to the surface dS. Hence, the surface dS moves with the velocity $\mathbf{C}' = \mathbf{c} - \mathbf{c}'$. Consider all the

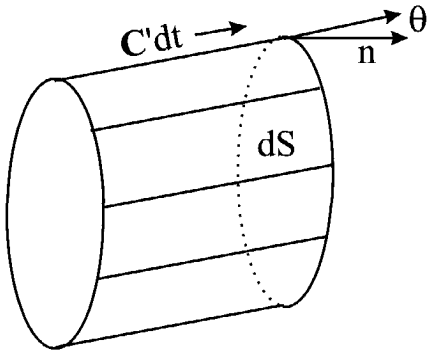

Figure 2.1: *The passage of particles across surface element* dS.

particles whose peculiar velocity lie in the range $(\mathbf{C}, \mathbf{C} + d\mathbf{C})$. If one of these particles crosses dS in a time dt, then at the beginning of dt, the particle must lie somewhere inside the cylinder on dS as base, with the geometry specified by C'dt (See Figure 2.1). If dr denotes the volume of this cylinder, the number of particles with velocities in the range $(\mathbf{C}, \mathbf{C} + d\mathbf{C})$ crossing dS during dt is $fd\mathbf{C}dr$. The volume of the cylinder is given by $dr = \pm C'\cos\theta dt dS$, where θ is the angle between n and C'. The flow of any property ϕ of a particle is given by

$$\phi(\mathbf{C}' \cdot \mathbf{n}) f d\mathbf{C} dt dS$$

referring to the number of particles with a velocity in the range $(\mathbf{C}, \mathbf{C} + d\mathbf{C})$ that cross dS in dt and carrying amount of ϕ property with it. The total flow of ϕ across dS during dt is

$$dSdt \int (\mathbf{C}' \cdot \mathbf{n}) \phi f d\mathbf{C} = dSdt <n(\mathbf{C}' \cdot \mathbf{n})\phi> \qquad (2.21)$$

Now, $\mathbf{C}' = \mathbf{C} + \langle \mathbf{c} \rangle - \mathbf{c}'$, so that

$$n \langle \mathbf{C}'\phi \rangle = n \langle \mathbf{C}\phi \rangle + n(\langle \mathbf{c} \rangle - \mathbf{c}') \langle \phi \rangle \tag{2.22}$$

The second term of Equation 2.22 is driven by the number flow, $n(\langle \mathbf{c} \rangle - \mathbf{c}')$, which denotes the mean velocity of the particles relative to the surface element. If the surface element dS moves with velocity $\langle \mathbf{c} \rangle$, the number flow is zero, independent of the orientation of the surface. Hence, the second term on the right-hand side represents the contribution to the rate of flow of ϕ due to the net number-flow of particles across dS.

The first term on the right-hand side is independent of the number flow, and its component normal to dS represents the rate of flow of ϕ when the number flow vanishes, thus when dS moves with the mean velocity of the particles. Thus, the vector $n \langle \mathbf{C}\phi \rangle$ is a flux-vector for the property ϕ.

If we consider the momentum of each particle as a flow property, i.e. $\phi = mc$, and insert this into Equation 2.21, we can express the flow of momentum across a surface dS as

$$dSdt \int (\mathbf{C}' \cdot \mathbf{n}) mc f d\mathbf{C} = dSdt n m \langle (\mathbf{C}' \cdot \mathbf{n}) \mathbf{c} \rangle$$

which represents the normal stress tensor due to kinetic transport of momentum. Rewriting this further, we can obtain

$$\begin{aligned} \langle C'_n \mathbf{c} \rangle &= \langle C'_n (\langle \mathbf{c} \rangle + \mathbf{C}) \rangle = \langle C'_n \mathbf{C} \rangle \\ &= \langle \mathbf{n} \cdot (\mathbf{C} + \langle \mathbf{c} \rangle - \mathbf{c}') \mathbf{C} \rangle = \langle C_n \mathbf{C} \rangle \end{aligned}$$

Hence the total stress tensor equals

$$\overline{\overline{P}} = \rho \langle \mathbf{C}\mathbf{C} \rangle \tag{2.23}$$

Likewise, the flux vector of energy is expressed as

$$\mathbf{q} = \frac{1}{2} \rho \langle C^2 \mathbf{C} \rangle \tag{2.24}$$

Note that the stress tensor and flux vector derived in this section are only due to the transport of particles; the influence of collisions has not been considered.

2.6 Particle collisions

In kinetic theory for granular flow, collisions are considered binary and instantaneous. Since only smooth and spherically symmetrical particles are

considered, the force which either exerts on the other is directed along the line joining their centers. Moreover, rotation is not considered. It is supposed that the effect of any external force which acts on the particle during collision can be neglected compared to the dynamic effect of the collision. With these assumptions, the velocities before and after a collision have definite values, which are denoted $\mathbf{c}_i, \mathbf{c}_j$ before the collision, and $\mathbf{c}'_i, \mathbf{c}'_j$ after the collision. The details of the collision itself are of no importance for the theory; it is only important to know the relation between the initial and the final velocities.

Before the collision, the relative velocity of the two particles is $\mathbf{g} \equiv (\mathbf{c}_i - \mathbf{c}_j)$, and by definition $\mathbf{g} \cdot \mathbf{n} > 0$ (otherwise the particles move away from each other), where $\mathbf{n}$ is the normal unit vector lying in the direction of the vector joining the center of the two particles, defined with its origin at the point of contact (see Figure 2.2). The collision impulse $\mathbf{P}$ exerted by particle j on

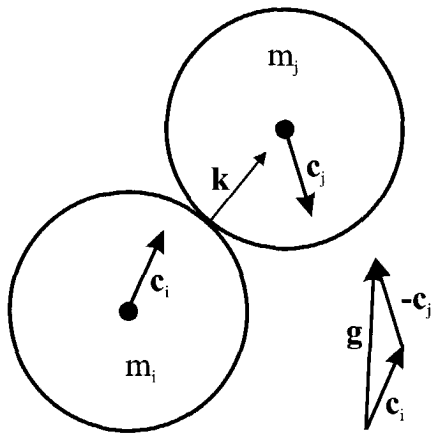

Figure 2.2: *A pair of colliding particles*

particle i is directed along the line connecting the centers,

$$\mathbf{P} = m_i(\mathbf{c}'_i - \mathbf{c}_i) = -m_j(\mathbf{c}'_j - \mathbf{c}_j) \tag{2.25}$$

$\mathbf{P}$ can be obtained by characterizing the incomplete restitution of the normal component of the relative velocity, using the coefficient of restitution e, with $0 \leq e \leq 1$:

$$\mathbf{g}' \cdot \mathbf{n} = -e\mathbf{g} \cdot \mathbf{n} \tag{2.26}$$

With equations 2.25 and 2.26 the equation for $\mathbf{P}$ can be derived:

$$\mathbf{P} = -\frac{m_i m_j}{m_i + m_j}(1 + e)(\mathbf{g} \cdot \mathbf{n})\mathbf{n} \tag{2.27}$$

Consider the motion of the center of particle j relative to the center of the first particle, so relative to axes moving with the center of particle i (see Figure 2.3). For such a collision to occur, the center of particle j must cut a plane through $(\sigma_i + \sigma_j)^2 \mathbf{n} d\mathbf{n}$, where σ_i represents the radius of particle i. Hence, the center of particle j must lie in a volume $(\mathbf{g}dt)[(\sigma_i + \sigma_j)^2 \mathbf{n} d\mathbf{n}]$. In a collision between two particles, the value ϕ_j, representing a property of particle j, is changed to ϕ_j'. Thus the particle property ϕ for this particle is changed by the amount $\phi_j' - \phi_j$. The change in $\sum \phi_j$ due to all collisions where particle i has a velocity in $(\mathbf{c}_i, \mathbf{c}_i + d\mathbf{c}_i)$, particle j has a velocity in $(\mathbf{c}_j, \mathbf{c}_j + d\mathbf{c}_j)$, occurring in the direction in $(\mathbf{n}, \mathbf{n} + d\mathbf{n})$, and in time $(t, t + dt)$ is

$$(\phi_j' - \phi_j) f_{(2)}(\mathbf{c}_i, \mathbf{r}_i, \mathbf{c}_j, \mathbf{r}_i + (\sigma_i + \sigma_j)\mathbf{n}, t)(\sigma_i + \sigma_j)^2 (\mathbf{g} \cdot \mathbf{n}, t) d\mathbf{n} d\mathbf{c}_i d\mathbf{c}_j d\mathbf{r} dt \tag{2.28}$$

$f_{(2)}(\mathbf{c}_i, \mathbf{r}_i, \mathbf{c}_j, \mathbf{r}_j, t)$ represents the pair probability density function, indicating the number density of a pair of particles, where the first particle is located at $\mathbf{r}_i$ with velocity $\mathbf{c}_i$, and the second particle located at $\mathbf{r}_j$ with velocity $\mathbf{r}_j$ at time t. $f_{(2)}$ characterizes the statistics of binary collisions.
Integration over all values of $\mathbf{c}_1$ and $\mathbf{c}_2$ gives the total change during dt in $\sum \phi_i$, summed over all particles in dr, due to collisions. Since the number of particles in dr is ndr, this integral must equal $n d\mathbf{r} \mathbb{C}(\phi) dt$. Dividing by drdt, results in:

$$n\mathbb{C}(\phi)_j = \iiint_{\mathbf{g}\cdot\mathbf{n}>0} (\phi_j' - \phi_j) f_{(2)}(\mathbf{c}_i, \mathbf{r}_i, \mathbf{c}_j, \mathbf{r}_i + (\sigma_i + \sigma_j)\mathbf{n}, t)(\sigma_i + \sigma_j)^2 (\mathbf{g} \cdot \mathbf{n}) d\mathbf{n} d\mathbf{c}_i d\mathbf{c}_j \tag{2.29}$$

where the condition $\mathbf{g} \cdot \mathbf{n} > 0$ indicates that the integration is to be taken over all values of $\mathbf{n}$, $\mathbf{c}_i$, and $\mathbf{c}_2$ for which a collision is impending. For the particle

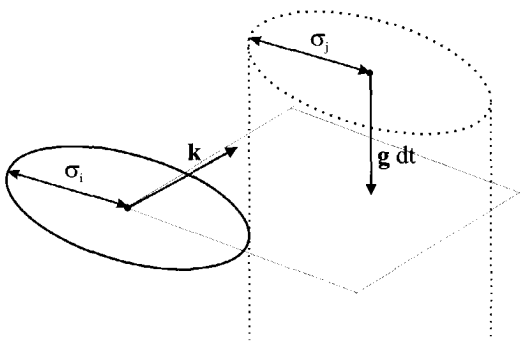

Figure 2.3: *The outlines of two possible colliding particles. Both particles must lie in a volume* $(\mathbf{g}dt)[(\sigma_i + \sigma_j)^2 \mathbf{n} d\mathbf{n}]$ *to possibly collide.*

j the rate of increase of property ϕ can be found by the same arguments as above, only by interchanging the roles of the colliding particles by interchanging subscripts i and j and replacing $\mathbf{n}$ by $-\mathbf{n}$. This contribution may thus be written as

$$n\mathbb{C}(\phi)_i = \iiint_{\mathbf{g}\cdot\mathbf{n}>0} (\phi_i' - \phi_i) f_{(2)}(\mathbf{c}_i, \mathbf{r}_j - (\sigma_i + \sigma_j)\mathbf{n}, \mathbf{c}_j, \mathbf{r}_j)(\sigma_i + \sigma_j)^2(\mathbf{g}\cdot\mathbf{n})d\mathbf{n}d\mathbf{c}_i d\mathbf{c}_j \tag{2.30}$$

A more symmetric form of $n\mathbb{C}(\phi)$ is obtained by taking one half of the sum of $n\mathbb{C}(\phi)_j$ and $n\mathbb{C}(\phi)_i$. To this effect, $f_{(2)}(\mathbf{c}_i, \mathbf{r}_j - (\sigma_i + \sigma_j)\mathbf{n}, \mathbf{c}_j, \mathbf{r}_j, t)$ is expanded in a Taylor series about $\mathbf{r} = \mathbf{r}_i$. On solving the first term in this series,

$$\begin{aligned} f_{(2)}(\mathbf{c}_i, \mathbf{r}, \mathbf{c}_j, \mathbf{r} + (\sigma_i + \sigma_j)\mathbf{n}, t) = \\ f_{(2)}(\mathbf{c}_i, \mathbf{r} - (\sigma_i + \sigma_j)\mathbf{n}, \mathbf{c}_j, \mathbf{r}\mathbf{n}, t) + (\sigma_i + \sigma_j)\mathbf{n}\frac{\partial}{\partial \mathbf{r}}\left(1 - \frac{\sigma_i + \sigma_j}{2!}\mathbf{n}\frac{\partial}{\partial \mathbf{r}}\right. \\ \left. + \frac{(\sigma_i + \sigma_j)^2}{3!}\mathbf{n}\mathbf{n}\frac{\partial^2}{\partial \mathbf{r}\mathbf{r}} - \ldots\right) f_{(2)}(\mathbf{c}_i, \mathbf{r}, \mathbf{c}_j, \mathbf{r} + (\sigma_i + \sigma_j)\mathbf{n}, t) \end{aligned} \tag{2.31}$$

By inserting Equation 2.31 into Equation 2.30, and taking one half of the sum of equations 2.29 and 2.30, the collisional rate of change may then be written as

$$\begin{aligned} n\mathbb{C}(\phi) = \frac{1}{2}\iiint_{\mathbf{g}\cdot\mathbf{n}>0} (\phi_j' - \phi_j) f_{(2)}(\mathbf{c}_i, \mathbf{r}_i, \mathbf{c}_j, \mathbf{r}_i + (\sigma_i + \sigma_j)\mathbf{n}, t)(\sigma_i + \sigma_j)^2(\mathbf{g}\cdot\mathbf{n})d\mathbf{n}d\mathbf{c}_i d\mathbf{c}_j \\ + \frac{1}{2}\iiint_{\mathbf{g}\cdot\mathbf{n}>0} (\phi_i' - \phi_i) f_{(2)}(\mathbf{c}_i, \mathbf{r}_i, \mathbf{c}_j, \mathbf{r}_i + (\sigma_i + \sigma_j)\mathbf{n}, t)(\sigma_i + \sigma_j)^2(\mathbf{g}\cdot\mathbf{n})d\mathbf{n}d\mathbf{c}_i d\mathbf{c}_j \\ + \frac{\sigma_i + \sigma_j}{2}\iiint_{\mathbf{g}\cdot\mathbf{n}>0} (\phi_i' - \phi_i)\mathbf{n}\frac{\partial}{\partial \mathbf{r}}\left(1 - \frac{\sigma_i + \sigma_j}{2!}\mathbf{n}\frac{\partial}{\partial \mathbf{r}} + \frac{(\sigma_i + \sigma_j)^2}{3!}\mathbf{n}\mathbf{n}\frac{\partial^2}{\partial \mathbf{r}\mathbf{r}} - \ldots\right) \\ \cdot f_{(2)}(\mathbf{c}_i, \mathbf{r}, \mathbf{c}_j, \mathbf{r} + (\sigma_i + \sigma_j)\mathbf{n}, t)(\sigma_i + \sigma_j)^2(\mathbf{g}\cdot\mathbf{n})d\mathbf{n}d\mathbf{c}_i d\mathbf{c}_j \end{aligned} \tag{2.32}$$

The first two integrals on the right-hand side can now be combined. With this, the collisional rate of change can be expressed into three terms:

$$n\mathbb{C}(\phi) = \chi(\phi) - \frac{\partial\Theta(\phi)}{\partial \mathbf{r}} - \frac{\partial <\mathbf{c}>}{\partial \mathbf{r}}\Theta\left(\frac{\partial\phi}{\partial \mathbf{C}}\right) \tag{2.33}$$

where Θ can be seen as a 'transfer' contribution, and χ is a source-like contribution. The last term on the right-hand side arises from extracting the term $\frac{\partial}{\partial \mathbf{r}}$ from the integral, and must be included when the particle property ϕ is a function of $\mathbf{C}$. The expressions for χ and Θ, which represent a source-like

contribution and a flux contribution, respectively, are

$$\chi(\phi) = \frac{1}{2} \iiint_{\mathbf{g}\cdot\mathbf{n}>0} (\phi_i' + \phi_j' - \phi_i - \phi_j) \cdot f_{(2)}(\mathbf{c}_i, \mathbf{r}_i, \mathbf{c}_j, \mathbf{r}_i + (\sigma_i + \sigma_j)\mathbf{n}, t)(\sigma_i + \sigma_j)^2(\mathbf{g}\cdot\mathbf{n})d\mathbf{n}d\mathbf{c}_i d\mathbf{c}_j \quad (2.34)$$

$$\Theta(\phi) = -\frac{\sigma_i + \sigma_j}{2} \iiint_{\mathbf{g}\cdot\mathbf{n}>0} (\phi_i' - \phi_i)\mathbf{n}\left(1 - \frac{\sigma_i + \sigma_j}{2!}\mathbf{n}\frac{\partial}{\partial \mathbf{r}} + \frac{(\sigma_i + \sigma_j)^2}{3!}\mathbf{n}\mathbf{n}\frac{\partial^2}{\partial \mathbf{r}\mathbf{r}} - \ldots\right) \cdot f_{(2)}(\mathbf{c}_i, \mathbf{r}, \mathbf{c}_j, \mathbf{r} + (\sigma_i + \sigma_j)\mathbf{n}, t)(\sigma_i + \sigma_j)^2(\mathbf{g}\cdot\mathbf{n})d\mathbf{n}d\mathbf{c}_i d\mathbf{c}_j \quad (2.35)$$

For the second order of velocity fluctuation, Equation 2.27 is inserted for the change of momentum due a collision. When the expression for $f_{(2)}$ is known, these integrals can be evaluated.

2.7 Solving Boltzmann's equation

One of the ways to obtain an expression for f and f_2 from the Boltzmann and Enskog equations, is through method the of direct numerical simulation of particles (i.e. follow the trajectories of each individual particle). This requires the integration of the second law of Newton for each particle, and the collision algorithm described in the beginning of the previous paragraph. When the system with particles is not correlated with the initial state, the particle probability density function can be written as

$$f(\mathbf{c}, \mathbf{r}, t) = <\delta(\mathbf{r} - \mathbf{x})\delta(\mathbf{c} - \mathbf{u})> \quad (2.36)$$

in which the averaging is an ensemble averaging over a very large number of particles and realizations, for all possible locations $\mathbf{x}$ and velocities $\mathbf{u}$ occurring in the system. The operator $\delta(x)$ is one for $x = 0$ and zero for all other x. This method is computationally very expensive and even with today's computers can only be used to compute a relatively small number of particles.

Another discrete particle method which can be applied is the Monte-Carlo simulation method. In this method, the equations described in the last paragraphs are solved through a probability process, in which certain random states are rejected, and some random states are accepted. From the characteristics and number of accepted states, the probability density function f can be calculated through the averaging over these states with Equation 2.36. Although this method can be used for a relatively large number of particles, it is sometimes necessary to sacrifice detailed physical description of the system, and again, this method does not reach the number of particles occurring in practical situations. Therefore, the Boltzmann and Enskog equations are most often solved through means of calculus.

2.8 Boltzmann's equation in steady, ideal state

Consider a simple particulate suspension in which the particles possess only energy of translation, are subject to no external forces, and no momentum is lost during the collisions (equal to setting $e = 1$ in the last paragraph). If the state is uniform so that the probability distribution function f is independent of $\mathbf{r}$, the probability distribution function is equal before and after collisions, so

$$f_i' f_j' = f_i f_j \tag{2.37}$$

or

$$\ln f_i' + \ln f_j' = \ln f_i + \ln f_j \tag{2.38}$$

Thus not only is the state of the particulate system steady, collisions as a whole produce no effect of f. Hence, the effect of every type of collision is exactly balanced by the effect of the inverse process. This is called *detailed balancing.*

The particle properties which remain unaltered by collisions are called *summational invariants.* For the above assumptions, the particle system has three summational invariants:

$$\phi^{(1)} = 1,\ \boldsymbol{\phi}^{(2)} = m\mathbf{C},\ \text{and}\ \phi^{(3)} = mC^2 \tag{2.39}$$

which represent the conservation of mass, momentum, and kinetic energy. Any linear combination of the three conserved functions $\phi^{(i)}$ is also a summational invariant. But no further summational invariant which is linearly independent of $\phi^{(i)}$ can exist for particles whose energy is purely translatory. From this, we can conclude that $\ln f$ is a summational invariant for collisions, and must thus be a linear combination of $\phi^{(i)}$, hence

$$\ln f = \sum_{i=1}^{3} \alpha^{(i)} \phi^{(i)} \tag{2.40}$$

where $\alpha^{(1)}$ and $\alpha^{(3)}$ are scalars and $\boldsymbol{\alpha}^{(2)}$ is a vector. Because the particle system is uniform, $\alpha^{(i)}$ must be independent of $\mathbf{r}$ and t. Then we find

$$\ln f = \ln \alpha^{(1)} + \alpha^{(3)} m \left(\mathbf{c} + \frac{\boldsymbol{\alpha}^{(2)}}{\alpha^{(3)}} \right)^2 - \left(\frac{\boldsymbol{\alpha}^{(2)}}{\alpha^{(3)}} \right)^2 m^2 \alpha^{(3)} \tag{2.41}$$

when we now define $\mathbf{C}' = \mathbf{c} - \frac{\boldsymbol{\alpha}^{(2)}}{\alpha^{(3)}}$, we can find

$$f = \alpha^{(0)} e^{-\alpha^{(3)} \cdot \frac{1}{2} m C'^2} \tag{2.42}$$

where $\alpha^{(0)}$ is a new constant. This result was first obtained by Maxwell in 1867, and the state of the system is therefore said to be a Maxwellian state. The constants $\alpha^{(i)}$ can be evaluated in terms of the number density n, the mean velocity $<\mathbf{c}>$ and the velocity fluctuations $\mathbf{C}$:

$$\begin{aligned} n &= \int f d\mathbf{c} = \alpha^{(0)} \int e^{-\alpha^{(3)} \cdot \frac{1}{2} m C'^2} d\mathbf{C}' \\ &= \alpha^{(0)} \int_0^\infty C'^2 e^{-\alpha^{(3)} \cdot \frac{1}{2} m C'^2} dC' \int_0^\pi \sin\Theta d\Theta \int_0^{2\pi} d\varphi \\ &= \alpha^{(0)} \left(\frac{2\pi}{m\alpha^{(3)}} \right)^{\frac{3}{2}} \end{aligned} \tag{2.43}$$

Using the equation for the average momentum,

$$\begin{aligned} n <\mathbf{c}> &= \int \mathbf{c} f d\mathbf{c} \\ &= \int \left(\frac{\boldsymbol{\alpha}^{(2)}}{\alpha^{(3)}} + \mathbf{C}' \right) f d\mathbf{C}' \\ &= n \frac{\boldsymbol{\alpha}^{(2)}}{\alpha^{(3)}} + \alpha^{(0)} \int \mathbf{C}' e^{-\alpha^{(3)} \cdot \frac{1}{2} m C'^2} d\mathbf{C}' \end{aligned} \tag{2.44}$$

The second term vanishes because the integrand form is an odd function of the components of $\mathbf{C}'$. Hence, $<\mathbf{c}> = \frac{\boldsymbol{\alpha}^{(2)}}{\alpha^{(3)}}$ and $\mathbf{C}'$ is identical with $\mathbf{C}$, the peculiar velocity. Finally, from the definition of energy in the uniform steady state

$$\begin{aligned} \frac{1}{2} m <C^2> &= \frac{m}{2n} \int C^2 f d\mathbf{c} \\ &= \frac{m}{2} \left(\frac{m\alpha^{(3)}}{2\pi} \right)^{\frac{3}{2}} \int C^2 e^{-\alpha^{(3)} \cdot \frac{1}{2} m C^2} d\mathbf{C} \\ &= \frac{3}{2\alpha^{(3)}} \end{aligned} \tag{2.45}$$

Hence, $\alpha^{(3)} = \frac{3}{m<C^2>}$. Consequently the final form for the probability distribution function in the ideal steady state is equivalent to

$$f = n \left(\frac{3m}{2\pi m <C^2>} \right)^{\frac{3}{2}} e^{-3mC^2/(2m<C^2>)} \tag{2.46}$$

which is the usual form of the Maxwell probability distribution function. The Maxwellian distribution is a Gaussian type distribution, as can be seen in Figure 2.4.

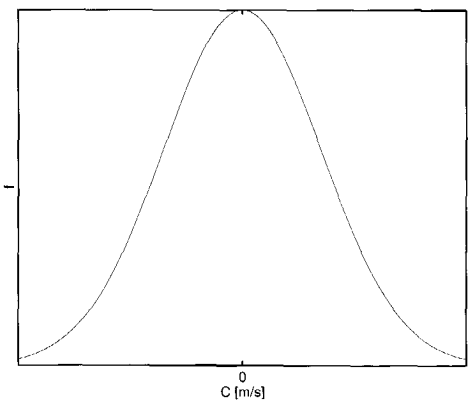

Figure 2.4: *A Maxwellian distribution. The numbers indicating the X and Y-axis are dependent upon the magnitude of* $<C^2>$.

2.9 Expressing $f_{(2)}$ in f

In early development of kinetic theory, the pair probability distribution function was expressed as the product of the two individual probability distribution functions:

$$f_{(2)}(\mathbf{c}_i, \mathbf{r}_i, \mathbf{c}_j, \mathbf{r}_j, t) \approx f(\mathbf{c}_i, \mathbf{r}_i) f(\mathbf{c}_j, \mathbf{r}_j) \tag{2.47}$$

This is called the assumption of *molecular chaos.* In the molecular chaos assumption, particles are assumed to be randomly distributed, without their volume playing a role. Hence, particles may overlap. In very dilute systems this may not lead to a large deviation, as the chance that two particles overlap is very small. For denser gases, Equation 2.47 is rewritten to

$$f_{(2)}(\mathbf{c}_i, \mathbf{r}_i, \mathbf{c}_j, \mathbf{r}_j, t) \approx g_0 f(\mathbf{c}_i, \mathbf{r}_i) f(\mathbf{c}_j, \mathbf{r}_j) \tag{2.48}$$

where g_0 is called the radial distribution function at contact. g_0 is equal to one for a dilute particle system, and increases with increasing particle number density, becoming infinite as the particle system approaches the state in which the particles are packed so closely together that motion is impossible. The effect of g_0 is to reduce the volume in which the center of any particle can lie, and so to increase the probability of a collision. By the assumption of molecular chaos, g_0 is only a function of the position and not a function of the velocity. The function g_0 needs only to be evaluated at the point of contact and not for every position in the system.

2.10 Solving the PDF for the non-ideal state: Enskog approach

The present section deals with the method by which Enskog solved the Boltzmann equation in a general case. We consider here a simple particle system, with only one type of particle. The extension to a bimodal case is, however, not a difficult one and can be found in section 2.12.
The Enskog method is one of successive approximation. Suppose that the solution is expressible in the form of an infinite series

$$f = f^{(0)} + f^{(1)} + f^{(2)} + \dots \tag{2.49}$$

It can be shown that $f^{(0)}$ is proportional to n, $f^{(1)}$ is independent of n, $f^{(2)}$ is proportional to $1/n$, and so on. This implicates that the more dilute the system is, the more important the higher orders become. Theoretically, it is possible to describe only a few particles in a space using this method. Practically, however, this implicates that it is necessary to take an enormous number of higher orders of $f^{(i)}$ into account.

Suppose that when ξ operates on this series, the result can be expressed as a series in which the i-th term involves only the first i terms of the series,

$$\begin{aligned}\xi(f) = \xi(f^{(0)} + f^{(1)} + f^{(2)} + \dots) = &\xi^{(0)}(f^{(0)}) + \xi^{(1)}(f^{(0)}, f^{(1)}) \\ &+ \xi^{(2)}(f^{(0)}, f^{(1)}, f^{(2)}) + \dots\end{aligned} \tag{2.50}$$

which together ensure that $\xi(f) = 0$. Substituting this equation into the Boltzmann equation, we can find

$$\xi(f_i) = J(f_i f_j) + \mathfrak{D} f_i \tag{2.51}$$

where the first term denotes the changes due to particle collisions, and the second term is the left-hand side of the Boltzmann equation, as defined earlier. Then, by substituting Equation 2.49

$$\xi(f_i) = J\{(\sum_r f_i^{(r)})(\sum_s f_j^{(s)})\} + \sum_r \mathfrak{D} f_i^{(r)} \tag{2.52}$$

If we take $f^{(0)}$ to be the Maxwellian distribution,

$$\xi(f_i^{(0)}) = \mathfrak{D} f_i^{(0)} = J\{f_i^{(0)} f_j^{(0)}\} = 0 \tag{2.53}$$

because the influence of collisions then does not affect the probability distribution itself. We can thus interpret higher orders of f, $f^{(i)}$ with $i > 0$ as corrections to the Maxwellian state.

2.10.1 The second approximation to f for a slightly inelastic granular material

The remainder of this section is devoted to the evolution of the second approximation to f without an external force. Moreover, the hydrodynamic equations resulting from the second approximation to f will be presented. The equation from which $f^{(1)}$ is to be determined is

$$\xi(f_i^{(0)}, f_i^{(1)}) = \mathfrak{D} f_i^{(1)} + J\{f_i^{(1)} f_j^{(0)}\} + J\{f_i^{(0)} f_j^{(1)}\} \tag{2.54}$$

As we have expressed $f^{(0)}$ in terms of $\mathbf{C}$, it is convenient to express $\mathfrak{D} f_i^{(1)}$ in a form analogous to that form of $\mathfrak{D}$ given in $\mathbf{C}$, as in Equation 2.9. Now, supposing we can express $\mathfrak{D} f_i^{(1)}$ in terms of $f_i^{(0)}$:

$$\mathfrak{D} f^{(1)} = \frac{Df^{(0)}}{Dt} + \mathbf{C} \cdot \frac{\partial f^{(0)}}{\partial \mathbf{r}} + <\mathbf{a} \cdot \frac{\partial f^{(0)}}{\partial \mathbf{C}}> - \frac{D <\mathbf{c}>}{Dt} \cdot \frac{\partial f^{(0)}}{\partial \mathbf{C}} - \frac{\partial f^{(0)}}{\partial \mathbf{C}} \mathbf{C} : \frac{\partial <\mathbf{c}>}{\partial \mathbf{r}} \tag{2.55}$$

We have now expressed $f^{(1)}$ in terms of the known function $f^{(0)}$, and this can be analytically solved

$$\mathfrak{D} f^{(1)} = f^{(0)} \left\{ \left(\frac{3mC^2}{2m <C^2>} - \frac{5}{2} \right) \mathbf{C} \left[\frac{\partial \ln \frac{1}{3} <C^2>}{\partial \mathbf{r}} + \frac{\partial \ln n}{\partial \mathbf{r}} \right] + \frac{3}{<C^2>} \overset{\circ}{\mathbf{C}\mathbf{C}} : \frac{\partial <\mathbf{c}>}{\partial \mathbf{r}} \right\} \tag{2.56}$$

in which the fluctuating external forces on the particles are not taken into account. We now substitute $f^{(1)} = f^{(0)} \Phi^{(1)}$. We then find for the right hand side of Equation 2.54

$$J\{f_i^{(1)} f_j^{(0)}\} + J\{f_i^{(0)} f_j^{(1)}\} = \iiint_{\mathbf{g} \cdot \mathbf{k} > 0} (\Phi_i'^{(1)} + \Phi_j'^{(1)} - \Phi_i^{(1)} - \Phi_j^{(1)}) g_0 f_i^{(0)} f_j^{(0)} (\sigma_i + \sigma_j)^2 (\mathbf{g} \cdot \mathbf{k}) d\mathbf{k} d\mathbf{c}_i d\mathbf{c}_j \tag{2.57}$$

Φ is called a perturbation function, because it denotes the first order alteration of f from a Maxwellian distribution. Because Φ is, like f, a scalar, it suffices to look only at the scalar solutions of Equation 2.57. The right-hand side of Equation 2.57 is linear in Φ, and the right-hand side of Equation 2.56 is linear in the space-derivatives of $\frac{\ln <C^2>}{3}$, $<\mathbf{c}>$ and n. Hence, the most general scalar solution of Φ is a sum of four parts:

1. A linear combination of the components of $\frac{\partial \ln <C^2>}{\partial \mathbf{r}}$. For this to be a scalar this must be given in the form of the inproduct of $\frac{\partial \ln <C^2>}{\partial \mathbf{r}}$ with another tensor.
2. A linear combination of the components of $\frac{\partial <\mathbf{c}>}{\partial \mathbf{r}}$; this must similarly be the scalar product of this with another tensor.
3. A linear combination of the components of $\frac{\partial \ln n}{\partial \mathbf{r}}$; this must be the scalar product of this with another tensor.
4. The most general scalar solution of the equation

$$\iiint_{\mathbf{g}\cdot\mathbf{k}>0} (\Phi_i'^{(1)} + \Phi_j'^{(1)} - \Phi_i^{(1)} - \Phi_j^{(1)}) g_0 f_i^{(0)} f_j^{(0)} (\sigma_i + \sigma_j)^2 (\mathbf{g}\cdot\mathbf{k}) d\mathbf{k} d\mathbf{c}_i d\mathbf{c}_j = 0 \tag{2.58}$$

Thus we can write

$$\Phi^{(1)} = -\frac{1}{n}\sqrt{\frac{2}{3}<C^2>}\mathbf{A}\cdot\frac{\partial \ln \frac{1}{3}<C^2>}{\partial \mathbf{r}} - \frac{2}{n}\overline{\overline{B}} : \frac{\partial <\mathbf{c}>}{\partial \mathbf{r}} - \frac{1}{n}\sqrt{\frac{2}{3}<C^2>}\mathbf{D}\cdot\frac{\partial \ln n}{\partial \mathbf{r}} + \alpha^{(1,1)} + \boldsymbol{\alpha}^{(1,2)}\cdot m\mathbf{C} + \alpha^{(1,3)}\frac{1}{2}mC^2 \tag{2.59}$$

where $\mathbf{A}$ and $\mathbf{D}$ are vectors which are functions of $\mathbf{C}$, $\overline{\overline{B}}$ is a tensor which is a function of $\mathbf{C}$. $\alpha^{(1,1)}$, $\boldsymbol{\alpha}^{(1,2)}$, and $\alpha^{(1,3)}$ are constants. Substituting this equation into Equation 2.57 we can obtain three different equations,

$$\frac{1}{n}\iiint_{\mathbf{g}\cdot\mathbf{k}>0} (\mathbf{A}_i' + \mathbf{A}_j' - \mathbf{A}_i - \mathbf{A}_j) g_0 f_i^{(0)} f_j^{(0)} (\sigma_i + \sigma_j)^2 (\mathbf{g}\cdot\mathbf{k}) d\mathbf{k} d\mathbf{c}_i d\mathbf{c}_j = f_i^{(0)} \left(\frac{C^2}{3<C^2>} - \frac{5}{2}\right)\sqrt{\frac{1}{3<C^2>}}\mathbf{C} \tag{2.60}$$

$$\frac{1}{n}\iiint_{\mathbf{g}\cdot\mathbf{k}>0} (\mathbf{D}_i' + \mathbf{D}_j' - \mathbf{D}_i - \mathbf{D}_j) g_0 f_i^{(0)} f_j^{(0)} (\sigma_i + \sigma_j)^2 (\mathbf{g}\cdot\mathbf{k}) d\mathbf{k} d\mathbf{c}_i d\mathbf{c}_j = f_i^{(0)} \left(\frac{C^2}{3<C^2>} - \frac{5}{2}\right)\sqrt{\frac{1}{3<C^2>}}\mathbf{C} \tag{2.61}$$

$$\frac{1}{n}\iiint_{\mathbf{g}\cdot\mathbf{k}>0} (\overline{\overline{B}}_i' + \overline{\overline{B}}_j' - \overline{\overline{B}}_i - \overline{\overline{B}}_j) g_0 f_i^{(0)} f_j^{(0)} (\sigma_i + \sigma_j)^2 (\mathbf{g}\cdot\mathbf{k}) d\mathbf{k} d\mathbf{c}_i d\mathbf{c}_j = f_i^{(0)} \frac{3}{<C^2>}\mathring{\mathbf{C}}\mathbf{C} \tag{2.62}$$

The constants $\alpha^{(1,1)}$, $\alpha^{(1,2)}$, and $\alpha^{(1,3)}$ are to be chosen that the corresponding form for $f^{(1)}$ satisfies the equations

$$\int \phi^{(i)} f^{(1)} d\mathbf{c} = \int \phi^{(i)} f^{(0)} \Phi^{(1)} d\mathbf{c} = 0 \tag{2.63}$$

where $\phi^{(i)}$ denotes any of the summational invariants. When the particle system is a dissipative system, as with most practical cases, not all of these invariants go to zero; which makes them no longer invariant of course. If we substitute the change of momentum and energy due to the collisions, Equation 2.27, we can find closures for the α's. The **A**, **D** and $\overline{\overline{B}}$ are slightly more difficult to obtain. By the use of Sonine polynomials, however, the above three integrals for **A**, **D** and $\overline{\overline{B}}$ can be expressed. We can thus obtain for $\Phi^{(1)}$ the expression

$$\begin{aligned}\Phi^{(1)} = {} & a_1 \overset{\circ}{\mathbf{CC}} : \frac{\partial <\mathbf{c}>}{\partial \mathbf{r}} + a_2 \left(\frac{5}{2} - \frac{C^2}{3 <C^2>} \right) \mathbf{C} \cdot \frac{\partial \ln \frac{1}{3} <C^2>}{\partial \mathbf{r}} \\ & + a_3 \left(\frac{5}{2} - \frac{C^2}{3 <C^2>} \right) \mathbf{C} \cdot \frac{\partial \ln n}{\partial \mathbf{r}}\end{aligned} \tag{2.64}$$

where the constants a_1, a_2 and a_3 are a result of the above derivation, but may also be found by inserting simplified physical situations, as simple shear, constant granular temperature, or zero velocity.
From this Φ, we can express the stress tensor and the flux of fluctuating velocity as

$$\rho <\mathbf{CC}> = \frac{\rho}{3} <C^2> \overline{\overline{I}} - \frac{2\mu}{\eta(2-\eta) g_0} \left[1 + \frac{8}{5} \eta (3\eta - 2) \epsilon_s g_0 \right] \overline{\overline{S}} \tag{2.65}$$

$$\begin{aligned}\frac{1}{2} \rho <C^2 \mathbf{C}> = {} & - \frac{\zeta}{g_0} \left\{ \left[1 + \frac{12}{5} \eta^2 (4\eta - 3) \epsilon_s g_0 \right] \nabla \left(\frac{1}{3} <C^2> \right) \right. \\ & \left. + \frac{12}{5} \eta (2\eta - 1)(\eta - 1) \frac{d}{d\epsilon_s} \left(\epsilon_s^2 g_0 \right) \frac{<C^2>}{3n} \nabla n \right\}\end{aligned} \tag{2.66}$$

with the abbreviations

$$\zeta = \frac{8\lambda}{\eta(41 - 33\eta)} \tag{2.67}$$

$$\lambda = \frac{75m\sqrt{\frac{<C^2>}{3\pi}}}{64\sigma^2} \tag{2.68}$$

$$\eta = \frac{1}{2}(1 + e) \tag{2.69}$$

$$\mu = \frac{5m\frac{<C^2>}{3\pi}}{15\sigma^2} \tag{2.70}$$

$$\epsilon_s = \frac{nm}{\rho} = \frac{n}{V} \tag{2.71}$$

$$\bar{\bar{S}} = \frac{1}{2}\left(\nabla <\mathbf{c}> + \{\nabla <\mathbf{c}>\}^T\right) - \frac{1}{3}\left(\nabla \cdot <\mathbf{c}>\bar{\bar{I}}\right) \tag{2.72}$$

For the momentum equation, the source like contribution, χ, is zero (see Equation 2.35), and thus only the transport contribution Θ remains (see Equation 2.34). Thus, the total collisional contribution to the momentum equation has the exact same form as the stress tensor. Therefore, most researchers denote this contribution as 'the collisional contribution to the particle-particle stress'. The term for the momentum equation is

$$\bar{\bar{\Theta}}_{\text{momentum}} \equiv \bar{\bar{P}}_c = \frac{4}{3}\rho <C^2> \eta\epsilon_s g_0 \bar{\bar{I}} - \frac{16\mu\epsilon_s}{5(2-\eta)}\left[1 + \frac{8}{5}\eta(3\eta - 2)\epsilon_s g_0\right]\bar{\bar{D}}$$
$$- \frac{256}{5\pi}\eta\mu\epsilon_2^2 g_0\left[\frac{6}{5}\bar{\bar{D}} + (\nabla \cdot <\mathbf{c}>)\bar{\bar{I}}\right] \tag{2.73}$$

These equations can be directly used to solve the volume averaged momentum equations for a granular material, as they can be transformed to the hydrodynamic definitions of viscosities and normal pressure. For the energy equation, both Θ and χ are non-zero. The form of Θ is added in the same form as the flux of fluctuating energy, and is therefore often described as the addition to the flux of fluctuating energy due to collisions. These terms are

$$\Theta_{\text{energy}} \equiv q_c = -\frac{12\eta\zeta\epsilon_s}{5}\left\{\left[1 + \frac{12}{5}\eta^2(4\eta - 3)\epsilon_s g_0\right.\right.$$
$$\left. + \frac{16}{15\pi}(41 - 33\eta)\eta\epsilon_s g_0\right]\nabla\left(\frac{1}{3}<C^2>\right)$$
$$\left.\frac{125}{\eta}(2\eta - 1)(\eta - 1)\frac{d}{d\epsilon_s}\left(\epsilon_s^2 g_0\right)\frac{<C^2>}{3n}\nabla n\right\} \tag{2.74}$$

$$\chi_{\text{energy}} = \frac{48}{\sqrt{\pi}}\eta(1 - \eta)\frac{\rho\epsilon^2}{\sigma}g_0\left(\frac{<C^2>}{3}\right)^{\frac{3}{2}} \tag{2.75}$$

Inserting $e = 1$ ($\eta = 1$) into Equation 2.75 leads to $\chi = 0$, which shows that the energy equation becomes a conserved quantity for systems where collisions are fully elastic.

2.11 Solving the PDF with Grad's method

The method developed by Grad, Grads' 13^{th} moment approximation, is close to the Enskog approximation, but is slightly different in the treatment of the derivatives. The higher orders of f are expressed as

$$f(\mathbf{c},\mathbf{r},t) = \left(1 - a_1\frac{\partial}{\partial \mathbf{c}} + \frac{\mathbf{a}_2}{2!}\frac{\partial^2}{\partial \mathbf{cc}} - \frac{\overline{\overline{a}}_3}{3!}\frac{\partial^3}{\partial \mathbf{ccc}} + \ldots\right) f^{(0)}(\mathbf{c},\mathbf{r},t) \tag{2.76}$$

where $f^{(0)}$ denotes the Maxwellian distribution. The coefficients a_i which depend on $\mathbf{r}$ and t but not on $\mathbf{c}$ are first, second and higher order tensor values functions, symmetric in all of their indices. Inserting this equation, together with the Maxwellian distribution into Equation 2.1, leads to $a_1 = 0$ for the mean of the velocity fluctuation to equal zero. Moreover, physically the additional restriction $\mathbf{a}_2 \cdot \overline{\overline{I}} = 0$ must be imposed.

When Equation 2.76 is truncated after its first three non-zero terms, the remaining unknowns are n, $<\mathbf{c}>$, $<C^2>$, $\mathbf{a}_2$, and $\overline{\overline{a}}_3$. In principle, they are determined by equations: the balance of mass, the balance of linear momentum, the balance of energy, the balance of second moment, and the balance of third moment. Grad assumed that the tensor $\overline{\overline{a}}_3$, which lacks any physical interpretation, is related as

$$a_{ijk} = \frac{1}{5}\left(a_{imm}\delta_{jk} + a_{jmm}\delta_{ik} + a_{kmm}\delta_{ij}\right) \tag{2.77}$$

With this reduction 13 unknowns remain, leading to the name 13-moment system. Inserting this equation and the Maxwellian distribution into Equation 2.76, the following equation can be obtained

$$\frac{f(\mathbf{c},\mathbf{r})}{f_{(0)}(\mathbf{c},\mathbf{r})} = 1 + \frac{3\mathbf{a}_2}{<C^2>^2}\mathbf{CC} + \frac{3\overline{\overline{a}}_3}{5<C^2>^2}\left(\frac{3C^2}{<C^2>} - 5\right) \tag{2.78}$$

With this, the balances of the second and third moment equation can be expressed in terms of a_i's, together with the assumption made above regarding $\overline{\overline{a}}_3$.

In order to obtain a solution of the full 13-moment system for dense materials, some assumptions regarding the order of magnitude of the spatial derivatives of the mean fields must be made. This is because the positions of

the centers of two colliding particles are distinguished. Consequently, when the complete pair distribution function at a collision is assumed to be related to the velocity distribution functions of each particle, with the radial distribution function at contact, these velocity distribution functions are evaluated at different points in space. Because Grad solves the thirteen unknowns by introducing a truncated series expansion for the distribution function, the derivatives of the mean fields are supposed to be small.

The integrations are similar to the ones in the Enskog solution. The final result is, after omitting higher order terms and neglecting products of the perturbation of the Maxwellian velocity distribution. The method itself is, however, more elegant and is more easily extendible to a more exact analysis of the full 13-moment system.

2.12 Solving f for a bimodal particle distribution

When considering multicomponent mixtures, there are two ways of describing such systems. The first way is to solve the first, second and higher moment of velocity fluctuation equations for each particle species separately, and treat the collisions between species as additions to each of the separate equations.

In this work, however, the equations are evaluated for the mixture. For instance, the second moment of velocity fluctuation is written as

$$<\mathbf{CC}>=\frac{1}{n}(n_A <\mathbf{C}_A\mathbf{C}_A> + n_B <\mathbf{C}_B\mathbf{C}_B>) \tag{2.79}$$

where the subscript A of B denote the property of the individual species. Hence, the two equations for the second moment of velocity fluctuation can be combined:

$$n\frac{D\mathbf{CC}}{Dt} - \mathbf{CC}\cdot\frac{\partial(n_A\mathbf{v}_A + n_B\mathbf{v}_B)}{\partial\mathbf{r}} + \frac{\partial n <\mathbf{CCC}>}{\partial\mathbf{r}} = -2n <\mathbf{CC}>:\frac{\partial <\mathbf{c}>}{\partial\mathbf{r}} + 2n\sum_i a_i(n_A\mathbf{v}_A + n_B\mathbf{v}_B) + n\mathbb{C}(\mathbf{CC}) \tag{2.80}$$

where $\mathbf{v}_i$ is the diffusion velocity; the velocity of species i relative to the mean motion of the mixture,

$$\mathbf{v}_i = <\mathbf{C}_i> = <\mathbf{c}_i - <\mathbf{c}>> \tag{2.81}$$

in which $<\mathbf{c}>$ denotes the average velocity of the mixture.

In the last paragraph, we have already seen that the term $\overline{\overline{P}} = <\mathbf{CC}>$ is the particle stress tensor due to streaming, and $\nabla\mathbf{q} = <\mathbf{CCC}>$ is the flux of the

second moment of fluctuating velocity. The total particle stress tensor also consists out of a collisional part, due to Θ, just as the flux of second moment does. The total stress and flux term can therefore be written as

$$\mathbf{q} = \sum_{i=A,B} \left(\frac{1}{2} \rho_i <C_i^2 \mathbf{C}_i> + \sum_{k=A,B} \mathbf{q}_{ik} \right) \tag{2.82}$$

$$\overline{\overline{P}} = \sum_{i=A,B} \left(\rho_i <\mathbf{C}_i \mathbf{C}_i> + \sum_{k=A,B} \overline{\overline{P}}_{ik} \right) \tag{2.83}$$

There are four collisional contributions, that is

1. Collision of species A with species A
2. Collision of species A with species B
3. Collision of species B with species A
4. Collision of species B with species B

Both in the stress tensor and the flux of fluctuating energy, the transfer contribution Θ is taken into account In the dissipation of second moment of fluctuating velocity, γ, the sourcelike term, ξ, is also important. Of course, in the streaming parts of the stress tensor and flux of fluctuating velocity, there are only two contributions. The dissipation of fluctuating energy, the stress tensor and the flux of fluctuating energy are all similar to the form of the monodisperse kinetic theory; there are only twice or four times as much contributions.

The perturbation function Φ is more complex because it contains the average velocity and the diffusion velocity of each specie. From the form of Φ, a diffusion force vector, $\mathbf{d}_i$, which drives the diffusion velocity, can be defined. The diffusion force is driven by the solids phase normal pressure, the external forces α, the gradient in the second moment of fluctuating velocity, and the gradients in each number density times the 'chemical' potential. The exact form of these quantities can be found in Chapter 5.

Again, the momentum equation for the bimodal mixture is now physically closed.

2.13 Conclusions

In this chapter we have seen how the kinetic theory is developed from first principles. These principles have been discussed and it is shown how to analytically solve the Boltzmann equation in a steady-state case. It has also

been shown how inelastic collisions can be taken into account in the Boltzmann equation.

Two methods of solving the non-ideal transient Boltzmann equation have been briefly discussed, but without taking an external fluctuating force into account. From these techniques, it is shown how to derive the constitutive models for granular flow. Finally, a method to treat a bimodal particle size distribution is discussed.

Nomenclature

a	coefficients in Grads' method
$\mathbf{a}$	external forces on particle, $m\,s^{-2}$
$\mathbf{A}$	vector defined on page 26
$\overline{\overline{B}}$	matrix defined on page 26
$\mathbf{c}$	particle velocity, $m\,s^{-1}$
$\mathbf{c}'$	particle velocity relative to surface, $m\,s^{-1}$
$\mathbf{C}$	particle peculiar velocity, $m\,s^{-1}$
C_n	normal component of velocity, $m\,s^{-1}$
dS	surface, m^2
$\mathbf{D}$	vector defined on page 26
e	coefficient of restitution
f	probability density function
g_0	radial distribution function at contact
m	mass of one particle
n	number density, m^{-3}
$\mathbf{n}$	normal vector, m
$\overline{\overline{P}}$	total stress tensor, Pa
$\mathbf{r}$	location in space, m
$\overline{\overline{S}}$	rate of strain tensor, s^{-1}
t	time, s
T	thermodynamic temperature, K
U, V, W	particle velocity in (x, y, z) directions, $m\,s^{-1}$

Greek

α	variable defined on page 22
ϵ	volume fraction
ϕ	any particle property
μ	variable defined on page 28
ν	$= \frac{1}{2}(1+e)$

λ	variable defined on page 28
ρ	density, $kg\,m^{-3}$
θ	angle
Θ	flux of fluctuating energy due to collisions
χ	contribution to particle energy due to collisions
ζ	variable defined on page 28

Subscripts

e	change due to particle collisions
energy	applied to energy equation
momentum	applied to momentum equation
s	applicable to particle phase

Chapter 3

Comparison of CFD models for Dense Gas-Solid Flows

In this chapter a comparison is made between the equations and models describing dense gas-solid flow in the Eulerian framework. Two different sets of governing equations are used by researchers to describe dense gas-solid flow and this chapter shows with a rigorous derivation that only one set is correct. Also, the different closure models applied in gas-solid flow are shown and compared with each other. Finally, simulations of different test-cases are done with different governing equations and closure models to study the impact of the different governing equations and closure models on the simulations. The result of the simulations is compared with generally accepted data and empirical correlations.

This chapter has been submitted for publication:

B.G.M. van Wachem, J.C. Schouten, R. Krishna, C.M. van den Bleek, and J.L. Sinclair, (1999), Comparative Analysis of CFD Models of Dense Gas-Solid Systems, *submitted to AIChE Journal.*

Abstract

Many gas-solid CFD models have been put forth by academic researchers, government laboratories, and commercial vendors. These models often differ in terms of both the form of the governing equations as well as the closure relations, resulting in much confusion in the literature. This paper reviews these various forms of the models as employed in the literature and in commercial codes and compares the resulting hydrodynamics through CFD simulations of fluidized beds. The experimental data on fluidized beds of Hilligardt and Werther (1986), Kehoe and Davidson (1971), Darton *et al.* (1977), and Kuipers (1990) are used to quantitatively assess the various treatments.
It is shown that predictions based on the commonly used governing equations of Ishii (1975) and the governing equations of Anderson and Jackson (1967) do not differ in terms of macroscopic flow behavior, but do differ on a local scale. The flow predictions are not sensitive to the use of different solid stress models or radial distribution functions, as the different approaches are very similar in dense flow regimes. The application of a different drag model, however, significantly impacts the flow of the solids-phase. Finally, a simplified algebraic granular energy balance equation is proposed for determining the granular temperature, instead of solving the full granular energy balance. This simplification does not lead to significantly different results, but it does reduce the computational effort of the simulations by about 20%.

3.1 Introduction

Gas-solid systems are found in many operations in the chemical, petroleum, pharmaceutical, agricultural, biochemical, food, electronic, and power generation industries. Computational fluid dynamics (CFD) is an emerging technique for predicting the flow behavior of these systems as is necessary for scale-up, design, or optimization. For example, Barthod *et al.* (1999) have successfully improved the performance of a fluidized bed in the petroleum industries by means of CFD calculations. Although single-phase flow CFD tools are now widely and successfully applied, multiphase CFD is still not because of the difficulty in describing the variety of interactions in these systems. For example, to date there is no agreement on the appropriate closure models. Furthermore, there is still no agreement on even the governing equations. In addition, proposed constitutive models for the solid-phase stresses and the interphase momentum transfer are partially empirical.

CFD models of gas-solid systems can be divided into two groups, Lagrangian models and Eulerian models. Lagrangian models, or discrete particle models calculate the path and motion of each particle. The interactions between the particles are described by either a potential force (soft particle dynamics,

Tsuji *et al.*, 1993) or by collision dynamics (hard particle dynamics, Hoomans *et al.*, 1995). The drawbacks of the Lagrangian approach are the large memory requirements and the long calculation time and, unless the continuous phase is described using direct numerical simulations (DNS), empirical data and correlations are required to describe the gas-solid interactions. Eulerian models treat the particle phase as a continuum and average out motion on the scale of individual particles, thus enabling computations by this method to treat dense-phase flows and systems of realistic size. As a result, CFD modeling based on this Eulerian framework is still the only feasible approach for performing parametric investigation and scale-up and design studies.

This paper focuses on the Eulerian approach and compares the two sets of governing equations, the different closure models and their associated parameters that are employed in the literature to predict the flow behavior of gas-solid systems. Unfortunately, many researchers propose governing equations without citing, or with incorrectly citing, a reference for the basis for their equations. Both Anderson and Jackson (1967) and Ishii (1975) have derived multiphase flow equations from first principles, but the inherent assumptions in these two sets of governing equations constrain the types of multiphase flows to which they can be applied. One of the objectives of our current contribution is to show how these two treatments differ; it is shown that Ishii's (1975) treatment is appropriate for a dispersed phase consisting of fluid droplets, and Anderson and Jackson's (1967) treatment is appropriate for a dispersed phase consisting of solid particles. In the case of a solid dispersed phase, many researchers and commercial CFD codes employ kinetic theory concepts to describe the solid-phase stresses resulting from particle-particle interactions. Various forms of the constitutive models based on these concepts have been applied in the literature. The qualitative and quantitative differences between these are shown in this paper. The predictions of CFD simulations of bubbling fluidized beds, slugging fluidized beds, and bubble injection into fluidized beds incorporating these various treatments are compared to the "benchmark" experimental data of Hilligardt and Werther (1986), Kehoe and Davidson (1971), Darton *et al.* (1977), and Kuipers (1990).

3.2 Governing equations

Most authors who refer to the origin of their governing equations used, refer to the work of Anderson and Jackson (1967) or Ishii (1975). Anderson and Jackson (1967) and Jackson (1997) (with correction in Jackson (1998)) use a formal mathematical definition of local mean variables to translate the point Navier-Stokes equations for the fluid and the Newton's equation of motion for a single particle directly into continuum equations representing momentum balances for the fluid and solid phases. The point variables are averaged

over regions large with respect to the particle diameter but small with respect to the characteristic dimension of the complete system. A weighting function, $g(|\mathbf{x}-\mathbf{y}|)$, is introduced in forming the local averages of system point variables, where $|\mathbf{x}-\mathbf{y}|$ denotes the separation of two arbitrary points in space. The integral of g over the total space is normalized to unity:

$$4\pi \int_0^\infty g(r) r^2 dr = 1 \tag{3.1}$$

The 'radius' l of function g is defined by

$$\int_0^l g(r) r^2 dr = \int_l^\infty g(r) r^2 dr \tag{3.2}$$

Provided l is chosen to satisfy $a \ll l \ll L$, where a is the particle radius and L is the shortest macroscopic length scale, averages defined should not depend significantly on the particular functional form of g or its radius.

The gas-phase volume fraction $\epsilon(\mathbf{x})_g$ and the particle number density $n(\mathbf{x})$ at point $\mathbf{x}$ are directly related to the weighting function g:

$$\epsilon(\mathbf{x})_g = \int_{V_g} g(|\mathbf{x}-\mathbf{y}|) dV_y \tag{3.3}$$

$$n(\mathbf{x}) = \sum_p g(|\mathbf{x}-\mathbf{x}_p|) \tag{3.4}$$

where V_g is the fluid phase volume, and $\mathbf{x}_p$ is the position of the center of particle p. The local mean value of the fluid phase point properties, $\langle \mathbf{f} \rangle_g$ is defined by

$$\epsilon(\mathbf{x})_g \langle \mathbf{f} \rangle_g (\mathbf{x}) = \int_{V_g} \mathbf{f}(\mathbf{y}) g(|\mathbf{x}-\mathbf{y}|) dV_y \tag{3.5}$$

The solid-phase averages are not defined analogous to the fluid phase averages since the motion of the solid phase is determined with respect to the center of the particle and average properties need only depend on the properties of the particle as a whole. Hence, the local mean value of the solid-phase point properties is defined by

$$n(\mathbf{x}) \langle \mathbf{f} \rangle_s (\mathbf{x}) = \sum_p \mathbf{f}_s g(|\mathbf{x}-\mathbf{x}_p|) \tag{3.6}$$

The average space and time derivatives for the fluid and solid phases follow from the above definitions. The averaging rules are then applied to the point

continuity and momentum balances for the fluid. For the solid phase, the averaging rules are applied to the equation of motion of a single particle p:

$$\rho_s V_p \frac{\partial \mathbf{v}_s}{\partial t} = \int_{S_p} \bar{\bar{\sigma}}_g(\mathbf{y})\mathbf{n}(\mathbf{y})ds_y + \sum_{q \neq p} \mathbf{f}_{qp} + \rho_s V_p \mathbf{g} \tag{3.7}$$

where $\mathbf{v}_s$ is the particle velocity, ρ_s is the particle density, V_p is the volume of particle p, $\bar{\bar{\sigma}}_g$ is the gas-phase stress tensor, S_p denotes the surface of particle p, and $\mathbf{f}_{qp}$ represents the resultant force exerted on the particle p from contacts with other particles.

The resulting momentum balances for the fluid and solid phases, dropping the averaging brackets <> on the variables, are as follows:

$$\rho_g \epsilon_g \left[\frac{\partial}{\partial t}\mathbf{v}_g + \mathbf{v}_g \cdot \nabla \mathbf{v}_g\right] = \nabla(\epsilon_g \bar{\bar{\sigma}}_g) - \sum_p \int_{S_p} \bar{\bar{\sigma}}_g \cdot \mathbf{n}(\mathbf{y}) g|\mathbf{x} - \mathbf{y}| ds_y + \rho_g \epsilon_g \mathbf{g} \tag{3.8}$$

$$\rho_s \epsilon_s \left[\frac{\partial}{\partial t}\mathbf{v}_s + \mathbf{v}_s \cdot \nabla \mathbf{v}_s\right] = \sum_p g|\mathbf{x} - \mathbf{x}_p| \int_{S_p} \bar{\bar{\sigma}}_g \mathbf{n}(\mathbf{y}) ds_y + \nabla \cdot \bar{\bar{\sigma}}_s + \rho_s \epsilon_s \mathbf{g} \tag{3.9}$$

The first term on the right hand side of the gas phase equation of motion represents the effect of stresses in the gas phase, the second term on the right hand side represents the traction exerted on the gas phase by the particle surfaces, and the third term represents the gravity force on the fluid. The first term on the right hand side of the solid-phase equation of motion represents the forces exerted on the particles by the fluid, the second term on the right hand side represents the force due to solid-solid contacts, which can be described using concepts from kinetic theory, and the third term represents the gravity force on the particles. The averaged shear tensor of the gas phase can be rewritten with the Newtonian definition as

$$\bar{\bar{\sigma}}_g = -P_g \bar{\bar{I}} + \frac{\mu_g}{\epsilon_g}\left(\nabla \mathbf{v}_g + (\nabla \mathbf{v}_g)^T\right) \tag{3.10}$$

where the gas phase volume fraction is introduced in the volume process.

Note that the forces due to fluid traction are treated differently in the fluid-phase and solid-phase momentum balances. In the particle phase, only the resultant force acting on the center of the particle is relevant; the distribution of stress within each particle is not needed to determine its motion. Hence, in the solid-phase momentum balance, the resultant forces due to fluid traction acting everywhere on the surface of the particles are calculated first, then these are averaged to the particle centers. In the fluid-phase momentum balance, the traction forces at all elements of fluid-solid interaction are calculated, then they are averaged to the location of the surface elements. Hence,

the fluid-phase traction term is given as

$$\sum_p \int_{S_p} \bar{\bar{\sigma}}_g \cdot \mathbf{n}(\mathbf{y}) g|\mathbf{x}-\mathbf{y}| ds_y = \sum_p g|\mathbf{x}-\mathbf{x}_p| \int_{S_p} \bar{\bar{\sigma}}_g \cdot \mathbf{n}(\mathbf{y}) ds_y - \nabla \cdot \left[a \sum_p g|\mathbf{x}-\mathbf{x}_p| \int_{S_p} (\bar{\bar{\sigma}}_g \cdot \mathbf{n}(\mathbf{y}))\mathbf{n}(\mathbf{y}) ds_y \right] + O(\nabla^2) \tag{3.11}$$

which is a result of a Taylor series expansion in $g|\mathbf{x}-\mathbf{y}|$ about the center of the particle with radius a. Here terms of $O(\nabla^2)$ and higher have been neglected. Note that the first term on the right hand side of Equation 3.11 is the same as the fluid traction term in the particle-phase momentum balance. The difference in the manner in which the resultant forces due to fluid tractions act on the surfaces of the particles is a key distinction between the Jackson (1997) and Ishii (1975) formulations. In the Ishii (1975) formulation, applicable to fluid droplets, the fluid-droplet traction term is the same in the gas phase and the dispersed phase governing equations.

The integrals involving the traction on a particle surface have been derived by Nadim and Stone (1991) and are given in Jackson (1997) as

$$\sum_p g|\mathbf{x}-\mathbf{x}_p| \int_{S_p} \bar{\bar{\sigma}}_g \cdot \mathbf{n}(\mathbf{y}) ds_y = \frac{\beta}{\epsilon_g}(\mathbf{v}_g - \mathbf{v}_s) + \rho_g \epsilon_s \mathbf{g} + \rho_g \epsilon_s \frac{D_f \mathbf{v}_g}{Dt} \tag{3.12}$$

$$\nabla \cdot \left[a \sum_p g|\mathbf{x}-\mathbf{x}_p| \int_{S_p} (\bar{\bar{\sigma}}_g \cdot \mathbf{n}(\mathbf{y}))\mathbf{n}(\mathbf{y}) ds_y \right] = -\nabla(\epsilon_s P_g) \tag{3.13}$$

where β is the interphase momentum transfer coefficient. The final equations of motion for both phases according to Jackson (1997) are shown in Table 3.1, both in the form as originally presented in his paper, and in an equivalent alternative form, which is merely a linear combination of the original equations.

In Ishii's (1975) formulation, the fluid and dispersed phases are averaged over a fixed volume. This volume is relatively large compared to the size of individual molecules or particles. A phase indicator function is introduced, $X(\mathbf{r})$, which is unity when the point $\mathbf{r}$ is occupied by the dispersed phase, and zero if it is not. Averaging over this function leads to the volume fraction of both phases,

$$\epsilon_s = \frac{1}{V} \int_V X(\mathbf{r}) dV_r \tag{3.14}$$

where V is the averaging volume. Since both the continuous and dispersed phases are liquids, they are treated the same in the averaging process. Hence,

the momentum balances for both phases are the same.

$$\frac{\partial \epsilon_k \rho_k <\mathbf{v}_k>}{\partial t} + \nabla \cdot (\epsilon_k \rho_k <\mathbf{v}_k><\mathbf{v}_k>) = -\nabla(\epsilon_k <P_k>) + \nabla \cdot (\epsilon_k <\bar{\bar{\tau}}_k>) + \epsilon_k \rho_k \mathbf{g} + \mathbf{M}_k \tag{3.15}$$

where k is the phase number and $\mathbf{M}_k$ is the interphase momentum exchange between the phases, with $\mathbf{M}_g + \mathbf{M}_s = 0$. In the Ishii (1975) formulation, the distribution of stress within both phases is important since the dispersed phase is considered as fluid droplets. Hence, "jump" conditions are used to determine $\mathbf{M}_k$. The interphase momentum transfer is defined as

$$\begin{aligned}\mathbf{M}_k &= -\sum_j \frac{1}{L_j}\left(P_k \mathbf{n}_k - \mathbf{n}_k \cdot \bar{\bar{\tau}}_k\right) \\ &= \sum_j \frac{1}{L_j}((<P_{ki}> - P_k)\mathbf{n}_k - <P_{ki}>\mathbf{n}_k - \mathbf{n}_k \cdot (<\bar{\bar{\tau}}_{ki}> - \bar{\bar{\tau}}_k) + \mathbf{n}_k \cdot <\bar{\bar{\tau}}_{ki}>)\end{aligned} \tag{3.16}$$

where L_j is the interfacial area per unit volume, P_k is the pressure in the bulk of phase k, $<P_{ki}>$ is the average pressure of phase k at the interface, $\bar{\bar{\tau}}_k$ denotes the shear stress in the bulk, and $<\bar{\bar{\tau}}_{ki}>$ represents the average shear stress at the interface. The terms $(<P_{ki}> - P_k)\mathbf{n}_k$ and $\mathbf{n}_k \cdot (<\bar{\bar{\tau}}_{ki}> - \bar{\bar{\tau}}_k)$ are identified by Ishii (1975) as the form drag and the skin drag, respectively, making up the total drag force. The other terms can be written out as

$$\mathbf{M}_k = \text{drag} + <P_k> \nabla \epsilon_k + (<P_{ki}> - <P_k>)\nabla \epsilon_k - (\nabla \epsilon_k) \cdot <\bar{\bar{\tau}}_{ki}> \tag{3.17}$$

According to Ishii and Mishima (1984), the last term on the right hand side is an interfacial shear term and is important in a separated flow. According to Ishii (1975), the term $(<P_{ki}> - <P_k>)$ only plays a role when the pressure at the bulk is significantly different from that at the interface as in stratified flows. For many applications both terms are negligible, and

$$\mathbf{M}_k = \text{drag} + <P_k> \nabla \epsilon_k \tag{3.18}$$

The momentum equations for the gas phase and the dispersed phase following the original work of Ishii (1975) are shown in Table 3.1. Many researchers and commercial codes modify Ishii's (1975) equations to describe gas-solid flows (*e.g.* Enwald *et al.*, 1996). These modified equations are also shown in Table 3.1. When Ishii's (1975) equations are applied to gas-solid flows, the solid-phase stress tensor is not multiplied by the solids volume fraction, since the volume fraction functionality is already accounted for in the kinetic theory description.

3.2.1 Comparing the Ishii and Jackson governing equations

Comparing the Ishii (1975) and Jackson (1997) momentum balances, the differences are twofold. First, Jackson (1997) includes the solids volume fraction multiplied by the gradient of the total gas-phase stress tensor in the solid-phase momentum balance, whereas Ishii (1975) only includes the solids volume fraction multiplied by the gradient of the pressure. Secondly, in the Ishii (1975) approach in the gas-phase momentum balance, the pressure carries the gas volume fraction outside the gradient operator; the shear stress carries the gas volume fraction inside the gradient operator. In Jackson (1997) both stresses are treated equally with respect to the gas volume fraction and the gradient operators. When the gas phase shear stress plays an important role, these differences may be significant near large gradients of volume fraction, i.e. near bubbles or surfaces.

Table 3.1: *Governing equations according to Jackson (1997) and Ishii (1975) applied to gas-solid flow. The explanation of the symbols can be found in the Nomenclature.*

Continuity equations

$$\frac{\partial \epsilon_g}{\partial t} + \nabla \cdot (\epsilon_g \mathbf{v_g}) = 0$$

$$\frac{\partial \epsilon_s}{\partial t} + \nabla \cdot (\epsilon_s \mathbf{v_s}) = 0$$

Momentum equations of Jackson (1997)

$$\rho_g \left[\frac{\partial \mathbf{v_g}}{\partial t} + \mathbf{v_g} \cdot \nabla \mathbf{v_g} \right] = \nabla \cdot \bar{\bar{\tau}}_g - \nabla P - \frac{\beta}{\epsilon_g}(\mathbf{v_g} - \mathbf{v_s}) + \rho_g \mathbf{g}$$

$$\rho_s \epsilon_s \left[\frac{\partial \mathbf{v_s}}{\partial t} + \mathbf{v_s} \cdot \nabla \mathbf{v_s} \right] - \rho_g \epsilon_s \left[\frac{\partial \mathbf{v_g}}{\partial t} + \mathbf{v_g} \cdot \nabla \mathbf{v_g} \right] = \frac{\beta}{\epsilon_g}(\mathbf{v_g} - \mathbf{v_s}) + \epsilon_s(\rho_s - \rho_g)\mathbf{g} + \nabla \cdot \bar{\bar{\tau}}_s - \nabla P_s$$

in alternative form:

$$\rho_g \epsilon_g \left[\frac{\partial \mathbf{v_g}}{\partial t} + \mathbf{v_g} \cdot \nabla \mathbf{v_g} \right] = \epsilon_g \nabla \cdot \bar{\bar{\tau}}_g - \epsilon_g \nabla P - \beta(\mathbf{v_g} - \mathbf{v_s}) + \epsilon_g \rho_g \mathbf{g}$$

$$\rho_s \epsilon_s \left[\frac{\partial \mathbf{v_s}}{\partial t} + \mathbf{v_s} \cdot \nabla \mathbf{v_s} \right] = \epsilon_s \nabla \cdot \bar{\bar{\tau}}_g - \epsilon_s \nabla P + \nabla \cdot \bar{\bar{\tau}}_s - \nabla P_s + \beta(\mathbf{v_g} - \mathbf{v_s}) + \epsilon_s \rho_s \mathbf{g}$$

Momentum equations of Ishii (1975)

$$\rho_g \epsilon_g \left[\frac{\partial \mathbf{v_g}}{\partial t} + \mathbf{v_g} \cdot \nabla \mathbf{v_g} \right] = -\epsilon_g \nabla P + \nabla \cdot \epsilon_g \bar{\bar{\tau}}_g + \epsilon_g \rho_g \mathbf{g} - \beta(\mathbf{v_g} - \mathbf{v_s})$$

$$\rho_s \epsilon_s \left[\frac{\partial \mathbf{v_s}}{\partial t} + \mathbf{v_s} \cdot \nabla \mathbf{v_s} \right] = -\epsilon_s \nabla P + \nabla \cdot \epsilon_s \bar{\bar{\tau}}_s + \epsilon_s \rho_s \mathbf{g} + \beta(\mathbf{v_g} - \mathbf{v_s})$$

applied to gas-solid flow (Enwald *et al.*, 1996):

$$\rho_g \epsilon_g \left[\frac{\partial \mathbf{v_g}}{\partial t} + \mathbf{v_g} \cdot \nabla \mathbf{v_g} \right] = -\epsilon_g \nabla P + \nabla \cdot \epsilon_g \bar{\bar{\tau}}_g + \epsilon_g \rho_g \mathbf{g} - \beta(\mathbf{v_g} - \mathbf{v_s})$$

$$\rho_s \epsilon_s \left[\frac{\partial \mathbf{v_s}}{\partial t} + \mathbf{v_s} \cdot \nabla \mathbf{v_s} \right] = -\epsilon_s \nabla P + \nabla \cdot \bar{\bar{\tau}}_s - \nabla P_s + \epsilon_s \rho_s \mathbf{g} + \beta(\mathbf{v_g} - \mathbf{v_s})$$

Definitions

$$\bar{\bar{\tau}}_i = 2\mu_i \bar{\bar{D}}_i + \left(\lambda_i - \frac{2}{3}\mu_i \right) \mathrm{tr}\left(\bar{\bar{D}}_i\right) \bar{\bar{I}} \quad \text{with} \quad \bar{\bar{D}}_i = \frac{1}{2}\left(\nabla \mathbf{v_i} + (\nabla \mathbf{v_i})^T \right)$$

3.3 Closure relations

3.3.1 Kinetic theory

Closure of the solid-phase momentum equation requires a description for the solid-phase stress. When the particle motion is dominated by collisional interactions, concepts from gas kinetic theory (Chapman and Cowling, 1970) can be used to describe the effective stresses in the solid phase resulting from particle streaming (kinetic contribution) and direct collisions (collisional contribution). Constitutive relations for the solid-phase stress based on kinetic theory concepts have been derived by Lun *et al.* (1984), allowing for the inelastic nature of particle collisions.

Analogous to the thermodynamic temperature for gases, the granular temperature can be introduced as a measure of the particle velocity fluctuations.

$$\Theta = \frac{1}{3} <\mathbf{v}_s'^2> \tag{3.19}$$

Since the solid-phase stress depends on the magnitude of these particle velocity fluctuations, a balance of the granular energy ($\frac{3}{2}\Theta$) associated with these particle velocity fluctuations is required to supplement the continuity and momentum balance for both phases. This balance is given as

$$\frac{3}{2}\left[\frac{\partial}{\partial t}(\epsilon_s \rho_s \Theta) + \nabla \cdot (\epsilon_s \rho_s \Theta \mathbf{v}_s)\right] = \left(-\nabla P_s \bar{\bar{I}} + \bar{\bar{\tau}}_s\right) : \nabla \mathbf{v}_s - \nabla \cdot (\kappa_s \nabla \Theta) - \gamma_s - J_s \tag{3.20}$$

where the first term on the right hand side represents the creation of fluctuating energy due to shear in the particle phase, the second term represents the diffusion of fluctuating energy along gradients in Θ, γ_s represents the dissipation due to inelastic particle-particle collisions, and J_s represents the dissipation or creation of granular energy resulting from the working of the fluctuating force exerted by the gas through the fluctuating velocity of the particles. Rather than solving the complete granular energy balance given in Equation 3.20, some researchers (e.g. Syamlal *et al.*, 1993, Boemer *et al.*, 1995, Van Wachem *et al.*, 1998, Van Wachem *et al.*, 1999) assume the granular energy is in a steady state and dissipated locally and neglect convection and diffusion. Retaining only the generation and the dissipation terms, Equation 3.20 simplifies to an algebraic expression for the granular temperature:

$$0 = \left(-\nabla P_s \bar{\bar{I}} + \bar{\bar{\tau}}_s\right) : \nabla \mathbf{v}_s - \gamma_s \tag{3.21}$$

Because the generation and dissipation terms dominate in dense-phase flows, it is anticipated that this simplification is a reasonable one in dense regions of flow.

3.3.2 Solid-phase stress tensor

The solids pressure represents the solid-phase normal forces due to particle-particle interactions. In the literature there is general agreement on the form of the solids pressure, given by Lun *et al.* (1984) as

$$\begin{aligned} P_s &= \rho_s \epsilon_s \Theta [1 + 2(1+e) g_0 \epsilon_s] \\ &= \rho_s \epsilon_s \Theta + 2 g_0 \rho_s \epsilon_s^2 \Theta (1+e) \end{aligned} \tag{3.22}$$

The first part of the solids pressure represents the kinetic contribution, and the second part represents the collisional contribution. The kinetic part of the stress tensor physically represents the momentum transferred through the system by particles moving across imaginary shear layers in the flow; the collisional part of the stress tensor denotes the momentum transferred by direct collisions.

The solids bulk viscosity describes the resistance of the particle suspension against compression. In the literature, there is also general agreement on the form of the solids bulk viscosity, given by Lun *et al.* (1984) as

$$\lambda_s = \frac{4}{3} \epsilon_s{}^2 \rho_s d_s g_0 (1+e) \sqrt{\frac{\Theta}{\pi}}$$

However, the kinetic theory description for the solids shear viscosity often differs between the various two-fluid models. Gidaspow (1994) does not account for the inelastic nature of particles in the kinetic contribution of the total stress, as Lun *et al.* (1984) do, claiming this correction is negligible. The solids shear viscosity of Syamlal *et al.* (1993) neglects the kinetic or streaming contribution, which dominates in dilute-phase flow. Hrenya and Sinclair (1997) follow Lun *et al.* (1984), but constrain the mean free path of the particle by a dimension characteristic of the actual physical system. This is opposed to the Lun *et al.* (1984) theory which allows the mean free path to tend toward infinity and the solids viscosities tends toward a finite value as the solids volume fraction tends to zero. Hence, by constraining the mean free path, the limit of the Hrenya and Sinclair (1997) shear viscosity expression correctly tends to zero as the solids volume fraction approaches zero. The Syamlal *et al.* (1993) solids shear viscosity also tends to zero as the solids volume fraction tends to zero. In this case, however, this solids shear viscosity limit is reached because the kinetic contribution to the solids viscosity is neglected.

Table 3.2 presents the forms for the solids shear viscosity as presented in the original papers as well as in an equivalent form so that all of the models can be easily compared. Figure 3.1 shows a comparison of the constitutive models for the solids shear viscosity as a function of the solid volume fraction. All models yield the same solids shear viscosity at high solids volume

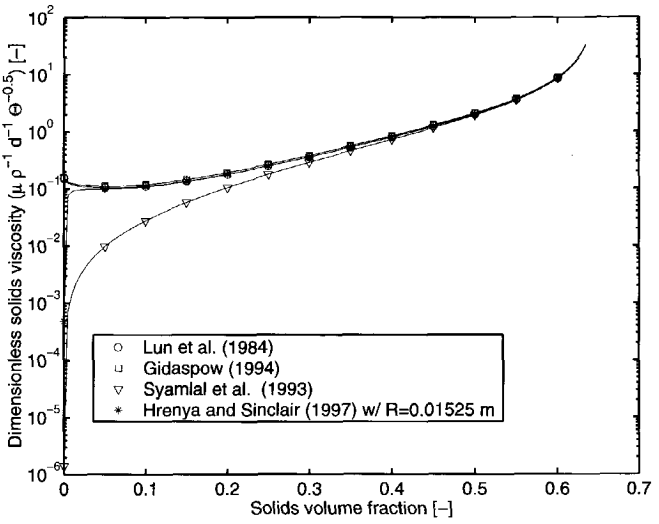

Figure 3.1: A comparison of the solids shear viscosities from different kinetic theory models. In this figure $e = 0.9$, $\epsilon_{max} = 0.65$.

fractions. Syamlal *et al.* (1993) deviate from the others for solids volume fractions less than 0.3. Hrenya and Sinclair (1997) show a rapid decrease in solids shear viscosity at extremely dilute solids concentrations.

Table 3.2: *Solids shear viscosity according to Lun* et al. *(1984), Syamlal* et al. *(1993), Gidaspow (1994), and Hrenya and Sinclair (1997). The symbols can be found in the Nomenclature.*

Lun *et al.* (1984)

$$\begin{aligned}\mu_s &= \frac{5\sqrt{\pi\Theta}}{96}\rho_s d_s\left[\left(\frac{1}{\eta g_0}+\frac{8\epsilon_s}{5}\right)\left(\frac{1+\frac{8}{5}\eta(3\eta-2)\epsilon_s g_0}{2-\eta}\right)+\frac{768}{25\pi}\eta{\epsilon_s}^2 g_0\right]\\ &= \frac{4}{5}{\epsilon_s}^2\rho_s d_s g_0(1+e)\sqrt{\frac{\Theta}{\pi}}+\frac{1}{15}\sqrt{\Theta\pi}\frac{\rho_s d_s g_0(1+e)(\frac{3}{2}e-\frac{1}{2})\epsilon_s{}^2}{(\frac{3}{2}-\frac{1}{2}e)}\\ &\quad+\frac{1}{6}\sqrt{\Theta\pi}\frac{\rho_s d_s\epsilon_s(\frac{3}{4}e+\frac{1}{4})}{(\frac{3}{2}-\frac{e}{2})}+\frac{10}{96}\sqrt{\Theta\pi}\frac{\rho_s d_s}{(1+e)(\frac{3}{2}-\frac{1}{2}e)g_0}\end{aligned}$$

Syamlal *et al.* (1993)

$$\begin{aligned}\mu_s &= \frac{4}{5}{\epsilon_s}^2\rho_s d_s g_0(1+e)\sqrt{\frac{\Theta}{\pi}}+\frac{\epsilon_s d_s\rho_s\sqrt{\pi\Theta}}{6(3-e)}\left[1+\frac{2}{5}(1+e)(3e-1)\epsilon_s g_0\right]\\ &= \frac{4}{5}{\epsilon_s}^2\rho_s d_s g_0(1+e)\sqrt{\frac{\Theta}{\pi}}+\frac{1}{15}\sqrt{\Theta\pi}\rho_s d_s g_0\frac{(1+e)(\frac{3}{2}e-\frac{1}{2})}{(\frac{3}{2}-\frac{e}{2})}{\epsilon_s}^2+\frac{1}{12}\frac{\epsilon_s d_s\rho_s\sqrt{\pi\Theta}}{(\frac{3}{2}-\frac{e}{2})}\end{aligned}$$

Gidaspow (1994)

$$\begin{aligned}\mu_s &= \frac{4}{5}{\epsilon_s}^2\rho_s d_s g_0(1+e)\sqrt{\frac{\Theta}{\pi}}+\frac{2\frac{5\sqrt{\pi}}{96}\rho_s d_s\sqrt{\Theta}}{(1+e)g_0}\cdot\left[1+\frac{4}{5}g_0\epsilon_s(1+e)\right]^2\\ &= \frac{4}{5}{\epsilon_s}^2\rho_s d_s g_0(1+e)\sqrt{\frac{\Theta}{\pi}}+\frac{1}{15}\sqrt{\Theta\pi}\rho_s d_s g_0(1+e){\epsilon_s}^2+\frac{1}{6}\sqrt{\Theta\pi}\rho_s d_s\epsilon_s\\ &\quad+\frac{10}{96}\sqrt{\Theta\pi}\frac{\rho_s d_s}{(1+e)g_0}\end{aligned}$$

Hrenya and Sinclair (1997)

$$\begin{aligned}\mu_s &= \frac{5\sqrt{\pi\Theta}}{96}\rho_s d_s\left[\left(\frac{1}{1+\frac{\lambda_{mfp}}{R}}\frac{1}{\eta g_0}+\frac{8\epsilon_s}{5}\right)\left(\frac{1+\frac{8}{5}\eta(3\eta-2)\epsilon_s g_0}{2-\eta}\right)+\frac{768}{25\pi}\eta{\epsilon_s}^2 g_0\right]\\ &= \frac{4}{5}{\epsilon_s}^2\rho_s d_s g_0(1+e)\sqrt{\frac{\Theta}{\pi}}+\frac{1}{15}\sqrt{\Theta\pi}\frac{\rho_s d_s g_0(1+e)(\frac{3}{2}e-\frac{1}{2})\epsilon_s{}^2}{(\frac{3}{2}-\frac{e}{2})}\\ &\quad+\frac{1}{6}\sqrt{\Theta\pi}\frac{\rho_s d_s\epsilon_s(\frac{1}{2}(1+\frac{\lambda_{mfp}}{R})+\frac{3}{4}e-\frac{1}{4})}{(\frac{3}{2}-\frac{1}{2}e)(1+\frac{\lambda_{mfp}}{R})}+\frac{10}{96}\sqrt{\Theta\pi}\frac{\rho_s d_s}{(1+e)(\frac{3}{2}-\frac{1}{2}e)g_0(1+\frac{\lambda_{mfp}}{R})}\end{aligned}$$

3.3.3 Conductivity of granular energy

Similar to the solids shear viscosity, the solids thermal conductivity, κ, consists of a kinetic contribution and a collisional contribution. Gidaspow (1994) only differs from Lun *et al.* (1984) in the dependency of the solids thermal conductivity on the coefficient of restitution. Syamlal *et al.* (1993) neglect the kinetic contribution to the thermal conductivity. Hrenya and Sinclair (1997) follow Lun *et al.* (1984) but also here constrain the mean free path of the particle by a dimension characteristic of the actual system. Hence, the limit of their conductivity expression, as with the shear viscosity, correctly tends to zero when approaching zero solids volume fraction. Syamlal *et al.* (1993) also correctly predict zero conductivity at zero solids volume fraction by neglecting the kinetic contribution.

Table 3.3 presents the equations for the solids thermal conductivity as given in the original papers, as well as in an equivalent form so that all of the closure models can be easily compared. Figure 3.2 shows a quantitative comparison of the constitutive models for the solids thermal conductivity as a function of the solids volume fraction. All models yield the same thermal conductivity at

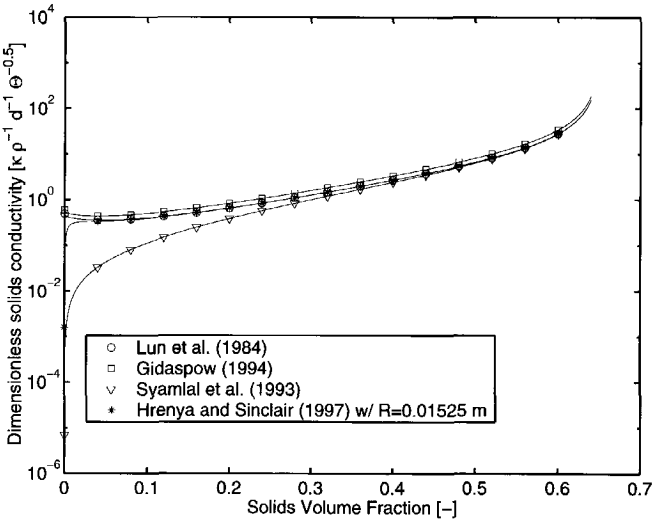

Figure 3.2: *A comparison of the solids thermal conductivity from different kinetic theory models. In this figure* $e = 0.9$, *and* $\epsilon_{max} = 0.65$.

high solids volume fraction. Syamlal *et al.* (1993) deviate from the others for solids volume fraction less than 0.3. Hrenya and Sinclair (1997) show a rapid decrease in thermal conductivity at extremely dilute solids concentration.

Table 3.3: *Solids thermal conductivity according to Lun* et al. *(1984), Syamlal* et al. *(1993), Gidaspow (1994), and Hrenya and Sinclair (1997). The symbols can be found in the Nomenclature.*

Lun *et al.* (1984)

$$\kappa = \frac{25\sqrt{\pi\Theta}}{128}\rho_s d_s\left[\left(\frac{8}{\eta g_0}+\frac{96\epsilon_s}{5}\right)\left(\frac{1+\frac{12}{5}\eta^2(4\eta-3)\epsilon_s g_0}{41-33\eta}\right)+\frac{512}{25\pi}\eta{\epsilon_s}^2 g_0\right]$$

$$= 2{\epsilon_s}^2\rho_s d_s g_0(1+e)\sqrt{\frac{\Theta}{\pi}}+\frac{9}{8}\sqrt{\Theta\pi}\frac{\rho_s d_s g_0(\frac{1}{2}+\frac{e}{2})^2(2e-1){\epsilon_s}^2}{(\frac{49}{16}-\frac{33}{16}e)}$$

$$+\frac{15}{16}\sqrt{\Theta\pi}\frac{\epsilon_s\rho_s d_s(\frac{e^2}{2}+\frac{1}{4}e+\frac{1}{4})}{(\frac{49}{16}-\frac{33}{16}e)}+\frac{25}{64}\sqrt{\Theta\pi}\frac{\rho_s d_s}{(1+e)(\frac{49}{16}-\frac{33}{16}e)g_0}$$

Syamlal *et al.* (1993)

$$\kappa = \frac{15 d_s\rho_s\epsilon_s\sqrt{\Theta\pi}}{4(41-33\eta)}\left[1+\frac{12}{5}\eta^2(4\eta-3)\epsilon_s g_0+\frac{16}{15\pi}(41-33\eta)\eta\epsilon_s g_0\right]$$

$$= 2{\epsilon_s}^2\rho_s d_s g_0(1+e)\sqrt{\frac{\Theta}{\pi}}+\frac{9}{8}\sqrt{\Theta\pi}\frac{\rho_s d_s g_0(\frac{1}{2}+\frac{e}{2})^2(2e-1){\epsilon_s}^2}{(\frac{49}{16}-\frac{33}{16}e)}+\frac{15}{32}\sqrt{\Theta\pi}\frac{\epsilon_s\rho_s d_s}{(\frac{49}{16}-\frac{33}{16}e)}$$

Gidaspow (1994)

$$\kappa_{dil} = \frac{75}{384}\rho_s d_s\sqrt{\pi\Theta}$$

$$\kappa = \frac{2}{(1+e)g_0}\left[1+\frac{6}{5}(1+e)g_0\epsilon_s\right]^2\kappa_{dil}+2{\epsilon_s}^2\rho_s d_s g_0(1+e)\sqrt{\frac{\Theta}{\pi}}$$

$$= 2{\epsilon_s}^2\rho_s d_s g_0(1+e)\sqrt{\frac{\Theta}{\pi}}+\frac{9}{8}\sqrt{\Theta\pi}\rho_s d_s g_0\left(\frac{1}{2}+\frac{e}{2}\right){\epsilon_s}^2+\frac{15}{16}\sqrt{\Theta\pi}\epsilon_s\rho_s d_s$$

$$+\frac{25}{64}\sqrt{\Theta\pi}\frac{\rho_s d_s}{(1+e)g_0}$$

Hrenya and Sinclair (1997)

$$\kappa = \frac{25\sqrt{\pi\Theta}}{128}\rho_s d_s\left[\left(\frac{1}{1+\frac{\lambda_{mfp}}{R}}\frac{8}{\eta g_0}+\frac{96\epsilon_s}{5}\right)\left(\frac{1+\frac{12}{5}\eta^2(4\eta-3)\epsilon_s g_0}{41-33\eta}\right)+\frac{512}{25\pi}\eta{\epsilon_s}^2 g_0\right]$$

$$= 2{\epsilon_s}^2\rho_s d_s g_0(1+e)\sqrt{\frac{\Theta}{\pi}}+\frac{9}{8}\sqrt{\Theta\pi}\frac{\rho_s d_s g_0(\frac{1}{2}+\frac{e}{2})^2(2e-1){\epsilon_s}^2}{(\frac{49}{16}-\frac{33}{16}e)}$$

$$+\frac{15}{16}\sqrt{\Theta\pi}\frac{\epsilon_s\rho_s d_s(\frac{e^2}{2}+\frac{1}{4}e+\frac{1}{4}+\frac{\lambda_{mfp}}{R})}{(\frac{49}{16}-\frac{33}{16}e)(1+\frac{\lambda_{mfp}}{R})}+\frac{25}{64}\sqrt{\Theta\pi}\frac{\rho_s d_s}{(1+e)(\frac{49}{16}-\frac{33}{16}e)(1+\frac{\lambda_{mfp}}{R})g_0}$$

3.3.4 Dissipation and generation of granular energy

Jenkins and Savage (1983) represent the dissipation of granular energy due to inelastic particle-particle collisions as

$$\gamma_s = 3(1-e^2)\epsilon_s^2\rho_s g_0\Theta\left(\frac{4}{d_s}\sqrt{\frac{\Theta}{\pi}} - \nabla\cdot\mathbf{v}_s\right) \tag{3.23}$$

For small mean-field gradients associated with a slight particle inelasticity, the term $\nabla\cdot\mathbf{v}_s$ is typically omitted, as in Lun *et al.* (1984):

$$\gamma_s = 12(1-e^2)\frac{\epsilon_s^2\rho_s g_0}{d_s\sqrt{\pi}}\Theta^{3/2} \tag{3.24}$$

The rate of energy dissipation per unit volume resulting from the acting of the fluctuating force exerted by the gas through the fluctuating velocity of the particles is given by $J_s = \beta(\overline{\mathbf{v}_s'\cdot\mathbf{v}_s'} - \overline{\mathbf{v}_g'\cdot\mathbf{v}_s'})$. The correlation $\overline{\mathbf{v}_s'\cdot\mathbf{v}_s'}$ is equal to 3Θ. The second correlation $\overline{\mathbf{v}_g'\cdot\mathbf{v}_s'}$ is neglected by Gidaspow (1994). However, Louge *et al.* (1991) have proposed a closure for this correlation based on the work of Koch (1990) which we apply here and

$$J_s = \beta\left(3\Theta - \frac{\beta d_s(\mathbf{v}_g-\mathbf{v}_s)^2}{4\epsilon_s\rho_s\sqrt{\pi\Theta}}\right) \tag{3.25}$$

Using the closure of Louge *et al.* (1991) for $\overline{\mathbf{v}_g'\cdot\mathbf{v}_s'}$, we have found that this term is of the same order of magnitude as $\overline{\mathbf{v}_s'\cdot\mathbf{v}_s'}$. It should be noted, however, that the correlation as proposed by Louge *et al.* (1991) does not tend to zero at closest solids packing. Therefore, Sundaresan (1999) has proposed dividing this correlation by the radial distribution function to correct the closure in this limit.

3.3.5 Radial distribution function

The solid-phase stress is dependent on the radial distribution function at contact. Lun *et al.* (1984) employed the Carnahan and Starling (1969) expression for the radial distribution function. The Carnahan and Starling (1969) expression, however, does not tend toward the correct limit at closest solids packing. Because particles are in constant contact at the maximum solid volume fraction, the radial distribution function at contact tends to infinity. Therefore, alternate expressions to the Carnahan and Starling (1969) expression have been proposed by Gidaspow (1994), Lun and Savage (1986), and Sinclair and Jackson (1989) which tend to the correct limit at closest packing. These various forms of the radial distribution function are given in Table 3.4 and are plotted in Figure 3.3 as a function of solids volume fraction, along

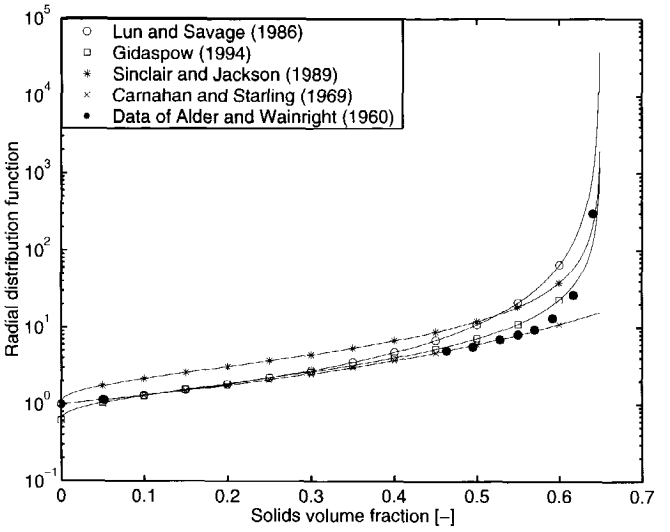

Figure 3.3: *Different radial distribution functions compared to the computational data of Alder and Wainright (1960)*

with the data from molecular simulations of Alder and Wainright (1960). The expression of Gidaspow (1994) most closely coincides with the data over the widest range of solids volume fractions. However the expression of Gidaspow (1994) does not approach the correct limit of one as the solids volume fraction approaches zero. In Figure 3.4, the effect of these different expressions for the radial distribution functions on the solids shear viscosity is presented. A difference of up to a factor of two in viscosity can result.

3.3.6 Frictional stress

At high solids volume fraction, sustained contacts between particles occur. The resulting frictional stresses must be accounted for in the description of the solid-phase stress. Zhang and Rauenzahn (1997) conclude that particle collisions are no longer instantaneous at very high solids volume fractions, as is assumed in kinetic theory. Several approaches have been presented in the literature to model the frictional stress, mostly originated from geological research groups. Typically, the frictional stress, $\overline{\overline{\sigma}}_f$, is written in a Newtonian form:

$$\overline{\overline{\sigma}}_f = P_f \overline{\overline{I}} + \mu_f \left(\nabla \mathbf{v} + (\nabla \mathbf{v})^T \right) \tag{3.26}$$

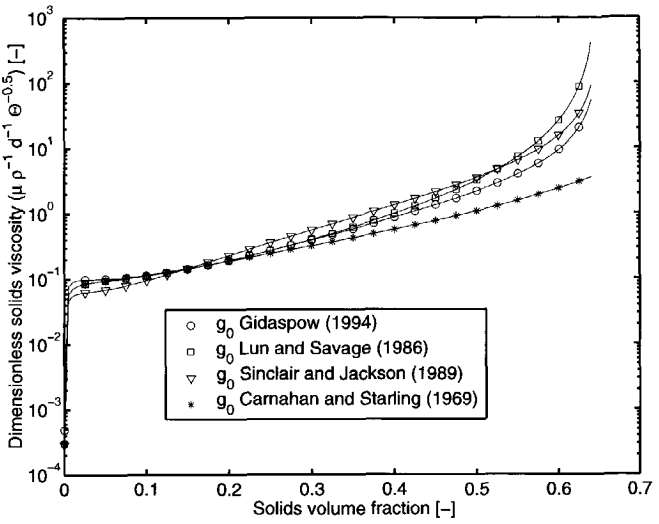

Figure 3.4: *Solids shear viscosity from different radial distribution functions. In this figure the solids shear viscosity follows Hrenya and Sinclair (1997);* $e = 0.9$, $R = 0.01525\,m$, *and* $\epsilon_{max} = 0.65$.

The frictional stress is added to the stress predicted by kinetic theory for $\epsilon_s > \epsilon_{s,min}$:

$$P_s = P_{kinetic} + P_f \tag{3.27}$$

$$\mu_s = \mu_{kinetic} + \mu_f \tag{3.28}$$

Johnson and Jackson (1987) propose a semi-empirical equation for the normal frictional stress, P_f

$$P_f = Fr\frac{(\epsilon_s - \epsilon_{s,min})^n}{(\epsilon_{s,max} - \epsilon_s)^p} \tag{3.29}$$

where Fr, n, and p are empirical material constants, and $\epsilon_s > \epsilon_{s,min}$, $\epsilon_{s,min}$ being the solid volume fraction when frictional stresses become important. Fr, n, and p, are material dependent constants. The frictional shear viscosity is then related to the frictional normal stress by the linear law proposed by Coulomb (1776)

$$\mu_f = P_f \sin\phi \tag{3.30}$$

where ϕ is the angle of internal friction of the particle. Representative values for the empirical constants employed in Equations 3.29 and 3.30 are given in Table 3.5. Another approach, originally from Schaeffer (1987), was employed

Table 3.4: *Radial distribution function according to Carnahan and Starling (1969), Lun and Savage (1986), Sinclair and Jackson (1989), and Gidaspow (1994). The symbols can be found in the Nomenclature.*

Carnahan and Starling (1969)
$g_0 = \frac{1}{1-\epsilon_s} + \frac{3\epsilon_s}{2(1-\epsilon_s)^2} + \frac{{\epsilon_s}^2}{2(1-\epsilon_s)^3}$
Lun and Savage (1986)
$g_0 = \left(1 - \frac{\epsilon_s}{\epsilon_{s,max}}\right)^{-2.5\epsilon_{s,max}}$
Sinclair and Jackson (1989)
$g_0 = \left[1 - \left(\frac{\epsilon_s}{\epsilon_{s,max}}\right)^{\frac{1}{3}}\right]^{-1}$
Gidaspow (1994)
$g_0 = \frac{3}{5}\left[1 - \left(\frac{\epsilon_s}{\epsilon_{s,max}}\right)^{\frac{1}{3}}\right]^{-1}$

by Syamlal *et al.* (1993) to describe frictional stress in very dense gas-solid systems:

$$P_f = A(\epsilon_s - \epsilon_{s,min})^n \tag{3.31}$$

$$\mu_f = \frac{P_f \cdot \sin\phi}{\epsilon_s \sqrt{\frac{1}{6}\left(\left(\frac{\partial u_s}{\partial x} - \frac{\partial v_s}{\partial y}\right)^2 + \left(\frac{\partial v_s}{\partial y}\right)^2 + \left(\frac{\partial u_s}{\partial x}\right)^2\right) + \frac{1}{4}\left(\frac{\partial u_s}{\partial y} + \frac{\partial v_s}{\partial x}\right)^2}} \tag{3.32}$$

Values of $A = 10^{25}$, $n = 10$, $\epsilon_{s,min} = 0.59$, and $\phi = 25^\circ$ are typically employed.

The approaches of Johnson and Jackson (1987) and Syamlal *et al.* (1993) are compared in Figure 3.5. It can be seen that resulting frictional normal stress can differ by orders of magnitude.

3.3.7 Interphase transfer coefficient

Generally, form drag and skin drag are combined in one empirical parameter, the interphase drag constant β, in the modeling of the momentum transfer

Table 3.5: *The values for the empirical parameters of Equations 3.29 and 3.30 as suggested by various researchers.*

Fr $[N/m^2]$	n	p	$\epsilon_{s_{min}}$	ϕ	d_s $[\mu m]$	ρ_s $[kg/m^3]$	material	reference
0.05	2	3	0.5	28°	150	2500	unknown	Ocone *et al.* (1993)
$3.65 \cdot 10^{-32}$	0	40	-	25.0°	1800	2980	glass	Johnson and Jackson (1987)
$4.0 \cdot 10^{-32}$	0	40	-	25.0°	1000	1095	poly-styrene	Johnson and Jackson (1987)
0.05	2	5	0.5	28.5°	1000	2900	glass	Johnson *et al.* (1990)

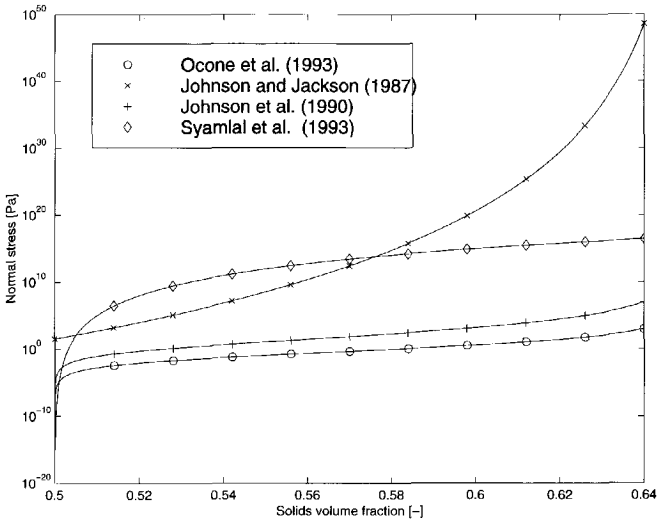

Figure 3.5: *A comparison of different expressions for the frictional normal stress.*

between the gas and solid phases. The drag coefficient β is typically obtained experimentally from pressure drop measurements in fixed, fluidized, or settling beds. Ergun (1952) performed measurements in fixed liquid-solid beds at packed conditions to determine the pressure drop. Wen and Yu (1966) have performed settling experiments of solid particles in a liquid over a wide range of solids volume fractions and have correlated their data and that of others for solids concentrations, $0.01 \leq \epsilon_s \leq 0.63$. Syamlal *et al.* (1993) use the empirical correlations of Richardson and Zaki (1954) and Garside and Al-Bibouni (1977) to determine the terminal velocity in fluidized and settling beds expressed as a function of the solids volume fraction and the particle Reynolds number. From this terminal velocity, the drag force can be readily computed.

The drag model of Gidaspow (1994) follows Wen and Yu (1966) for solid vol-

ume fractions lower than 0.2 and Ergun (1952) for solids volume fractions larger than 0.2. The motivation for this hybrid drag description of Gidaspow (1994) is unclear because the Wen and Yu (1966) expression incorporates experimental drag data for solids volume fractions larger than 0.2. Moreover, a step-change in the interphase drag constant is obtained at the "crossover" solids volume fraction of 0.2 which can possibly lead to difficulties in numerical convergence. The magnitude of this discontinuity in β increases with increasing particle Reynolds number. The drag coefficients are summarized in Table 3.6 and are compared quantitatively in Figure 3.6 for a range of solids volume fractions at a fixed particle Reynolds number.

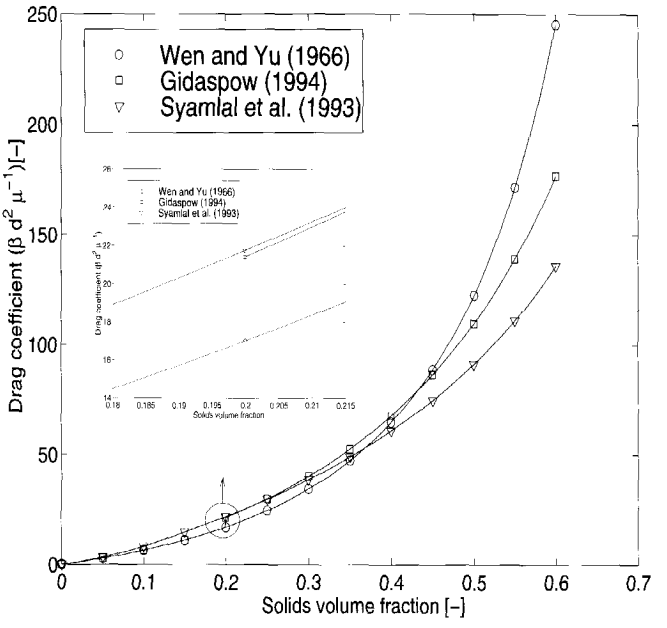

Figure 3.6: *A comparison of different expressions for the interphase drag coefficient as a function of solids volume fraction. In this figure* $Re_p = 45$. *The symbols can be found in the Notation.*

Table 3.6: *Drag coefficient according to Wen and Yu (1966), Gidaspow (1994), and Syamlal* et al. *(1993)*

Wen and Yu (1966)

$$\beta = \frac{3}{4} C_D \frac{(1-\epsilon_s)\epsilon_s \rho_g |\mathbf{v_g} - \mathbf{v_s}|}{d_s} (1-\epsilon_s)^{-2.65}$$

Rowe (1961):

$$C_D = \begin{cases} \dfrac{24}{Re_p(1-\epsilon_s)} \left[1 + 0.15\,((1-\epsilon_s)Re_p)^{0.687}\right] & \text{if } (1-\epsilon_s)Re_p < 1000 \\ 0.44 & \text{if } (1-\epsilon_s)Re_p \geq 1000 \end{cases}$$

$$Re_p = \frac{d_s \rho_g |\mathbf{v_g} - \mathbf{v_s}|}{\mu_g}$$

Gidaspow (1994) applies the Ergun (1952) equation for higher volume fractions.

$$\beta = \begin{cases} 150 \dfrac{\epsilon_s{}^2 \mu_g}{(1-\epsilon_s) d_s{}^2} + \dfrac{7}{4} \dfrac{\epsilon_s \rho_g |\mathbf{v_g} - \mathbf{v_s}|}{d_s} & \text{if } \epsilon_s > 0.2 \\ \dfrac{3}{4} C_D \dfrac{(1-\epsilon_s)\epsilon_s \rho_g |\mathbf{v_g} - \mathbf{v_s}|}{d_s} (1-\epsilon_s)^{-2.65} & \text{if } \epsilon_s \leq 0.2 \end{cases}$$

Syamlal *et al.* (1993)

$$\beta = \frac{3}{4} C_D \frac{\epsilon_s (1-\epsilon_s)\rho_g}{V_r{}^2 d_s} |\mathbf{v_g} - \mathbf{v_s}|$$

Dalla Valle (1948)

$$C_D = \left(0.63 + 4.8\sqrt{\frac{V_r}{Re}}\right)^2$$

Garside and Al-Dibouni (1977):

$$V_r = \frac{1}{2}\left(a - 0.06Re + \sqrt{(0.06Re)^2 + 0.12Re(2b - a) + a^2}\right)$$

$$a = (1-\epsilon_s)^{4.14}$$

$$b = \begin{cases} 0.8(1-\epsilon_s)^{1.28} & \text{if } \epsilon_s \geq 0.15 \\ (1-\epsilon_s)^{2.65} & \text{if } \epsilon_s < 0.15 \end{cases}$$

3.4 Simulations

The impact on the predicted flow patterns of the differences in the governing equations and constitutive models are compared for the test cases of a freely bubbling fluidized bed, a slugging fluidized bed, and a single bubble injection into a fluidized bed. The particles in a fluidized bed move due to the action of the fluid through the drag force, and bubbles and complex solid mixing patterns result. Typically, the average solids volume fraction in the bed is fairly large, averaging about 40 percent, whereas in the the free-board of the fluidized bed there are almost no particles ($\epsilon_s \approx 10^{-6}$).

The simulations in this work were carried out with the commercial CFD code CFX 4.2 from AEA Technology, Harwell, UK, employing the Rhie-Chow (Rhie and Chow, 1983) algorithm for discretization. For solving the difference equations, the higher-order total variation diminishing (TVD) scheme Superbee is used. This TVD scheme incorporates a modification to the higher-order upwind scheme (second order). The time discretization is done with the second order backward difference scheme. The solution of the pressure from the momentum equations requires a pressure correction equation, correcting the pressure and the velocities after each iteration; for this, the SIMPLE (Patankar, 1980) algorithm is employed. The calculated pressure is used to determine the density of the fluid phase; the simulations are performed allowing for compressibility of the gas phase. The grid spacing was determined by refining the grid until average properties changed by less than 4%. Due to the deterministic chaotic nature of the system, the dynamic behavior always changes with the grid. The simulations of the slugging fluidized bed and the freely bubbling fluidized bed were carried out for 25 seconds of real time. It was observed that after about five seconds of real time, the simulation has reached a state in which average properties stay unchanged. Averaged properties, such as average bubble size and average bed expansion were determined by averaging over the last 15 of seconds real time in each simulation. A bubble is defined as a void in the solid phase with a solids volume fraction less than 15%. The bubble diameter is defined as the diameter of a circle having the same surface as the void in the solid phase; this is called the equivalent bubble diameter.

3.4.1 Boundary conditions

All the simulations are carried out in a two-dimensional rectangular space in which front and back wall effects are neglected. The left and right walls of the fluidized bed are treated as no-slip velocity boundary conditions for the fluid phase, and free-slip velocity boundary conditions are employed for the particle phase. The boundary condition for the granular temperature follows

Johnson and Jackson (1987),

$$\mathbf{n}\cdot(\kappa\nabla\Theta) = \frac{\pi\rho_s\epsilon_s\sqrt{3\Theta}}{6\epsilon_{s,max}\left[1-\left(\frac{\epsilon_s}{\epsilon_{s,max}}\right)^{1/3}\right]}\left[\varphi'|\mathbf{v}_{slip}|^2-\frac{3\Theta}{2}(1-e_w{}^2)\right] \quad (3.33)$$

where the left hand side represents the conduction of granular energy to the wall, the first term on the right hand side represents the generation of granular energy due to particle slip at the wall, and the second term on the right hand side represents dissipation of granular energy due to inelastic collisions. Simulations we have done with an adiabatic boundary condition at the wall ($\nabla\Theta = 0$) show very similar results.

The boundary condition at the top the free-board (fluid phase outlet) is a so-called pressure boundary. The pressure at this boundary is fixed to a reference value, $1.013\cdot10^5$ Pa. Neumann boundary conditions are applied to the gas flow, requiring a fully-developed gas flow. For this, the free-board of the fluidized bed needs to be of sufficient height; this is validated through the simulations. In the freeboard, the solids volume fraction is very close to zero and this can lead to unrealistic values for the particle velocity field and poor convergence. For this reason, a solids volume fraction of 10^{-6} is set at the top of the free-board. This way the whole free-board is filled with a very small number of particles, which gives more realistic results for the particle phase velocity in the freeboard, but does not influence the behavior of the fluidized bed itself.

The bottom of the fluidized bed is made impenetrable for the solid phase by setting the solid-phase axial velocity to zero. For the freely bubbling fluidized bed and the slugging fluidized bed, Dirichlet boundary conditions are employed at the bottom with a uniform gas inlet velocity. To break the symmetry in the case of the bubbling and slugging beds, initially a small jet of gas is specified in the bottom left hand side of the geometry. In the case of the bubble injection, a Dirichlet boundary condition is also employed at the bottom of the fluidized bed. The gas inlet velocity is kept at the minimum fluidization velocity, except for a small orifice in the center of the bed, at which a very large inlet velocity is specified. Finally, the solids-phase stress, as well as the granular temperature, at the top of the fluidized bed are both set to zero.

3.4.2 Initial conditions

Initially, the bottom part of the fluidized bed is filled with particles at rest with a uniform solids volume fraction. The gas flow in the bed is set to its

Table 3.7: *System properties and computational parameters.*

Parameter	Description	Freely bubbling fluidized bed	Slugging fluidized bed	Bubble injection into fluidized bed (Kuipers, 1990)
ρ_s [kg/m^3]	solids density	2640	2640	2660
ρ_g [kg/m^3]	gas density	1.28	1.28	1.28
μ_g [Pa s]	gas viscosity	$1.7 \cdot 10^{-5}$	$1.7 \cdot 10^{-5}$	$1.7 \cdot 10^{-5}$
d_s [μm]	particle diameter	480	480	500
e [-]	coefficient of restitution	0.9	0.9	0.9
ϵ_{max} [-]	max. solids volume fraction	0.65	0.65	0.65
U_{mf} [m/s]	min. fluidization velocity	0.21	0.21	0.25
D_T [m]	inner column diameter	0.5	0.1	0.57
H_t [m]	column height	1.3	1.3	0.75
H_{mf} [m]	height at minimum fluidization	0.97	0.97	0.5
$\epsilon_{s,mf}$ [-]	solids volume fraction at minimum fluidization	0.42	0.42	0.402
Δx [m]	x mesh spacing	$7.14 \cdot 10^{-3}$	$6.67 \cdot 10^{-3}$	$7.50 \cdot 10^{-3}$
Δy [m]	y mesh spacing	$7.56 \cdot 10^{-3}$	$7.43 \cdot 10^{-3}$	$1.25 \cdot 10^{-2}$

minimum fluidization velocity. In the freeboard a solids volume fraction of 10^{-6} is set, as explained above. The granular temperature is initially set to 10^{-10} m^2 s^{-2}.

3.5 Test cases

With increasing gas velocity above the minimum fluidization velocity, U_{mf}, bubbles are formed as a result of the inherent instability of the gas-solid system. The behavior of the bubbles significantly affects the flow phenomena in the fluidized bed, i.e. solid mixing, entrainment, and heat and mass transfer. The test cases in this comparative study are used to investigate the effect of different closure models and governing equations on the bubble behavior and bed expansion. Simulation results of each test case are compared to generally accepted experimental data and (semi) empirical models. The system properties and computational parameters for each of the test cases are given in Table 3.7; the computational meshes are shown in Figure 3.7. The test cases are discussed in greater detail in the following sections.

3.5.1 Freely bubbling fluidized beds

In the freely fluidized bed case, the gas flow is distributed uniformly across the inlet of the system. Small bubbles form at the bottom of the fluidized bed which rise, coalesce, and erupt as large bubbles at the fluidized bed surface. In order to evaluate the CFD model predictions, we use the Darton *et*

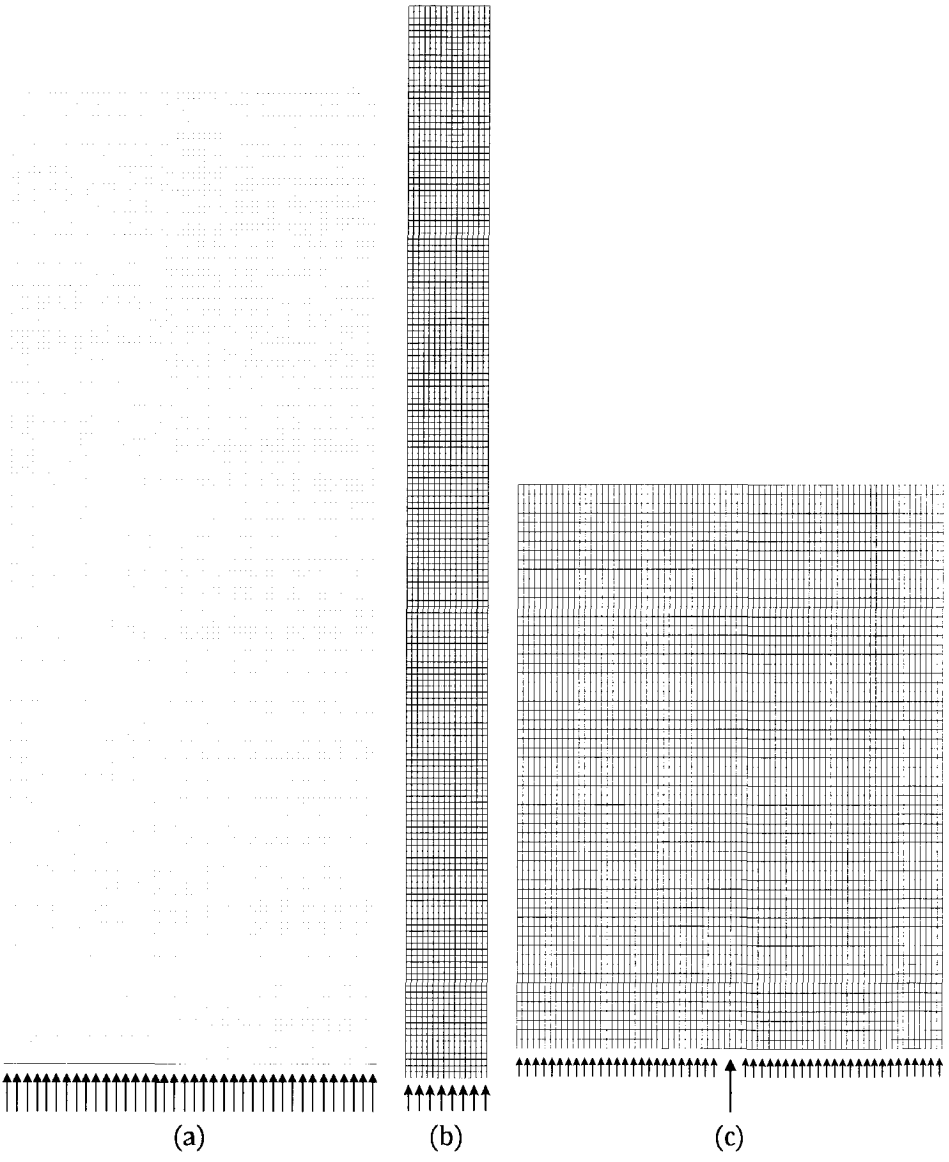

Figure 3.7: *The computational grid of the simulated fluidized beds with the gas inlet boundary condition. (a) freely bubbling fluidized bed, (b) slugging fluidized bed, and (c) bubble injection into a fluidized bed. See Table 3.7 for the exact mesh spacing.*

al. (1977) bubble model for bubble growth in freely bubbling fluidized beds. This model is based upon preferred paths of bubbles where the distance travelled by two neighbouring bubbles before coalescence is proportional to their lateral separation. Darton *et al.* (1977) have validated their model with measurements of many researchers. Their proposed bubble growth equation for Geldart type B particles is

$$D_b = 0.54(U - U_{mf})^{0.4}(h + 4\sqrt{A_0})^{0.8}\, g^{-0.2} \tag{3.34}$$

where D_b is the bubble diameter, h is the height of the bubble above the inlet of the fluidized bed, U is the actual superficial gas inlet velocity, and A_0 is the 'catchment area' which characterizes the distributor. For a porous plate gas distributor Darton *et al.* (1977) propose $4\sqrt{A_0} = 0.03\text{m}$.

Werther and Molerus (1973) have developed a small capacitance probe and the statistical theory to measure the bubble diameter and the bubble rise velocity in fluidized beds. This capacitance probe can be placed in the fluidized bed at different heights and radial positions in the bed. The bubble rise velocity is determined by placing two vertically spaced probes and correlating the obtained data. The capacitance probe measures the bubbles passing it, i.e. the bubble is pierced by the capacitance probe. The duration of this piercing is dependent upon the size of the bubble, the rise velocity of the bubble, and the vertical position of the bubble relative to the probe.

Hilligardt and Werther (1986) have done many measurements of bubble size and bubble velocity under various conditions using the probe developed by Werther and Molerus (1973) and have correlated their data in the form of the Davidson and Harrison (1963) bubble model. Hilligardt and Werther propose a variant of the Davidson and Harrison (1963) model for predicting the bubble rise velocity as a function of the bubble diameter,

$$u_b = \psi(U - U_{mf}) + \varphi\nu\sqrt{g d_b} \tag{3.35}$$

where φ is a constant. Pyle and Harrison (1967) have determined that $\varphi = 0.48$ for a two dimensional geometry, whereas in three dimensions the Davies-Taylor relationship gives $\varphi = 0.71$. The symbols ψ and ν, added by Hilligardt and Werther (1986), are empirical coefficients based on their data, which are dependent upon the type of particles and the width and height of the fluidized bed. For the particles and geometry employed in this study, Hilligardt and Werther (1986) propose $\psi \approx 0.3$ and $\nu \approx 0.8$. Proposals of values for ψ and ν under various fluidization conditions, determined by simulations, are given by Van Wachem *et al.* (1998).

Hilligardt and Werther (1986) also measured bed expansion under various conditions. Predictions of the bed expansion from the CFD simulations are compared to these data.

3.5.2 Slugging fluidized beds

In the case of the slugging fluidized beds, coalescing bubbles eventually reach a diameter of 70% or more of the column diameter, resulting from either a large inlet gas velocity or a narrow bed. The operating conditions employed in the simulations correspond to the slugging conditions reported by Kehoe and Davidson (1971), who present a detailed study of slug flow in fluidized beds. The experiments of Kehoe and Davidson (1971) were performed in slugging fluidized beds of 2.5, 5, and 10 cm diameter columns using Geldart B particles from 50 to 300 μm diameter and with superficial gas inlet velocities up to 0.5 m/s. X-ray photography was used to determine the rise velocity of slugs and to determine the bed expansion. Kehoe and Davidson (1971) use their data to validate two different equations for the slug rise velocity, both based on two-phase theory,

$$u_{slug} = U - U_{mf} + \frac{\varphi}{2}\sqrt{gD_T} \tag{3.36}$$

$$u_{slug} = U - U_{mf} + \frac{\varphi}{2}\sqrt{2gD_T} \tag{3.37}$$

Equation 3.36 is the exact two-phase theory solution. Equation 3.37 is a modification of Equation 3.36, based on the following observations:

1. For fine particles ($< 70\mu$m) the slugs travel symmetrically up in the fluidized bed, so the slug rise velocity is increased by coalescence.

2. For coarser particles ($> 70\mu$m) the slugs tend to move up the walls, which increases their velocity.

According to Kehoe and Davidson (1971), Equations 3.36 and 3.37 give upper and lower bounds on the slug rise velocity. Furthermore, Kehoe and Davidson (1971) measured the maximum bed expansion (H_{max}) during slug flow. They validated their theoretical analysis which led to the result that

$$\frac{H_{max} - H_{mf}}{H_{mf}} = \frac{U - U_{mf}}{u_{bub}} \tag{3.38}$$

where u_{bub} is the rise velocity of a slug without influence of the gas phase,

$$u_{bub} = \frac{\varphi}{2}\sqrt{gD_T} \quad \text{or} \tag{3.39}$$

$$u_{bub} = \frac{\varphi}{2}\sqrt{2gD_T} \tag{3.40}$$

corresponding to Equations 3.36 and 3.37. Hence, they also propose upper and lower bounds on the maximum bed expansion.

3.5.3 Bubble injection in fluidized beds

Single jets entering a minimum fluidized bed through a narrow single orifice provide details of bubble formation and growth. Such experiments were carried out by Kuipers (1990). Kuipers (1990) reported the shape of the injected bubble as well as the quantitative size and growth of the bubble with time using high-speed photography. The superficial gas inlet velocity from the orifice was $U = 10\text{m/s}$, and the orifice was $d = 1.5 \cdot 10^{-2}\text{m}$ wide.

3.6 Results and Discussion

Predictions based on simulations of these three test cases are used to compare the different governing and closure models. For this comparative study, only one particular closure model is varied at a time to determine the sensitivity of the model predictions to that particular closure. No coupling effects were investigated. The default governing equations are those given by Jackson (1997), and the default closure models are the solid phase stress of Hrenya and Sinclair (1997), the radial distribution function of Lun and Savage (1986), the frictional model of Johnson and Jackson (1987) with empirical values given by Johnson *et al.* (1990), the complete granular energy balance neglecting J_s, and the drag coefficient model of Wen and Yu (1966).

3.6.1 Governing equations

Simulations of the slugging bed case were performed with both the Ishii (1975) and the Jackson (1997) governing equations. Figure 3.8 shows the predicted maximum bed expansion with increasing gas velocity during the slug flow and the two correlations of Kehoe and Davidson (1971). Figure 3.9 shows the increasing slug rise velocity with increasing gas velocity. Clearly, the exact formulation of the governing equation does not have any significant influence on the prediction of these macroscopic engineering quantities, and both CFD models do a good job at predicting these quantities. Microscopically, however, there does seem to be a difference in the predictions as indicated in Figure 3.10. The flow of the gas phase in areas of large solids volume fraction gradient is slightly different, leading to a different solids distribution. Specifically, Figure 3.10 shows that the Jackson (1997) governing equations produce a more round-nosed bubble shape than the Ishii (1975) equations, because the path of the gas-phase is different.

3.6.2 Solids stress models

The exact solid-phase stress description does not influence either the freely bubbling or the slugging fluidized bed predictions, as is expected from Fig-

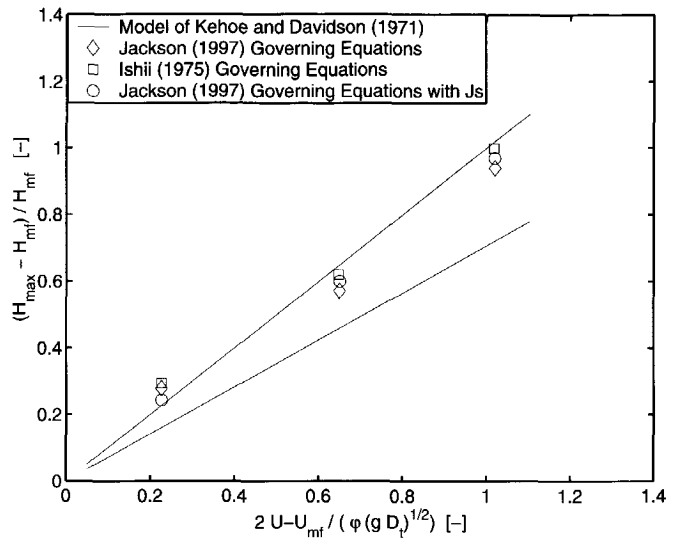

Figure 3.8: *Predicted maximum expansion of a slugging fluidized bed with increasing gas velocity with the governing equations of Jackson (1997) and Ishii (1975), and the additional term J_s in the granular energy equation (Equation 3.25). The predictions are compared with the two-phase theory as proposed and validated by Kehoe and Davidson (1971) (Equation 3.38).*

ure 3.1; this figure shows that between 0.4 and 0.6 solids volume fraction, which is dominant in the cases studied, all solids-phase stress predictions are equal. Moreover, the influence of the radial distribution upon the stress does not give rise to any variation in the predictions of the engineering quantities associated with these simulations; the variation of the solids phase stress as a function of radial distribution function, shown in Figure 3.4, is small between 0.4 and 0.6 solids volume fraction, as long as the Carnahan and Starling (1969) equation is not employed. From the magnitude of the terms on the solid-phase momentum balance during simulations of fluidized beds, it can be concluded that gravity and drag are the dominating terms and that solids-phase stress predicted by kinetic theory plays a minor role.

3.6.3 Drag models

Coordinating with results of the comparison of the drag models shown in Figure 3.6, the Syamlal *et al.* (1993) drag leads to a lower predicted pressure drop and lower predicted bed expansion than the other two drag models. Figure 3.11 shows the average simulated bed expansion employing different drag models in the freely bubbling fluidized bed case, compared to measurements

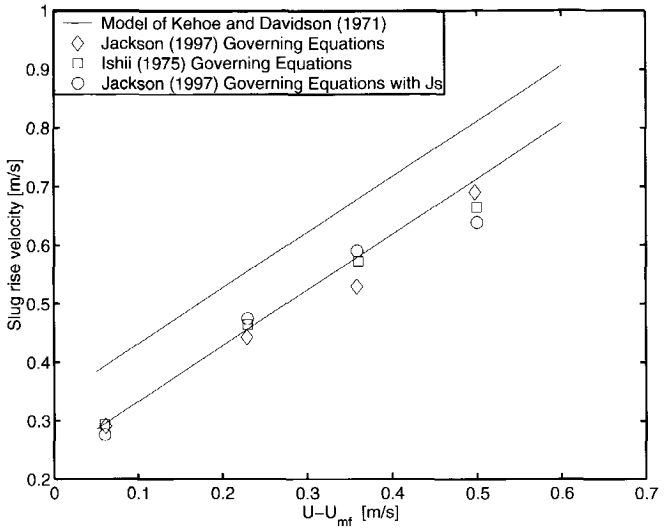

Figure 3.9: *Predicted slug rise velocity with increasing gas velocity with the governing equations of Jackson (1997) and Ishii (1975), and the additional term* J_s *in the granular energy equation (Equation 3.25). The predictions are compared with the two-phase theory as proposed and validated by Kehoe and Davidson (1971) (Equations 3.36 and 3.37). The constant* $\varphi = 0.48$.

of Hilligardt and Werther (1986). The drag model of Syamlal *et al.* (1993) underpredicts the bed expansion compared to the findings of Hilligardt and Werther (1986), and therefore also underpredicts the gas hold-up in the fluidized bed.

Figure 3.12 shows the simulated bubble size as a function of the bed height when employing different drag models, compared with the Darton *et al.* (1977) equation. Although the spread in the simulations is fairly large, all of the investigated drag models are in agreement with the equation put forth by Darton *et al.* (1977). Figure 3.13 shows the predicted bubble rise velocity employing different drag models in a freely bubbling fluidized bed, compared to the empirical correlation of Hilligardt and Werther (1986). All of the investigated drag models are in fairly good agreement with the empirical correlation.

Because the bubble sizes predicted by the different drag models are all close and the predicted bed expansion differs between the models, variations in the predicted solids volume fraction of the dense phase exist between the models, with the Syamlal *et al.* (1993) drag model predicting the highest solids volume fraction in the dense phase.

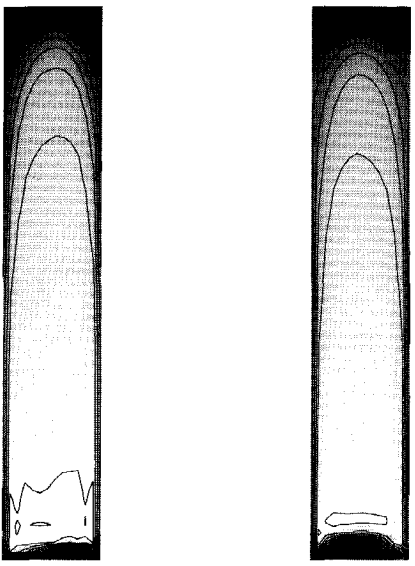

Figure 3.10: *A rising bubble in a slugging fluidized bed predicted by (a) the governing equations of Jackson (1997) and (b) by the governing equations of Ishii (1975) at the same real time. Increasing grey tones represent increasing solid volume fraction. The lines are contours of equal solids volume fraction.*

Figure 3.14 shows the quantitative bubble size prediction for a single jet entering a minimum fluidized bed based on the drag models of Wen and Yu (1966) and Syamlal *et al.* (1993) which are compared to the experimental data of Kuipers (1990). Moreover, in Figure 3.15 we show the resulting qualitative predictions of the bubble growth and shape and also compare these with photographs of Kuipers (1990). The Wen and Yu (1966) drag model yields better agreement with Kuipers' (1990) findings for both the bubble shape and size than the Syamlal *et al.* (1993) drag model. The Syamlal *et al.* (1993) drag model underpredicts the bubble size and produces a bubble that is more circular in shape than in the experiments of Kuipers (1990) and in the simulations with the Wen and Yu (1966) drag model.

3.6.4 Frictional stress

Frictional stresses can increase the total solid-phase stress by orders of magnitude and is an important contributing force in dense gas-solid modelling. The simulation of the single jet entering a fluidized bed reveals that the size

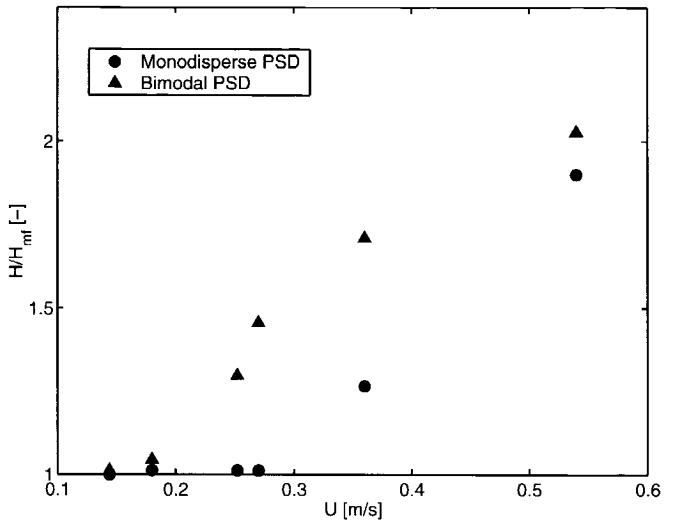

Figure 3.11: *Predicted bed expansion as a function of gas velocity based on different drag models and with and without frictional stress. The predictions are compared to the experimental data of Hilligardt and Werther (1986). The spread in the simulation data with the drag model of Gidaspow (1994) is indicated by the lines.*

of the bubble is not significantly influenced by the frictional stress, as shown in Figure 3.14. Figure 3.11 shows that the predicted bed expansion in the freely bubbling fluidized bed, however, is significantly less without frictional stress. Moreover, the number of iterations for obtaining a converged solution is almost doubled when frictional stress is omitted. Without frictional stress, there is less air in the dense phase, the maximum achieved solids packing is higher (maximum achieved solids volume fraction increased from 0.630 to 0.649), and the bed expansion is less. When frictional stress is neglected in the simulations, convergence difficulty arises because the maximum solids volume fraction specified in the radial distribution function is approached and the derivative of the radial distribution function near maximum solids volume fraction is extremely steep. Moreover, the solid-phase stress in the dense regions is significantly decreased because the predicted granular temperature in the dense regions of flow is very low ($\Theta \approx 10^{-5} m^2 s^{-2}$) due to the magnitude of the dissipation term. In order to still obtain convergence, we have written the radial distribution function as a Taylor series approximation at very high solids volume fraction. Adding frictional stress in the simulations prevents this problem because then the solids volume fraction does not approach the

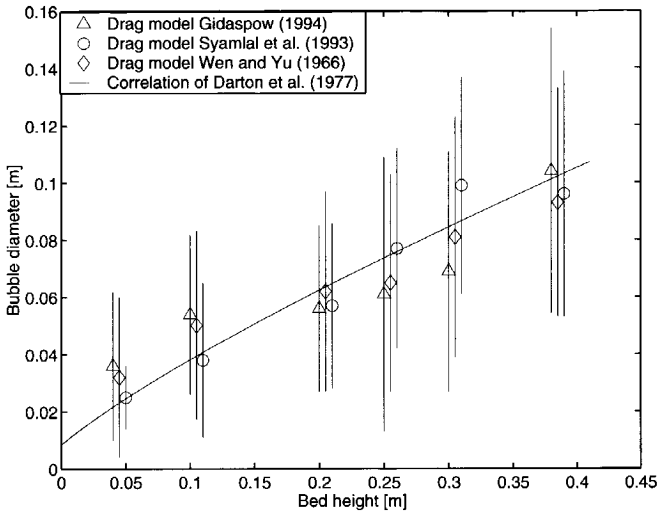

Figure 3.12: *Predicted bubble size as a function of bed height at* $U = 0.54 m/s$ *based on different drag models and compared to the correlation of Darton* et al. *(1977).*

maximum packing value.

3.6.5 Granular energy balance

The influence of the additional generation and dissipation term J_s in the granular energy balance is determined in the case of the slugging fluidized bed. Figure 3.8 shows the predictions of the maximum bed expansion as a function of increasing gas velocity for simulations with and without this additional term. Figure 3.9 also shows the predicted rise velocity of the slugs with and without this additional term. Although this additional term J_s results in as much as 20% higher granular temperature values (granular temperature increased from 0.138 m^2s^{-2} to 0.165 m^2s^{-2}), this does not seem to influence the predicted bed expansion or the slug rise velocity.

Simulations of slugging fluidized beds were also performed using the simplified algebraic granular energy equation, Equation 3.21. There were no differences in predicted bed expansion, bubble size, or bubble rise velocity due to this simplification versus using the full granular energy balance. This simplified equation does give rise to deviations in the granular temperature as much as 10% (granular temperature decreased from 0.138 m^2s^{-2} to 0.0127 m^2s^{-2}) from full granular energy balance predictions. The computational effort for solving the complete granular energy equation is about 20% higher

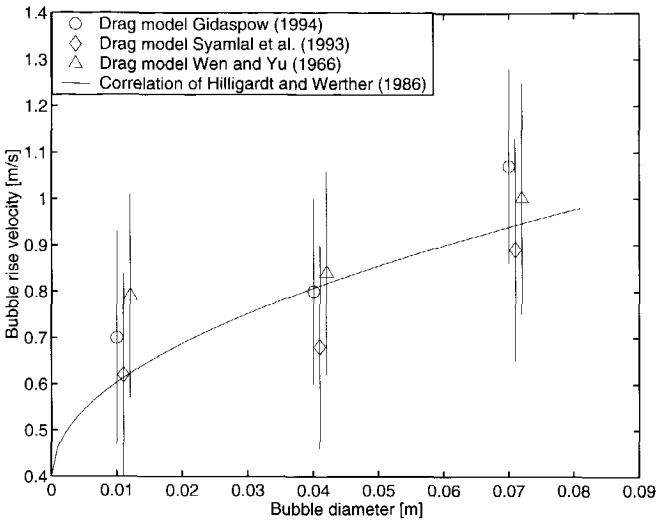

Figure 3.13: *Predicted bubble rise velocity as a function of the bubble diameter at* $U = 0.54 m/s$ *based on different drag models and compared to the experimental correlation of Hilligardt and Werther (1986).*

than calculating the granular temperature from the algebraic equation. More simulation results on the freely bubbling fluidized bed case with the algebraic equation are given in Van Wachem *et al.* (1998) and Van Wachem *et al.* (1999)

3.7 Conclusions

In this paper we have compared different formulations that are employed in CFD models for gas-solid flow in the Eulerian/Eulerian framework. We discussed the basis for the formulation of the two different sets of governing equations common to the two-fluid literature with respect to the nature of the dispersed phase. It is shown in detail that the modeling of gas-solid flows requires different governing equations than the modeling of gas-liquid flows. We have also compared various closure models both quantitatively and qualitatively. For example, we have shown how the hybrid drag model proposed by Gidaspow (1994) produces a discontinuity in the drag coefficient, how an order of magnitude difference in the normal stress is predicted by the various frictional stress models, and how the Syamlal *et al.* (1993) model predicts a lower bed expansion than with the other drag models.

Finally, we have studied the impact of the two governing equations and the various closure models on simulation predictions in three fluidized bed test

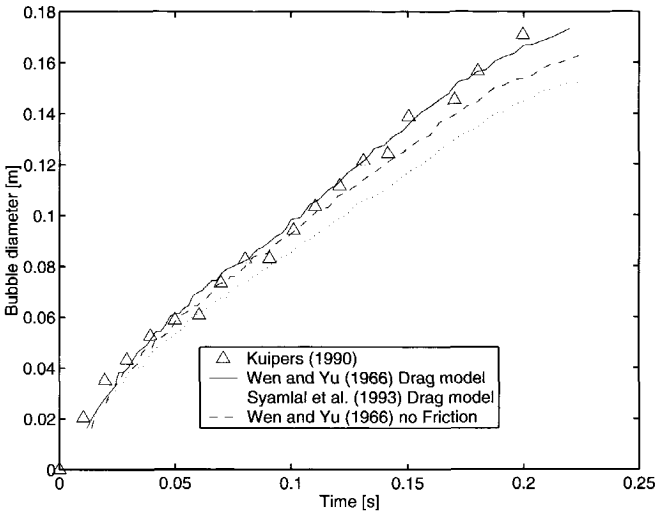

Figure 3.14: *Bubble diameter as a function of time for a bubble formed at a single jet of* $U = 10\text{m/s}$. *A comparison is made between the experiments of Kuipers (1990), model simulations using the drag coefficient of Wen and Yu (1966) with and without frictional stress, and model simulations using the interphase drag coefficient of Syamlal* et al. *(1993).*

cases. It is shown that the resulting predictions based on the two sets of governing equations are similar on an engineering scale but are different in terms of microscopic features associated with individual bubbles or localized solids distributions. It is also shown that the model predictions are not sensitive to the use of different solids stress models or radial distribution functions. In dense-phase gas-solid flow, the different approaches in the kinetic theory modeling predict similar values for the solid-phase properties. From an analysis of the individual terms on the momentum balance of the solid-phase momentum balance during the simulations, it can be concluded that gravity and drag are the most dominating terms; this is why the two different sets of governing equations predict similar results, and why the exact solid-phase stress prediction is of minor importance. At very high volume fraction, frictional stress can influence the hydrodynamic prediction due to its large magnitude.

Simplifying the granular energy balance by retaining only the generation and dissipation terms is a reasonable assumption in the case of fluidized bed modeling and reduces the computational effort by about 20%. Finally, the manner in which the drag force is modeled has a significant impact on the simulation results, influencing the predicted bed expansion and the solids concentration

in the dense-phase regions of the bed.

Nomenclature

A	empirical constant
A_0	catchment area of distributor
C_D	drag coefficient
d_s	particle diameter, m
$\overline{\overline{D}}_s$	strain rate tensor, s^{-1}
D	diameter, m
D_T	inner column diameter, m
e	coefficient of restitution
$\mathbf{f}$	fluid phase point property
Fr	empirical material constant, $N\,m^{-2}$
$\mathbf{g}(r)$	weighting function
$\mathbf{g}$	gravitational constant, $m\,s^{-2}$
g_0	radial distribution function
h	height of bubble in fluidized bed, m
H_{mf}	minimum fluidization bed height, m
H_t	column height, m
J	fluctuating velocity/force correlation, $kg\,m^{-3}s^{-1}$
L	interfacial area per unit volume, m^{-1}
$\mathbf{M}$	interphase momentum exchange
n	empirical constant in frictional stress
n	number density
$\mathbf{n}$	normal vector, m
p	empirical constant in frictional stress
P	pressure, $N\,m^{-2}$
r	point in space
R	characteristic length scale, m
Re	Reynolds number
S	surface, m^2
t	time, s
U	inlet (superficial) gas velocity, $m\,s^{-1}$
U_{mf}	minimum fluidization velocity, $m\,s^{-1}$
$\mathbf{v}$	velocity vector, $m\,s^{-1}$
V	volume, m^3
V_r	ratio of terminal velocity of a group of particles to that of an isolated particle
$\mathbf{x}$	position vector
X	phase indicator
Δx	x mesh spacing, m

Δy	y mesh spacing, m

Greek

β	interphase drag constant, $kg\,m^{-3}\,s^{-1}$
ϵ	volume fraction
η	$= \frac{1}{2}(1+e)$
ϕ	angle of internal friction
φ	constant
φ'	specularity coefficient
γ	dissipation of granular energy, $kg\,m^{-3}s^{-1}$
κ	solids thermal conductivity, $kg\,m^{-1}s^{-1}$
λ	bulk viscosity, Pa s
λ_{mfp}	mean free path, m
μ	shear viscosity, Pa s
ν	empirical coefficient
ψ	empirical coefficient
ρ	density, $kg\,m^{-3}$
$\overline{\overline{\sigma}}$	total stress tensor, $N\,m^{-2}$
$\overline{\overline{\tau}}$	viscous stress tensor, $N\,m^{-2}$
Θ	granular temperature, $m^2\,s^{-2}$

Subscripts

b	bubble
bub	single bubble
dil	dilute
f	frictional
g	gas phase
i	interface
k	either phase
mf	minimum fluidization
min	minimum; kick-in value
max	maximum
p	particle
s	solids phase
slip	slip
slug	slug
w	wall

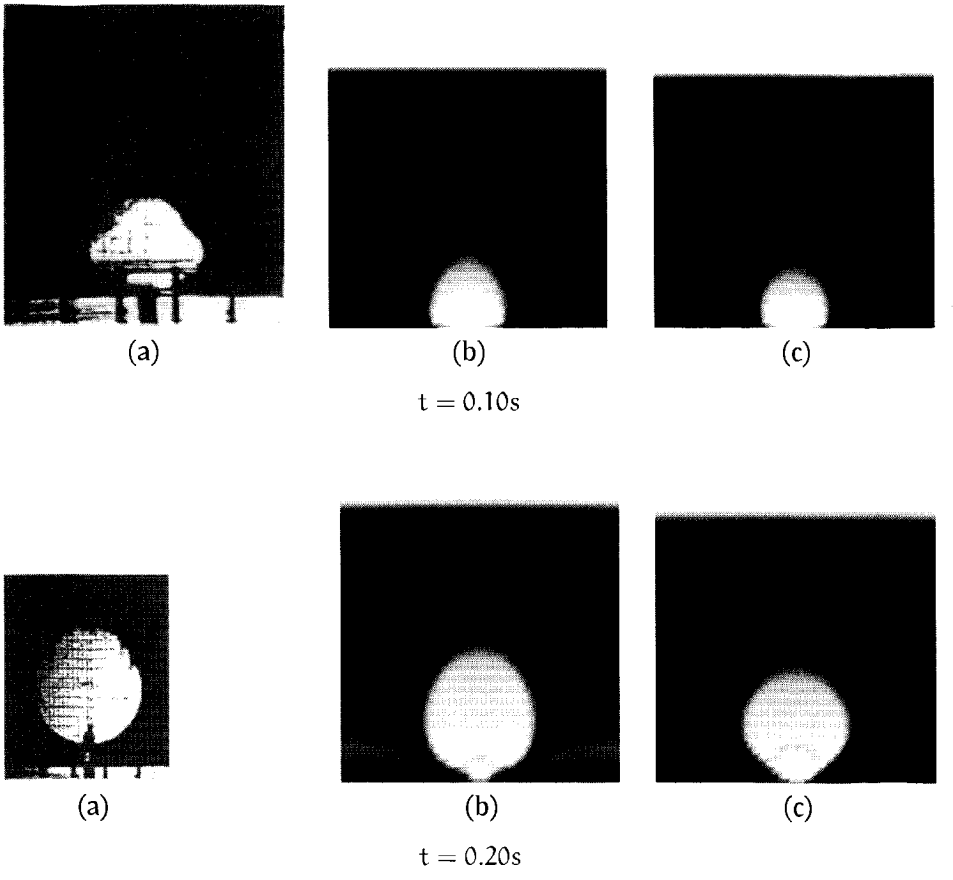

Figure 3.15: *Experimental and simulated bubble shapes associated with a single jet at* U = 10m/s *and at* t = 0.10s *and* t = 0.20s. *Comparison is made between the* (a) *experiment of Kuipers (1990),* (b) *model simulation using the interphase drag constant of Wen and Yu (1966), and* (c) *model simulation using the interphase drag coefficient of Syamlal* et al. *(1993).*

Chapter 4

Eulerian Simulations of Gas-Solid Fluidized Beds

In this chapter various simulations are done of freely bubbling fluidized beds. As seen in the previous chapter, the employed equations in this chapter are not always the optimum ones in physical sense. Because the equations in this chapter are used by many researchers and are employed by most commercial CFD codes, it is very interesting to elucidate the behavior of the simulations on an engineering scale.

Part A of this chapter researches steady state properties of fluidized beds, as the average bubble size and the average bubble rise velocity. Also, values are given predicting the bubble size and rise velocity of the simulated fluidized beds.

Part B adresses the dynamic behavior of the fluidized bed by looking at pressure and voidage waves, and the unpredictability of the fluidized bed behavior.

Part A:

Steady State Results from Simulations

This part has been published as:

B.G.M. van Wachem, J.C. Schouten, R. Krishna, and C.M. van den Bleek, (1998), Eulerian Simulations of Bubbling Behaviour in Gas-Solid Fluidized Beds, *Computers and Chemical Engineering*, **22**, pp S299-S307

Abstract

In literature little attempt has been made to verify experimentally Eulerian-Eulerian gas-solid model simulations of bubbling fluidized beds with existing correlations for bubble size or bubble velocity. In the present study, a CFD model for a free bubbling fluidized bed was implemented in the commercial code CFX of AEA Technology. This CFD model is based on a two fluid model including the kinetic theory of granular flow. Simulations of the bubble behavior in fluidized beds at different superficial gas velocities and at different column diameters are compared to the Darton *et al.* (1977) equation for the bubble diameter versus the height in the column and to the Hilligardt and Werther (1986) equation, corrected for the two dimensional geometry using the bubble rise velocity correlation of Pyle and Harrison (1967). It is shown that the predicted bubble sizes are in agreement with the Darton *et al.* (1977) bubble size equation. Comparison of the predicted bubble velocity with the Hilligardt and Werther (1986) equation shows a deviation for the velocity of smaller bubbles. To explain this, the predicted bubbles are divided into two bubble classes : bubbles that have either coalesced, broken-up, or have touched the wall, and bubbles without these occurrences. The bubbles of this second class are in agreement with the Hilligardt and Werther (1986) equation. Fit parameters describing the bubble behavior of Hilligardt and Werther (1986) are compared to the fit parameters obtained in this work. It is shown that coalescence, break-up, and direct wall interactions are very important effects, often dominating the dynamic bubble behavior, but these effects are not accounted for by the Hilligardt and Werther (1986) equation.

4.A.1 Introduction

Fluidized multiphase reactors are of increasing importance in nowadays chemical industries, even though their hydrodynamic behavior is complex and not yet fully understood. Especially the scale-up from laboratory towards industrial equipment is a problem. For example, equations describing the bubble behavior in gas-solid fluidized beds are (semi) empirical and often determined

under laboratory conditions. For that reason there is little unifying theory describing the bubble behavior in fluidized beds.

Computational fluid dynamics (CFD) is becoming more and more an engineering tool to predict flows in various types of apparatus on industrial scale. Although the tools for applying single phase flow CFD are widely available, application of multiphase CFD is however still complicated from both a physical and a numerical point of view. Moreover, experimental validation of multiphase CFD models is still in its infancy because simulations are time consuming and reliable predictions of average flows in large scale equipment are therefore not readily obtained.
Almost all the work on the simulation of gas-solid fluidized beds is limited to a qualitative (visual) comparison of simulated bubble shapes or bubble sizes with pictures of bubbles obtained from single orifice experiments of bubble formation and bubble growth (e.g., Kuipers *et al.*, 1991). Obvious reasons for this are the already mentioned time consuming character of the simulations as well as the lack of reliable measurements for validating the calculated predictions. Moreover the research efforts of most groups working in this field are aimed at development of still more detailed CFD models for two phase flow, while little attention is paid to the evaluation of the simulation results from an engineering point of view. This is strange, because at the one hand, nowadays the computational power of modern computers is increasing considerably, enabling the simulation of many bubbles in relatively large scale equipment; at the other hand, in the classical fluidization literature an abundance of data is available in the many (semi) empirical correlations that relate bubble sizes and rise velocities in single and multiple bubble beds to fluidization conditions.

Recently for Geldart group A powders, Ferschneider and Mège (1996) have used a Eulerian CFD model for the simulation of free bubbling fluidized beds, for one fluidization condition, showing the bubble sizes and bed expansion. They concluded that although the model predicts the bubble sizes throughout the bed correctly for *one* specific fluidization condition, the model is *not* suitable to predict the bed expansion of this type of particles.

The purpose of the work presented in this paper is to quantitatively compare the Eulerian-Eulerian simulation of bubble sizes and rise velocities in fluidized beds with Geldart group B particles, at different fluidization conditions, with predictions by generally accepted and applied equations that can be found throughout the literature. This will provide insight into the validity of this type of CFD codes used in the simulations of free bubbling fluidized beds. If these codes appear to be applicable, they can be used to generate engineering correlations to be used in the design of bubbling fluidized bed

reactors.

4.A.2 Gas-solid multiphase model

In spite of the increasing computational power, the number of particles in gas-solid flow in large scale equipment is still much too large to handle each particle separately. Simulating each particle separately is called a Lagrangian method, which can be used to study microscopic properties of fluidized beds (Tsuji *et al.*, 1993). The CFD model used in this work, however, is based on a two fluid model (TFM) extended with the kinetic theory of granular flow as derived from the kinetic theory of gases (Chapman and Cowling, 1970). In a TFM both phases are considered to be continuous and fully interpenetrating. The TFM has first been proposed by Anderson and Jackson (1967) and Pritchett *et al.* (1978). These firstly proposed models have zero gas and solids viscosities. Physical behavior dominated by the drag between the solids phase and the gas phase, like the formation of bubbles at a single orifice, is successfully predicted by these models. To overcome the deficiency of these inviscid models, for instance not being able to describe the forces on tubes, a solids viscosity was added to the model by Jackson (1985). Unfortunately realistic physical values for this solids viscosity as well as for the solids stresses were not known.

Jenkins and Savage (1983), Lun *et al.* (1984), and Ding and Gidaspow (1990) described the solids phase as a non-interstitial fluid. This approach is based on the kinetic theory of dense gases, as presented by Chapman and Cowling (1970). In this approach the usual thermodynamic temperature is replaced by the granular flow temperature. The solids viscosity and stress are a function of this granular temperature, which varies with time and position in the fluidized bed.

Continuity and momentum equations

Different physical TFM models exist in literature, and have been described and compared to each other by Boemer *et al.* (1995). The most promising set of equations in the sense of fast numerical convergence and accurate physical results is used in this work.

The well-known continuity equation, or mass balance for phase i (gas or solid) reads :

$$\frac{\partial}{\partial t}(\epsilon_i \rho_i) + \nabla \cdot (\epsilon_i \rho_i \mathbf{v}_i) = 0 \tag{4.1}$$

$$\epsilon_g + \epsilon_s = 1 \tag{4.2}$$

where ϵ is the volume fraction of each phase, $\mathbf{v}$ the velocity, and ρ the density. Mass exchange between the phases, e.g. due to reaction or combustion, is not considered.

The momentum balance for the gas phase is given by the Navier-Stokes equation, modified to include an interphase momentum transfer term :

$$\frac{\partial}{\partial t}(\epsilon_g \rho_g \mathbf{v}_g) + \nabla \cdot (\epsilon_g \rho_g \mathbf{v}_g \mathbf{v}_g) = \nabla \cdot \bar{\bar{\tau}}_g + \epsilon_g \rho_g \mathbf{g} + \\ -\epsilon_g \nabla P - \beta(\mathbf{v}_g - \mathbf{v}_s) \tag{4.3}$$

where $\bar{\bar{\tau}}$ is the viscous stress tensor, $\mathbf{g}$ is the gravity acceleration, P is the thermodynamic pressure, and β is the interphase momentum transfer coefficient. The solids phase momentum balance is given by :

$$\frac{\partial}{\partial t}(\epsilon_s \rho_s \mathbf{v}_s) + \nabla \cdot (\epsilon_s \rho_s \mathbf{v}_s \mathbf{v}_s) = \nabla \cdot \bar{\bar{\tau}}_s + \epsilon_s \rho_s \mathbf{g} + \\ -\epsilon_s \nabla P - \nabla P_s^* + \beta(\mathbf{v}_g - \mathbf{v}_s) \tag{4.4}$$

where P_s^* is the solids pressure obtained from the kinetic theory of granular flow, as discussed below. Both the shear viscosity and the bulk viscosity are used in the viscous stress tensor, which is discussed by Bird *et al.* (1960).

Kinetic theory of granular flow

Equivalent to the thermodynamic temperature for gases, the granular temperature can be introduced as a measure for the energy of the fluctuating velocity of the particles. The granular temperature is defined as

$$\Theta_s = \frac{1}{3}\mathbf{v}'^2 \tag{4.5}$$

where Θ_s is the granular temperature, and $\mathbf{v}'$ is the solids fluctuating velocity. The equation of conservation of the solids fluctuating energy can be found in Ding and Gidaspow (1990) :

$$\frac{3}{2}\left[\frac{\partial}{\partial t}(\epsilon_s \rho_s \Theta_s) + \nabla \cdot (\epsilon_s \rho_s \Theta_s)\mathbf{v_s}\right] = \\ \left(-\nabla P_s^* \bar{\bar{I}} + \bar{\bar{\tau}}_s\right) : \nabla \mathbf{v} + \nabla \cdot (k_\Theta \nabla \Theta_s) - \gamma_\Theta + \Phi_\Theta \tag{4.6}$$

where k_Θ is the diffusion coefficient, γ_Θ is the dissipation of fluctuating energy, and Φ_Θ is the exchange of fluctuating energy between the phases.

The dissipation of fluctuating energy is described by Jenkins and Savage (1983) :

$$\gamma_\Theta = 3(1 - e^2)\epsilon_s^2 \rho_s g_0 \Theta_s \left(\frac{4}{d_s}\sqrt{\frac{\Theta_s}{\pi}} - \nabla \cdot \mathbf{v}_s\right) \tag{4.7}$$

where g_0 is the radial distribution function, which is discussed below, e is the coefficient of restitution of colliding particles, and d_s is the particle diameter.

The solids pressure represents the solids phase normal forces due to particle-particle interactions. Its description based on the kinetic theory of granular flow was developed by Jenkins and Savage (1983) and Lun *et al.* (1984). In this approach both the kinetic and the collisional influences are taken into account. The kinetic part describes the influence of particle translations, whereas the collisional term accounts for the momentum transfer by direct collisions. The solids pressure of Lun *et al.* (1984) is used in this work :

$$P_s^* = \epsilon_s \rho_s \Theta_s (1 + 2 g_0 \epsilon_s (1 + e)) \tag{4.8}$$

The bulk viscosity is a measure for the resistance of a fluid against compression. It is obvious that the importance of the bulk viscosity depends strongly on the velocity gradients. In a fluidized bed, the bulk viscosity and the shear viscosity are in the same order of magnitude, and thus the bulk viscosity should not be neglected, as is done in simulating Newtonian fluids. The equation of Lun *et al.* (1984) is used in this work :

$$\lambda_s = \frac{4}{3} \epsilon_s \rho_s d_s g_0 (1 + e) \sqrt{\frac{\Theta_s}{\pi}} \tag{4.9}$$

where λ_s is the bulk viscosity of the solids phase.

Whereas pressure and bulk viscosity describe normal forces, the shear viscosity accounts for the tangential forces. It was shown by Lun et al. (1984) that it is possible to combine different inter-particle forces and to use a momentum balance similar to that of a true continuous fluid. Similar to the solids pressure, a solids phase viscosity can be derived from the kinetic theory. The shear viscosity is built up out of two terms : one term for the dilute region and one term for the dense region. In literature different expressions for the solids shear viscosity can be found. In this work the approach of Gidaspow *et al.* (1982) is used, because this approach is validated by comparison with measured data :

$$\mu_s = \frac{4}{5} \epsilon_s \rho_s d_s g_0 (1 + e) \sqrt{\frac{\Theta_s}{\pi}} + \\ + \frac{2 \frac{5\sqrt{\pi}}{96} \rho_s d_s \sqrt{\Theta_s}}{(1 + e) \epsilon_s g_0} \cdot \left[1 + \frac{4}{5} g_0 \epsilon_s (1 + e) \right]^2 \tag{4.10}$$

where μ_s is the shear viscosity of the solids phase.

In the extreme dense regions of the bed ($\epsilon_s \approx \epsilon_{s,max}$), the particle stresses are dominated by inter-particle friction rather than by collisions and fluctuating

motion. The two-dimensional stress tensor for a granular material which is about to yield is proposed by Sokolovski (1965) and Jackson (1983) :

$$\mu_s = \frac{P_s^* \cdot \sin\phi}{\epsilon_s \sqrt{\frac{1}{6}\left(\left(\frac{\partial u_s}{\partial x} - \frac{\partial v_s}{\partial y}\right)^2 + \left(\frac{\partial v_s}{\partial y}\right)^2 + \left(\frac{\partial u_s}{\partial x}\right)^2\right)} \ldots} \ldots \sqrt{+\frac{1}{4}\left(\frac{\partial u_s}{\partial y} + \frac{\partial v_s}{\partial x}\right)^2} \tag{4.11}$$

where ϕ is the angle of internal friction, u and v are the velocity components, and x and y are the Cartesian directions of u and v.

The radial distribution function used in the equations above is the equilibrium radial distribution at particle contact derived from statistical mechanics. It can be seen as a measure for the probability of inter-particle contact. The equation of Ding and Gidaspow (1990) is used in this work :

$$g_0 = \frac{3}{5}\left[1 - \left(\frac{\epsilon_s}{\epsilon_{s,max}}\right)^{\frac{1}{3}}\right]^{-1} \tag{4.12}$$

where $\epsilon_{s,max}$ is the maximum solids packing, usually between 0.6 and 0.7.

Instead of solving the complete balance of the solids fluctuating energy, equation (4.6), an algebraic expression was proposed by Syamlal *et al.* (1993) . This approach assumes that the granular energy is dissipated locally, neglecting the convection and diffusion, and retaining only the generation and the dissipation terms, resulting to :

$$0 = \left(-P_s^* \bar{\bar{I}} + \bar{\bar{\tau}}_s\right) : \nabla \mathbf{v}_s - \gamma_\Theta \tag{4.13}$$

This approach is only valid under the assumption that the volume fraction of the solids phase stays high, and the velocity of the solids phase stays relatively low. In this regime most granular energy is dissipated locally, and little is left

to flow away. Equation (4.13) can then be rewritten into :

$$\Theta_s = \left(\frac{-(K_1\epsilon_s + \rho_s)\,\mathrm{tr}\left(\overline{\overline{D}}_s\right) + \ldots}{\ldots} \right.$$
$$\ldots \frac{+\sqrt{(K_1\epsilon_s + \rho_s)^2\,\mathrm{tr}^2\left(\overline{\overline{D}}_s\right) + 4K_4\epsilon_s \cdot}}{\ldots}$$
$$\left. \ldots \frac{\left[2K_3\,\mathrm{tr}\left(\overline{\overline{D}}_s^2\right) + K_2\,\mathrm{tr}^2\left(\overline{\overline{D}}_s\right)\right]}{2\epsilon_s K_4} \right)^2 \qquad (4.14)$$

where $\overline{\overline{D}}_s$ is the solids strain rate tensor, and with the abbreviations :

$$K_1 = 2(1+e)\rho_s g_0$$
$$K_2 = \frac{4}{3\sqrt{\pi}} d_s \rho_s (1+e)\epsilon_s g_0 - \frac{2}{3}K_3$$
$$K_3 = \frac{d_s \rho_s}{2}\left(\frac{\sqrt{\pi}}{3(3-e)} \ldots\right.$$
$$\left. \ldots \left[1 + \frac{2}{5}(1+e)(3e-1)\epsilon_s g_0\right] + \frac{8\epsilon_s}{5\sqrt{\pi}} g_0 (1+e)\right)$$
$$K_4 = \frac{12(1-e^2)\rho_s g_0}{d_s\sqrt{\pi}}$$

When using this algebraic equation in stead of solving the balance for the granular temperature, much faster convergence is obtained during simulations. It has been shown by Boemer *et al.* (1995) that using this approach hardly affects the granular temperature in the bubbling regime.

Interphase momentum exchange

In this work the interphase drag function of Syamlal *et al.* (1993) is used. This drag function is based upon Richardson and Zaki (1954), Dalla Valle (1948), and Garside and Al-Dibouni(1977) :

$$\beta = \frac{3}{4} C_D \frac{\epsilon_s \epsilon_g \rho_g}{V_r^2 d_s} \cdot |\mathbf{v}_g - \mathbf{v}_s| \qquad (4.15)$$

with

$$C_D = \left(0.63 + 4.8\sqrt{\frac{V_r}{Re}}\right)^2$$

$$V_r = 0.5 \cdot \left(a - 0.06Re + \sqrt{(0.06Re)^2 + 0.12Re(2b - a) + a^2}\right)$$

$$a = \epsilon_g^{4.14}$$

$$b = \begin{cases} 0.8\epsilon_g^{1.28} & \text{if } \epsilon_s \geq 0.15 \\ \epsilon_g^{2.65} & \text{if } \epsilon_s < 0.15 \end{cases}$$

$$Re = \frac{d_s \rho_g \cdot |\mathbf{v}_g - \mathbf{v}_s|}{\mu_g}$$

where C_D is the drag coefficient, V_r is the ratio of terminal velocity of a group of particles to that of an isolated particle, Re is the particle Reynolds number, and μ_g is the gas viscosity.

This approach is only valid if the distribution of particles on the size of the grid cells can be assumed homogeneous. The size of the grid cells in multiphase simulations is in the order of one square centimetre. Especially in systems with very low solids concentration, like for instance circulating fluidized beds, the number of particles in a grid cell is largely fluctuating compared to the total number of particles, and this approach can give incorrect results.

4.A.3 Simulations

Simulation code

The differential equations (1), (3) and (4) mentioned in the previous section all express a conservation principle and are solved on a unit-volume basis. Thus the conservations need to yield over all possible finite volumes covering the whole problem space. Solving differential equations this way is called finite volumes. The differential equations express the conservation over an infinitesimal control volume and need to be discretized over the used finite volumes. This mathematical process is described by Patankar (1980).

The simulations were carried out with the commercial CFD code CFX4.1c from AEA Technology, Harwell, UK. This package allows free implementation of extra equations, boundary conditions, and differencing schemes. The granular kinetic theory and the granular equations described in the previous section were implemented into this code. The discretization used by CFX is the so called Rhie-Chow (Rhie and Chow, 1983) algorithm. This algorithm can be used with a non staggered grid : all the discretized variables are stored at the same boundary points.

For solving the difference equations obtained from the differential equations, the higher order TVD scheme min-mod is used. This TVD scheme incorporates a modification to the higher-order upwind scheme. Sokolichin *et al.* (1997) have shown that solutions obtained with the TVD scheme result in less numerical diffusion than lower order schemes. Less numerical diffusion leads to a sharper interface between the gas and the solid boundary (e.g. at bubbles or at the freeboard). The solution of the pressure from the momentum equations requires a pressure correction equation, correcting the pressure and the velocities after each iteration of the discretized momentum equations. In this work the SIMPLE algorithm developed by Patankar (1980) is used for this purpose. The calculated pressure is used to calculate the density of the gas phase.

Table 4.1: *List of values of model parameters used in the simulations.*

Symbol	Description	Value	Comment/reference
ρ_s	solids density	2600 kg m^{-3}	glass beads
ρ_g	gas density	1.28 kg m^{-3}	air at ambient conditions
d_p	particle diameter	500 μm (Geldart B)	no size distribution
e	coefficient of restitution	0.60	Boemer *et al.* (1995)
ϵ_{max}	maximum solids packing	0.61	Syamlal *et al.* (1993)
ϕ	angle of internal friction	25°	Johnson and Jackson (1987)
U_{mf}	min. fluidization velocity	0.25 ms^{-1}	from Ergun (1952)
Δt	time step	1.0 10^{-5} – 10^{-4} s	for convergence
Δx	mesh spacing	6.0 10^{-3} – 10 ^{2} m	to reduce numeric diffusion
Θ_s	granular temperature	10^{-5} – 0.1 m^{2}s^{-2}	Balzer and Simonin (1993)
U_0	superficial gas velocity	0.5 – 1.0 ms^{-1}	a range is used
D_t	column diameter	0.2 – 0.4 m	a range is used
H_t	column height	0.6 m	fixed value
H_{mf}	settled bed height	0.34 m	fixed value

Fluidization conditions

The values used for the parameters needed in the simulations can be seen in Table 4.1. The simulated fluidized bed is a two-dimensional rectangular column. Air at ambient temperature and pressure is used for the fluidizing gas. The gas is treated compressible and thus the density is coupled to the pressure, according to the ideal gas law. For the solids, uniform sized glass beads were used. It has been shown by De Groot (1967) that the diameter

distribution has a large influence on the fluidization behavior of the granular material. De Groot states it is difficult to fluidized monodisperse solids, especially in larger beds. There is however little known yet about the exact cause and effect and it is unknown how a physical diameter distribution should be implemented into a TFM, and what the effect would be. The TFM is not an exact model of a fluidized granular material, and it is questionable whether an implemented diameter distribution or not would make a large difference.

The size of the time step influences two effects : the convergence of the iterations regarding the solution of the differential equations, and the computation time. The time step used for the highest simulated fluidization velocity, (i.e., four times U_{mf}) is $1.0 \cdot 10^{-4} s$ and for the lowest velocity (i.e., two times U_{mf}) twice this size is used. Both were checked to be sufficiently small.

The size of the grid spacing in multiphase flow is of the order of one square centimetre. This is found to be an optimum between computational effort and numerical diffusion. The larger the grid spacing is, the more numerical diffusion will take place. At high fluidization velocities, diffusion of mass is less important than at lower fluidization velocities. In this work it is found that lower fluidization velocities require a finer mesh. Using a coarse mesh at lower fluidization velocities leads to lower porosities in bubbles, and thus to less realistic results. The mesh chosen in this work for two times U_{mf} is $\Delta x = 7.0 \cdot 10^{-3}$ m, and for four times U_{mf} is $\Delta x = 1.0 \cdot 10^{-2}$ m. These values lead to similar volume fraction inside bubbles at all simulated fluidization conditions.

Boundary and initial conditions

All simulations are carried out in a pseudo two-dimensional square space in which there are no front and back wall effects. In the simulations particles cannot travel freely in the third dimension : the momentum equations are only solved for two dimensions. Numerically this can be seen as two symmetry planes placed right in the front and at the back of the fluidized bed.

The left and right wall of the fluidized bed are treated as no slip boundary conditions for the gas phase : the velocity of the gas phase is set to zero at the wall. For the solids phase a different condition should be used: particles can move downwards while touching the wall. It seems not very important what kind of slip condition is chosen at the wall, as long as particles are able to fall down at the wall. In this work a free slip condition is chosen : the particles find no hinder in their downward or upward velocity when they are near a wall.

The boundary condition at the top of the fluidized bed is a so-called pres-

sure boundary. The pressure in the mesh cells at the top of the fluidized bed are fixed at a specific value. Neumann boundary conditions are applied to the gas flow velocity. This is also called 'fully developed flow' : the derivatives of the upward velocity in the horizontal direction are assumed zero. It is important that the freeboard of the fluidized bed is high enough, so that fully developed flow can be physically expected.

From the momentum balances, the mass flux, containing the concentration, is solved. If the concentration is zero or within the computational inaccuracy, this can lead to unrealistic values for the particle velocity field, resulting in an unrealistic drag force and that leading to an unrealistic gas velocity field. For that reason, a very small solids concentration ($\sim 10^{-6}$) for the particle phase is set in the top cells, leading to particle 'leakage' into the fluidized bed (Balzer and Simonin, 1996). This way the whole freeboard is filled with a very small number of particles. The number of particles in the freeboard is chosen small enough not to have any influence on the physics in the fluidized bed.

At the bottom of the fluidized bed, the gas inflow is specified. This is called a Dirichlet boundary condition. In the beginning of the simulation a small perturbation is specified in one of the cells of the bottom. This is to break the horizontal symmetry. In an actual fluidized bed this is caused by the random packing of the particles. The distributor is made impenetrable for the solids phase: the solids downward velocity is set to zero in the bottom cells.

For the initial condition the bottom half of the bed is filled with particles at a particle concentration of 0.58. The gas flow in the bed is set to minimum fluidization velocity at $t = 0$. In the freeboard a very small number of particles is set, as was explained above.

4.A.4 Classical bubble size and velocity relations

A lot of experimental work has been done in the 70's and 80's regarding the bubble behavior in gas-solid fluidized beds. The Darton *et al.* (1977) bubble model is a generally accepted semi-empirical model for bubble growth. The model is based upon the preferred paths of bubbles where the distance travelled by two neighbouring bubbles before coalescence is proportional to their lateral separation. The proposed equation is :

$$D_b = 0.54(U_0 - U_{mf})^{0.4}(h + 4\sqrt{A_0})^{0.8}/g^{0.2} \qquad (4.16)$$

where D_b is the bubble diameter, h is the height of the bubble above the distributor, and A_0 is the 'catchment area' which characterises the distributor; 0.54 is the only experimentally determined constant. This model is not applicable to slug flow, nor to Geldart C powders. Werther and Molerus

Figure 4.1: *The visual representation of a simulation of 0.4 m width column at 4 times* U_{mf}.

(1973) developed a small capacitance probe to measure the bubble diameter and the bubble velocity. This capacitance probe can be placed in the fluidized bed, at different heights and radial positions. The bubble velocity can be determined by placing two capacitance probes above each other, and correlating the data obtained. The main problem in this approach is translating the measured pierced lengths into an average bubble diameter with a distribution. To accomplish this, Werther (1974) assumed the bubble shape to be elliptical. Knowing the total number of bubbles that have passed the probe, he determined an average bubble diameter and diameter distribution from the measured pierced lengths.

Davidson and Harrison (1963) proposed a bubble rise velocity according to the two phase theory of fluidization :

$$u_b = U - U_{mf} + \varphi\sqrt{g d_b} \tag{4.17}$$

where φ is the analytically determined square root of the Froude number of a single rising bubble in an infinitely large homogeneous area. Pyle and Harrison (1967) have determined that $\varphi = 0.48$ for a two dimensional geometry, whereas in three dimensions $\varphi = 0.71$. Equation 4.17, however, did not satisfy the results obtained by Werther (1974). Hilligardt and Werther (1986) explained the differences between Werther's measurements and the two phase flow equation by the following observations : Il

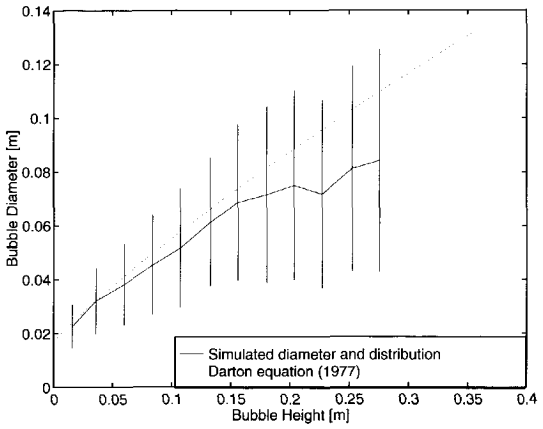

Figure 4.2: *Bubble diameters versus bed height at 2 times* U_{mf} *in a 0.4* m *width column.*

1. under normal operating conditions for bubble formation without slugging, the visible flow rate is clearly lower than the excess gas velocity $(U - U_{mf})$;

2. bubbles of a given size rise faster in a fluidized bed of larger diameter.

They proposed an adapted equation for the bubble rise velocity :

$$u_b = \psi(U - U_{mf}) + \varphi\nu\sqrt{g d_b} \tag{4.18}$$

to correct for the two differences mentioned. Hilligardt and Werther (1986) have determined empirical correlations for the parameters ψ and ν for different types of solids. They have done experiments with similar particles as used in this work ($\rho_s = 2640 kg\,m^{-3}$, $d_p = 480\mu m$), and have used these simulations to establish the values for the parameters of Geldart group D particles, because Molerus (1982) has characterised this solid under group D. The parameter ψ describes the deviation of the visible bubble flow rate, $\dot{V}_b$, from the two phase theory :

$$\psi = \frac{\dot{V}_b}{U - U_{mf}} \tag{4.19}$$

Values for ψ have been experimentally obtained by Hilligardt and Werther (1986) :

$$\psi = \begin{cases} 0.26 & \frac{h}{D_t} < 0.55 \\ 0.35\left(\frac{h}{D_t}\right)^{0.5} & 0.55 \leq \frac{h}{D_t} \leq 8 \end{cases} \tag{4.20}$$

for Geldart group D particles. This was later simplified by Kunii and Levenspiel (1991) to a similar, but bubble height independent formula.

The parameter ν accounts for that part of the deviation from the behavior from a single bubble, which is not reflected by the additive term $\psi(U - U_{mf})$. Hilligardt and Werther (1986) have experimentally determined for Geldart group D solids :

$$\nu = 0.87 \tag{4.21}$$

4.A.5 CFD simulation results

The fluidized state of the bed can be visualised by plotting different grey tones, assigned to different solid volume fraction regions, in the grid cells. This is done in Figure 4.1 by assigning darker grey tones to increasing solid volume fractions.

In this paper a bubble is defined as an area where the solid volume fraction is below a certain value. The value in this work is chosen at 15%. This value is also used by other authors and does not depend on the mesh coarseness : the value of 15% lies before the largest solid volume fraction gradient leading to a bubble edge. To ensure this, the mesh for the lower fluidization velocities is finer than for higher velocities. Confined areas with more than one cell with a solid volume fraction below 20% are defined as bubbles. The diameter of this bubble is calculated as if its shape is circular and the diameters and centres of all bubbles in the bed are recorded. Bubble velocities are determined by studying the bubble diameter and centre in consecutive time steps, thus enabling the calculation of the complete bubble trajectory.

The main objective of this work is to validate the outcome of the CFD model with existing empirical equations for bubble size and velocity. This validation can be difficult, because it is not always exactly clear what authors have measured in reality : have they taken all the bubbles into account, or only the larger bubbles; have they included effects as coalescence, break-up, and wall effects? Experimentally it can be very hard to obtain precise physical data from a fluidized bed, whereas simulations like in this work produce an abundance of data. *When comparing a model to measurements, it is important to retrieve similar data from the model as is retrieved from the measurements.* For the empirical models of Hilligardt and Werther (1986) and Darton *et al.* (1977), bubbles touching the column walls were not considered. The determination of the bubble velocity by Werther (1974) was done by not taking effects like coalescence and break-up during the observation into account. These effects should not be considered when comparing the predicted bubble trajectories to the correlation of Hilligardt and Werther (1986). For compar-

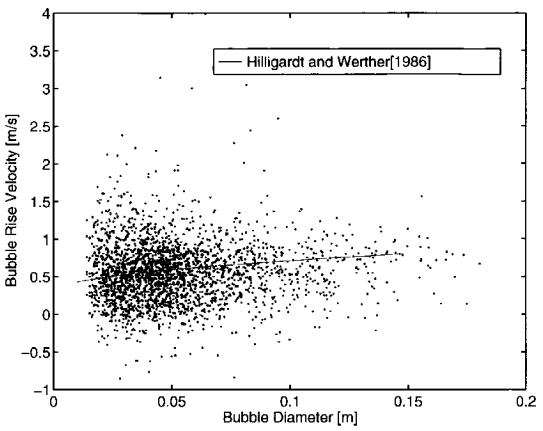

Figure 4.3: *Bubble rise velocity versus bubble diameter at 4 times* U_{mf} *in a 0.4* m *width column. All bubbles predicted from the simulation are shown.*

ison with the Darton *et al.* (1977) equation, the bubbles in each simulation are divided into twelve categories of increasing bubble diameter. Figure 4.2 shows the bubble diameter and the distribution of each category together with the estimated average bubble diameter by the Darton *et al.* equation for one condition. It can be seen that the predicted bubble diameters are slightly smaller in the higher part in the fluidized bed, but not in disagreement. This can be due to a deficiency of the used measuring technique by Darton *et al.* (1977) in measuring very small bubbles.

The bubble rise velocities versus the bubble diameters are shown in Figure 4.3. This figure shows an enormous spread in bubble rise velocities, due to coalescence, break-up, and bubbles interacting directly with the wall. Figure 4.4 shows the same bubbles averaged into eight classes with increasing bubble diameter. It can be seen that especially smaller bubbles show deviating behavior : the average small bubbles rise faster through the bed than predicted by Hilligardt and Werther (1986), whom have only used bubbles of 0.04m and larger to establish their correlation; a wake of a bubble has a larger effect on a trailing small bubble than on a trailing larger one. Figure 4.5 shows part of bubble trajectories without coalescence, break-up, and bubbles touching the wall. The symbol '+' is used for bubbles which are not within ± 30% of the Darton *et al.* (1977) equation, and the symbol 'x' is used for the remaining bubbles. In this figure also the equation proposed by Hilligardt and Werther (1986) is shown. The unaffected bubble trajectories averaged in classes and a fit of this data is shown in Figure 4.5. The values for the coefficients ψ and ν proposed by Hilligardt and Werther (1986), and the resulting values of the fits from all simulated fluidization conditions are shown in Table 4.2. For

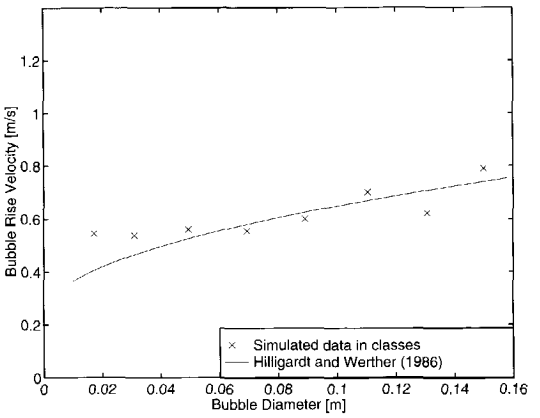

Figure 4.4: *Bubble rise velocity versus bubble diameter at 4 times* U_{mf} *in a 0.4* m *width column : the bubbles of Figure 4.3 have been averaged into eight classes.*

the determination of the parameters at each fluidization condition, over 3000 bubbles are used. The simulation results are in reasonable agreement with the values proposed by Hilligardt and Werther (1986). One of the main issues in testing the CFD model is comparing the abundance of data out of each simulation to the empirical relations developed by measurements. Measuring techniques and the processing of the outcome of these measurements do not always reflect the exact physical behavior of a system. In the Hilligardt and Werther (1986) bubble model, coalescence, break-up, and direct wall effects are not included. This work shows however, that these effects are very important in the bubble behavior, especially with smaller bubbles. Figure 4.3 shows that a large number of bubbles do coalesce, break-up, or have wall interactions, and that these bubbles do not necessarily have the rising velocity predicted by the Hilligardt and Werther (1986) equation.

4.A.6 Conclusions

The predicted values of the bubble diameter at a certain bed height are in agreement with the Darton *et al.* (1977) bubble equation. The comparison of the parameters ψ and ν with Hilligardt and Werther (1986) show that the values are in the same order of magnitude, and that the model of Hilligardt and Werther (1986) is in agreement with the (larger) bubbles predicted by simulations. In this work, however, some dependency is seen of both parameters upon the fluidization condition. Hilligardt and Werther do not state which fluidization conditions they have used to obtain the values for ψ. Possibly ψ is less fluidization condition independent as reported by Hilligardt and Werther (1986).

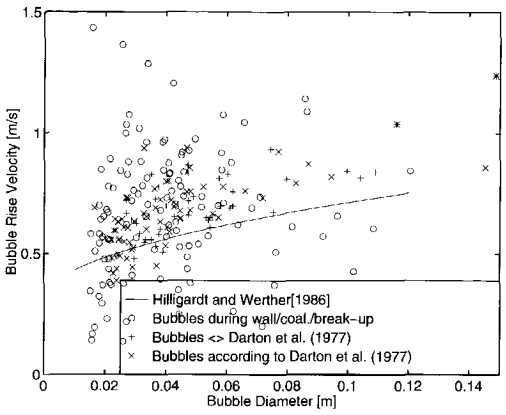

Figure 4.5: *Bubble rise velocity versus bubble diameter at 4 times* U_{mf} *in a 0.4 m width column. Bubbles affected by coalescence, break-up, and bubbles touching the wall during the calculation of their velocity are shown with 'o', while other bubbles with 'x' or '+'.*

The large abundance of data obtained from a simulation gives much information about the dynamic behavior in fluidized beds and can be a very valuable tool, not only in the validation of existing empirical correlations, but also in the improvement of existing correlations, the determination of new correlations, or the calculation of specific physical properties of a certain configuration.

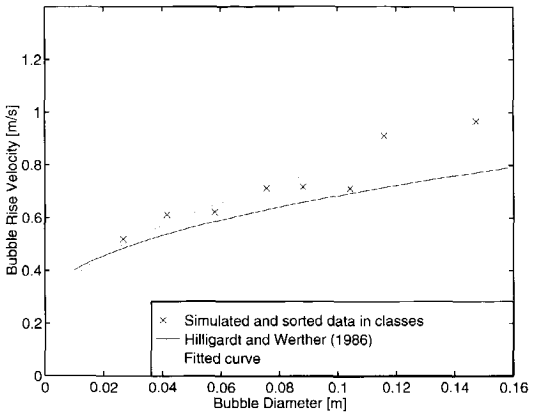

Figure 4.6: *Bubble rise velocity versus bubble diameter at 4 times* U_{mf} *in a 0.4 m width column. Predicted bubbles not affected by coalescence, break-up, and bubbles touching a wall during the calculation of the velocity grouped into eight classes.*

Table 4.2: *Comparison of calculated values for* ψ *and* ν *from the CFD model simulations at different column diameters and fluidization velocities with the values from the Hilligardt and Werther (1986) model.*

		CFD model	H. & W.	CFD model	H. & W.	CFD model	H. & W.
U_0 [m/s]	Para-meter	Column diameter 20 cm		30 cm		40 cm	
0.50	ψ	1.1	0.26 - 0.35	1.0	0.26 - 0.35	0.90	0.26 - 0.35
	ν	0.62	0.87	0.61	0.87	0.63	0.87
0.625	ψ	0.71	0.26 - 0.35	0.62	0.26 - 0.35	0.81	0.26 - 0.35
	ν	0.74	0.87	0.70	0.87	0.66	0.87
0.75	ψ	0.32	0.26 - 0.35	0.40	0.26 - 0.35	0.48	0.26 - 0.35
	ν	0.79	0.87	0.87	0.87	0.95	0.87
0.875	ψ	0.24	0.26 - 0.35	0.24	0.26 - 0.35	0.49	0.26 - 0.35
	ν	1.01	0.87	1.26	0.87	0.81	0.87
1.0	ψ	0.22	0.26 - 0.35	0.34	0.26 - 0.35	0.50	0.26 - 0.35
	ν	0.86	0.87	0.91	0.87	0.74	0.87

Part B:

Dynamic behavior of fluidized beds

This part has been published as:

B.G.M. van Wachem, J.C. Schouten, R. Krishna, and C.M. van den Bleek, (1999), Validation of the Eulerian Simulated Dynamic Behaviour of Gas-Solid Fluidized Beds, *Chemical Engineering Science*, **54**, pp 2141-2149.

Abstract

In this paper, a Eulerian-Eulerian CFD model for a freely bubbling gas-solid fluidized bed containing Geldart-B particles is developed for studying its dynamic characteristics. This CFD model is based on the kinetic theory of granular flow. Van Wachem *et al.* (1998) have shown that this model is capable of providing reasonable predictions of the *time-averaged* properties, such as the time-averaged bubble size and bubble rise velocity. In this paper, the *dynamic* characteristics of the gas-solids behaviour at different superficial gas velocities, at different column diameters, and at different pressures are evaluated, namely (**A**) the velocity of pressure and voidage waves through the bed, (**B**) the power of the low and high frequencies of the pressure and voidage fluctuations, (**C**) the reorientation of the gas-solids flow just above minimum fluidization and the effect of elevated pressure upon this reorientation, and (**D**) the Kolmogorov entropy. The CFD simulation results for items (**A**) through (**D**) are compared with experimental data and with appropriate correlations from the literature.

A good agreement is found between the Eulerian-Eulerian CFD simulations of bubbling fluidized bed dynamics, and the data from experiments in the literature. This is a strong incentive for the further development of this type of simulation models in fluidized bed reactor design and scale-up.

4.B.1 Introduction

Fluidized beds are increasingly important in today's chemical industry; however, their hydrodynamic behaviour, and hence their scale-up, is still poorly understood. Models describing the behaviour of fluidized beds are often (semi-)empirical and have been mostly determined under laboratory conditions. There is still no unifying theory available to describe the hydrodynamic behaviour of fluidized beds.

There is an increasing use of Computational Fluid Dynamics (CFD) as an engineering tool for predicting the flow behaviour in various types of equipment on an industrial scale. Although the tools for applying single-phase flow CFD are widely available, application of multiphase CFD remains complicated from both a physical and a numerical point of view. Moreover, experimental validation of multiphase CFD calculations is still in its infancy because simulations are time-consuming, so reliable predictions of flows in large-scale equipment are not easily obtained. Van Wachem *et al.* (1998) have shown that a Eulerian-Eulerian multiphase CFD model correctly predicts the time-averaged bubble properties (i.e., bubble size and rise velocity) of a gas-solid fluidized bed consisting of Geldart-B particles at various column diameters and superficial gas velocities. This result indicates that CFD models will be useful tools for the steady-state design of fluidized bed reactors. Besides the time-averaged properties, the dynamic characteristics of the fluidized bed's behaviour are important for choosing the appropriate conditions for stable operation and control.

Time-series analysis of pressure fluctuation data in bubbling fluidized beds has revealed that the fluid dynamics of fluidized beds are chaotic and low-dimensional (Schouten *et al.*, 1996). These chaotic dynamics are supposed to be due to the behaviour of the rise and interaction of bubbles.

The goal of the present work is to validate these dynamic characteristics of the Eulerian-Eulerian gas-solid model applied to freely bubbling fluidized beds containing Geldart-B particles, by comparing the simulated behaviour of the CFD model with trends predicted by appropriate empirical correlations and experimental data. With this goal in mind, the operating conditions applied are the same as those were used in the development of the empirical correlations and measurements.

4.B.2 Gas-solid CFD models

CFD models of gas-solid systems can be divided into two groups: Lagrangian models and Eulerian models. Lagrangian models, or discrete particle models, calculate the path of each particle in the gas-solid system. The interaction of these particles can be modelled by either a potential force (soft particle dynamics), or by collision dynamics (hard particle dynamics). The drawback of these models is the long calculation time needed to simulate the gas-solid motion in an apparatus of realistic size, while still requiring *empirical* data and correlations to describe the gas-solid interaction. Lagrangian models can be used to generate granular properties for use in the simpler Eulerian models. Eulerian models describe the locally averaged properties of gas-solid flow, which smooth out discontinuities, thus enabling computation by this model

to cover much larger geometries. A strategy for this averaging, however, must be chosen. The Eulerian CFD model used in this work, is based on a two-fluid model (TFM), which uses an extended Navier-Stokes equation to describe the solids phase and the gas phase so both phases are considered to be continuous and fully interpenetrating. Granular viscosities and granular pressure are derived from the kinetic theory of granular flow, which is derived from an analogy with the kinetic theory of gases (Chapman and Cowling, 1970). In this approach, thermodynamic temperature is replaced by granular flow temperature, as a measure of the fluctuating velocity of the particles. The interaction of the gas and solids phases is modelled empirically (Syamlal *et al.*, 1993). There is as yet no fundamental theory to describe gas-solid interactions in a rigorous manner.

Different TFM models have been described in the literature and are compared by Boemer *et al.* (1995). The most promising set of equations in the sense of fast numerical convergence and accurate physical results is used in this work.

The time-averaged equations of conservation of mass and momentum, in the Eulerian framework, are given in Table 4.3. The solids pressure and viscosities, needed for the conservation equation for the solids momentum, and the quantities needed to calculate the solids pressure and viscosities are summarized in Table 4.4. The interphase momentum exchange equations are given in Table 4.5. A description of the symbols can be found in the Nomenclature, and a complete explanation of these quantities is found in Van Wachem et al. (1998).

Table 4.3: *The mass and momentum balances of the Eulerian-Eulerian CFD model. The symbols are explained in the Nomenclature.*

$$\frac{\partial}{\partial t}(\epsilon_g \rho_g) + \nabla \cdot (\epsilon_g \rho_g \mathbf{v}_g) = 0$$
$$\frac{\partial}{\partial t}(\epsilon_s \rho_s) + \nabla \cdot (\epsilon_s \rho_s \mathbf{v}_s) = 0$$
$$\epsilon_g + \epsilon_s = 1$$
$$\frac{\partial}{\partial t}(\epsilon_g \rho_g \mathbf{v}_g) + \nabla \cdot (\epsilon_g \rho_g \mathbf{v}_g \mathbf{v}_g) = \nabla \cdot \bar{\bar{\tau}}_g + \epsilon_g \rho_g \mathbf{g} + -\epsilon_g \nabla P - \beta(\mathbf{v}_g - \mathbf{v}_s)$$
$$\frac{\partial}{\partial t}(\epsilon_s \rho_s \mathbf{v}_s) + \nabla \cdot (\epsilon_s \rho_s \mathbf{v}_s \mathbf{v}_s) = \nabla \cdot \bar{\bar{\tau}}_s + \epsilon_s \rho_s \mathbf{g} + -\epsilon_s \nabla P - \nabla P_s^* + \beta(\mathbf{v}_g - \mathbf{v}_s)$$

4.B.3 Model validation and dynamic simulation results

There are different techniques to determine dynamic characteristics of fluidized beds. Experimentally, for example, a pressure probe, an optic probe, or an X-ray probe can be used to study these characteristics. The pressure probe measures pressure fluctuations, indirectly caused by the rising and interaction of gas bubbles, bed mass oscillation, and turbulence. Optic probes

Table 4.4: *The granular equations in the Eulerian-Eulerian CFD model are taken from Syamlal* et al. *(1993), Boemer et al. (1995), Ding and Gidaspow (1990), Lun* et al. *(1984), and Jenkins and Savage (1983). An explanation of the symbols can be found in the Nomenclature.*

$$\Theta_s = \left(\frac{-(K_1\epsilon_s+\rho_s)\,\mathrm{tr}\left(\overline{\overline{D}}_s\right)+\sqrt{(K_1\epsilon_s+\rho_s)^2\,\mathrm{tr}^2\left(\overline{\overline{D}}_s\right)+4K_4\epsilon_s\left[2K_3\,\mathrm{tr}\left(\overline{\overline{D}}_s^2\right)+K_2\,\mathrm{tr}^2\left(\overline{\overline{D}}_s\right)\right]}}{2\epsilon_s K_4} \right)^2$$

$$K_1 = 2(1+e)\rho_s g_0$$

$$K_2 = \frac{4}{3\sqrt{\pi}} d_s \rho_s (1+e)\epsilon_s g_0 - \frac{2}{3}K_3$$

$$K_3 = \frac{d_s\rho_s}{2}\left(\frac{\sqrt{\pi}}{3(3-e)}\left[1+\frac{2}{5}(1+e)(3e-1)\epsilon_s g_0\right]+\frac{8\epsilon_s}{5\sqrt{\pi}}g_0(1+e)\right)$$

$$K_4 = \frac{12(1-e^2)\rho_s g_0}{d_s\sqrt{\pi}}$$

$$P_s^* = \epsilon_s\rho_s\Theta_s(1+2g_0\epsilon_s(1+e))$$

$$\lambda_s = \frac{4}{3}\epsilon_s\rho_s d_s g_0(1+e)\sqrt{\frac{\Theta_s}{\pi}}$$

$$\mu_s = \frac{4}{5}\epsilon_s\rho_s d_s g_0(1+e)\sqrt{\frac{\Theta_s}{\pi}} + \frac{2\frac{5\sqrt{\pi}}{96}\rho_s d_s\sqrt{\Theta_s}}{(1+e)\epsilon_s g_0}\cdot\left[1+\frac{4}{5}g_0\epsilon_s(1+e)\right]^2$$

$$g_0 = \frac{3}{5}\left[1-\left(\frac{\epsilon_s}{\epsilon_{s,max}}\right)^{\frac{1}{3}}\right]^{-1}$$

Table 4.5: *The interphase momentum exchange equations used, taken from Syamlal (1993), Richardson and Zaki (1954), Dalla Valle (1948), and Garside and Al-Dibouni (1977). An explanation of the symbols can be found in the Nomenclature.*

$$\beta = \frac{3}{4}C_D\frac{\epsilon_s c_g\rho_g}{V_r^2 d_s}\cdot|\mathbf{v}_g-\mathbf{v}_s|$$

$$C_D = 0.5\left(a-0.06\mathrm{Re}+\sqrt{(0.06\mathrm{Re})^2+0.12\mathrm{Re}(2b-a)+a^2}\right)$$

$$a = \epsilon_g^{4.14}$$

$$b = \begin{cases} 0.8\epsilon_g^{1.28} & \text{if } \epsilon_s \geq 0.15 \\ \epsilon_g^{2.65} & \text{if } \epsilon_s < 0.15 \end{cases}$$

$$\mathrm{Re} = \frac{d_s\rho_g\cdot|\mathbf{v}_g-\mathbf{v}_s|}{\mu_g}$$

and X-ray probes measure voidage fluctuations, indirectly caused by circulating solids, gas and particle turbulence, and especially rising bubbles.

The processing of these signals can be done in different ways. Firstly, the velocity of the fluctuations can be studied. This velocity can be found by multiplying bed height by the frequency at which the power spectral density (PSD) is maximal. Another way of finding this velocity is by correlating the fluctuations determined in different parts of the bed and dividing the distance between the measuring points by the time at which the correlation is maximal. Secondly, the PSD of the fluctuations gives information about how powerful a certain frequency in the signal is. Thirdly, fluctuations can be stud-

ied by looking at their predictability, expressed in the Kolmogorov entropy. Analysis of pressure fluctuations by Schouten and Van den Bleek (1992), Daw and Halow (1991), and Schouten *et al.* (1996) have revealed that fluidized beds are chaotic and low-dimensional. Using this technique, Van den Bleek and Schouten (1993) show a reorientation of the gas-solids flow occurring in fluidized beds just above minimum fluidization.

This work validates the dynamics of the Eulerian-Eulerian gas-solid CFD model applied to fluidized beds, by (**A**) comparing the velocity of the pressure waves to the work of Baskakov *et al.* (1986) and the velocity of voidage waves to the bubble rise velocity, (**B**) studying the fall off of frequencies above 10 Hz, (**C**) comparing the predictability of the voidage and pressure fluctuations just above minimum fluidization velocity with Van den Bleek and Schouten (1993), and (**D**) comparing the predictability of the voidage and pressure fluctuations at higher gas velocities with Schouten *et al.* (1996).

The differential and granular equations mentioned in this paper are solved with the commercial finite volume CFD package CFX4.1c from AEA Technology, Harwell, UK. This package allows free implementation of extra equations, boundary conditions, and differencing schemes. The granular equations (Table 4.8) and the momentum transfer equations (Table 4.9) have been implemented in this code. The simulations are carried out in a two-dimensional Cartesian space in which there are no front and back wall effects. Particles cannot travel in the third dimension; the momentum and mass conservation equations are only solved in two directions.

The solution of the pressure from the momentum equations requires a pressure correction equation, correcting the pressure and the velocities after each iteration of the discretized momentum equations. In this work the SIMPLE algorithm developed by Patankar (1980) is used for this purpose. The gas phase is treated as a compressible fluid and density is coupled to pressure, according to the ideal gas law.

For solving the difference equations obtained from the differential equations, the higher order Total Variation Diminishing (TVD) scheme min-mod is used. This TVD scheme incorporates a modification into the higher-order upwind scheme.

The choice of time step for integrating the differential conservation equations influences both the convergence of the solution and the total computation time. The time step used for the highest simulated fluidization velocity (i.e., four times U_{mf}) is $1.0 \cdot 10^{-4} s$ and for the lowest velocity (i.e., two times U_{mf}) twice this size is used. Both were found to be sufficiently small.

Table 4.6: *List of values of model parameters used in the simulations.*

Symbol	Description	Value	Comment/reference
ρ_s	solids density	2600 kg m^{-3}	glass beads
ρ_g	gas density	1.28 kg m^{-3}	air at ambient conditions
d_p	particle diameter	500 μm (Geldart B)	no size distribution
e	coefficient of restitution	0.60	Boemer *et al.* (1995)
ϵ_{max}	maximum solids packing	0.61	Syamlal *et al.* (1993)
ϕ	angle of internal friction	25°	Johnson and Jackson (1987)
U_{mf}	min. fluidization velocity	0.25 ms^{-1}	from Ergun (1952)
Δt	time step	1.0 10^{-5} – 10^{-4} s	for convergence
Δx	mesh spacing	6.0 10^{-3} – 10^{-2} m	to reduce numeric diffusion
Θ_s	granular temperature	10^{-5} – 0.1 m^{2}s^{-2}	Balzer and Simonin (1993)
U_0	superficial gas velocity	0.5 – 1.0 ms^{-1}	a range is used
D_t	column diameter	0.2 – 0.4 m	a range is used
H_t	column height	0.6 m	fixed value
H_{mf}	settled bed height	0.34 m	fixed value

The size of the grid spacing in multiphase flow is of the order of one square centimetre. This was found to be an optimum between computational effort and numerical diffusion. The larger the grid spacing is, the more numerical diffusion will take place. At high fluidization velocities, diffusion of mass is less important than it is at lower fluidization velocities. In this work it is found that lower fluidization velocities require a finer mesh. Using a coarse mesh at lower fluidization velocities leads to higher solids volume fractions in bubbles, and thus to less realistic results. The mesh chosen in this work for two times U_{mf} is $\Delta x = 7.0 \cdot 10^{-3}$ m, and for four times U_{mf} is $\Delta x = 1.0 \cdot 10^{-2}$ m.

Fluidization conditions

The values of the model parameters used can be seen in Table 4.10. For the gas phase, the properties of air at ambient temperature and pressure were used. At low fluidization velocities, simulations with two times ambient pressure were also performed. The density of the air at this elevated pressure is calculated according to the ideal gas law. For the solids phase, uniform glass beads were used. The minimum fluidization velocity, U_{mf}, of this material is almost independent of the density of the gas phase in the region between ambient pressure and two times ambient pressure.

All simulations were started by fluidizing the bed at four times U_{mf} to fully mix the solids phase. During the first period of 0.1 seconds of the simulation, the fluidizing gas is injected in a slightly asymmetrical manner in order to initiate an asymmetric situation. If the boundary conditions are fully symmetrical, the solution will remain symmetrical for a period of about 5 seconds, leading to rectangular bubbles. Eventually the numerical round-off errors will lead to the same, asymmetric solution. In reality the asymmetric situation will be caused by an asymmetric particle packing. After about 8 seconds, when an averaged stationary behaviour is achieved, the superficial gas velocity is instantly lowered to the required value.

To study the reorientation phenomenon, simulations were performed with superficial gas velocities of 0.25, 0.30, 0.35, 0.40, 0.50, and 0.60 m/s in a column of 0.3 m ID. These simulations were performed at two different pressures to study the pressure effect upon the reorientation of fluidized bed hydrodynamics.

To study the power spectral densities of the voidage and pressure signals and to calculate the Kolmogorov entropy for comparison with the correlation of Schouten *et al.* (1996), superficial gas velocities of 0.50, 0.63, 0.75, 0.88 and 1.0 m/s are applied. The column diameter is varied between 0.2 and 0.4 m ID.

Since one of the goals of this work is to validate our dynamic CFD simulation results with published experimental data, we would need to extract the same information from these dynamic simulations as that measured by the experimentalist. For the simulated pressure signal, pressure in a small volume, a computational mesh cell was recorded to describe an experimental pressure sensor as accurately as possible. Measuring the voidage or solids volume fraction optically or by an X-ray technique, implies measuring the voidage or solids volume fraction of a volume in a horizontal plane, which is done by obtaining these fluctuations in a complete horizontal plane of mesh cells from the simulations.

4.B.4 (A) Velocity of pressure and voidage waves in fluidized beds

Pressure waves

Pressure fluctuations have been studied experimentally by many researchers because they are relatively simple and inexpensive to measure. It is difficult, however, to construct a model from pressure fluctuations, predicting the complete dynamics of the fluidized bed. The dominant frequency in the pressure signal, however, is commonly reported and associated with a regular fluctuation in bed height (Roy *et al.*, 1990).

Roy *et al.* (1990) discuss several models describing the mechanism and the velocity of the dominant pressure waves in fluidized beds and conclude that the velocity of the dominant pressure wave in a fluidized bed is on the order of 10 m/s (the velocity of sound under these conditions). One of the models discussed by Roy *et al.* (1990), originally developed by Baskakov *et al.* (1986), describes a fluidized bed where only one bubble at a time erupts at the bed surface. The theory of this model is founded on the assumption that pressure fluctuations in the fluidized bed are similar to the oscillations of a liquid in U-shaped tubes. From this model the following can be derived:

$$t_n = \pi\sqrt{\frac{H_{mf}}{g}} \tag{4.22}$$

where t_n is the natural period of oscillation of the fluidized bed, H_{mf} the minimum fluidization bed height, and g the gravity constant. The natural period of oscillations, dominating the pressure waves, is most often experimentally assumed to coincide with the highest power in a frequency spectrum of a fluidized bed pressure time series. This natural period can also be found by cross-correlating two pressure fluctuation signals, measured at different heights in the bed. The vertical distance of the measuring probes, divided by the time delay found by the highest cross-correlation, is then used as the velocity of the most dominating pressure wave in the fluidized bed. In this work, the velocity of the most dominant pressure waves is determined by the highest power in the frequency spectrum, as in the work of Van der Schaaf *et al.* (1998).

Figure 4.7 shows an example of a simulated pressure fluctuation signal. In Figure 4.8 the most dominant frequency in the pressure fluctuations obtained from CFD simulations is compared with the theory of Baskakov *et al.* (1986). There does not appear to be any systematic trend in dependence of this dominant frequency on the superficial gas velocity, the column diameter, or the height of the measuring probe in the fluidized bed. Prediction of the frequency of the most dominant pressure wave is in good agreement with the theory developed by Baskakov *et al.* (1986), especially at higher gas velocities.

Voidage waves

Little is known about voidage fluctuations in gas-solids fluidized beds because they are hard to determine and especially to interpret. The velocity of voidage waves can be found in the same manner as the velocity of pressure waves, either by looking at the power spectrum of one series or by cross-correlating two spatially separated voidage fluctuation time series.

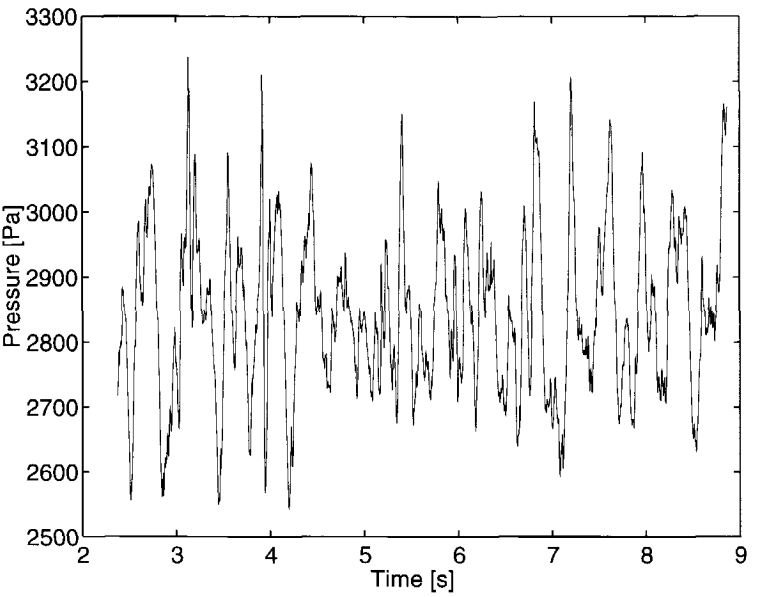

Figure 4.7: *Simulated pressure fluctuations in a fluidized bed,* D_t = 0.2 m, U_0 = 0.50 m/s, h = 0.1 m. *The type of particle used is given in Table 4.6.*

In this work, the rise velocity of voidage waves is compared to the rise velocities of the bubbles to establish a relationship between the voidage signal, which is measurable, and the bubble rise velocity.

The natural period of oscillation is smaller for pressure fluctuations than for voidage fluctuations (the velocity of pressure waves is larger than the velocity of voidage waves). In this work, the velocity of the voidage waves is determined by cross correlating because this method is more accurate for short time series than for the natural period of oscillation.

Figure 4.9 is an example of a simulated voidage signal. In Figure 4.10 we compare the velocity at which the vertical component of the voidage fluctuations propagates through the column with the bubble rise velocity determined from the simulations by tracking the position of individual bubbles. It is clear from Figure 4.10 that though there is a good correlation between these two velocity measures, other factors such as large-scale solids circulation will influence the voidage fluctuations velocity.

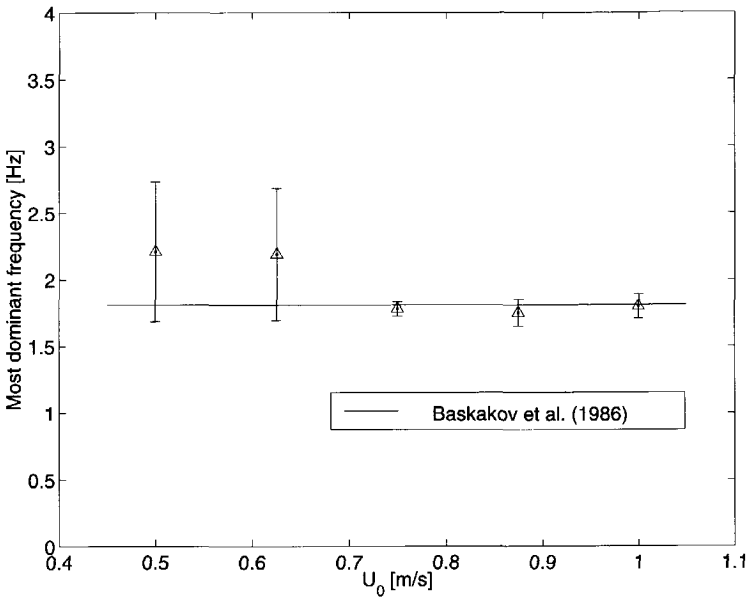

Figure 4.8: *The dominant frequency in the simulated pressure fluctuations as a function of the superficial gas velocity, compared to the theory of Baskakov* et al. *(1986). The error bars denote the spread due to data obtained at different heights in the fluidized bed and for different column diameters.*

4.B.5 (B) Power of pressure and voidage waves in fluidized beds

At higher frequencies, the power spectral density function (PSD) of pressure fluctuations obtained in a fluidized bed shows a power-law decay with increasing frequency (Ding and Tam, 1994), often with a non-integer value for the slope of the power-law decay in a log-log plot. The underlying physics of this power-law decay at increasing frequency, are believed to originate from bubble coalescence and bubble formation (Van der Schaaf *et al.*, 1998). Experimentally, it has been found that the slopes of the power-law decay of the PSD of pressure fluctuations in a bubbling fluidized bed in a log-log plot lie between -2 and -5 (Van der Schaaf *et al.*, 1998).

Ding and Tam (1994) showed that the power spectral densities of voidage fluctuations at high frequencies also obey a power-law decay. The slope of this power-law decay in a log-log plot, however, is different from the slope of the power-law decay obtained from the PSD of pressure fluctuations in a log-log plot, but it also is a non-integer.

Several explanations for the power-law decay of the pressure fluctuations ob-

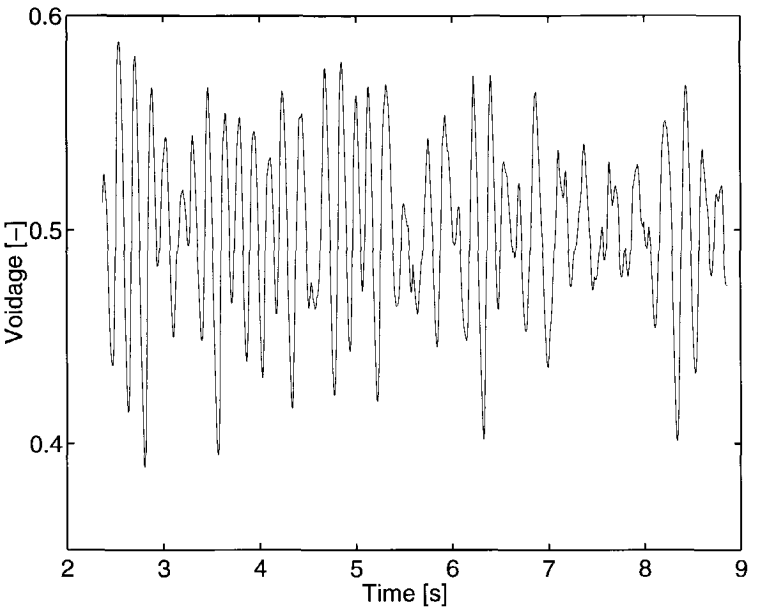

Figure 4.9: *Simulated voidage fluctuations in a fluidized bed,* D_t = 0.2 m, U_0 = 0.50 m/s, h = 0.1 m.

tained in a fluidized bed can be found in the literature (Van der Schaaf *et al.*, 1998). Supposing the fluctuations originate from a Brownian system, an explanation can be found in Gaspard and Wang (1993). They conclude that Brownian systems exhibit a power-law decay at increasing frequencies. Particles in a Brownian system can move in a specific direction without being correlated to their previous movement, in contrast to the particles or bubbles in a fluidized bed. Ding and Tam (1994) suggest that the number of possible derivatives of the measured pressure fluctuation is equal to the slope of the power-law decay in a log-log plot. This is only true, however, if the slope of the power-law decay is an integer.

Another approach to explaining power-law decay, is to study a pressure or voidage fluctuation originating from a single rising bubble in a fluidized bed: this somewhat resembles a triangular signal, increasing prior to the passing of a bubble, and decreasing right after the bubble passes (Figure 4.11). The PSD of a signal consisting of triangular waves gives a very spiky power-law decay, as depicted in Figure 4.12. The average slope of this power-law decay in a log-log plot, depends upon the height, width, and the number of discontinuities per period of the triangular signal. When a signal is formed from an increasing number of triangular waves, each with different characteristics

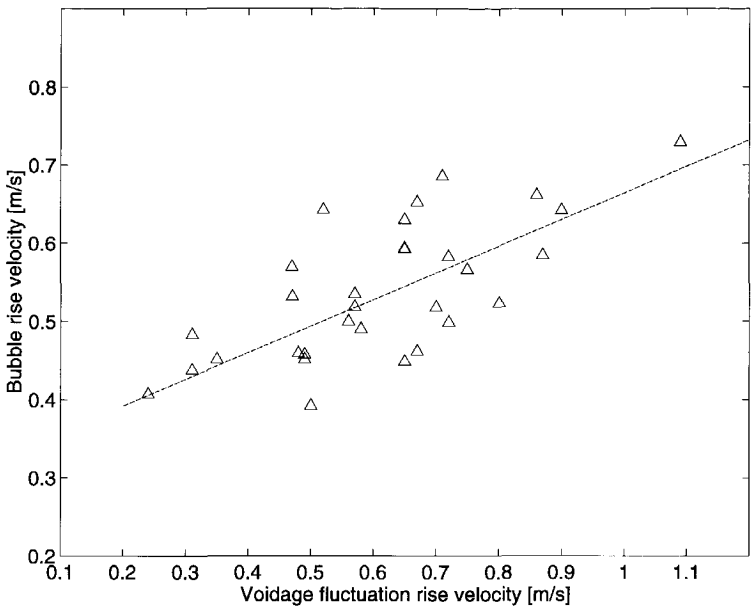

Figure 4.10: *Bubble rise velocity versus the vertical voidage fluctuation velocity. The line is drawn to show the trend.*

(i.e., height and width), more and more spikes arise in the higher frequencies of the PSD, eventually leading to a smooth power-law behaviour, because all the valleys between two spikes are filled up by other spikes. The passage of different sizes of bubbles may somewhat resemble a measured signal with differing triangular waves, where the amplitude (a function of bubble diameter), and the width of the triangular wave (a function of passage time) are physically coupled.

In Figures 4.13 and 4.14, the PSDs of the simulated pressure and voidage fluctuations are shown. In Figure 4.15, the slopes of the power-law decay in the log-log figures for all simulated fluidization operating conditions are depicted. Figure 4.15 shows that the operating conditions have very little influence on the slope of the power-law decay and that the values for the power-law decay of the pressure fluctuations are in good agreement with the values reported by Van der Schaaf *et al.* (1998), i.e., between -2 and -5. The simulated voidage fluctuations exhibit a different power-law decay than simulated pressure fluctuations, which is also shown in a simulation by Ding and Tam (1994).

The true underlying physics and the meaning of the slope of the power at higher frequencies remain unknown. The idea that every bubble emits a tri-

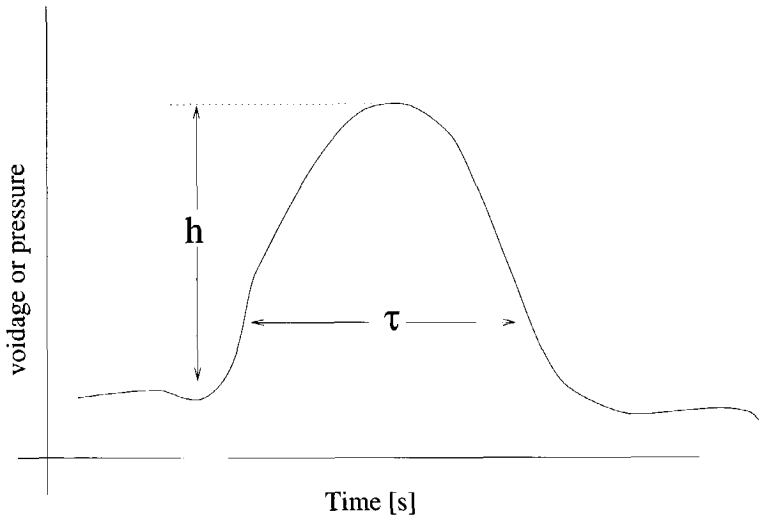

Figure 4.11: *A passing bubble leads to a triangular wave in the voidage or pressure signal. The larger the bubble diameter, the larger the amplitude of the triangular wave (h) will be. The duration of the wave (τ) is coupled with the diameter of the bubble and the bubble rise velocity.*

angular wave, where the width and height of the wave are physically coupled, leads to a PSD similar to the pressure waves from fluidized beds.

4.B.6 (C) Reorientation effect in fluidized beds

Van den Bleek and Schouten (1993) measured the predictability of pressure fluctuations in a gas-solid fluidized bed, expressed by the Kolmogorov entropy, as a function of the superficial gas velocity just above the minimum fluidization velocity, to investigate the onset of chaos in gas-solid fluidized beds. It was found that between minimum fluidization and the freely-bubbling state an intermediate regime exists, where predictability first increases and then decreases, and then increases again. This local minimum of predictability denotes a sort of reorientation of the fluidized bed.

The so-called particle array model, consisting of five particles in a one-dimensional vertical array with these two basic forces, drag and gravity, shows the same type of reorientation (Van den Bleek and Schouten, 1993). Also, the cellular automata model with thousands of particles in a two-dimensional space, incorporating drag and gravity forces, shows this reorientation (Van Wachem *et al.*, 1997). The underlying physics of this reorientation are not yet fully understood.

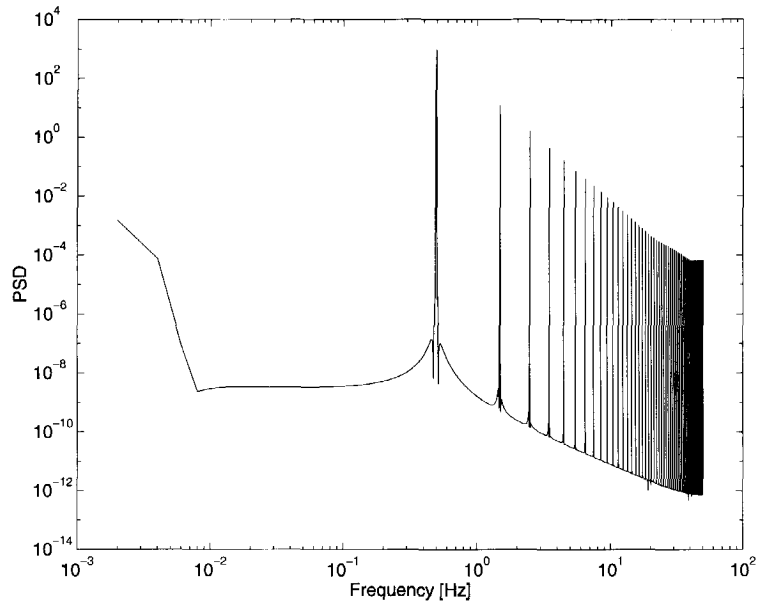

Figure 4.12: *The Power Spectral Density (PSD) of a triangular wave.*

In this work, simulations are performed with Geldart-B type particles, with seven increasing superficial gas velocities, each just above the minimum fluidization velocity. The particle type used in this work differs somewhat from the particle type used by Van den Bleek and Schouten (1993); the qualitative reorientation effect, however, is believed to be independent of particle types, and is even observed in bubble columns.

This work also presents reorientation at a higher pressure. Yates (1996) reports that elevated pressure increases the superficial gas velocity at which bubbles are formed. This should be clearly visible in the entropy plot showing reorientation.

The pressure and voidage time series obtained from the simulations with a superficial gas velocity just above the minimum fluidization velocity at ambient pressure, performed with two different column diameters, show the same qualitative reorientation effect as that experimentally observed by Van den Bleek and Schouten (1993), as is depicted in Figure 4.16. The simulations performed at two times the ambient pressure show that the valley shifts to higher gas velocities; the reorientation predicted by the simulations done at a higher pressure starts (decrease of entropy) and ends (increase of entropy) at a higher gas velocity, as can be seen in Figure 4.16. This implies a delay in the gas velocity at which bubbles are formed, in conformity with available

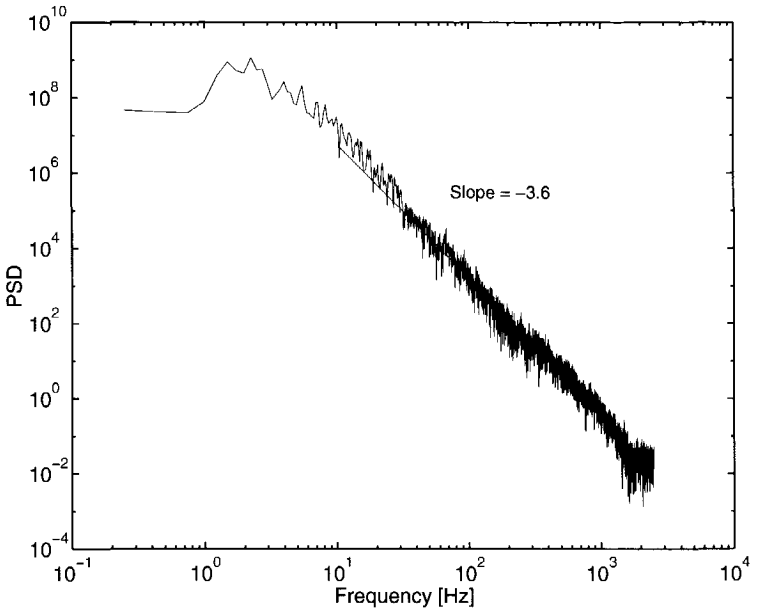

Figure 4.13: *Power spectral density of the simulated pressure fluctuations in a fluidized bed,* $D_t = 0.2$ m, $U_0 = 0.50$ m/s, $h = 0.1$ m.

experimental data (Yates, 1996).

4.B.7 (D) Chaotic behaviour of fluidized beds

The hydrodynamic behaviour of bubbling gas-solid fluidized beds can be described as chaotic (Schouten and Van den Bleek, 1992; Daw and Halow, 1991; and Schouten *et al.*, 1996). The low-dimensional chaotic behaviour is due to rising and interacting bubbles. The chaotic characteristics of dynamic systems can be estimated from a time series of only one of the systems' characteristic variables, such as pressure or voidage fluctuations in bubbling fluidized beds. One important characteristic is the Kolmogorov entropy, which measures the rate of loss of information (expressed in bits of information per unit of time) and quantifies the *unpredictability* of chaotic systems. The limiting values for the Kolmogorov entropy are infinity for completely random systems and zero for completely deterministic systems. Schouten *et al.* (1996) derived the following empirical relationship between the Kolmogorov entropy, K, and characteristic fluidized bed operating conditions, such as the superficial gas velocity, U_0, the minimum fluidization velocity, U_{mf}, the bed diameter, D_T,

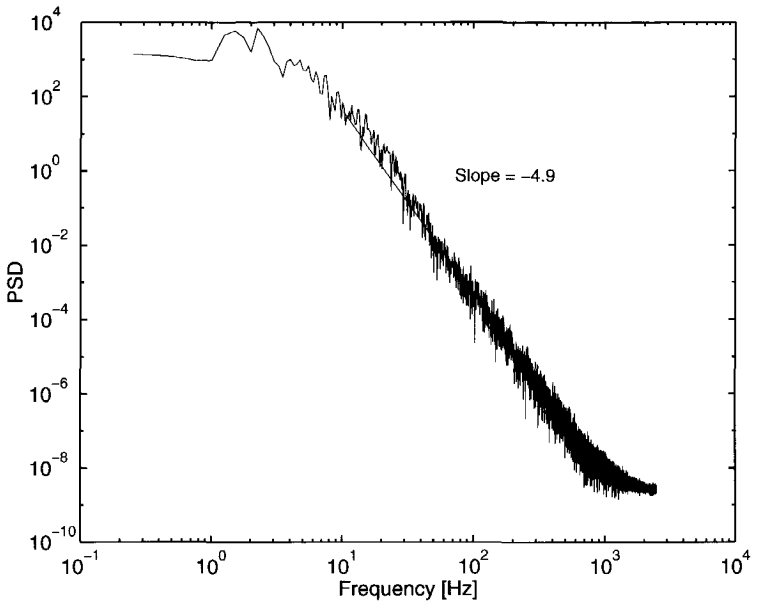

Figure 4.14: *Power spectral density of the simulated voidage fluctuations in a fluidized bed,* $D_t = 0.2$ m, $U_0 = 0.50$ m/s, $h = 0.1$ m.

and the settled bed height, H_s :

$$K(\text{bits/s}) = 10.7 \left(\frac{U_0 - U_{mf}}{U_{mf}} \right)^{0.4} \frac{{D_T}^{1.2}}{{H_s}^{1.6}} \tag{4.23}$$

In this work, the Kolmogorov entropy is calculated from pressure and voidage time series produced using CFD simulations at settled bed height. The CFD simulations are performed with similar operating conditions used to establish the correlation given by Equation 4.23.

The comparison between Equation 4.23 and the simulations is made in Figure 4.17. Although the quantitative comparison is not excellent, the simulations do reflect the behaviour of Equation 4.23. Furthermore, the spread of the experimental measurements used to establish Equation 4.23 is also very large.

4.B.8 Conclusions

In this paper we have carried out simulations of the dynamic behaviour of laboratory-scale gas-solid fluidized beds containing Geldart-B powders. The dominant frequency of the pressure fluctuations of these simulations agrees with that in the theory of Baskakov *et al.* (1986). The velocity at which the

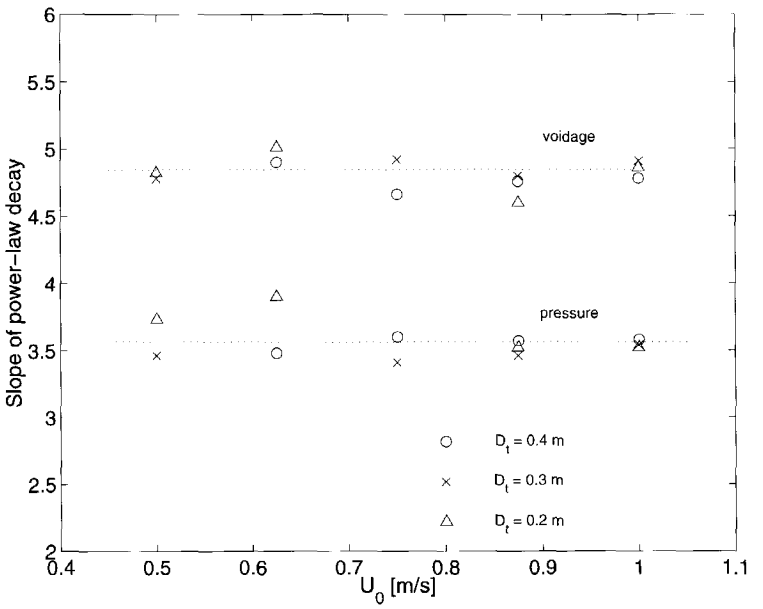

Figure 4.15: *The slopes of the power-law decay after about 10 Hz in the PSD figure (Figures 4.13 and 4.14) for different column diameters, superficial gas velocities and either simulated pressure or voidage fluctuations.*

voidage fluctuations propagate vertically through the column appears to correlate with the bubble rise velocity. The power-law decay characteristics of the PSD of the pressure and voidage fluctuations match those observed by Ding and Tam (1994) and Van der Schaaf et al. (1998).

Our dynamic Eulerian simulations are able to reproduce the reorientation effects in fluidized beds in the vicinity of the point at which the first bubbles are formed. Simulations with increasing pressure show that the valley in the plot of the Kolmogorov entropy versus gas velocity (Figure 4.16) shifts to the right. This implies delayed bubbling, in conformity with experiments. It appears that Eulerian simulations have the intrinsic capability to portray the influence of increased system pressures.

Since we have demonstrated that Eulerian simulations are able to correctly reproduce the dynamic characteristics of laboratory scale-fluidized beds, we are reasonably confident that such simulations could be used to study the influence of column diameter and height on fluidized bed performance. Therefore, Eulerian CFD simulations could be useful scale-up tools.

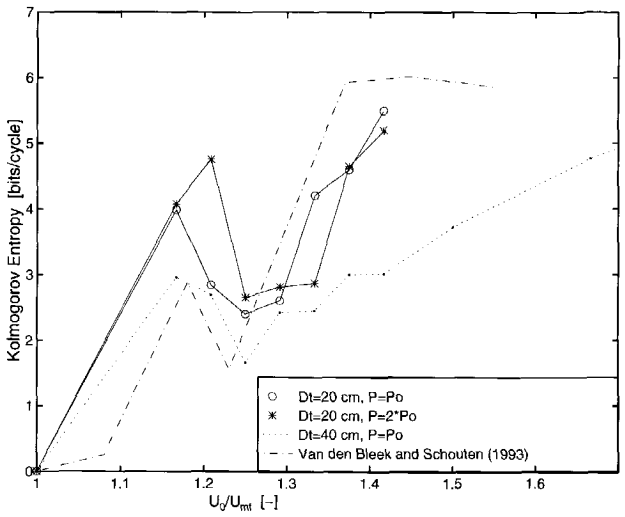

Figure 4.16: *The Kolmogorov entropy just above the minimum fluidization velocity in four cases: that predicted by Van den Bleek and Schouten (1993), a simulation of a 20 cm ID column at standard temperature and pressure (STP) conditions, a simulation of a 20 cm ID column at two times the standard pressure, and a simulation of a 40 cm ID column at STP conditions.*

Nomenclature

a	defined in Table 4.5
b	defined in Table 4.5
C_D	drag coefficient
d_s	particle diameter, m
$\overline{\overline{D}}_s$	strain rate tensor, s^{-1}
D_T	column diameter, m
e	coefficient of restitution
$\mathbf{g}$	gravitational constant, $m\,s^{-2}$
g_0	radial distribution function
h	height in fluidized bed, m
H_{mf}	minimum fluidization bed height, m
H_s	settled bed height, m
H_t	column height, m
K	Kolmogorov entropy, *bits* s^{-1}
K_1, K_2, K_3, K_4	variables defined in Table 4.4
P	pressure, $N\,m^{-2}$
PSD	Power Spectral Density
Re	Reynolds number

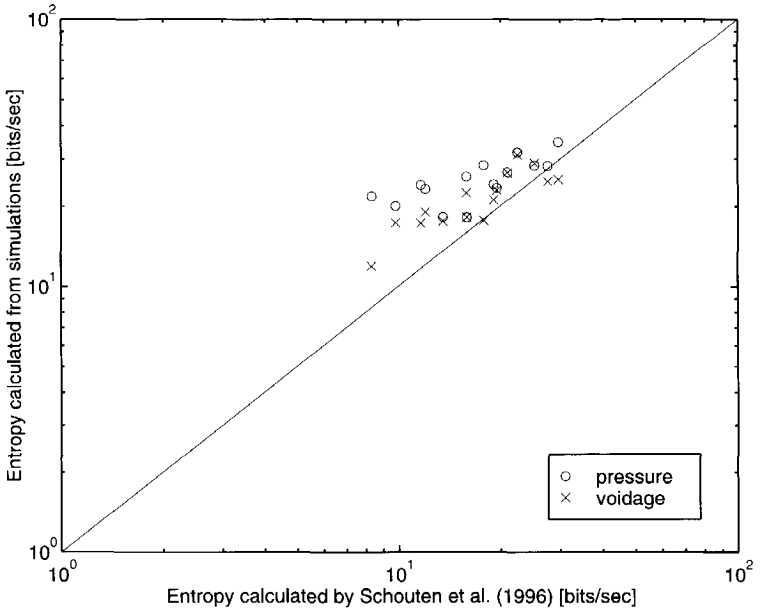

Figure 4.17: *The Kolmogorov entropy calculated from simulated voidage and pressure fluctuations just under settled bed height, compared to Equation 4.23.*

Δt	time step, s
t_n	natural period of oscillation, s
U_0	superficial gas velocity, $m\,s^{-1}$
U_{mf}	minimum fluidization velocity, $m\,s^{-1}$
$\mathbf{v}$	velocity vector, $m\,s^{-1}$
V_r	ratio of terminal velocity of a group of particles to that of an isolated particle
Δx	mesh spacing, m

Greek Letters

β	interphase drag constant, $kg\,m^{-3}\,s^{-1}$
ϵ	voidage
ϕ	angle of internal friction, °
λ_s	bulk viscosity, Pa s
μ_s	shear viscosity, Pa s
ρ	density, $kg\,m^{-3}$
$\bar{\bar{\tau}}$	viscous stress tensor, $N\,m^{-2}$
Θ_s	granular temperature, $m^2\,s^{-2}$

Subscripts

g	gas phase
mf	minimum fluidization
max	maximum
s	solids phase

Chapter 5

Modeling of Fluidized Beds with Bimodal Particle Distribution

In this chapter the kinetic theory for a mixture of two particle species is developed, in the framework of the theory outlined in Chapter 2. The developed kinetic theory describing a bimodal mixture of smooth, nearly elastic spheres, is implemented in an Eulerian-Eulerian CFD model. Trends reported in literature describing the behavior of a fluidized bed containing a bimodal particle mixture are compared with outcome of simulations with the kinetic theory for a bimodal particle mixture. Also the phenomenon "inversion", which denotes the change of the segregation direction at higher gas velocities compared to lower, is physically explained directly from the bimodal kinetic theory.

This chapter has been submitted for publication:

B.G.M. van Wachem, J.C. Schouten, R. Krishna, C.M. van den Bleek, and J.L. Sinclair, (1999), Modeling of Gas-Fluidized Beds with Bimodal Particle Distribution, *submitted to AIChE Journal.*

Abstract

This chapter develops a computational fluid dynamics (CFD) model for gas-solid fluidized beds containing a mixture of two particle species. In order to calculate the stresses of the solid phase, the kinetic theory of granular flow is extended to take account of a binary mixture of smooth, nearly elastic, spheres.

Simulations with the developed model are used to demonstrate some key features of binary mixture fluidization:

1. The bed expansion with a binary mixture of particles of different sizes, but identical densities, is significantly higher than that of a system consisting of mono-sized particles of the same mean size as the bimodal mixture. Furthermore, the minimum fluidization velocity for the binary particle system is significantly lowered. The mixing behavior of the binary mixture of particles, characterized by the mixing index, increases with increasing superficial gas velocity.

2. For a binary mixture of particles consisting of larger sized particles of lower density and smaller sized particles of higher density,the larger, lighter, particles segregate to the top of the fluid bed while the smaller, heavier, particles segregate to the bottom. With increasing fluidization velocity, this segregation pattern reverses and the phenomenon of "inversion" occurs.

5.1 Introduction

It is well known in practice that the particle size distribution (PSD) plays an important role in the behavior of gas-solid mixtures. Many researchers have studied the effect of the PSD on the hydrodynamic behavior of fluidized beds. For instance, De Groot (1967) concluded that the bed expansion of industrial fluidized beds may increase by a factor of two when a large PSD is employed instead of a monodisperse distribution.

Grace and Sun (1991) performed numerous fluidized bed experiments with a monodisperse, a bimodal, and a wide particle size/weight distribution of Geldart type A particles. Grace and Sun (1991) studied the influence of "fines" on the hydrodynamics in the fluidized bed. They defined fines as particles with a diameter less than approximately $40\mu m$. They reported that the minimum fluidization velocity was higher with the wide or bimodal PSD versus the monodisperse PSD with the same mean size. Also, as previously concluded by De Groot (1967), the bed expansion was larger for a wide or bimodal PSD than

for a monodisperse PSD. This difference of bed expansion is small around the minimum fluidization velocity and increased with increasing superficial gas velocity. Although the experiments of Grace and Sun (1991) were carried out with small particles of Geldart A type, their results present a good qualitative description of the different types of behavior of fluidized beds with a monodisperse PSD and a bimodal PSD.

In a fluidized bed reactor, the mixing action is produced by the rising of bubbles, whose associated wake and drift leads to the motion of particles. The bubbles in a fluidized bed containing a binary mixture also cause segregation. In fluidized beds containing a binary particle mixture, either by size or density, complete mixing is only achieved under specific hydrodynamic conditions. Wu and Baeyens (1998) experimentally studied the effect of a bimodal PSD on the mixing action in fluidized beds with fairly large particle types, both Geldart B and D type particles. They defined a mixing index M,

$$M = \frac{X}{<X>} \tag{5.1}$$

where X is the concentration of larger/heavier particles in the top region of the dense bed, and $<X>$ is the average concentration of larger/heavier particles in the entire bed. M equal to 1 corresponds to perfect mixing. Wu and Baeyens (1998) correlated the mixing index to the superficial gas velocity, the bed aspect ratio (H/D_1), the minimum fluidization velocity of the smaller and larger particles, and the particle diameter ratio. The mixing index was small for gas velocities near the minimum fluidization velocity, and increased with gas velocity. The scatter on their correlation was, however, very large.

Rasul et al. (1999) studied the different types of segregation occurring in fluidized beds containing a bimodal PSD, by studying the "segregation potential" of fluidized beds containing a bimodal PSD. Specifically, they studied the case of a binary mixture with small, heavy particles and large, lighter particles. At a low fluidization gas velocity, the small, heavy particles were preferentially segregated at the bottom of the fluidized bed, and large, lighter particles were at the top. With increasing gas velocity, "inversion" can occur. This means that the small,heavy particles moved preferentially upward in the bed and the light, larger particles moved downward.

The main goal of our work is to simulate the flow behavior of fluidized beds containing a bimodal PSD and to compare this flow behavior with that of fluidized beds containing a monodisperse PSD. The simulation predictions are compared with the experimental data and observations of the authors mentioned above. The details of the physics behind the previous experimental results are elucidated via the simulations.

5.2 Governing equations

The two-fluid model is applied to describe the flow of the dense gas-solid mixture. The continuity equations of the gas phase and the particle mixture phase are

$$\frac{\partial \epsilon_g}{\partial t} + \nabla \cdot (\epsilon_g \mathbf{u}_g) = 0 \tag{5.2}$$

$$\frac{\partial \epsilon_s}{\partial t} + \nabla \cdot (\epsilon_s \mathbf{u}_s) = 0 \tag{5.3}$$

where $\mathbf{u}_g$ is the gas phase velocity and ϵ_g is the gas phase volume fraction. The momentum balances for the gas phase and the particle mixture follow Jackson (1997),

$$\rho_g \epsilon_g \left[\frac{\partial \mathbf{u_g}}{\partial t} + \mathbf{u_g} \nabla \mathbf{u_g}\right] = \epsilon_g \nabla \cdot \bar{\bar{\tau}}_g - \epsilon_g \nabla P - \beta(\mathbf{u_g} - \mathbf{u_s}) + \epsilon_g \rho_g \mathbf{g} \tag{5.4}$$

$$\rho_s \epsilon_s \left[\frac{\partial \mathbf{u_s}}{\partial t} + \mathbf{u_s} \nabla \mathbf{u_s}\right] = \epsilon_s \nabla \cdot \bar{\bar{\tau}}_g - \epsilon_s \nabla P + \nabla \cdot \bar{\bar{P}}_s + \beta(\mathbf{u_g} - \mathbf{u_s}) + \epsilon_s \rho_s \mathbf{g} \tag{5.5}$$

where P is the gas phase pressure, g is the gravity acceleration, β is the interphase momentum transfer coefficient, $\bar{\bar{\tau}}_g$ is the gas phase shear stress tensor which is assumed Newtonian, and $\bar{\bar{P}}_s$ is the solids phase stress tensor with a kinetic and collisional contribution (given by kinetic theory) and also a frictional contribution:

$$\bar{\bar{P}}_s = \bar{\bar{P}}_{s,kinetic} + \bar{\bar{P}}_{s,collision} + \bar{\bar{P}}_{s,friction} \tag{5.6}$$

Pirog (1998) proposed the following modification of Wen and Yu (1966) equation for the drag force exerting on a particle in the vicinity of other particles

$$F_i = \frac{3}{4} f_i(\epsilon_{s,A}, \epsilon_{s,B}) C_D \frac{\epsilon_g \epsilon_{s,i} \rho_s |\mathbf{u}_g - \mathbf{u}_s|}{d_s} \tag{5.7}$$

where $f_i(\epsilon_s)$ is the hindered settling velocity function, which is defined as $f_i(\epsilon_{s,A}, \epsilon_{s,B}) = V_i/V_{i,0}$. V_i is the actual settling velocity for the particle in the suspension and $V_{i,0}$ is the settling velocity of an isolated particle. The drag coefficient proposed by Rowe (1961) is employed:

$$C_D = \begin{cases} \dfrac{24}{Re_p(1-\epsilon_s)}\left[1 + 0.15\left((1-\epsilon_s)Re_p\right)^{0.687}\right] & \text{if } (1-\epsilon_s)Re_p < 1000 \\ 0.44 & \text{if } (1-\epsilon_s)Re_p \geq 1000 \end{cases} \tag{5.8}$$

In the case of a bimodal particle mixture, $i = A$ or B, the total interphase momentum transfer coefficient is $\beta = F_A + F_B$. Pirog (1998) proposed for the settling velocity function for species i in a bimodal suspension

$$f_i(\epsilon_{s,A}, \epsilon_{s,B}) = \prod_{q=A,B} (1 - \epsilon_{s,q})^{\alpha_{iq}} \tag{5.9}$$

where α_{ij} are empirically determined constants in the form of

$$\alpha_{ij} = a_0 + a_1 \left(\frac{\sigma_j}{\sigma_i}\right) + a_2 \left(\frac{\sigma_j}{\sigma_i}\right)^2 \tag{5.10}$$

Values for a_0, a_1, and a_2 are given by Pirog (1998) for different particles and solids volume fractions based on the results of his settling experiments.

5.3 Kinetic Theory for a Bimodal Particle Mixture

In order to describe solid-phase stresses in the framework of the two-fluid model for dense gas-solids flows typically concepts from kinetic theory are employed. The kinetic theory for granular materials has been developed by Jenkins and Savage (1983), Lun et al. (1984), and others, analogous to the kinetic theory of gases (Chapman and Cowling, 1970), accounting for the inelastic nature of particle-particle collisions. This theory has been used by many researchers to successfully describe both dense and dilute dry particulate flows, as well as dense and dilute fluidized particulate flows. Almost all work to date has considered monodisperse particulate systems. However, Jenkins and Mancini (1987) have developed kinetic theory for a mixture of bimodal disks and a mixture of bimodal spheres assuming a Maxwellian velocity distribution of the disks or spheres. Lopez de Haro et al. (1983) have developed kinetic theory for a gas consisting of a mixture of multiple components, employing a revised Enskog method (Van Beijeren and Ernst, 1973). Using the approach of Lopez de Haro et al. (1983) as a basis, Jenkins and Mancini (1989), Zamankhan (1995), and Arnarson and Willits (1998) developed kinetic theory for a binary particle mixture of spheres involving perturbations to the Maxwellian velocity distribution. These latter theories, with modifications outlined below, are used in this work to describe the solid phase stress and fluctuating velocities of the bimodal particle mix.

We consider a mixture of smooth, nearly elastic spheres of two different species *A* and *B*. These spheres have mass m_i, number density n_i, radius σ_i, and velocity $\mathbf{c}_i$, where i is either species A or B. The mass density ρ_i is given by the product of m_i and n_i. The number density n and the mass density ρ of the mixture are given by the sum of the corresponding densities of the two

constituents. The mean velocity of each species is denoted by $\mathbf{u}_i \equiv <\mathbf{c}_i>$. The mass average velocity of the mixture can be written as:

$$\mathbf{u}_s = \frac{1}{\rho}(\rho_A \mathbf{u}_A + \rho_B \mathbf{u}_B) \tag{5.11}$$

The peculiar velocity of each species is defined as: $\mathbf{C}_i \equiv \mathbf{c}_i - \mathbf{u}_s$. The diffusion velocity, $\mathbf{v}_i$, which is absent from the kinetic theory for monodisperse mixture of particles, is defined as:

$$\mathbf{v}_i \equiv <\mathbf{C}_i> = <\mathbf{c}_i - \mathbf{u}_s> \tag{5.12}$$

It then follows that

$$\rho_A \mathbf{v}_A + \rho_B \mathbf{v}_B = 0 \tag{5.13}$$

The granular temperature is related to the peculiar velocity and, unlike the monosized particle theory, also to the mass of the individual particle specie:

$$T_i = \frac{1}{3} m_i <\mathbf{C}_i^2> \tag{5.14}$$

The mixture temperature can be written as $T = \frac{1}{n}(n_A T_A + n_B T_B)$. The mixture balance of granular energy is:

$$\frac{3}{2} n \left[\frac{\partial T}{\partial t} + \nabla \cdot (T \mathbf{u}_s)\right] - \frac{3}{2} T \nabla \cdot (n_A \mathbf{v}_A + n_B \mathbf{v}_B) = -\nabla \cdot \mathbf{q} - \overline{\overline{P}}_s : \nabla \mathbf{u}_s + \sum_{k=A,B} (\mathbf{F}_i + \rho_i \mathbf{g}) \cdot (n_A \mathbf{v}_A + n_B \mathbf{v}_B) - \gamma \tag{5.15}$$

where $\mathbf{q}$ is the mixture energy flux, $\overline{\overline{P}}_s$ is the total solids stress tensor of the mixture, $\mathbf{F}_i$ is the total force acting on species i, and γ is the rate of granular energy dissipation. The first term on the left hand side denotes the time dependency of the mixture granular energy, the second term is the convection of the mixture granular energy, and the third term denotes the convection of mixture granular energy due to the relative species movement. On the right hand side, the first term denotes the diffusion of the mixture granular energy along the gradients in the mixture granular temperature, the second term is the creation of mixture granular energy due to shear in the particle phase, the third term denotes the creation or dissipation of mixture granular energy due to external forces, and the last term is the dissipation of granular energy due to inelastic particle-particle collisions.

The mixture energy flux is defined as:

$$\mathbf{q} = \sum_{i=A,B} \left(\frac{1}{2} <\rho_i \mathbf{C}_i C_i^2> + \sum_{k=A,B} \mathbf{q}_{ik} \right) \tag{5.16}$$

The first term on the right hand side is a transport or kinetic contribution to the mixture energy flux and the second term, $\mathbf{q}_{ik}$, is a collisional contribution.

Similarly, the kinetic and collisional contributions to the solid phase stress tensor are given as

$$\bar{\bar{P}}_{s,kinetic\ +\ collision} = \sum_{i-A,B} \left(<\rho_i \mathbf{C}_i \mathbf{C}_i> + \sum_{k-A,B} \bar{\bar{P}}_{ik} \right) \tag{5.17}$$

where the first term represents the kinetic or transport contribution to the pressure tensor and the second part, P_{ik}, the collisional contribution. Using the revised Enskog theory, the equations for the pressure tensor and the energy flux can be expressed in terms of particle and flow parameters as (Jenkins and Mancini, 1989)

$$<\rho_i \mathbf{C}_i \mathbf{C}_i> = n_i T \bar{\bar{I}} - n_i T b_{i0} (\bar{\bar{D}} - \frac{1}{3} \nabla \mathbf{u}_s \bar{\bar{I}}) \tag{5.18}$$

$$\bar{\bar{P}}_{ik} = \frac{2}{3} \pi \sigma_{ik}^3 n_i n_k T \bar{\bar{I}} - \frac{8}{15} n_i n_k \pi \sigma_{ik}^3 g_{ik} T \left[b_{i0} M_{ki} + \sqrt{\frac{2 m_i m_k}{m_{ik} \pi T}} \sigma_{ik} \right] \cdot \cdot \left[\bar{\bar{D}} - \frac{1}{3} \nabla \mathbf{u}_s \bar{\bar{I}} \right] \tag{5.19}$$

and

$$\frac{1}{2} <\rho_i \mathbf{C}_i C_i^2> = \frac{5}{4} n_i a_{i1} \sqrt{\frac{2T}{m_i}} \nabla T + \frac{5}{2} n_i \sqrt{\frac{T^3}{2 m_i}} (n t_{i0} \mathbf{d}_i + a_{i0} \nabla (\ln T)) \tag{5.20}$$

$$\mathbf{q}_{ik} = 2 \sqrt{\frac{2T}{m_i}} n_i n_k \sigma_{ik}^3 \pi g_{ik} M_{ik} M_{ki} \left[a_{i1} - \frac{2}{3} \sigma_{ik} \sqrt{\frac{1}{\pi M_{ki}}} \right] \nabla T - \sqrt{\frac{T^3}{2}} \frac{2}{3} n_i n_k \pi \sigma_{ik}^3 g_{ik} \cdot \left[\sqrt{\frac{1}{m_i}} (n t_{i0} \mathbf{d}_i + a_{i0} \nabla \ln T)(M_{ik} - M_{ki}) + \sqrt{\frac{1}{m_k}} (n t_{k0} \mathbf{d}_k + a_{k0} \nabla \ln T) \right] \tag{5.21}$$

where $\sigma_{ik} \equiv \sigma_i + \sigma_k$, $m_{ik} \equiv m_i + m_k$, and $M_{ik} \equiv m_i / m_{ik}$. For the coefficient b_{i0}, Jenkins and Mancini (1989) give for $i \neq k$,

$$b_{i0} = 5 \frac{b_i (n_i + \frac{2}{5} K_{ii} + \frac{4}{5} K_{ik} M_{ki}) + \frac{32}{3} \sqrt{\pi M_{ik} M_{ki} / 2 m_{ik}} \sigma_{ik}^2 (n_k + \frac{2}{5} K_{kk} + \frac{4}{5} K_{ik} M_{ik})}{g_{ik} n_i n_k \sqrt{T} [b_i b_k - \frac{512}{9} \sigma_{ik}^4 \pi (M_{ik} M_{ik} / m_{ik})]} \tag{5.22}$$

$$b_i = 40 \sigma_{ik}^2 \sqrt{\frac{\pi M_{ik} M_{ki}}{2 m_{ik}}} \left(\frac{2}{3} + \frac{2 m_i}{5 m_k} \right) + 8 \sigma_{kk}^2 \frac{n_k g_{kk}}{n_i g_{ik}} \sqrt{\frac{\pi}{m_k}} \tag{5.23}$$

where $K_{ik} \equiv \frac{2}{3}\pi n_i n_k g_{ik} \sigma_{ik}^3$. For the coefficients a_{i0} and t_{i0}, there has been some confusion in the literature. Arnarson and Willits (1998) claim that Jenkins and Mancini (1989), Zamankhan (1997) and Hsiau and Hunt (1996) have developed incorrect expressions for these coefficients. Moreover, Kincaid et al. (1987) have investigated the convergence of the orders of the Enskog approximation and found that the first order Enskog approximation is not accurate, even for small differences in particle size and/or mass. Therefore, Arnarson and Willits (1998) calculate the necessary coefficients correctly and up to the second order. With $i \neq k$ their results are:

$$a_{i0} = \frac{1}{2\rho}\sqrt{m_{ik} m_k} n_k \left(M_{ki}^{3/2} a_{i1} - M_{ik}^{3/2} a_{k1} \right) \tag{5.24}$$

$$a_{i1} = -\frac{15}{8\sqrt{\pi} n_i n_k g_{ik} \sigma_{ik}^2 \sqrt{M_{ki}}} \left(\frac{\alpha_i n_i K_i + 13 M_{ik} M_{ki} n_k K_k}{\alpha_i \alpha_k - 169 M_{ik}^2 M_{ki}^2} \right) \tag{5.25}$$

$$\alpha_i = 15 M_{ki}^2 + 8 M_{ik} M_{ki} + 6 M_{ik}^2 + 2\sqrt{2} \frac{n_k g_{kk} \sigma_{kk}^2}{n_i g_{ik} \sigma_{ik}^2 \sqrt{M_{ik}}} \tag{5.26}$$

$$t_{i0} = \frac{1}{2\rho}\sqrt{m_{ik} m_k} n_k \left(M_{ki}^{3/2} t_{i1} + M_{ik}^{3/2} t_{k1} \right) + \frac{3 m_k}{8\sqrt{\pi} \rho n_i g_{ik} \sigma_{ik}^2 \sqrt{M_{ki}}} \tag{5.27}$$

$$t_{i1} = \frac{3\sqrt{M_{ki}}}{8\sqrt{\pi} n_i n_k g_{ik} \sigma_{ik}^2} \left(\frac{\alpha_i - 13 M_{ik}^2}{\alpha_i \alpha_k - 169 M_{ik}^2 M_{ki}^2} \right) \tag{5.28}$$

$$K_i = 1 + \frac{2}{5}\pi n_i g_{ii} \sigma_{ii}^3 + \frac{8}{5} M_{ik} M_{ki} \pi n_k g_{ik} \sigma_{ik}^3 \tag{5.29}$$

Because Jenkins and Mancini (1989) and Arnarson and Willits (1998) have only used bimodal kinetic theory to study the case of steady homogeneous shear, contributions to the total solids stress tensor linear in $\nabla \cdot \mathbf{u}_s$ were not considered. When this term does play a role, the solids stress must be extended with a contribution incorporating the solids bulk viscosity. The bulk viscosity contribution can be expressed as (Bird et al. 1960):

$$\overline{\overline{P}}_{s,bulk} = (\lambda - \frac{2}{3}\mu) tr\left(\overline{\overline{D}}\right) \overline{\overline{I}} \tag{5.30}$$

where λ is the solids bulk viscosity and μ is the solids shear viscosity, which can be determined from Equations 5.19 and 5.18 by considering the terms linear in $\overline{\overline{D}}$. Following the derivation for a binary mixture of gas molecules by Lopez de Haro and Cohen (1984), an equation for the bulk viscosity of elastic spheres can be derived:

$$\lambda = \frac{2}{3} \sum_{i=A,B} \sum_{k=A,B} K_{ik} \sigma_{ik} \sqrt{\frac{2 T m_i m_k}{\pi m_{ik}}} \tag{5.31}$$

For nearly elastic particles, the perturbation on the Maxwellian velocity distribution can be employed to derive an expression for the total rate of energy

dissipation. Jenkins and Mancini (1989) present the rate of energy dissipation in the lowest Enskog approximation. In the second order Enskog approximation, it can be written as

$$\gamma = \sum_{i=A,B} \sum_{k=A,B} 2g_{ik}\sigma_{ik}^2 n_i n_k \frac{m_k}{m_{ik}}(1-e_{ik}^2)\sqrt{\frac{2\pi m_{ik}T^3}{m_i m_k}} \tag{5.32}$$

where e_{ik} is the coefficient of restitution for a collision of particle species i with particle species k. For the diffusion velocity of each specie, Jenkins and Mancini (1989) give

$$\mathbf{v}_i = -\sqrt{\frac{T}{2m_i}}(nt_{i0}\mathbf{d}_i + a_{i0}\nabla \ln T) \tag{5.33}$$

dependent on the diffusion force

$$\begin{aligned}\mathbf{d}_i &= -\frac{\rho_i}{n\rho T}\left[\nabla P + \rho_k\left(\frac{\mathbf{F}_i}{m_i} - \frac{\mathbf{F}_k}{m_k}\right)\right] + \frac{1}{n}(n_i + 2M_{ik}K_{ik} + K_{ii})\nabla \ln T \\ &+ \frac{n_i}{nT}\left(\frac{\partial \mu_i}{\partial n_k}\nabla n_k + \frac{\partial \mu_i}{\partial n_i}\nabla n_i\right)\end{aligned} \tag{5.34}$$

Using the thermodynamic relationships (Reed and Gubbins, 1973),

$$P = -\left(\frac{\partial A}{\partial V}\right)_{T,N_k} \qquad \mu_i = \left(\frac{\partial A}{\partial N_k}\right)_{T,N_{k\neq i}}$$

and by using the dependency of P and μ_i on T, it can be shown that

$$\mathbf{d}_A = -\mathbf{d}_B \tag{5.35}$$

Because the chemical potential, μ_i, is only dependent upon T, n_i, and n_k,

$$\nabla \mu_i = \frac{\partial \mu_i}{\partial n_k}\nabla n_k + \frac{\partial \mu_i}{\partial n_i}\nabla n_i + \frac{\partial \mu_i}{\partial T}\nabla T \tag{5.36}$$

The latter equation can be used to replace the derivatives in n_i and n_k in Equation 5.34, and rewrite Equation 5.34 in terms of derivatives depending upon the location only.

To date, all authors investigating binary particle mixtures use the radial distribution function of Mansoori et al. (1971)

$$g_{ik} = \frac{1}{1-\epsilon_s} + \frac{3\sigma_i\sigma_k}{\sigma_i+\sigma_k}\frac{\xi_2}{(1-\epsilon_s)^2} + 2\left(\frac{\sigma_i\sigma_k}{\sigma_i+\sigma_k}\right)^2\frac{\xi_2^2}{(1-\epsilon_s)^3} \tag{5.37}$$

where $\xi_p = 4\pi(n_A\sigma_A^p + n_B\sigma_B^p)/3$, and thus $\epsilon_s \equiv \xi_3$. This expression however, does not tend to infinity when the total solids volume fraction,ϵ_s, approaches the maximum packing of spheres. Therefore, we propose a similar radial distribution function which has the correct limit for the solids volume fraction when approaching the maximum packing limit for a bimodal mixture of spheres

$$g_{ik} = \frac{1}{1 - \frac{\epsilon_s}{\epsilon_{s,max}}} + \frac{3\sigma_i\sigma_k}{\sigma_i + \sigma_k}\frac{\xi_2}{\left(1 - \frac{\epsilon_s}{\epsilon_{s,max}}\right)^2} + 2\left(\frac{\sigma_i\sigma_k}{\sigma_i + \sigma_k}\right)^2 \frac{\xi_2^2}{\left(1 - \frac{\epsilon_s}{\epsilon_{s,max}}\right)^3} \tag{5.38}$$

where $\epsilon_{s,max}$ is the maximum solids volume fraction. The two radial distribution functions are compared in Figure 5.1. At high solids volume fraction, which often occurs in fluidized beds, the difference in radial distribution functions is large. The chemical potential is a function of the radial distribution

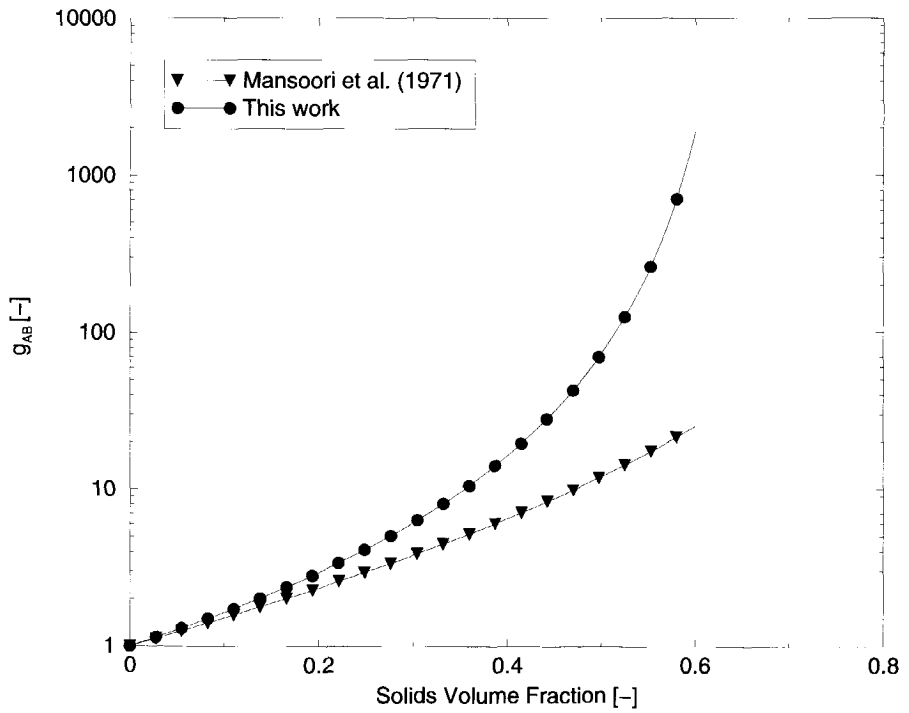

Figure 5.1: *The radial distribution function of Mansoori et al. (1971) compared to the radial distribution function proposed in this work, for a 50/50 mix with* $\sigma_A = 250\mu m$ *and* $\sigma_B = 100\mu m$.

function and for a binary gaseous mixture (Reed and Gubbins, 1973)

$$\mu_i = kT \ln \frac{\rho_i \Lambda}{q_i^{int}} - \frac{2}{3}\pi kT \left(\frac{\partial}{\partial N_i} \left[\sum_{\alpha=A,B} \sum_{\beta=A,B} N_\alpha N_\beta \sigma_{\alpha\beta}^3 \int_\infty^V \frac{1}{V^2} g_{\alpha\beta} dV \right] \right)_{T,V,N_{k\neq i}} \tag{5.39}$$

where N_A and N_B are the total number of particles of each species, and thus $n_A = N_A/V$. Equation 5.39 has been solved with the new radial distribution function given in Equation 5.38 using Mathematica (Wolfram, 1988), and the result is given in Appendix A. Shauly et al. (1988) use a semi-empirical model to predict the increase in the maximum solids volume fraction with different compositions of the binary mixture

$$\frac{\epsilon_{s,max}}{\epsilon_{s,max,mono}} = \left[1 + \frac{3}{2}|b|^{3/2} \left(\frac{\epsilon_{s,A}}{\epsilon_s} \right)^{3/2} \left(\frac{\epsilon_{s,B}}{\epsilon_s} \right) \right] \tag{5.40}$$

with $b = (\sigma_A - \sigma_B)/(\sigma_A + \sigma_B)$ and $\epsilon_{s,max,mono}$ is the maximum solids volume fraction in case of a monodisperse particle mixture equal to 0.65. Figure 5.2 shows an example of the variation of $\epsilon_{s,max}$ as a function of mixture composition.

5.4 Frictional stress

In regions with very high solids volume fractions, as frequently present in fluidized beds, sustained contacts between particles occur. These frictional stresses must be accounted for in the description of the total solids-phase stress. The frictional stress is added to the kinetic and collisional contributions to the stress given by kinetic theory when the solid volume fraction exceeds some kick-in value, $\epsilon_{s,min}$. The frictional stress is in a Newtonian form (Johnson et al., 1990) and is added to the total stress tensor when $\epsilon_s > \epsilon_{s,min}$, and the frictional stress is described by

$$\bar{\bar{P}}_{s,\,friction} = \begin{cases} P_f \bar{\bar{I}} + \mu_f \left(\nabla \mathbf{v} + (\nabla \mathbf{v})^T \right) & \text{if } \epsilon_s > \epsilon_{s,min} \\ 0 & \text{if } \epsilon_s \leq \epsilon_{s,min} \end{cases} \tag{5.41}$$

where P_f represents the normal frictional stress and μ_f represents the frictional shear viscosity. For the normal frictional stress, the semi-empirical equation of Johnson and Jackson (1987) is employed

$$P_f = Fr \frac{(\epsilon_s - \epsilon_{s,min})^q}{(\epsilon_{s,max} - \epsilon_s)^p} \tag{5.42}$$

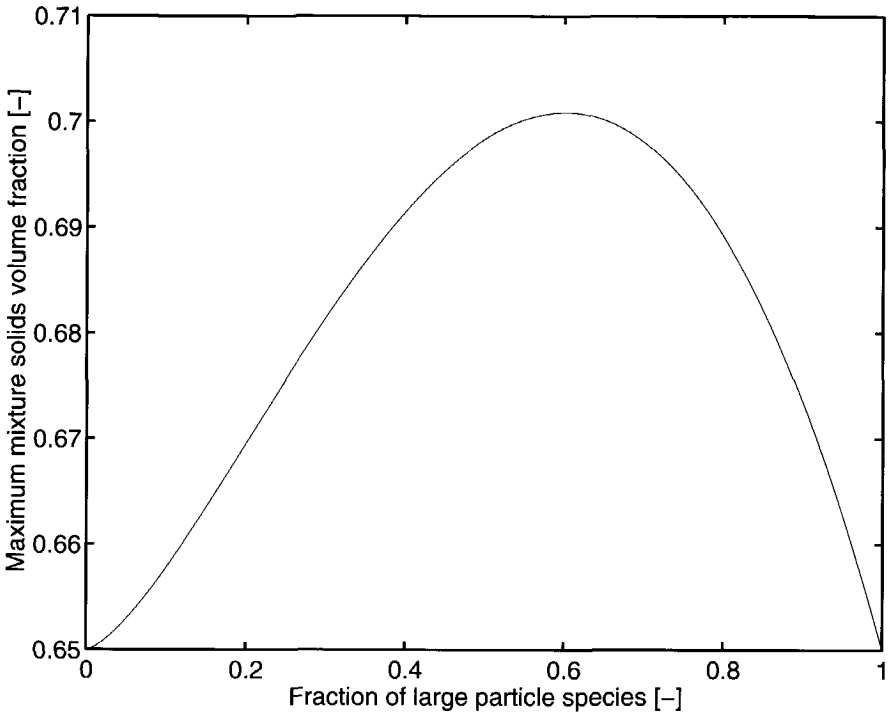

Figure 5.2: *The maximum solids volume fraction,* $\epsilon_{s,max}$*, of a mixture with* $\sigma_A = 250\mu m$ *and* $\sigma_B = 100\mu m$ *as a function of mixture composition.*

The values proposed by Johnson et al. (1990) for the empirical material constants are $Fr = 0.05\,Nm^{-2}$, $q = 2$, and $p = 5$, for particles similar to those studied in this work. The frictional shear viscosity is related to the frictional normal stress by the linear law proposed by Coulomb (1776),

$$\mu_f = P_f \sin\phi \tag{5.43}$$

where ϕ represents the angle of internal friction. This frictional stress model assumes a monodisperse PSD and does not contribute to or initiate segregation.

5.5 Simulations

The CFD model as just described is used to simulate two-dimensional gas-solid fluidized beds at different superficial gas velocities and with different particle weights and sizes. In summary, the solution of the nine primary variables $\mathbf{u_s}$, $\mathbf{u_g}$, n_a, n_b, ϵ_s, T, and P, is achieved by solving the nine Equations 5.2, 5.3, 5.4, 5.5, 5.13, and 5.15. From these variables, the individual

solids phase velocities can be calculated by solving Equations 5.11 and 5.13 by employing Equation 5.12.

Simulations of fluidized beds have been performed with a bimodal PSD for two cases of particles and mixture properties as given in Table 5.1. In Case 1, we have also performed a simulation of a fluidized bed with a monodisperse PSD exhibiting the same Sauter mean diameter as the bimodal PSD. The employed fluidization and computational parameters are given in Table 5.2. The calculation of the minimum fluidization velocities is based upon the empirical correlation of Wen and Yu (1966). Due to the coarseness of the particles, the minimum fluidization velocity is equal to the minimum bubbling velocity.

The simulations in this work were carried out with the commercial CFD code CFX 4.2 from AEA Technology, Harwell, UK. The equations for the solids phase stress for the bimodal particle mixture, the solids mixture temperature, the drag on the particle mixture, and the diffusion velocities were implemented into this code. For solving the differential equations, the higher-order total variation diminishing (TVD) scheme Superbee is employed. This scheme is a modification of the higher-order upwind scheme. The SIMPLE algorithm is used to correct the pressure from the gas phase velocities (Patankar, 1980). The gas phase is assumed to be compressible and the calculated pressure is used to determine the gas-phase density. Initially, the bottom part of the

Table 5.1: *Physical properties of the binary and monodisperse particle systems*

Particles	diameter ($2\,\sigma$) [μm]	density [kg m^{-3}]	U_{mf} [m/s]	Terminal Velocity [m/s]	Average Mass Fraction
		Case 1			
		Bimodal mixture			
glass beads	500	2640	0.19	20	0.5
glass beads	200	2640	0.04	3.2	0.5
	Monodisperse mixture with same Sauter mean diameter				
glass beads	485	2640	0.18	19	1.0
		Case 2			
		Bimodal mixture			
polystyrene	500	1150	0.09	8.2	0.30
glass beads	200	2640	0.04	3.2	0.70

fluidized bed is filled with a random mixture of two particles at rest with a uniform solids volume fraction. In Case 1, the mass fraction is set 0.5 for both the large and small particles. In Case 2, the solids volume fraction is set equal; the mass fractions are not equal because the density of each species is different.

Table 5.2: *System properties and computational parameters.*

Parameter	Description	value
ρ_g [kg/m^3]	gas density	1.28
μ_g [Pa s]	gas viscosity	$1.7 \cdot 10^{-5}$
e [-]	coefficient of restitution	0.9
e_w [-]	wall coefficient of restitution	0.9
a_0 [-]	empiric constant Eq. 5.10	11.28
a_1 [-]	empiric constant Eq. 5.10	-9.69
a_2 [-]	empiric constant Eq. 5.10	1.49
ϵ_{max} [-]	maximum monodisperse solids volume fraction	0.65
ϕ [-]	angle of internal friction	28
D_T [m]	inner column diameter	0.15
H_t [m]	column height	0.3
H_{mf} [m]	height at minimum fluidization	0.16
$\epsilon_{s,mf}$ [-]	solids volume fraction at minimum fluidization	0.42
Δx [m]	x mesh spacing	$1.00 \cdot 10^{-2}$
Δy [m]	y mesh spacing	$1.00 \cdot 10^{-2}$
Δt [s]	timestep	$1.00 \cdot 10^{-5}$

Limiting case validation runs were performed with the CFD code describing the bimodal particle mixture by setting the volume fraction of one particle species to 10^{-5} and the other to a realistic value; hence, the hydrodynamics of the flow should be completely determined by the particle species with the large volume fraction. The results in terms of bed expansion and bubble size gave results at two simulated superficial gas velocities equal to the CFD code employing the granular kinetic theory for a monodisperse particle mixture, as employed by Van Wachem et al. (1998, 2000). The computational effort for a run with the CFD code describing the bimodal particle mixture, however, is increased by one order of magnitude over a run involving the monodisperse particle mixture. Because of the magnitude of the required computational effort, each simulation has been performed up to fourteen seconds of real time. One simulation takes almost four weeks of computational time on a 166 Mhz IBM RS 6000 computer. Hence, on these short time-scales it was impossible to obtain good statistics on bubble behavior or on the dynamics of the pressure fluctuations.

5.5.1 Boundary conditions

All the simulations were carried out in a two-dimensional Cartesian space in which front and back wall effects are neglected. The left and right walls of the fluidized bed are treated as no-slip boundaries for the gas phase and free-slip boundaries for the particle mixture. The boundary condition for the mixture temperature follows the equation of Johnson and Jackson (1987) for a monosized particle configuration, but is corrected for the difference in definition of the mixture temperature (Equation 5.14),

$$\mathbf{n}\cdot\mathbf{q} = \frac{\pi\rho\epsilon_s\sqrt{\frac{3\Theta}{\rho\epsilon_s}}}{6\epsilon_{s,max}\left[1-\left(\frac{\epsilon_s}{\epsilon_{s,max}}\right)^{1/3}\right]}\left[\varphi'|\mathbf{u}_{slip}|^2 - \frac{3\Theta}{2\rho\epsilon_s}(1-e_w{}^2)\right] \qquad (5.44)$$

where φ' is the specularity coefficient. The first term represents the generation of mixture temperature due to particle slip at the wall, while the second term represents dissipation of fluctuating energy due to inelastic particle-wall collisions. Simulations performed with an adiabatic boundary condition at the wall ($\nabla\Theta = 0$) show very similar results.

The boundary condition at the top of the free-board (fluid phase outlet) is a pressure boundary; the pressure at this boundary is fixed to a reference value. Neumann boundary conditions are applied to the gas flow, requiring fully developed gas flow. The solids volume fraction is held constant to 10^{-6} at the outlet to ensure convergence and a physical solids velocity field in the free-board. In this way, the whole freeboard is filled with a very small number of particles, which does not influence the behavior of the fluidized bed.

At the bottom of the fluidized bed, Dirichlet boundary conditions are employed for the gas phase in which the superficial gas velocity is specified. The bottom is made impenetrable for the solids phase by setting the solids axial velocity to zero.

5.6 Results and Discussion

5.6.1 Bimodal mixture Case 1

Figure 5.3 shows a visual representation of the total solids volume fraction and the relative diffusion velocity of the larger species for bimodal mixture Case I. It can be clearly seen that the time-dependent segregation mainly occurs in and near voids, and that bubbles are the cause of this segregation behavior. From Figure 5.4 it can be clearly seen that the bed expansion is

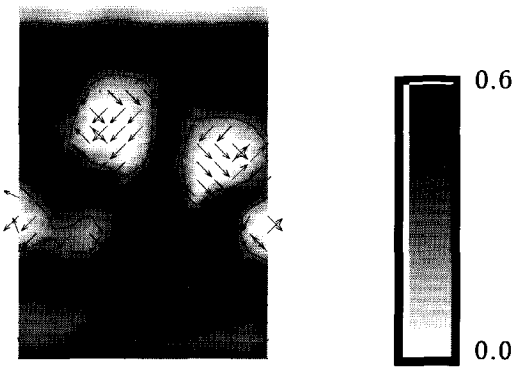

Figure 5.3: *A visual representation of the total solids volume fraction indicating the bubbles and the bed surface with contour lines and indicating the relative velocity of the larger particles.*

larger in the fluidized bed with a bimodal mixture than in the fluidized bed with a monodisperse mixture. This is mainly due to the upward diffusion of the smaller particle species. Figure 5.5, which gives the variation in bed expansion as a function of the fluidization velocity, also shows that the bed expansion is higher in the fluidized bed with a bimodal mixture than in the fluidized bed with a monodisperse mixture. This result is consistent with the experimental observations of De Groot (1967) and Grace and Sun (1991). In the case of the bimodal mixture, a layer of the smaller particles dominates the mixture in the top 25% of the bed. The difference in the bed expansion between the bimodal and monodisperse cases with increasing gas velocity reaches a maximum and then begins to decrease as the particle mixing in the bimodal case improves., as well shown in Figure 5.6. The minimum fluidization velocity of the bimodal mixture determined from the simulation results is $U_{mf} = 0.14 m/s$, whereas the minimum fluidization velocity of the equivalent monodisperse mixture is $U_{mf} = 0.19 m/s$. This observation also agrees with the studies done by De Groot (1967) and Grace and Sun (1991). Part of the difference between the bed expansion behavior and the shift of the minimum fluidization velocity can be explained because the drag force and the gravity force depend on different types of averaging(see Equation 5.9).

Figure 5.6 shows the result of the computation of the mixing index based on the simulations of the bimodal mixture Case 1. The mixing index was determined by dividing the solids volume fraction of the large particles in the top 25% of the fluidized bed by the average solids volume fraction of the large particles in the entire bed. At velocities above the minimum fluidization velocity,

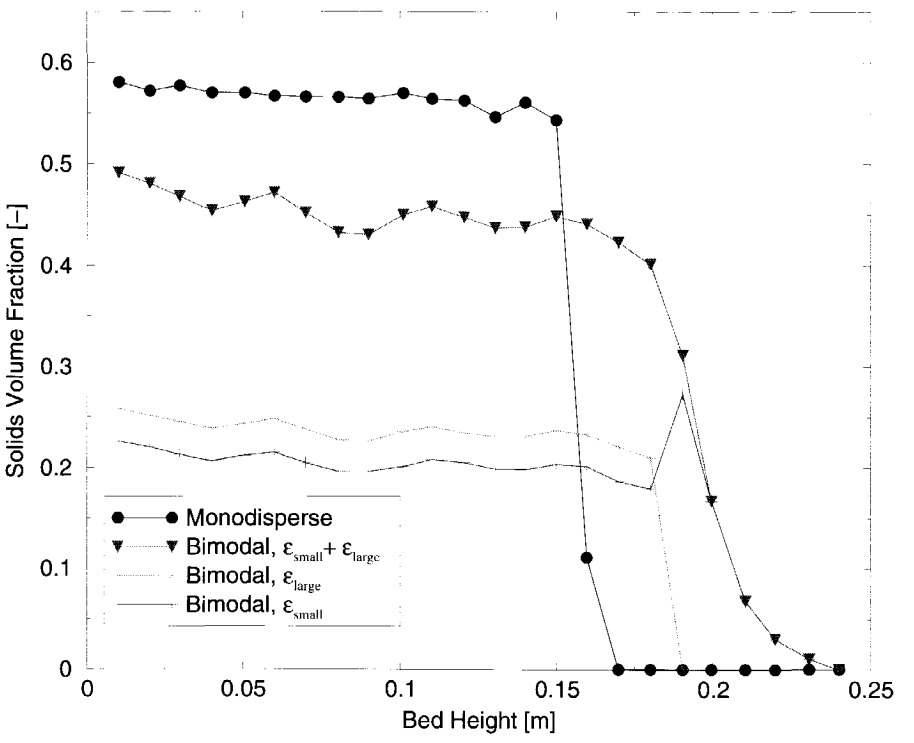

Figure 5.4: *The strip-averaged solids volume fraction as a function of bed height for the the bimodal mixture and the monodisperse mixture Case 1 (Table 5.1) at* $U = 0.27\,m/s$. *For the bimodal mixture, the total solids volume fraction and the solids volume fraction of the individual large and small particle species are shown.*

the predicted mixing index increases with superficial gas velocity, conforming with the experiments and observations of Wu and Baeyens (1998). The thickness of the layer of finer species occurring in the top of the bed decreases with increasing superficial gas velocity and the top layer of particles in the fluidized bed is getting increasingly better mixed.

5.6.2 Bimodal Mixture Case 2

Two simulations were performed of a fluidized bed containing the bimodal particle mixture capable of inversion. Figure 5.7 shows the strip- and the last four seconds of fourteen seconds s time-averaged solids volume fraction as a function of bed height with a fluidization velocity of $U = 1.08\,m/s$. It is clearly seen that the larger, lighter particles segregate to the top of the fluidized bed and the smaller and heavier particles segregate downwards. Due to the short

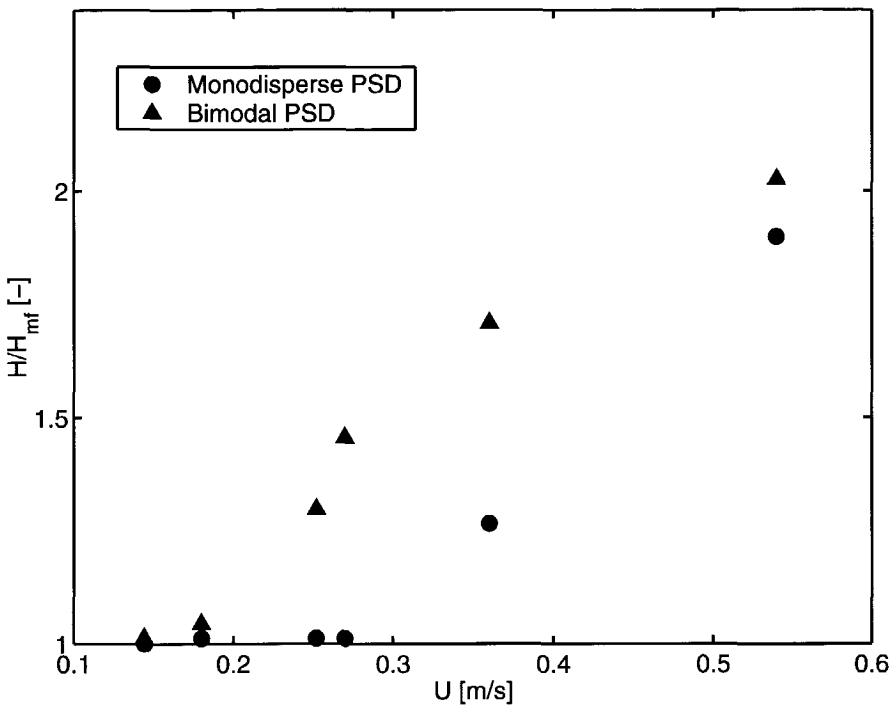

Figure 5.5: *The predicted bed expansion as a function of superficial gas velocity for the bimodal particle mixture Case 1 (Table 5.1) compared with a monodisperse particle mixture.*

time averaging, the spread on the points is fairly large. The results for a higher gas velocity, U = 1.85 m/s, shown in Figure 5.8, show the opposite segregation behavior. Due to the much larger granular temperature and granular temperature gradients, the diffusion force is directed in the opposite direction compared to the diffusion force at the lower gas velocity. Both averages were determined in the interval between 10 and 14 s of real time. These times are much too short to predict the final segregated state. Therefore, a quantitative comparison with the literature is therefore not possible. The trends shown, however, are the same as reported by Rasul et al. (1999). Rasul et al. (1999) show rules of thumb when inversion can take place, but from the kinetic theory of a binary mixture of particles, inversion can be easily explained. The diffusion force and diffusion velocity, described by Equations 5.33 and 5.34, are dependent on four quantities; the gradient in granular pressure, the gradient in granular temperature, the gradient in chemical potential, and the difference in force between one particle species and the other. In the case

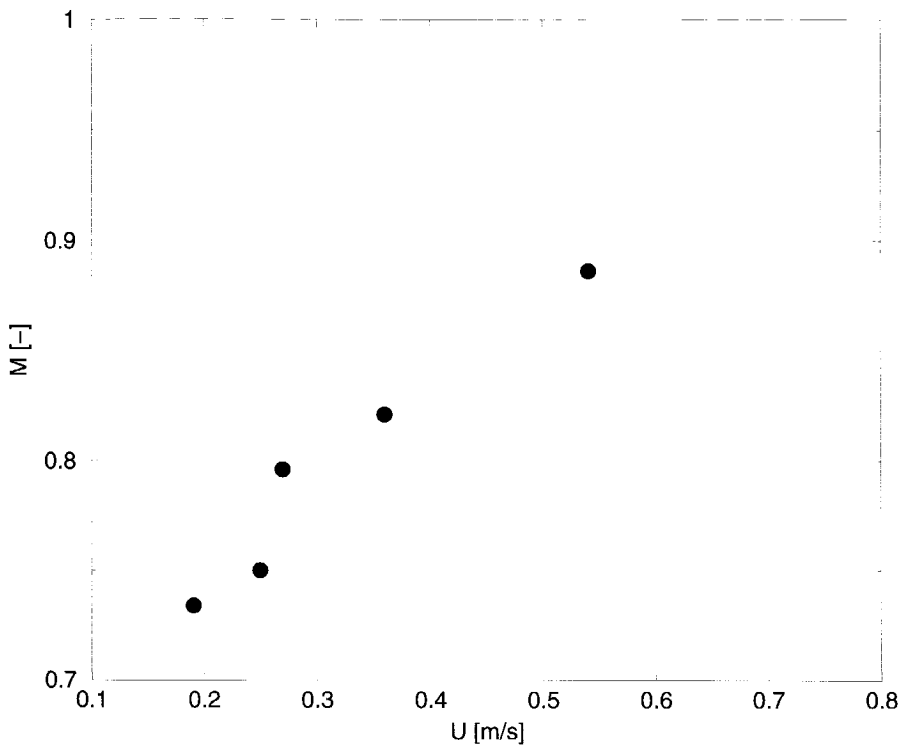

Figure 5.6: *The predicted mixing index as a function of superficial gas velocity for the bimodal particle mixture Case 1 (Table 5.1).*

that Rasul et al. (1999) studied, the force difference between the small and heavy particles and the large and light particles is dominant at low gas velocity. Both the gravity force and the upward drag force lead to a much smaller upward force for the small and heavy particles. Hence, the diffusion force and thus the diffusion velocity cause a downward movement of the small and heavy particles. When the gas velocity is increased, however, the gradients in granular temperature and granular pressure become dominant terms in the equations for the diffusion force and the diffusion velocity.

5.7 Conclusions

In this paper we describe a CFD model for gas-fluidized beds containing a bimodal particle size distribution. The particle phase stress in the fluidized are predicted by means of the granular kinetic theory for a binary mixture of smooth, nearly elastic spheres.

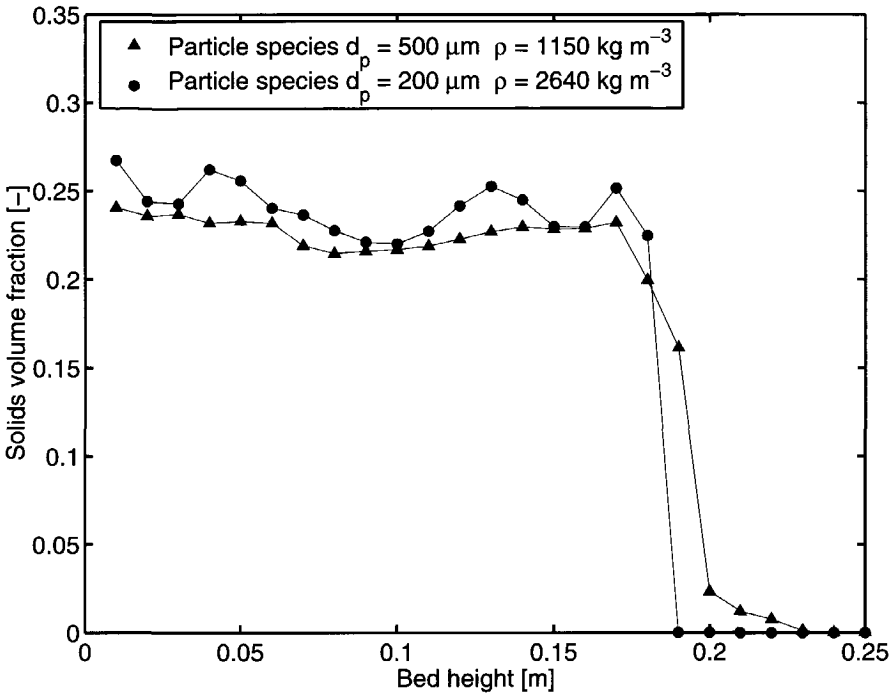

Figure 5.7: *The strip- and 4 s time-averaged solids volume fraction of the bimodal mixture Case 2 fluidized bed at* $U = 1.08\,\mathrm{m/s}$. *The lines are drawn to guide the eye.*

The employed CFD model correctly predicts the increased bed expansion compared to fluidized beds with a monodisperse particle size distribution, as observed in experiments by de Groot (1967). Related to this, the minimum fluidization velocity is also significantly lowered in the simulations with a bimodal particle size distribution, as experimentally observed by Grace and Sun (1991). The CFD model with a bimodal particle size distribution is also able to show inversion, as observed by Rasul et al. (1999). The three physical effects derived from first principles causing inversion are presented, based upon the granular kinetic theory for a bimodal mixture.

Finally, it is noted that the calculation times are extremely large. Therefore, it is not possible to predict the behavior of fluidized beds containing a bimodal mixture over a time-scale of a few seconds of fluidized beds with a realistic size.

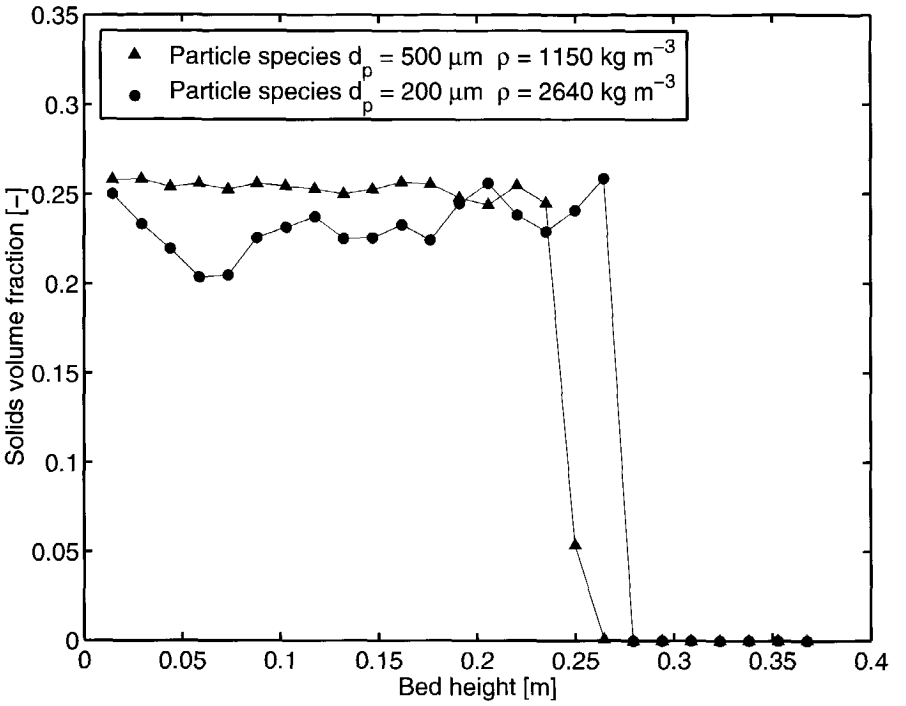

Figure 5.8: *The strip- and 4 s time-averaged solids volume fraction of the bimodal mixture Case 2 fluidized bed at* $U = 1.85\,m/s$. *The lines are drawn to guide the eye.*

5.8 Nomenclature

A	Free energy, $kg\,m^2\,s^{-2}$
b	empirical constant
c	particle velocity, $m\,s^{-1}$
C	peculiar particle velocity, $m\,s^{-1}$
C_D	drag coefficient
d	particle diameter, m
d	diffusion force, m^{-7}
D_T	inner column diameter, m
$\overline{\overline{D}}$	rate of strain tensor $= \frac{1}{2}\left(\nabla\mathbf{u} + (\nabla\mathbf{u})^T\right)$, s^{-1}
F	external force/drag force, N
Fr	empirical material constant, $N\,m^{-2}$
g	radial distribution function
g	gravitational constant, $m\,s^{-2}$
H	height in fluidized bed, m

m	particle mass, kg
M	mixing index
$\mathbf{n}$	normal vector, m
n	number density, m^{-3}
p	empirical material constant
P	normal pressure, $N\,m^{-2}$
Re_p	Particle Reynolds number
q	empirical material constant
$\mathbf{q}$	mixture energy flux, $kg\,m^2\,s^{-3}$
T	granular temperature, $kg\,m^2\,s^{-2}$
$\mathbf{u}$	average velocity, $m\,s^{-1}$
U	superficial gas velocity, $m\,s^{-1}$
$\mathbf{v}$	diffusion velocity, $m\,s^{-1}$
V	volume of a particle, m^3
X	small species volume fraction

Greek

β	interphase drag constant, $kg\,m^{-3}\,s^{-1}$
ϵ	volume fraction
ϕ	angle of internal friction
φ'	specularity coefficient
γ	rate of granular energy dissipation, $kg\,m\,s^{-3}$
λ	bulk viscosity, Pa s
μ	shear viscosity, Pa s
μ_i	chemical potential
ρ	density
σ	particle radius, m
$\bar{\bar{\tau}}$	viscous stress tensor, $N\,m^{-2}$

subscripts

A	first particle species
B	second particle species
g	gas phase
i	i-th particle species
k	k-th particle species
ik	employ properties of species i and k
max	maximum
mf	at minimum fluidization
min	minimum; kick-in value

mono	monodisperse particle size distribution
s	solids mixture
slip	slip
w	wall

5.A Appendix

The chemical potential for the radial distribution coefficient as defined in Equation 5.39

$$
\begin{aligned}
\mu_i = T\Bigg[&\ln(n_i) - \frac{1}{(\sigma_i{}^3 n_i + n_k\sigma_k^3)^4}\cdot\Bigg\{\frac{2\epsilon_m\sigma_i^2}{(4\pi(\sigma_i^3 n_i + n_k\sigma_k^3) - 3\epsilon_m)^3}\cdot \\
&\Big(4\pi(\sigma_i^3 n_i + n_k\sigma_k^3)(32\sigma_i\pi^2(\sigma_i^3 n_i + n_k\sigma_k^3)^4(\sigma_i^3 n_i^2 + n_k^2\sigma_k^3) - 9\epsilon_m^4(\sigma_i^2 n_i + n_k\sigma_k^2) \\
&(\sigma_i^8 n_i^3 - \sigma_i^6 n_i^2 n_k\sigma_k^2 + 4\sigma_i^5 n_i^2 n_k\sigma_k^3 + \sigma_i^3 n_i n_k^2\sigma_k^5 - 3\sigma_i n_k^3\sigma_k^7 + 2n_k^3\sigma_k^8) \\
&+ 3\epsilon_m^3(\sigma_i^3 n_i + n_k\sigma_k^3)(\sigma_i^7 n_i^3(9 + 10\sigma_i^3 n_i\pi) + \sigma_i^4 n_i^2 n_k(27 + 40\sigma_i^3 n_i\pi)\sigma_k^3 \\
&- \sigma_i^3 n_i n_k^2(9 + 10\sigma_i^3 n_i\pi)\sigma_k^4 + 2\sigma_i^2 n_i n_k^2(9 + 25\sigma_i^3 n_i\pi)\sigma_k^5 - 18\sigma_i n_k^3\sigma_k^6 - n_k^3(20\sigma_i^3 n_i\pi - 9)\sigma_k^7 \\
&+ 20\sigma_i^2 n_i n_k^3\pi\sigma_k^8 - 30\sigma_i n_k^4\pi\sigma_k^9 + 20n_k^4\pi\sigma_k^{10}) - 48\epsilon_m\pi(\sigma_i^3 n_i + n_k\sigma_k^3)^3(\sigma_i^5 n_i^2 n_k\pi\sigma_k^2 \\
&+ 2\sigma_i^3 n_i n_k^2\pi\sigma_k^4 - 2\sigma_i^2 n_i n_k^2\pi\sigma_k^5 - n_k^3\pi\sigma_k^7 + \sigma_i^4 n_i^2(1 - 3n_k\pi\sigma_k^3) \\
&+ \sigma_i n_k^2\sigma_k^3(1 + 3n_k\pi\sigma_k^3)) - 2\epsilon_m^2(\sigma_i^3 n_i + n_k\sigma_k^3)^2(4\sigma_i^{10} n_i^4\pi^2 - 16\sigma_i^8 n_i^3 n_k\pi^2\sigma_k^2 \\
&- 20\sigma_i^6 n_i^2 n_k^2\pi^2\sigma_k^4 + 24\sigma_i^2 n_i n_k^2\pi\sigma_k^5(3 + n_k\pi\sigma_k^3) \\
&+ 12n_k^3\pi\sigma_k^7(3 + 2n_k\pi\sigma_k^3) + 6\sigma_i^7 n_i^3\pi(3 + 8n_k\pi\sigma_k^3) + 9\sigma_i^4 n_i^2(12n_k\pi\sigma_k^3 - 1) \\
&- 2\sigma_i^3 n_i n_k^2\pi\sigma_k^4(27 + 20n_k\pi\sigma_k^3) + 2\sigma_i^5 n_i^2 n_k\pi\sigma_k^2(26n_k\pi\sigma_k^3 - 9) \\
&- \sigma_i n_k^2\sigma_k^3(9 + 2n_k\pi\sigma_k^3(45 + 22n_k\pi\sigma_k^3)))\Big) \\
&+ \Big[(2 - \epsilon_m)(\epsilon_m - 1)\sigma_i^{10} n_i^4 - 2\sigma_i^7 n_i^2\{2(\epsilon_m - 2)(\epsilon_m - 1)n_i - n_k\}n_k\sigma_k^3 \\
&+ (\epsilon_m - 3)\epsilon_m\sigma_i^6 n_i^2 n_k^2\sigma_k^4 - \epsilon_m(5\epsilon_m - 6)\sigma_i^5 n_i^2 n_k^2\sigma_k^5 + \sigma_i^4 n_i n_k^2((9\epsilon_m - 10)n_i + 4n_k \\
&- 6\epsilon_m n_k)\sigma_k^6 + 2\epsilon_m^2\sigma_i^3 n_i n_k^3\sigma_k^7 - 2(\epsilon_m - 3)\epsilon_m\sigma_i^2 n_i n_k^3\sigma_k^8 + \sigma_i n_k^3((2 + 3(\epsilon_m - 2)\epsilon_m)n_k \\
&- 4n_i)\sigma_k^9 + (3 - 2\epsilon_m)\epsilon_m n_k^4\sigma_k^{10}\Big]\ln(3) \\
&- \Big[(\epsilon_m - 2)(\epsilon_m - 1)\sigma_i^{10} n_i^4 + 2\sigma_i^7 n_i^2(2(\epsilon_m - 2)(\epsilon_m - 1)n_i \\
&- n_k)n_k\sigma_k^3 - (\epsilon_m - 3)\epsilon_m\sigma_i^6 n_i^2 n_k^2\sigma_k^4 + \epsilon_m(5\epsilon_m - 6)\sigma_i^5 n_i^2 n_k^2\sigma_k^5 - \sigma_i^4 n_i n_k^2((9\epsilon_m - 10)n_i \\
&+ 4n_k - 6\epsilon_m n_k)\sigma_k^6 - 2\epsilon_m^2\sigma_i^3 n_i n_k^3\sigma_k^7 + 2(\epsilon_m - 3)\epsilon_m\sigma_i^2 n_i n_k^3\sigma_k^8 + \sigma_i n_k^3(4n_i - (2 \\
&+ 3(\epsilon_m - 2)\epsilon_m)n_k)\sigma_k^9 + \epsilon_m(2\epsilon_m - 3)n_k^4\sigma_k^{10}\Big](\ln(\epsilon_m) - \ln(3\epsilon_m - 4\pi(\sigma_i^3 n_i + n_k\sigma_k^3)))\Big\}\Big]
\end{aligned}
$$

Chapter 6

Experimental validation of Lagrangian Simulations

This chapter describes the Lagrangian-Eulerian model in which the trajectories of individual particles in a continuous gas-phase flow are calculated. Also, experiments were performed in a small laboratory-scale experimental setup and compared to simulations of the same geometry and particle properties. Both voidage and pressure time-series obtained from the simulations and the experiments are compared to each other, to obtain insight into the accuracy of the physical assumptions made in this Lagrangian model.

This chapter has been accepted for publication:

B.G.M. van Wachem, J.C. Schouten, R. Krishna, and C.M. van den Bleek, (2000), Experimental validation of Lagrangian-Eulerian Simulations of Fluidized Beds, *accepted for publication in Powder Technology.*

Abstract

The present study aims to validate two-dimensional Lagrangian-Eulerian simulations of gas-solid fluidized beds by comparing these with dedicated experimental data obtained with polystyrene Geldart type D particles of 1.545 mm size.

Experimental data on pressure, voidage, and bed height fluctuations, and the power spectral density are compared with three different implementations of the Eulerian-Lagrangian model. Though qualitative trends found in the experiment are correctly reproduced by the simulations, it is found that the simulations are particularly sensitive to porosity estimation procedures used in the three different simulation strategies employed. Furthermore, the phenomenon of particle clustering predicted by the model do not conform to experimental observations; this is because the physics of the break-up of clusters is not properly captured in the model.

6.1 Introduction

Due to increasing computer power, discrete particle models, or Lagrangian models, have become a very useful and versatile tool to study the hydrodynamic behavior of particulate flows. In these models, the Newtonian equations of motion are solved for each individual particle, and a collision model is applied to handle particle encounters. Recently, such particle models have been combined with an Eulerian fluid model to simulate freely bubbling fluidized beds and circulating fluidized beds (*e.g.* Tsuji et al., 1993, Hoomans et al., 1995, Xu and Yu, 1997). Up to date, however, these models have not been properly validated by comparison with experiments.

Another approach in simulating the behavior of fluidized beds is through Eulerian-Eulerian modeling. In this approach the particle phase is averaged and thus the particles are not seen as separate objects, as in Jackson (1997) (volume averaging) or Zhang and Prosperetti (1994) (ensemble averaging). After the correct particle and gas governing equations are obtained, closure relations need to be applied to describe the particle-particle interactions and the gas-particle interactions. The conservation laws applicable during a hard sphere collision are volume averaged to describe the particle-particle interactions. This was done for an ideal gas consisting of fully elastic particles by, for instance, Chapman and Cowling (1970). For more realistic particles, Lun et al. (1984) successfully derived the kinetic theory of granular flow (KTGF). This theory provides the particle-particle closure derived from first principles.

The drawback of volume averaging the particle phase, as in the Eulerian-

Eulerian approach, is the loss of small-scale information. In the Eulerian-Eulerian approach, it is impossible to predict the paths of individual particles, while Lagrangian models can be used to study the flow of each individual particle. In the Lagrangian-Eulerian approach, in which the paths of individual particles are calculated, many researchers do employ a coarser grid resolution for the gas phase equations than the length-scale that is used in the particle-phase calculations. Hence, the gas-phase does not perceive, initiate, group, or break-up particle clusters when the clusters are smaller than the length scale of the gas-phase solution. As a result, microscale cluster formation is not driven by gas flow, but only by particle-particle collisions. Also, due to the different averaging scales, the gas does not flow around small clusters of particles, but flows through them as if the clusters are a fixed porous medium. Only when clustering is mainly initiated by particle-particle collisions and clusters are much larger than the gas-phase averaging scale, the use of a coarser gas-phase grid resolution is justified.

The goal of this work is to validate the predictions of the Lagrangian-Eulerian model with experiments of a small fluidized bed with Geldart D particles, to gain insight in the effect of the assumptions made in the Lagrangian-Eulerian model derivation. The small bed geometry and the large particles make the computationally expensive Lagrangian-Eulerian simulations of this system feasible. Results obtained from simulations of the pressure fluctuations, voidage fluctuations, bed expansion, and the visual representation of the location of the particles are compared to experiments with the same geometry, particle type, and superficial gas velocities.

6.2 Particle phase

We consider flows of homogeneous, inelastic, frictional spheres in a two-dimensional geometry. The path of each individual particle is calculated, this is called a Lagrangian calculation. The calculation of the paths of the particles consists of two steps: (i) the motion of the particles, and (ii) the treatment of the collision of a particle with another particle.

6.2.1 Motion of particles

The motion of individual particles is completely determined by Newton's second law of motion. The forces acting on each particle are gravity and the traction force of the gas phase on the particle. Thus, the momentum equation describing the acceleration of the particle is (Jackson, 1997)

$$m_s \mathbf{a}_s = m_s \mathbf{g} + V_s \nabla \cdot \bar{\bar{\tau}} - V_s \nabla P + \beta \frac{V_s}{\epsilon_s} (\mathbf{v}_g - \mathbf{v}_s) \tag{6.1}$$

where $\mathbf{a}_s$ is the acceleration of one particle, V_s is the volume of one particle, $\bar{\bar{\tau}}$ is the local gas phase shear tensor, P is the local normal pressure, ϵ_s is the local solid volume fraction, and β represents the interphase momentum exchange coefficient, as is well-known from two-fluid models. The gas phase shear tensor is defined as

$$\bar{\bar{\tau}} = 2\mu\bar{\bar{D}} - \frac{2}{3}\mu\,\mathrm{tr}\left(\bar{\bar{D}}\right)\bar{\bar{I}} \tag{6.2}$$

where $\bar{\bar{D}}$ is the strain rate tensor,

$$\bar{\bar{D}} = \frac{1}{2}\left(\nabla\mathbf{v} + (\nabla\mathbf{v})^T\right) \tag{6.3}$$

and μ the gas-phase viscosity. In most cases, the magnitude of the gas-phase shear tensor is not significant and its contribution can be safely omitted, as it is an order of magnitude smaller than the pressure drop. Xu and Yu (1997) omit the pressure drop term in their particle phase momentum equation. This pressure drop term, however, is not negligible but the same order of magnitude as the interphase momentum transfer coefficient.

The interphase momentum transfer coefficient β is given by Wen and Yu (1966) as

$$\beta = \frac{3}{4}C_D\frac{(1-\epsilon_s)\epsilon_s\rho_g|\mathbf{v_g}-\mathbf{v_s}|}{d_p}(1-\epsilon_s)^{-2.65}, \tag{6.4}$$

with the drag coefficient C_D given by Rowe (1961) as

$$C_D = \begin{cases} \dfrac{24}{Re_p(1-\epsilon_s)}\left[1+0.15\left((1-\epsilon_s)Re_p\right)^{0.687}\right] & \text{if } (1-\epsilon_s)Re_p < 1000 \\ 0.44 & \text{if } (1-\epsilon_s)Re_p \geq 1000 \end{cases} \tag{6.5}$$

where the particle Reynolds number Re_p is defined as

$$Re_p = \frac{d_p\rho_g|\mathbf{v_g}-\mathbf{v_s}|}{\mu_g} \tag{6.6}$$

The interaction of the particle rotation with the gas-phase is neglected. This assumption is verified in the results section.

6.2.2 Collision of particles

The collisions between two particles are assumed binary, and the velocities of the particles emerging from a collision are calculated by considering the

balance of linear and angular momenta in the collision. The simplified model proposed by Louge (1994), originally developed by Maw et al. (1976), is employed to describe the dynamics of individual collisions. During a collision, energy is stored in elastic deformations associated with both the normal and the tangential displacements of the contact point relative to the center of the sphere. Because the release of this energy may affect the rebound significantly, coefficients of restitution associated with both the normal and tangential components of the velocity point of contact are taken into account. This model is employed for both particle-particle and particle-wall collisions.

We consider two colliding spheres with diameters d_1 and d_2 with masses m_1 and m_2 with centers located at $\mathbf{r}_1$ and $\mathbf{r}_2$. The unit normal along the line joining the centers of two spheres is $\mathbf{n} = (\mathbf{r}_1 - \mathbf{r}_2)/|\mathbf{r}_1 - \mathbf{r}_2|$. During the collision, sphere 2 exerts an impulse $\mathbf{J}$ onto sphere 1. Prior to the collision the spheres have translational velocities $\mathbf{c}_1$ and $\mathbf{c}_2$ and angular velocities ω_1 and ω_2. The corresponding velocities after the collision are denoted by primes. The velocities before and after collision are related by

$$m_1(\mathbf{c}_1' - \mathbf{c}_1) = -m_2(\mathbf{c}_2' - \mathbf{c}_2) = \mathbf{J} \tag{6.7}$$

and

$$\frac{2I_1}{d_1}(\omega_1' - \omega_1) = -\frac{2I_2}{d_2}(\omega_2' - \omega_2) = -\mathbf{n} \times \mathbf{J} \tag{6.8}$$

where $I = md^2/10$ is the moment of inertia about the center of a homogeneous sphere. In order to determine the impulse $\mathbf{J}$, the relative velocity $\mathbf{q}$ at the point of contact is defined:

$$\mathbf{q} = (\mathbf{c}_1 - \mathbf{c}_2) - \left(\frac{d_1}{2}\omega_1 + \frac{d_2}{2}\omega_2\right) \times \mathbf{n} \tag{6.9}$$

With the above equations, the contact velocities before and after the collision are given by

$$\mathbf{q}' - \mathbf{q} = \frac{7}{2}\left(\frac{1}{m_1} + \frac{1}{m_2}\right)\mathbf{J} - \frac{5}{2}\left(\frac{1}{m_1} + \frac{1}{m_2}\right)\mathbf{n}(\mathbf{J} \cdot \mathbf{n}) \tag{6.10}$$

The coefficient of restitution, e, characterizes the incomplete restitution of the normal component of $\mathbf{q}$:

$$\mathbf{n} \cdot \mathbf{q}' = -e\mathbf{n} \cdot \mathbf{q} \tag{6.11}$$

where $0 \leq e \leq 1$. In collisions that involve sliding, the sliding is assumed to be resisted by Coulomb friction and the tangential and normal components of the impulse are related by the coefficient of friction μ:

$$|\mathbf{n} \times \mathbf{J}| = \mu(\mathbf{n} \cdot \mathbf{J}) \tag{6.12}$$

where $\mu \geq 0$. Combining Equations 6.10 through 6.12 provides an expression for the impulse transfer in the case when the collision is sliding:

$$\mathbf{J}^{(1)} = \frac{(1+e)(\mathbf{q}\cdot\mathbf{n})\mathbf{n} + \mu(1+e)\cot\gamma[\mathbf{q} - \mathbf{n}(\mathbf{q}\cdot\mathbf{n})]}{\left(\frac{1}{m_1} + \frac{1}{m_2}\right)} \tag{6.13}$$

where γ is the angle between $\mathbf{q}$ and $\mathbf{n}$ and the superscript 1 denotes that the collision involves sliding. With small γ the collision is sliding, and as γ increases the sliding stops when

$$\mathbf{n} \times \mathbf{q}' = -\xi \mathbf{n} \times \mathbf{q} \tag{6.14}$$

or equivalently

$$\cot\gamma_0 = \frac{2(1+\xi)}{7(1+e)\mu} \tag{6.15}$$

where $0 \leq \xi \leq 1$ is the tangential coefficient of restitution. Collisions with $\gamma \geq \gamma_0$ do not involve sliding but sticking, and in this case the impulse is found by combining Equations 6.10, 6.11 and 6.14:

$$\mathbf{J}^{(2)} = -\frac{(1+e)(\mathbf{q}\cdot\mathbf{n})\mathbf{n} + \frac{2}{7}(1+\xi)[\mathbf{q} - \mathbf{n}(\mathbf{q}\cdot\mathbf{n})]}{\left(\frac{1}{m_1} + \frac{1}{m_2}\right)} \tag{6.16}$$

In this expression, the superscript 2 denotes the collision does not involve sliding, but sticking. The three parameters e, μ, and ξ are taken to be constant and independent of the velocities.

Collisions with a flat wall are treated by considering the wall as a particle with infinite mass and with the appropriate wall values of e, μ, and ξ.

6.2.3 From two dimensions to three dimensions

If the local porosity, ϵ_g, is calculated by dividing the empty space (not occupied by particles) by the total space, this will give a different result in two dimensions and in three dimensions. To correct for this inconsistency, Hoomans et al. (1995) suggests to transform the two-dimensional porosity with the following equation:

$$\epsilon_{3D} = 1 - \frac{2}{\sqrt{\pi\sqrt{3}}}(1 - \epsilon_{2D})^{\frac{3}{2}} \tag{6.17}$$

where ϵ_{2D} is the porosity defined as the area occupied by disks in the two-dimensional space. The basis of this equation is to assume equal spacing between the two-dimensional disks in a hexagonal lattice and three-dimensional

particles in a FCC lattice. Xu and Yu (1997) propose a different equation,

$$\epsilon_{3D} = 1 - \frac{\sum_{i=1}^{K} V_i}{\Delta V} \tag{6.18}$$

in which the summation is taken over all the particles in the volume ΔV, which is the volume of a computational cell with the thickness of one particle, thus $\Delta V = \Delta x \Delta y d_p$, and V_i is the volume of particle i. This equation gives slightly different predictions for ϵ_{3D} than the equation proposed by Hoomans et al. (1995).

Because of the ideal spherical particles in the two-dimensional simulations, the ideal solids packing can be easily obtained. In practice, however, this packing is never obtained. A third method should also be considered, namely the one proposed by Hoomans et al. (1995) with an empirical parameter containing the maximum experimental solids packing in practice, ν, thus

$$\epsilon_{3D} = 1 - \nu \frac{2}{\sqrt{\pi\sqrt{3}}} (1 - \epsilon_{2D})^{\frac{3}{2}} \tag{6.19}$$

$$\nu = \frac{1 - \epsilon_{3D,\text{experimental minimum}}}{1 - \epsilon_{3D,\text{theoretical minimum}}} \tag{6.20}$$

Both the Equations 6.17 and 6.19 are used in this work and the results of simulations employing both forms are compared with each other.

A fundamental problem regarding the translation of the corresponding number of particles in two-dimensions to the number of particles in three-dimensions is the pressure drop. When the two-dimensional bed is filled with particles up to a certain height, the number of two-dimensional particles is not equal to the number of particles as experienced by the gas-phase, due to the translation of the voidage from two-dimensions to three-dimensions. Hence, the pressure drop calculated in the gas-phase is less than the weight of the particles, by the pre-factor in Equation 6.17. Thus, the pressure drop calculated by two-dimensional Lagrangian simulations will predict too low a pressure drop compared to experiments with the same initial bed height. Increasing the number of particles to correct for this loss of weight will increase the pressure drop, but will also change the dynamics of the particle phase because the height over diameter ratio of the dense fluidized bed is changed.

6.3 Gas phase

The motion of the gas-phase is calculated from the volume averaged gas-phase governing equations as put forward by Jackson (1997). The continuity

equation for the gas phase is

$$\frac{\partial \epsilon_g \rho_g}{\partial t} + \nabla \cdot \epsilon_g \mathbf{v}_g = 0 \tag{6.21}$$

and the momentum balance is

$$\frac{\partial \epsilon_g \rho_g \mathbf{v}_g}{\partial t} + \nabla \cdot (\epsilon_g \rho_g \mathbf{v}_g \mathbf{v}_g) = -\epsilon_g \nabla P + \epsilon_g \nabla \cdot \bar{\bar{\tau}}_g + \epsilon_g \rho_g \mathbf{g} - \sum_{i=1}^{K} \frac{V_{s,i} \beta (\mathbf{v}_g - \mathbf{v}_{s,i})}{\epsilon_s} \delta(\mathbf{x} - \mathbf{x}_{s,i}) \tag{6.22}$$

in which the last term represents the interphase momentum transfer between the gas phase and each individual particle. δ represents a pulse function, which is one if its argument is zero and zero otherwise. The last term is to ensure that the interphase momentum transfer is only taken into account in the gas-phase momentum equation at the location of the corresponding particle.

The left and right walls of the fluidized bed are treated as no-slip velocity boundary conditions for the gas-phase. Dirichlet boundary conditions are employed at the bottom with a uniform gas inlet velocity. The boundary condition at the top the fluidized bed is a so-called pressure boundary. The pressure at this boundary is fixed to a reference value, $1.013 \cdot 10^5$ Pa and Neumann boundary conditions are applied to the gas-phase velocity, requiring a fully-developed gas flow.

As was indicated earlier, a problem of this Lagrangian-Eulerian approach is the length-scale of the averaging. In the Eulerian-Eulerian approach the length scales of the averaged gas-phase and particle-phase are equal and the "sub-grid" behavior of the particles is described with the kinetic theory of granular flow. In the Lagrangian-Eulerian approach, the length-scale of the gas-phase is larger than the length-scale of the particle phase. The information of gas induced movement of particles, as well as particle induced movement of gas, cannot be transferred between the phases on the eddy or individual particle scale. Hence, a computational cell in which a small cluster of particles is present is penetrated by the gas-phase, similar as a fixed porous medium; the gas phase does not discriminate between homogeneously distributed particles or clustered particles within one cell. In reality, the gas-phase "dodges" the particle cluster and moves perpendicular to the initial flow before the cluster. Particle clustering due to the local gas flow is thus not captured in the Lagrangian-Eulerian approach. This treatment of the particle-gas phase coupling should be well kept in mind when attempting to use this simulation method.

6.4 Solution method

The gas-phase is calculated on a computational grid with individual grid size of four to eight particle diameters. The gas-phase governing equations have been solved on a staggered grid (Patankar, 1980) employing the SIMPLE algorithm to determine the pressure of the gas phase. The discretization of the terms is done with a second order TVD scheme in space and the second order Crank-Nicholson scheme in time. The preconditioned bi-conjugent gradient method was employed to solve the discretized gas-phase equations. The gas-phase solution was verified to be grid independent on the employed grid size, by means of grid refinement.

The solid volume fraction in the gas-phase momentum equation is determined from the number of particles in the gas-phase computational cell, by employing Equation 6.17. The interphase momentum transfer is calculated from the last term of the gas-phase momentum balance, and this coupling is treated explicit. To justify this, a very small time-step is employed, $\Delta t \approx 1.0 \cdot 10^{-4}$ s. The gas-phase properties at the particle surface are calculated by area weighted averaging, as shown in Figure 6.1. This method is not mesh-size independent, as there is a direct coupling between average particle properties, such as particle porosity and velocity, and the gas-phase. The mesh-size of the gas-phase needs to be small enough to predict realistic gas-particle interactions, and large enough to determine an accurate average value for the particle porosity, momentum transfer, and velocity. We have found that the length of one gas-phase grid cell should be in the order of four to ten particle diameters. After initialization of both phases, first the shortest collision time of each particle is determined. This is done by comparing the location and velocity of each particle with the other particles in the near vicinity by using a particle-phase mesh, without checking a pair of particles twice, as indicated by Figure 6.2. The collision time between two particles is determined by (Allen and Tildesley, 1980)

$$t_{col} = \frac{-\mathbf{r}_{12} \cdot \mathbf{c}_{12} - \sqrt{(\mathbf{r}_{12} \cdot \mathbf{c}_{12})^2 - c_{12}^2 \left[r_{12}^2 - (\frac{1}{2}d_1 + \frac{1}{2}d_2)^2\right]}}{c_{12}^2} \tag{6.23}$$

where $\mathbf{r}_{12} \equiv \mathbf{r}_1 - \mathbf{r}_2$ and $\mathbf{c}_{12} \equiv \mathbf{c}_1 - \mathbf{c}_2$. If the inproduct $\mathbf{r}_{12} \cdot \mathbf{c}_{12} > 0$, the particles are moving away from each other and will not collide. If the overall shortest collision time (of all the particles) is larger than the time-step of the gas-phase calculation, the particle positions are updated by the integration of Equation 6.1 with the same time-step as the gas-phase. Hereafter, the gas-phase properties are computed and the forces exerted by the gas phase on each individual particle are calculated. Now, the shortest collision times are determined again and the process is repeated from the beginning.

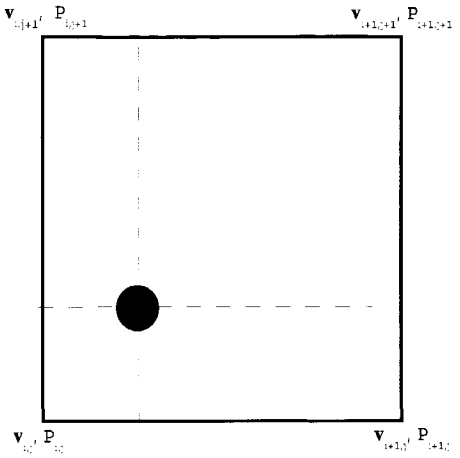

Figure 6.1: *The principle of area weighted averaging. The gas-phase properties are given in the corners of the gas-phase cell by the gas-phase solution and are averaged to the center of the particle (denoted by the black dot) by using the overlying areas as weighting factors. This figure has been adapted from Hoomans et al. (1995).*

If the overall shortest collision time is smaller than the time-step of the gas-phase, the particle positions are updated by this shortest overall collision time. Hereafter, the collision of the two particles in question is executed. Then again, the shortest collision times of all particles are calculated. This is repeated, until the overall shortest collision time is shorter than the time-step of the gas-phase calculation minus the time-steps of all previous collisions during this iteration. When the overall shortest collision time is larger than the time remaining until the end of the gas-phase time-step, the gas-phase is updated. This process is repeated until the required real time of simulation is obtained.

6.5 Experiments and simulations

6.5.1 Experimental set-up

The experimental set-up consisted of a two-dimensional plexiglass rectangular column, 500 mm high, 90 mm wide, and 8 mm deep. A schematic representation of the set-up is given in Figure 6.3. The gas flow was controlled with a variable area flow meter and a valve. The dry air from the compressor system was humidified to reduce static electricity build-up in the fluidized

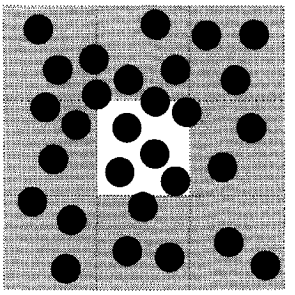

Figure 6.2: *A three-by-three particle mesh. The shortest times of collision of the particles in the center cell are determined by comparing the locations and velocities of the particles in the white center cell with all the particles in the nine particle cells. For the calculation times in the next particle cell, comparing the particles in that cell with the particles in the white cell is no longer necessary.*

bed. The gas was only humidified partially to prevent condensation of water in the bed (operating temperature 17 °C); polystyrene spheres with a density of 1150 kg m^{-3} and a diameter of 1.54 mm (1.41 - 1.68 mm sieve fraction) were used as particle system. The bed was filled to a height of 90 mm, corresponding to 39 g of particles, which leads to a packed bed voidage of 0.475. The minimum fluidization velocity calculated using Ergun's equation is 0.74 m/s, agreeing quite well with the experimentally determined value of 0.72 m/s. The experiments were carried out at superficial gas velocities of $U = 0.80$ m/s, $U = 0.90$ m/s, and $U = 1.0$ m/s.

6.5.2 Measurements

Absolute pressure fluctuations were measured with Kistler piezo electric pressure transducers, type 7261 at the side of the bed at heights of 45, 85, and 225 mm from the distributor plate. This sensor type measures the pressure fluctuation relative to the average pressure with an accuracy of 2 Pa. The sensors were connected to 0.10 m long copper tubes of 4 mm ID, the total dead volume of sensor and tube was 2500 mm^3. The tubes were equipped with 40 μm mesh wire gauze at the tips, to prevent particles from entering. This set-up has been thoroughly tested for distortion of pressure fluctuation amplitude and phase (Van Ommen et al., 1999). No significant influence was found at frequencies typical for gas-solids fluidized beds (0-150 Hz). Also, the absolute pressure was measured with a Validyne differential pressure transducer, type DP15, at a height of 5 mm. For each time-series, 300,032 data points were recorded to file with 16 bits ADC using a SCADAS II data acquisition system (LMS, Breda, The Netherlands). The sample frequency was set to 1000 Hz with a filter frequency of 314 Hz. The time-series were analyzed

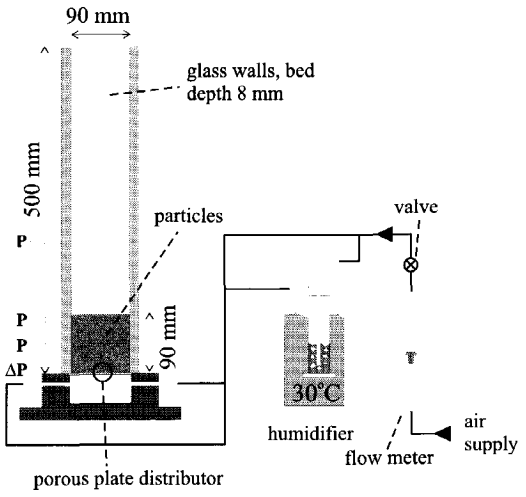

Figure 6.3: *The experimental set-up employed in this work. The symbols* P *indicate where the pressure signals are determined.*

using Fourier analysis and compared to the simulations. In addition to pressure measurements, digital video recordings (25 frames/s, 60 s long) of the fluidized bed were made and analyzed. The local voidage was calculated, from the light intensity determined by the video recording, using the Lambert-Beer relation,

$$\epsilon_s = -\frac{1}{a} \ln\left(\frac{I}{I_0}\right) \tag{6.24}$$

where I is the measured light intensity, I_0 is the minimum light intensity, and a is obtained from calibration of the measured light-intensity and the corresponding known solids concentration.

6.5.3 Simulations

There are several ways of determining the number of particles which need to be used in a two-dimensional simulation in order to be able to mimic the experiments. The solids volume fraction in the two-dimensional configuration at the minimum fluidization velocity can be determined by transforming the measured solids volume fraction with Equation 6.17 to the appropriate two-dimensional solids volume fraction. When the diameter-height aspect ratio of the fluidized bed is equal to the experiments, this approach leads to 3110 required particles. When the ideal two-dimensional maximum solids volume fraction is used, the number of required particles is 4080. The particle specifications used in the simulations are the same as in the experiments. The empirical parameter in the fit equation to translate the porosity from

two dimensions to three dimensions, Equation 6.19, is determined experimentally to be $\nu = 0.89$. For the coefficient of restitution and coefficient of friction, generally proposed values were employed. As long as the coefficient of restitution is well above 0.5 and not very close to 1.0, the dependency of the simulation results on the coefficient of restitution is not very large. The coefficient of friction has little influence, as the total rotational energy of the particles in the fluidized bed is very small. The details of the simulation conditions are specified in Table 6.1. Both the simulations and the experiments were carried out at superficial gas velocities of $U = 0.8\,m/s$, $U = 0.9\,m/s$, and $U = 1.0\,m/s$.

Three different simulation strategies were followed. In strategy **A**, the equation of Hoomans et al. (1995) is employed to translate the two-dimensional porosity into a three-dimensional one. The simulations with this strategy contain 3110 particles. In strategy **B**, the fit equation (Equation 6.19) to translate the porosity from two dimensions to three dimensions is employed. Simulations with this strategy also contain 3110 particles. Strategy **C** also employs the Hoomans et al. (1995) equation, but the simulations contain 4080 particles. Figure 6.4 shows the kinetic energy and the rotational energy as a function of time. The average rotational energy is an order of magnitude smaller than the average kinetic energy. Hence, rotational effects, including influence of particle rotation on the gas-phase, can be safely neglected.

6.5.4 Comparison

The locations of all the particles in the simulations of the fluidized bed are qualitatively compared to the digital video recordings made of the fluidized bed at the same operating conditions. More quantitatively, the simulation predictions of the total time-averaged pressure drop over the fluidized bed, the pressure fluctuations at 45 mm above the distributor, the average voidage fluctuations in a plane at 45 mm above the distributor, and the time-dependent bed expansion are compared with experiments employing the same operating conditions. Furthermore, the power spectral densities (PSD) of the simulated pressure fluctuations are compared with the experimentally determined predicted fluctuations.

6.6 Results and discussion

Figure 6.5 shows a visual comparison of the location of the particles in three simulations at a superficial gas velocity at $U = 0.9\,m/s$ and snapshots from the corresponding experiment covering a complete period from bubble formation to bubble eruption. In all three simulation strategies employed, large clusters of particles were found to be present at the top of the bubble during bubble

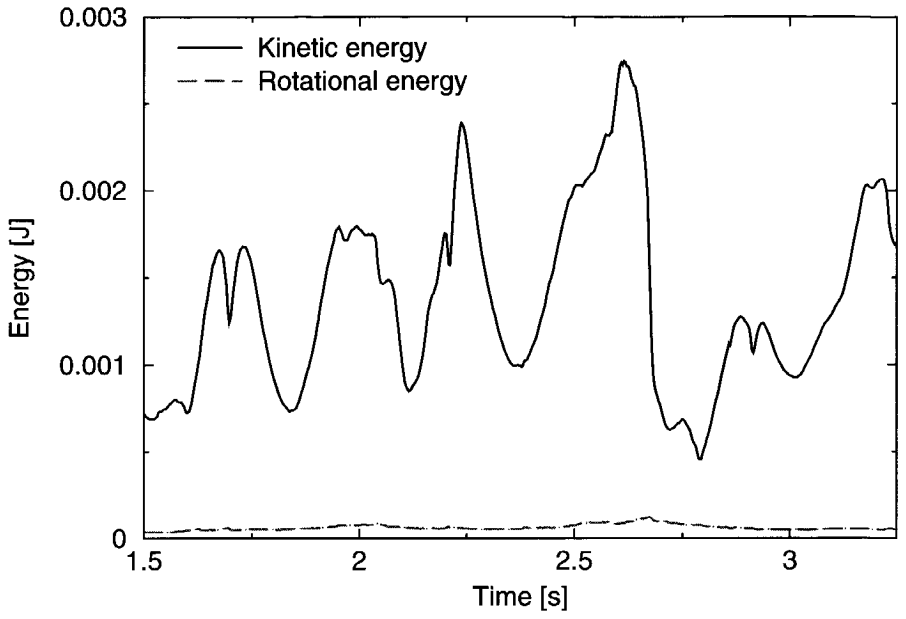

Figure 6.4: *The total kinetic energy and rotational energy as a function of time predicted by a simulation of a fluidized bed with a superficial gas velocity* $U = 0.9\,m/s$.

eruption. This phenomenon is not observed in the experiments. The simulated particle clusters are too stable, which is attributed to the Lagrangian-Eulerian approach, as discussed earlier. The top series of snapshots in Figure 6.5 represents the simulation as a result of employing strategy **A**. The period of bed oscillation from bubble formation to bubble eruption of the simulation is visually in fair agreement with the experiment. The second series represents a simulation as a result of employing strategy **B**. Although the bed oscillation is similar to the one observed in the experiment, the bubble dynamics are not. Due to the extra decreased mass effect because of the fit parameter in Equation 6.19, the gas-phase experiences too little resistance from the particle phase. The third series represents a simulation as a result of employing strategy **C**. The bubble eruption of this series gives a too high bed height compared with the experiment, because the height of the simulated fluidized bed is larger than employed in the experiment. The agreement of the time between bubble formation and bubble eruption of the comparison between all simulations and the experiments is reasonable. Comparison of the simulations and experiments at superficial gas velocities of $U = 0.8\,m/s$ and $U = 1.0\,m/s$ show similar results.

Table 6.1: *Properties of the particles and fluidized bed used in the experiments and the Lagrangian-Eulerian simulations.*

Parameter	Description	Value
ρ_s [kg/m^3]	solid density	1150
ρ_g [kg/m^3]	gas density	1.28
μ_g [Pa s]	gas viscosity	$1.7 \cdot 10^{-5}$
d_p [mm]	particle diameter	1.545
e [-]	coefficient of restitution	0.9
μ [-]	coefficient of friction	0.3
U_{mf} [m/s]	minimum fluidization velocity	0.74
D_T [m]	inner column diameter	0.0898
H_{mf} [m]	height at minimum fluidization	0.09
$\epsilon_{s,mf}$ [-]	solids volume fraction at minimum fluidization	0.525
ν [-]	empirical parameter in Equation 6.19	0.89
Δx [m]	x mesh spacing	$9.97 \cdot 10^{-3}$
Δy [m]	y mesh spacing	$9.97 \cdot 10^{-3}$

The pressure drop in the simulations with 3110 particles is lower (strategy **A** 340 Pa, strategy **B** 300 Pa) than the pressure drop measured in the experiments (480 Pa). The predicted pressure drop by the simulation applying strategy **C** is in very good agreement (483 Pa) with the experiment.

Figure 6.6 shows a comparison of a sample of the pressure fluctuation time-series determined at 45 mm above the distributor at $U = 0.9\,m/s$. In strategy **A**, the shape and amplitude of the pressure fluctuations deviate clearly from the experiment; the maximum amplitudes are higher and the peaks are sharper. This suggests that the gas voids in the simulation are larger. The time-scale of the pressure fluctuations is in fairly good agreement with the experiment. The shape and time-scale of the pressure fluctuations obtained by following strategy **B** are in reasonable agreement with the pressure fluctuations determined in the experiment; the amplitude of the fluctuations, however, is much smaller. This suggests that in the simulation voids are much smaller than observed in the experiment, confirmed by the visual observations of Figure 6.5. The time-scale of the pressure fluctuations obtained from simulations following strategy **C** agrees reasonably with the experimentally determined pressure fluctuations, but the amplitude is much too high. This suggests that the voids in this simulation are much larger than observed in the experiment. Also the shape of the fluctuations is somewhat different compared to the experimentally determined pressure fluctuations.

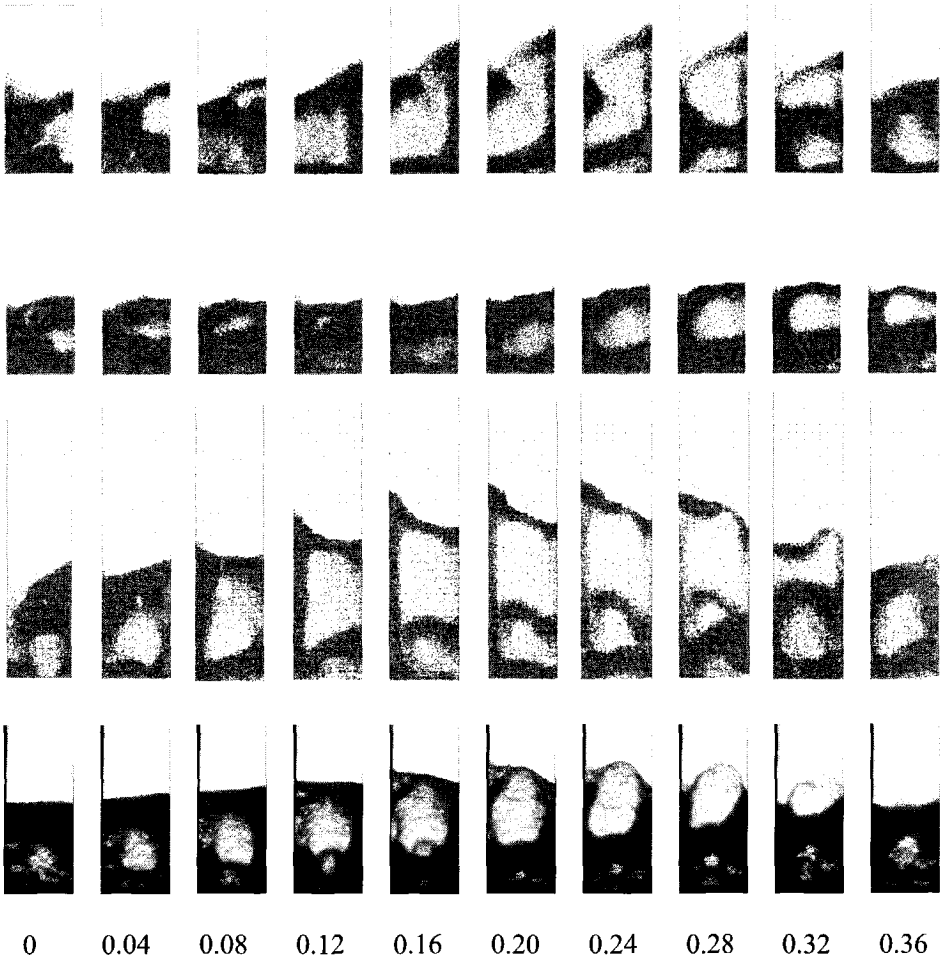

Figure 6.5: *Ten snapshots of a visual representation of the location of the particles at equidistant times (given at the bottom of the series in* s*) at a superficial gas velocity of* $U = 0.9\,m/s$. *The top series represents a simulation employing strategy* **A**, *the second series is a result of strategy* **B**, *and the third series is a result of employing strategy* **C**. *The bottom series are snapshots of the experiment taken by a video camera.*

The power spectral densities (PSD) of the complete pressure fluctuating time-series determined at $U = 0.9\,m/s$ at $45\,mm$ above the distributor are shown in Figure 6.7. This figure shows that the location of the dominant frequency at approximately 3 Hz, imposed by the bubble behavior, is similar in the experi-

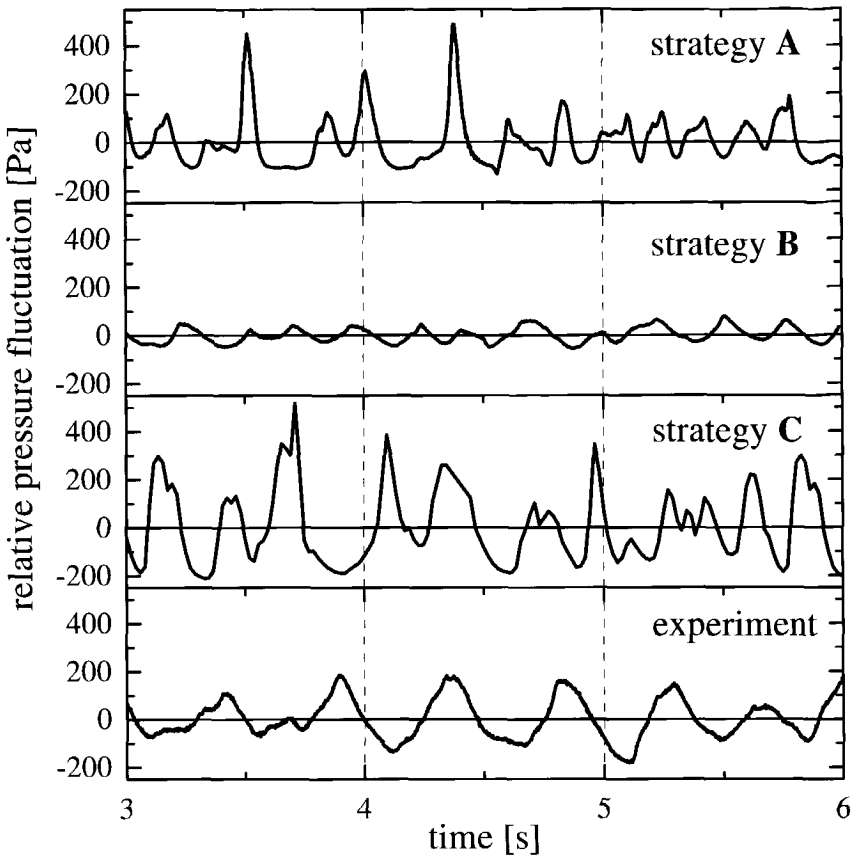

Figure 6.6: *Pressure fluctuation samples taken at* $U = 0.9\,m/s$ *at* $45\,mm$ *above the distributor, resulting from the three simulation strategies compared to the experiment.*

ment and in all the simulations. This figure confirms that this most dominant frequency is less pronounced in the simulations than in the experiment, denoted by the more broad maxima in the PSD of the simulations at the most dominant frequency. The decrease in the PSD curve in Figure 6.7 at frequencies exceeding 5 Hz, a power law fall-off, is a typical feature of gas-solid fluidized beds (Van Wachem et al., 1999); the agreement between experiment and simulations is remarkably good on this point.

Figure 6.8 shows the voidage fluctuations, as a function of time, averaged in a horizontal plane at $45\,mm$ above the distributor, at $U = 0.9\,m/s$, of the three simulation strategies in comparison with the experiment. Simulated

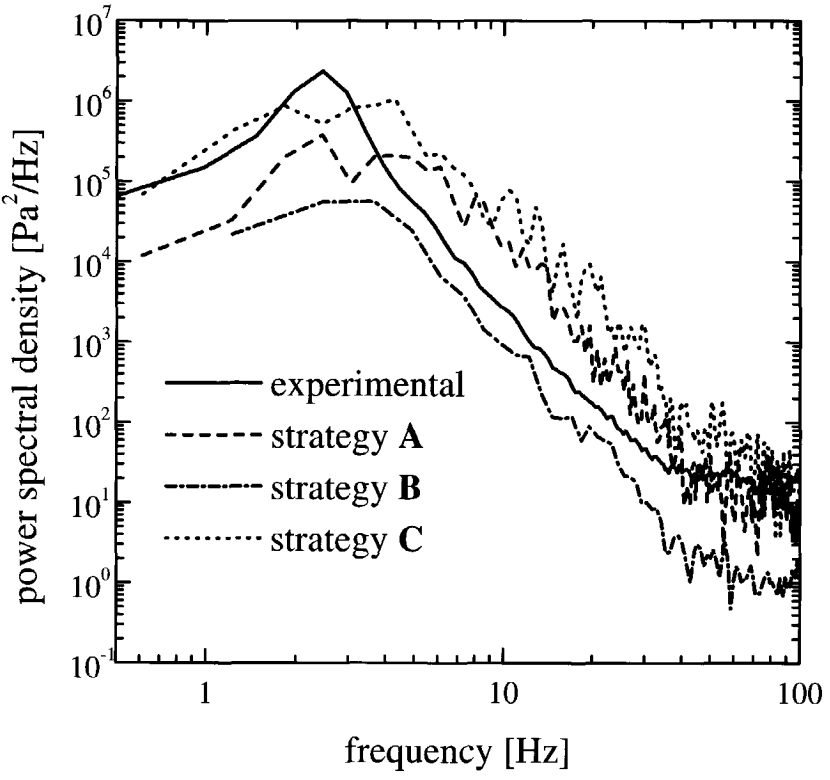

Figure 6.7: *The power spectral density (PSD) as a function of frequency of the pressure fluctuation series at* 45 mm *above the distributor at* $U = 0.9\,m/s$, *resulting from the three simulation strategies compared to the experiment.*

voidage fluctuations as a result of strategies **A** and **C** show too large fluctuations and also the shape of the fluctuations is too sharp in comparison with the experiment. This also suggests that the voids present in the simulations following strategies **A** and **C** are too large. Simulations performed with strategy **B** show shapes and amplitudes that are much more similar to the measured voidage fluctuations. All three simulation strategies predict a slightly too small time-scale of the voidage fluctuations. Figure 6.9 shows the bed height as a function of time as a result of the three simulation strategies and the experiment at $U = 0.9\,m/s$. All simulation strategies show quite different results compared to the experiment. The average time-scale of the bed fluctuation is in fairly good agreement, which can also be seen from Figure

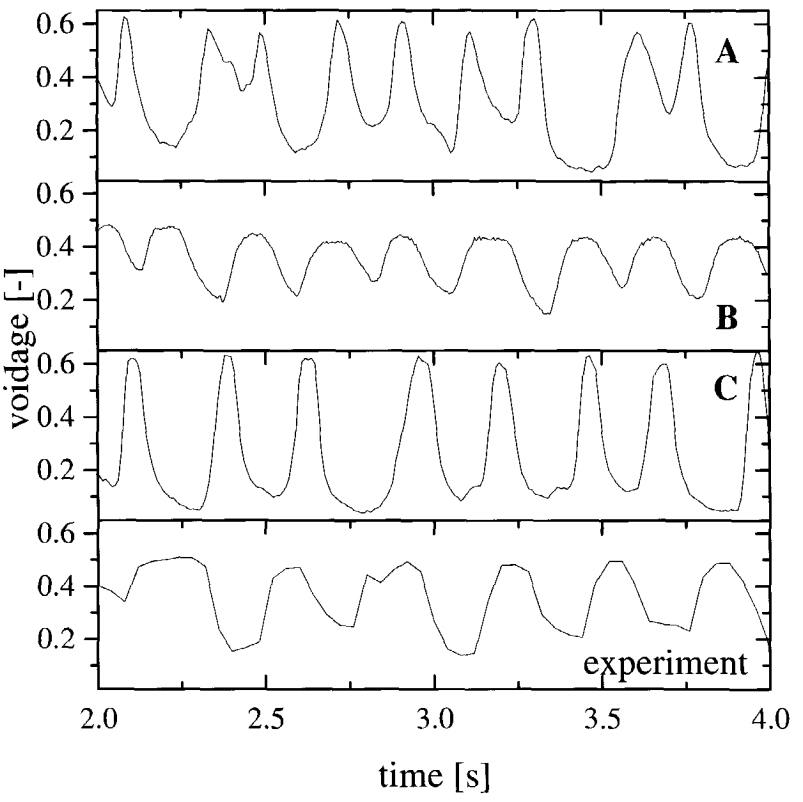

Figure 6.8: *Fluctuations of the solids volume fraction averaged in a horizontal plane at* 45 mm *above the distributor at* $U = 0.9\,\mathrm{m/s}$*, as a function of time, resulting from the three simulation strategies compared to the experiment.*

6.5. The amplitudes of the bed expansion in simulations by strategy **A** and **C** are too large. This is a result of too vigorous bubbling, indicating larger gas voids than present in the experiments. The bed expansion amplitude from simulations following strategy **B** is too small. Enlarging the empirical factor ν in Equation 6.19 will improve the results, as this translation equation will then produce results closer to strategies **A** and **C**.

The average bed expansion and its standard deviation for the three simulation strategies and the experiment are shown in Table 6.2. Strategy **A** compares well to the experiment; it seems that the increase in void size, due to the interphase-momentum transfer equation, is accounted for by the number of

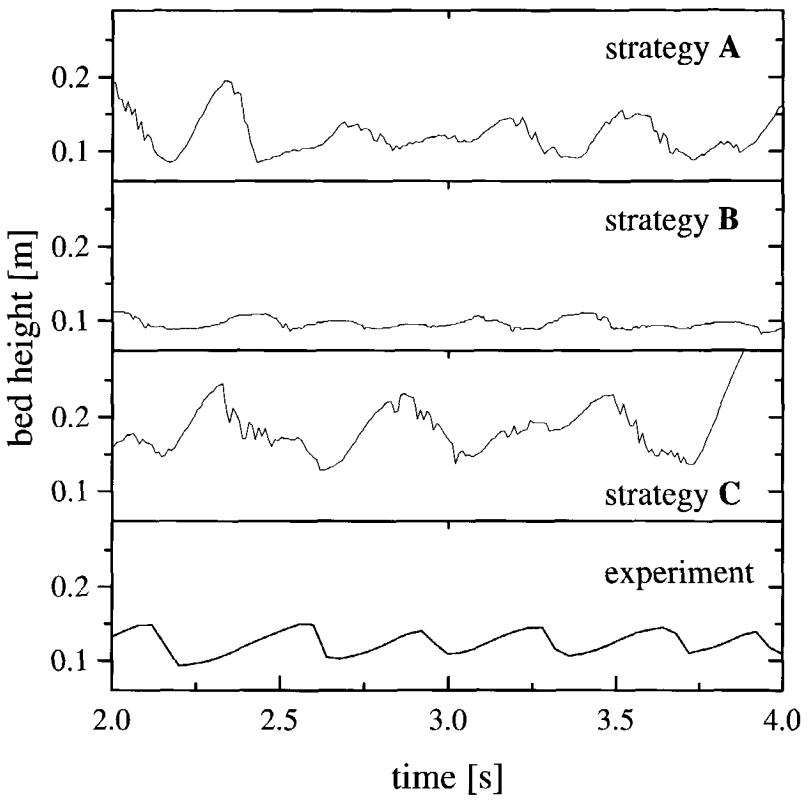

Figure 6.9: *Fluctuations of the bed height at* $U = 0.9\,m/s$, *as a function of time, resulting from the three simulation strategies compared to the experiment.*

particles.

6.7 Conclusions

The goal of this paper is to validated two-dimensional Lagrangian-Eulerian simulations of a gas-solid fluidized bed containing polystyrene particles with laboratory-scale experiments of the same geometry. One difficulty in the two-dimensional Lagrangian-Eulerian model is the translation of the two-dimensional porosity of the particles to a three-dimensional one, required by the gas-phase and the interphase momentum transfer. To tackle this prob-

Table 6.2: *The average bed expansion and the standard deviation determined for the three simulation strategies and the experiment.*

Gas velocity:	0.8 m/s	0.9 m/s	1.0 m/s
Strategy	Bed expansion [m]		
A	0.119 ± 0.021	0.124 ± 0.027	0.146 ± 0.332
B	0.094 ± 0.003	0.097 ± 0.008	0.104 ± 0.180
C	0.162 ± 0.041	0.190 ± 0.046	0.212 ± 0.298
experiment	0.114 ± 0.009	0.120 ± 0.019	0.138 ± 0.019

lem we have followed three strategies, **A**, **B**, and **C**, in performing simulations, each with different assumptions. In one of the strategies, we have included an empirical parameter to fine-tune the pressure drop or the bed expansion with the experimentally determined one. We have not found a strategy, however, that can successfully predict all features of the fluidized bed as observed in the experiments. Performing three-dimensional Lagrangian simulations either with a two-dimensional or three-dimensional Eulerian gas-phase will overcome the difficulty in translating the two-dimensional porosity to a three-dimensional one, but will increase the computational cost as the number of particles to obtain the required bed height in three-dimensions is much larger than in two-dimensions.

Because the gas-phase hydrodynamics are resolved on a larger scale than the particle-phase dynamics, the method is not grid independent and "micro-scale" clustering cannot be captured. Animations show that "micro-scale" clustering does contribute to the total fluidized bed behaviour. Resolving the gas phase on a scale smaller than the particle size, either by direct numerical simulation (DNS) (Hu, 1996) or by the more elegant fictitious domain method (Glowinski *et al.*, 1999), can resolve this problem.

Overall, the two-dimensional Lagrangian-Eulerian simulations are in fair agreement with the experiments. With an added empirical parameter in the translation from the two-dimensional porosity to the three-dimensional porosity the pressure drop or the bed expansion can be fine-tuned. To capture the behaviour of the physics of the fluidized bed more precisely, applying a three-dimensional Lagrangian-Eulerian method is advised.

Nomenclature

a	empirical parameter
$\mathbf{a}$	particle acceleration, $\mathrm{m\,s^{-2}}$
$\mathbf{c}$	particle velocity, $\mathrm{m\,s^{-1}}$

C_D	drag coefficient
d_p	particle diameter, m
D_T	column width, m
e	coefficient of restitution
g	gravitational constant, $m\,s^{-2}$
H	height, m
I	moment of inertia, $kg\,m^2$
J	impulse transfer during collision, $kg\,m\,s^{-1}$
K	number of particles
L	light intensity, cd
m	particle mass, kg
n	normal vector, m
P	pressure, Pa
q	relative velocity, $m\,s^{-1}$
Re	Reynolds number
r	point in space, m
t	time, s
U	inlet (superficial) gas velocity, $m\,s^{-1}$
U_{mf}	minimum fluidization velocity, $m\,s^{-1}$
v	velocity vector, $m\,s^{-1}$
ΔV	volume of computational cell, m^3
V_s	particle volume m^3
Δx	x mesh spacing, m
Δy	y mesh spacing, m

Greek

β	interphase drag constant, $kg\,m^{-3}\,s^{-1}$
γ	angle between impact and normal
ϵ	volume fraction
μ	friction coefficient
ν	empirical parameter
ρ	density, $kg\,m^{-3}$
$\bar{\bar{\tau}}$	viscous stress tensor, $N\,m^{-2}$
ξ	tangential coefficient of restitution

Subscript

0	minimum intensity
1,2	particle index
2D	two-dimensional
3D	three-dimensional
g	gas phase

mf	at minimum fluidization
p	particle
s	solids phase

Chapter 7

Conclusions and Outlook

This chapter gives a brief overview of the research described in this thesis. Goals and conclusions of this thesis are presented in the framework of research performed by other workers in the past. Finally, a short outlook to the near future is given.

7.1 Developments since 1967

In 1967 Anderson and Jackson derived the volume-averaged governing equations to describe gas-solid flow. In 1978 Pritchett et al. performed simulations of a bubble injection with similar governing equations. In these models, it was unknown how to treat the solid-phase stresses. Physical behavior dominated by drag between the solid-phase and the gas-phase, like the formation of bubbles at a single orifice, can be successfully predicted by these models. To overcome the deficiency of these governing equations without a proper treatment of the solid-phase stresses, Jackson proposed a solid-phase viscosity model in 1985. Realistic values for the solid phase stress were, however, unknown. In 1983 Jenkins and Savage started to derive the kinetic theory for granular flow for a mixture of identical, smooth, nearly elastic, spherical particles, analogously to the kinetic theory for gases, as derived by Chapman and Cowling in 1970. The main difference of the kinetic theory for granular flow compared to the kinetic theory for gases, is that collisions occur without conserving energy and momentum. Not only the total energy in the system but also the energy of the vibration of the particles is no longer conserved, making the derivation of the theory more complex. In 1984 Lun et al. presented their final equations of the kinetic theory of granular flow. The research done in the present thesis is largely based on these equations. Some authors have presented their own derivation of the kinetic theory of granular flow. Gidaspow (1994) has presented kinetic theory of granular flow

equations with particular assumptions regarding the elasticity of the particles. Syamlal et al. (1993) neglect streaming contributions (contributions due to particle movement) dominating in the dilute flow regime, studying only dense flow of particles in gas with these equations. Also, some work has been done in describing the influence of the gas-particle interactions on the particle fluctuating velocity.

7.2 Aim and scope of this work

The work presented in this thesis provides an overview of all the different approaches in the literature and assesses the qualitative and quantitative differences. Furthermore, the different models described in the literature are compared directly and by their impact on the simulation results. It is shown that the differences between the theories are negligible in the case of a dense gas-solid fluidized bed; the "newer" theories predict the same solid-phase stress as the "classic" Lun et al. theory. Gas turbulence and gas-solid turbulent interactions can be safely omitted due to the dense character of the system. Moreover, an analytical equation predicting the granular temperature is recommended. Simulations show that this analytical equation predicts the same granular temperature as obtained when solving the full granular energy balance, but the computational effort is significantly decreased.

7.3 Comparing governing equations

In 1975 Ishii has rigorously derived a set of governing equations for fluid-fluid flow. Many researchers, however, use Ishii's equations for gas-solid flow. This thesis shows that these governing equations are fundamentally different from the equations derived by Anderson and Jackson. The Anderson and Jackson governing equations are correct for gas-solid flow and the Ishii governing equations are correct for fluid-fluid (*i.e.* gas-liquid) flow. The differences between simulations with each of the sets of governing equations applied to gas-solid fluidized beds are not large in terms of bed expansion or bubble behavior, but are clearly present on the scale of local solids volume fraction and local solids volume fraction gradients. In other gas-solid flows, in which sharp gradients in solids volume fraction occur, the difference between the Ishii and the Anderson and Jackson governing equations may be even more pronounced.

7.4 Interphase momentum transfer

In 1952 Ergun has determined a (semi) analytical equation predicting the pressure drop over a fixed bed as a function of gas flow and bed porosity. The determined pressure drop can be translated into the gas-solid interphase momentum transfer. Richardson and Zaki (1954) extended this work by determining the influence of the settling velocity of one particle in a liquid-solid fluidized bed in the vicinity of other particles. Wen and Yu (1966) have extended the work of Ergun (1952) by increasing the range of solids volume fraction and taking the measurements of many researchers into account. All three of the mentioned theories, or a combination of these theories have been used in simulations of gas-solids flows by researchers. This thesis shows that these three theories in determining the gas-solid interphase momentum transfer may lead to very different results. The equation proposed by Wen and Yu gives the best results in simulations of fluidized beds. An unresolved problem so-far, is that the scale on which the interphase momentum transfer equation is applied is much smaller than the scale on which the equation was determined by experimentalists. Possibly Lagrangian-Eulerian simulations with a very detailed gas-phase solution, or Lattice-Boltzmann simulations can resolve this in the near future and result in a more fundamental theory to describe gas-solid interphase momentum exchange.

7.5 Validation

Some researchers have described simulations of freely bubbling fluidized beds or a bubble injection into a fluidized bed, but hardly any researchers have properly validated the outcome of these types of simulations. This validation, when performed at all, mostly consists of qualitatively comparing photographic material with the simulation results. One of the major goals of this thesis is to rigorously validate the outcome of simulations of freely bubbling fluidized beds, slugging fluidized beds, and bubble injection into fluidized beds. In this work the time-averaged properties, such as bed expansion and bubble behavior, and the dynamic properties, such as the frequency behavior of voidage and pressure fluctuations, and the unpredictability of the behavior quantified by the Kolmogorov entropy of the fluidized bed, are validated by comparison with experimental data and correlations from the literature. Two-dimensional CFD simulations of gas-solid fluidized beds described in this thesis predict the time-averaged and dynamic behavior of fluidized beds fairly well. Quantities as bubble size, bubble rise velocity, dominant frequency of the pressure fluctuations at a point in the fluidized bed, and the Kolmogorov entropy are in good agreement with existing theory, measurements and empirical correlations. This work shows that dense gas-solid CFD models are capable of giving a good prediction of the actual flow patterns in fluidized

beds, and are a very valuable tool, not only in the validation of existing empirical correlations, but also in the improvement of existing correlations, the determination of new correlations, and in the calculation of specific physical properties of a certain configuration.

7.6 Granular theory for a bimodal particle mixture

This thesis also presents the derivation of the kinetic theory of granular flow for a bimodal particle mixture. With this theory, the behavior of a fluidized bed containing two spherical particle species with different densities and/or diameters can be predicted. This theory also predicts the diffusion velocity of one species relative to the other species and can thus predict segregation. From the basis of this theory, the driving physics behind segregation can be divided into three main causes: gradients in granular temperature, gradients in the "chemical" potential, and the difference in external force between the two particle species. The results of simulations described in this work of fluidized beds containing a bimodal particle size distribution show the correct trends, as an increased bed expansion and the possibility of inversion, compared to experiments described in the literature. However, the computational effort for this model is tremendous. Hence, it is still impossible to achieve simulations of a large enough time-scale to fully validate this bimodal theory.

7.7 Lagrangian-Eulerian fluidized bed simulations

Finally, this thesis presents Lagrangian-Eulerian simulations of gas-solid fluidized beds, and the results of the simulations are compared to experiments also described in this thesis. Lagrangian models have been put forward in the literature as powerful tools in predicting the small-scale behavior of particles. In the Lagrangian model, the locations and trajectories of each particle are tracked. The gas-phase is solved on a fairly coarse grid and the forces on the particles are calculated by interpolation of the grid points on which gas-phase solution is predicted. Hence, calculation of detailed flow of the gas phase is neglected, leading to some deviating results compared to experiments described in this work. Also, the translation from two-dimensional to three-dimensional simulations is a major problem. Some results, like the dynamics of the particle phase, however, are predicted fairly well when comparing to experiments. The Lagrangian-Eulerian model in this form seems less promising than claimed by some authors.

7.8 Conclusion

The overall conclusion of this thesis is that gas-solid CFD models for fluidized beds are capable of capturing all important physics and give a good prediction of the hydrodynamic behavior of fluidized beds. In the near future, this model can be used to improve or derive empirical correlations capturing the behavior of fluidized beds, like bubble behavior or bed expansion, or can be directly used to scale-up gas-solid fluidized beds.

7.9 Two- versus three-dimensions

To obtain even better predictions of fluidized beds, preferably three-dimensional simulations should be performed instead of two-dimensional. Currently, there are two bottlenecks in performing three-dimensional simulations. First, the required computational effort is very large. With the current growth of computational power, however, it is expected that this problem will be overcome within a few years. Secondly, it is fundamentally more difficult to invert a three-dimensional discretization matrix than a two-dimensional one. However, mathematicians have achieved major improvements on the solving algorithms for sparse three-dimensional matrices and also this problem will be surely overcome within the next few years. Therefore, the current trend in multiphase flow to perform two-dimensional simulations will shift to performing three-dimensional simulations.

7.10 Outlook

With increasing computational power, Lagrangian-Eulerian simulations can solve the gas phase on a scale much finer than the particle size, so that no empiric equations are necessary in describing the gas-solid interphase momentum transfer and the gas can easily move around every individual particle or cluster. This simulation technique will then provide a very powerful tool in predicting the gas and solids flow behavior in specific areas of the gas-solid flow apparatus, or predict the correct gas-solid interphase momentum transfer on the scale required by the Eulerian-Eulerian models, hence functioning as an "input" model. The Lagrangian-Eulerian technique can emerge to become a very promising technique in describing gas-particle flows on a very small scale.

On the long term, much effort will be devoted to studying simulation techniques capable of describing non-spherical, non-elastic, deformable multi-component particle mixtures. In the Lagrangian-Eulerian method this requires an order of magnitude increase in computational power and a difficult

extension of the granular dynamics algorithm. In the Eulerian-Eulerian technique this will require a fundamental difference in the derivation of both the governing equations and closure models.

Appendix A

The software manual

This chapter describes the software present on the CD belonging with this thesis.

A.1 PartGas: Lagrangian code with Eulerian coupling

A.1.1 Introduction

PartGas is a two-dimensional computer code to calculate the individual trajectories of particles in (disks) in a two-dimensional confined space. In the same space, it is possible to solve a continuous fluid, applying two-way coupled drag interactions with the particle phase. The theory behind this code is described in Chapter **6** of the thesis.

First, the structure of the solving method is presented. Then, the structure of the software is presented. Finally, it is shown how to enter the physical parameters and run the code.

A.1.2 Structure of the solving method

The problem space is divided up into a number of particle cells. The particles in the problem space are all located inside these particle cells. When the smallest collision time (see Chapter 6) needs to be calculated, the location and velocities of particles in a specific particle-cell are only compared with particles in the same particle cell or neighbouring particle cells, see Figure A.1 and Chapter **6** of the thesis. The gas phase is solved on Eulerian cells.

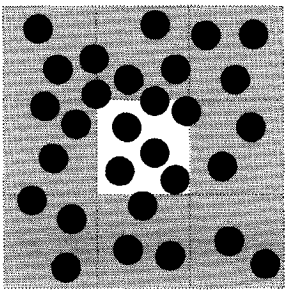

Figure A.1: *A three by three particle mesh. The shortest calculation times of the particles in the center cell are calculated by comparing the location and velocity of the particles in the white center cell with all the particles in the nine particle cells. For the calculation times in the next particle cell, comparing the particles in that cell with the particles in the white cell is no longer necessary.*

The coupling of the gas-phase variables to each individual particle is done by means of surface averaging, see Figure A.2.

In the computer code, one or more particle cells must fit into one Eulerian cell!

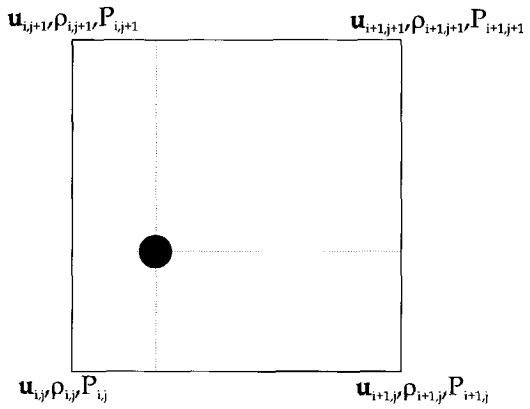

Figure A.2: *The principle of surface weighted averaging. The gas-phase properties are given in the corners of the gas-phase cell by the gas-phase solution and are averaged to the center of the particle (denoted by the black dot) by using the overlying areas as weighting factors.*

This is a very important restriction. In practical situations, however, this restriction is not a limiting one. Figure A.3 shows an example configuration.

A.1.3 Structure of the code

All the software has been developed in C++. The most important classes (In C++ a class is a specific collection of variables and functions) in the software are:

- `GasPhase` contains the staggered variables (velocities) and the non-staggered variables (pressure and density) of the gas phase. Furthermore, this class contains all the procedures to calculate an update of the gas phase, including the SIMPLE pressure correction iteration, solving the momentum equations, and calculating the coefficients of the descritization method. In this specific code, only a UPWIND and CENTRAL scheme are available. The time can be descretized with Cranck-Nicholson or first order.

- `ParticleCell` contains the particle cells and a linked list to the particles belonging into the cell. `ParticleCell` also contains pointers to all neighbouring particle cells. `ParticleCell` does not contain any procedures.

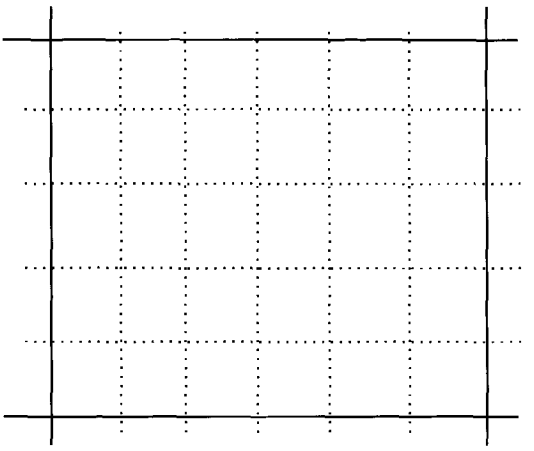

Figure A.3: *One Eulerian cell (continuous line) contains six by five particle cells (dashed lines).*

- `Eulerian` contains pointers to the particle cells belonging in the specific Eulerian cell. The class `Eulerian` also contains functions to calculate the forces on the particles from the gas phase and vice-versa. `Eulerian` does not contain any pointer to the particles; particles must be allocated through the pointers to the particle cells.

- `Particles` is the main class of the particle phase. It contains the array with the particles, functions to place and move the particles, and performs the input/output of the particle information through the classes `OUTput` and `INput`.

- `Particle` is a very small class containing the diameter, velocity, and rotation of each particle.

The file `code.cpp` is the main program that glues the gas-phase and the particle-phase together. This is done by calling C-like functions from the file `cfunc.cpp`. Due to the organized structure of C++ the code is easily readable.

A.1.4 Running the code

The files in the directory `PartGas` can be read on most MS-DOS and UNIX based computers and contains the C++ header files, denoted by `*.hpp`, the C++ program files, denoted by `*.cpp`, a `Makefile`, the inputfile `infile`, and two MatLab, denoted by `*.m`, files for post-processing.

A.1.5 Makefile

First, edit the `Makefile` for your specific computer. An example of the `Makefile` is shown in Program A.1 The `CFLAGS` variable contains the achieved optimization of the compiler. `-g -G` denotes the code will be suitable for debugging and profiling. `O2` and `O4` are specific optimizations. Please refer to the manual of your C++ compiler. The `CC` variable contains the name of the C++ compiler. In the case of the GNU compiler this will be g++, wheras this above example is suitable for HP-UX. The rest of the makefile contains the rules for compiling the executable partgas and the dependencies.

A.1.6 info.hpp

The file `info.hpp` contains the neccesary physical parameters and particle-phase properties, and the debug and geometry information. An example of the file `info.hpp` is given in Programs A.2 and A.3. The file `info.hpp` contains 10 different sections:

1. The geometry of the system. In this section the total number of particle cells is specified, as well as the number of particlecells in one Eulerian cell. Also, the X and Y dimensions of the system are given in m.

2. The particle properties. The amount of particles, the initial perturbation velocity (granular temperature), the particle density (in $\mathrm{kg\ m^{-3}}$), the particle diameter (m), and the particle-particle and particle-wall restitution and friction coefficients are specified.

3. The timestep of the system. Please note that this MUST be the same timestep as specified in the gas phase.

4. The gas constants are specified which again need to equal the gas constants in the gas-phase solver.

5. The gravity acceleration. This way the gravity can also be put under a specific angle.

6. The input/output and restart options can be specified. Also how often the intermediate results are written to disk is specified here.

7. The NULL pointer. In most compilers (in all of the ones I know) this should be a zero.

8. The debug options. This might be an important section if you want to add/alter/improve the code. Debug options include to verify the energy conservation during particle/particle collisions, to verify that particles do not overlap and input/output options to ensure correct working of the code. Options with a C++ comment symbol, are turned OFF.

Program A.1 *The* `Makefile` *for the* `PartGas` *executable.*

```
# .SUFFIXES: .hpp .cpp

CFLAGS=+04
# CFLAGS=-g -G
#  CFLAGS=+02

CC=aCC
LIBS=-lm
OBJECTS = partlist.o particb.o particle.o general.o
          cfunc.o io.o Cell.o parser.o energy.o
HFILES =  particb.hpp particle.hpp partlist.hpp general.hpp
          types.hpp cfunc.hpp info.hpp parser.hpp Cell.hpp
          info.hpp

# generic rule (van .C -> .o)
.cpp.o:
$(CC) -c $(CFLAGS) $<

### Executables creeren :
partgas:         $(OBJECTS) code.o $(OBJS2) Makefile
$(CC) $(CFLAGS) -o $@ code.o $(OBJECTS) $(OBJS2) $(LIBS)

#### dependencies:
code.o: code.cpp $(HFILES) Makefile
particb.o:              particb.cpp $(HFILES) Makefile
io.o:                   io.cpp io.hpp types.hpp Makefile info.hpp
particle.o:             particle.cpp $(HFILES) Makefile
part.o:                 part.cpp $(HFILES) Makefile
partlist.o:             partlist.cpp $(HFILES) Makefile
general.o:              general.cpp $(HFILES) Makefile
cfunc.o:                cfunc.cpp $(HFILES) Makefile
Cell.o: Cell.cpp $(HFILES) Makefile
parser.o: parser.cpp $(HFILES) Makefile
energy.o: energy.cpp $(HFILES) Makefile
```

Program A.2 *The file* `info.hpp` *in which the partilce-phase and debug options are given. Part 1 of 2.*

```
#include <math.h>
#ifndef INFO_
#define INFO_
//
// 1. Geometry of the system:
//
#define XBOX 36  // Amount of particle cells in X-direction
#define YBOX 88  // Amount of particle cells in Y-direction
#define EULERX 4 // Amount of particlecells in ONE EULERCELL in X-direction
#define EULERY 4 // Amount of particlecells in ONE EULERCELL in Y-direction
#define XSIZ  0.08975     // total geometry size in X-direction
#define YSIZ  0.219388888    // total geometry size in Y-direction

//
// 2. Particle properties :
//
#define NPART 3110      // amount of particles
#define NBEADS_ 0       // void
#define PERTUBVELOC 0.05 // amount of fluctuating initial velocity
#define MASS  1150    // particle density
#define DIAM  0.001545 // particle diameter
#define COR   0.95      // coefficient of restitution of particle/particle
#define CORW  0.95       // coefficient of restitution of particle/wall
#define FC    0.15      // friction coefficient of particle/particle
#define FCW   0.1       // friction coefficient of particle/wall
#ifndef PI
#define PI 3.141592654  // PI
#endif
#ifndef M_PI
#define M_PI 3.141592654
#endif

#define ALIGNPLACE_          // place particle neatly instead of random

// 3. Timestep of the system. PLEASE note that this timestep
//    MUST equal the timestep specified in the gas phase file infile
//

#define TS_    1.0E-4       // Timestep

//
// 4. Gas constants :
//
#define TEMP  293.0         // temperature of gas
#define MG    28.8E-03      // molecular weight of gas
#define MUG   18.0E-06      // gas viscosity.
#define R     8.3143        // gas constant.
.. continued ..
```

Program A.3 *The file* `info.hpp` *in which the partilce-phase and debug options are given. Part 2 of 2.*

```
//
// 5. Gravity
//
#define gravityy 9.810
#define gravityx 0.00
//
// 6. Input/Output specifications
//
#define RESTART 1 // Restart from previous run?
// #define RESTART_VELOCITY_ZERO_     // Put velocities on zero restart
#define TIMERESTART_ 0.891       // Restart at which time
#define FNAME "visc.dta" // Filename for OUTput
#define FN2 "energy.dta" // Filename for Energyoutput
#define FN3 "shear.dta"          // Filename for detailed shear info
#define WEGSCHRIJF 10            // Write data to disk each XX timesteps
#define IFNAME "inzak.dta" // Filename for INput (only when RESTART=1)

//
// 7. NULL-pointer
//
#define NULL 0

// 8. Debug options
//
// #define DEBUG_ENERGY_  // verify enery consevation during collisions
// #define DEBUG_COL_ONSCREEN_ // place particle velocities on screen
                               // before and after each collision
// #define CHECK_OVERLAP_       // Check overlap of particles
// #define OUTPUT_DATA_TO_SCREEN_   // write particle data of 1 cell to
                                    // screen each timestep.
// #define DEBUG_DIMENSION_          // Check dimensions of cells
// #define DEBUG_CELL_               // Write all information about cells to
                                    // screen.
#define  COLL_LOW_VELOC_CORRECT_    // Correct C.O.R. for very low veloc.
#define DIAGONAL_                  // ALWAYS LEAVE ON!

//
// 9. Gas-Coupling options
//
// #define DECOUPLEGAS_ // Leave Gas Pase OUT if uncommented

//
// 10. Periodic boundary conditions
//

// #define PERIODIC_UP_DOWN_ // periodically couple up/down walls
#define STRESSCALC_ // calculate particle stresses in geometry
// #define LEFTVELOC_ -1.0              // VOID
// #define RIGHTVELOC_ 1.0              // VOID
#endif
```

9. Gas coupling. If this option is turned on, NO gas phase information is calculated and the particle paths are updated as if they move in vacuum.
10. Periodic boundaries. Here the upper and lower geometry can be specified as a periodic boundary for the particles.

> It is important to realize that the code `PartGas` must be recompiled every time you change `info.hpp` and you want the changes to affect the simulation.

A.1.7 `infile`

Program A.4 *An example of the file `infile` containing the properties of the gas-phase solver*

```
# inputfile for gas-phase solver
#
# (c) Berend van Wachem, 1998, 1999, 2000

# timestep : <amount of variations> <timestep size #1> <timestep amount #1> etc.
timestep: 3 5.0e-4 10 2.0e-4 10 1.0e-4 100000

inletvelocity: 0.80
viscosity: 1.8e-5
Xwidth: 0.08975
Yheight: 0.21938888
Xcells: 9
Ycells: 22
Unauwkeurig: 1.0e-12
Vnauwkeurig: 1.0e-11
Pnauwkeurig: 1.0e-8

#masssource <waarde> (relatieve massa verlies toelaatbaar)
masssource: 1.0e-6

#maxiter <waarde> (maximaal aantal toelaatbare iteraties)
maxiter: 50

# beginwaardes:
vstart: 0.28
ustart: 0.0
pstart: 0.0
epsstart: 1.0

# gaswaarde :
molmas: 28.8e-3
pomgeving: 1.013e+5
```

The file `infile` contains the input parameters regarding the gas-phase solver. The line specifying the timesteps contains 3 types of timesteps: the

first two timesteps and the number of timesteps are carried out without any particles present. The last timestep is the actual timestep of the gas-phase solver coupled with the particle-phase solver. This timestep MUST equal the timestep specified in `info.hpp`. Also, the sizes of `Xwidth`, `Ywidth` must equal the actual domainsize specified in `info.hpp`. The numbers behind `Xcells` and `Ycells` denote the number of Eulerian cells in the X and Y directions. `Xcells` must equal $\frac{XBOX}{EULERX}$, and the same for the Y direction. The rest of the file is fairly straightforward, and contains information regarding the gas velocity at the inlet, the physical parameters of the gas, the accuracy and maximal effort of the solver, and the initial conditions.

> Be sure to check that the information you specify in `infile` regarding the geometry size, the amount of Eulerian cells, and the gas-phase properties equal the ones stated in `info.hpp`!

A.1.8 Output

The program `PartGas` creates three outputfiles, `visc.dta`, `shear.dta`, and `energy.dta`. The first file contains the information regarding the particle locations, velocities, rotations, average particle volume fraction, and the local gas phase pressure. The file `shear.dta` contains the data of the particle shear tensor split up in two by two directions, and in the effects of particle-particle collisions and particle streaming. The file `energy.dta` contains the information regarding the energy of the particles. This file is now obsolete due to the functionality of `visc.dta`.

Two MatLab files are supplied with this package:

- `particle.m` plots the location of every particle in the geometry and shows the Eulerian mesh in the same figure. A second figure shows the local pressure field, and a third figure shows the local solids volume fraction field.
- `shear.m` shows the local kinetic and collisional stress in the two dominant directions.

Both files are short and are easily to extend to specific output wishes.

A.2 Eulerian-Eulerian gas-solid codes

The Eulerian-Eulerian codes described in this section need the commercial softwarepackage CFX 4.x to run!

A.2.1 Introduction

Multiple Eulerian-Eulerian gas-solid codes are available with this thesis. The first code describes the gas-solid flow with the equilibrium assumption for the granular energy, as discussed in thesis chapter 3. This software is located in the directory `equilib`. The gas-solid code which solves the full granular energy equation is located in the directory `fullgran`. Finally, the code that described the gas-solid flow with a bimodal particle distribution is located in the directory `bimodal`.

Next to the FORTRAN files required for CFX, the codes also contains a MatLab file for post-processing and a C++ file for mesh generation.

A.2.2 FORTRAN and CFX

CFX is a commercial flow solver (finite volume solver) in which there is a large amount of freedom to change physical models, properties of flow, or to introduce a complete new flow-type. Within CFX, different file types exist:

1. The command file, or `*.fc` file. This file is fairly self-explanatory. In this file, the outline of the problem is specified. For instance, how much memory the total run wil use, how much additional variables are needed, which FORTRAN files should be incorporated, the size of the timestep and the number of timesteps, and the simple physics of the problem, as the gas-density, the temperature and pressure. It is also possible to specify output options in the command file. With the FORTRAN file `USRINT.F` this option is obsolete.

2. The grid file, or `*.geo` file. This file contains the specifics regarding the mesh. It can either be made with CFX-BUILD or with the file `meshgen.cc` added with these packages.

3. The FORTRAN files, or `*.F` files. In these files the variables within CFX can be changed. These FORTRAN files will be called every iteration and directly interact with the numerics in CFX. This way, all the different variables and equations can be monitored and/or altered.

To run CFX, the CFX executable (runf3d) needs to be called with the appropriate options. Examples of how to call CFX are given in the files parrun and parrund.

> You do NOT have to compile the FORTRAN files yourself; If you specify the FORTRAN files to CFX apropriately, CFX will compile the files for you

A.2.3 equilib

The equilibrium code in the directory equilib contains the files:

1. m01.fc This is the CFX command file for a "startup-from-scratch" run (no restart). You can change some of the physical properties in this code, but you also need to change these in the FORTRAN file. Be sure to set the correct timestep and the correct amount of timesteps on line 85.

2. m01.f This is the CFX FORTRAN file for a no-restart run. The physical properties you can change are:

   - Particle diameter (DP). Change the code on lines: 494, 1364, and 1773
   - Particle restitution coefficient (EEE). Change the code on lines: 1358 and 1767
   - Maximum particle volume fraction (FRMAX). Change the code on lines: 1352 and 1764
   - Angle of internal friction (FI). Change the code on line: 1368
   - Minimum fluidization velocity (VFLOWMIN). Change the code on lines: 204 and 2176
   - Actual fluidization velocity (VFLOW). Change the code on line: 2177
   - Location of the initial jet to break symmetry (JSTART and JEND). Change the code on lines: 2172 and 2173
   - Initial gas volume fraction in bottom of the bed (VFG0). Change the code on line: 200
   - Initial fraction of the filling height of the fluidized bed (VULH). Change the code on line: 218

> If you cange partice properties please do so in the command file and on all places in the FORTRAN file.

3. `m02.fc` This is the CFX command file for a restart run, continuing from a previous run. You can change some of the physical properties in this code, but you also need to change these in the FORTRAN file. Be sure to set the correct timestep and the correct amount of timesteps on line 86.

4. `m01.f` This is the CFX FORTRAN file for a restart run. The physical properties you can change are:

   - Particle diameter (DP). Change the code on lines: 219, 1089, and 1498
   - Particle restitution coefficient (EEE). Change the code on lines: 966, 1083 and 1492
   - Maximum particle volume fraction (FRMAX). Change the code on lines: 1077 and 1489
   - Angle of internal friction (FI). Change the code on line: 1093
   - Minimum fluidization velocity (VFLOWMIN). Change the code on line: 1905
   - Actual fluidization velocity (VFLOW). Change the code on line: 1906

5. `m01.geo` This is the file containing the geometry information for the run. This file can be created with the CFX package CFX BUILD or with a C++ file explained later.

6. `usrtrn.f` and `bubble.f`. These FORTRAN files are for creating individual timeseries of variables and to track the bubbles formed in the simulation. They may be omitted.

7. `parrun` The scriptfile for an initial run. This file contains only a few lines and calls CFX with the neccesary command and fortran files. Be sure to specify an appropriate temporary directory.

8. `parrund` The scriptfile for a restart run. This file contains only a few lines and calls CFX with the neccesary command and fortran files. Be sure to specify an appropriate temporary directory and a restart file.

A.2.4 fullgran

This directory contains the code to simulate a gas-solid flow with solving the full granular energy equation. The structure of this code is slightly different as the previous code, because the FORTRAN files are not grouped in `m0x.f`, as in the previous code, but are stand-alone. The files contained in the directory

- `USRBCS.F` This is the file in which the initial boundary conditions are specified; with small jet to perturb the symmetry of the system.

- USR2BCS.F This is the file in which the boundary conditions in case of a restart are specified; witout any perturbing jet.
- USRINT.F This is the file in which the initial conditions are specified; how high the bed is filled and at which solids volume fraction.
- USRSRC.F In this file the neccesary source terms on the momentum equations and on the granular energy balance are added.
- USRVIS.F In this file the solids phase viscosity is calculated.
- USRBF.F In this file the gravity is added to the solids and gas phase momentum balaces.
- USRDIF.F This file contains the calculations for the conductivity of fluctuating energy.
- USRIPT.F This file contains the interphase momentum tranfer between the gas and the solids phase as described by Wen and Yu (1966). Two additional models can be used instead of this file, namely USRIPT-ERGUN.F is the Gidaspow (1994) drag model, and USRIPT-SYAMLAL.F describes the Syamlal et al. (1993) drag model.
- USRCVG.F controls the convergence criteria.
- GNULL.F contains the radial distribution function.
- PACK.F calculates the neccesary frictional stress, as described in the thesis.
- parrun is the scriptfile to run an initial problem. Specify the correct temporary directory.
- parrund is the scriptfile to run a restart problem. Specify the correct temporary directory.

Please refer to the CFX 4.x user manual for details on the FORTRAN programming and the variable names

The physical properties you can change are:

- Particle diameter (DP). Change line 239 in USRDIF.F, line 273 in USRSRC.F, line 234 in USRVIS.F, and line 248 in USRIPT.F.
- Particle restitution coefficient (COR). Change line 237 in USRDIF.F, line 275 in USRSRC.F, and line 232 in USRVIS.F

- Maximum particle volume fraction (MX or MAXFRAC or VFMAX). Change line 268 in USR2BCS.F, line 274 in USRBCS.F, line 5 in PACK.F, and line 5 in GNULL.F.
- Minimum fluidization velocity (VFLOWMIN). Change line 264 in USR2BCS.F, line 270 in USRBCS.F, and line 256 in USRINT.F.
- Actual fluidization velocity (VFLOW). Change line 265 in USR2BCS.F and line 272 in USRBCS.F.
- Particle-wall coefficient of restitution (CORW). Change line 266 in USR2BCS.F and line 272 in USRBCS.F.
- Specularity coefficient (SPEC). Change line 269 in USR2BCS.F and line 275 in USRBCS.F.
- Mean free path restriction length (R). Change line 241 in USRDIF.F, line 276 in USRSRC.F, and line 235 in USRVIS.F.
- Amount of gas volume fraction in dense fluidized bed (VFGO). Change line 252 in USRINT.F.
- Fraction of filling height (VULH). Change line 269 in USRINT.F.

A.2.5 bimodal

The directory bimodal contains all the neccesary files to perform simulations of fluidized beds containing a bimodal particle distribution. The physics and equations are described in Chapter 6 of the thesis. The structure of the code is very similar with the previous code, full. The only important difference is, that it is much more easy to change the particle properties. This can be done in the file called PARTSPEC.F, shown in Figure A.5. The file is reasonable self-explanatory; DP is the particle diameter, RHO is the particle density, COR is the coefficient of restitution, and TMAX is the maximum solids volume fraction. The number between the brackets indicates the specie number. This is the only place where particle properties need to be changed.

The gas phase properties need to be changed in multiple places:

1. The time steps and the number of timesteps in the files m01.fc and m02.fc.
2. The miminum fluidization velocity (VFLOWMIN) in USRBCS.F on line 299, in USR2BCS.F on line 292, and in USRINT.F on line 279.
3. The fluidization velocity (VFLOW) in USRBCS.F on line 300, and in USR2BCS.F on line 293.

Program A.5 The file PARTSPEC.F in which the physical properties of the particles are specified.

```
SUBROUTINE PARTINFO

COMMON /PARTSPEC/DP,RHO,PI,VP,QM,COR,SR,TMAX
       DOUBLE PRECISION DP(2),RHO(2),PI,VP(2),QM(2),COR
       DOUBLE PRECISION SR(2),TMAX

      DP(1) = 500.0D-6
      DP(2) = 200.0D-6
      RHO(1) = 2640.0D0
      RHO(2) = 2640.0D0
      PI=3.141592D0
      VP(1)=PI*(DP(1)**3)/6.0D0
      VP(2)=PI*(DP(2)**3)/6.0D0
      QM(1)=RHO(1)*VP(1)
      QM(2)=RHO(2)*VP(2)
      COR=0.90D0
      SR(1)=0.5D0*DP(1)
      SR(2)=0.5D0*DP(2)
      TMAX=0.65D0

      END
```

The file `chemk.cc` is a C++ file which calculates the chemical potential needed to predict the behavior of a granular mixture of two species. CFX will NOT compile C++ files. You need to compile this file with your own C++ compiler and link the resulting object (`*.o`) file within CFX. Be sure to specify the correct optimization options when compiling. An example of this is shown in the `parrun` script.

For the initial condition, lines 267 through 275 are shown in Program A.6. The variable `ONDT1` defined on line 270 specifies the fraction of species A : species B. For example, if `ONDT1=QM(2)/QM(1)` as in the current example, the mass fraction of species A is equal to that of specie B. The overall solids volume fraction is specified in last line shown in Program A.6. The relative filling height (`VULH`) is specified in `USRINT.F` on line 292.

Program A.6 *Lines 267 through 275 of `USRINT.F` indicating the initial conditions of species A and B.*

```
C
C       ONDT1 = mass fraction of species 1. So X*QM(2)/QM(1)
C               then mass1:mass2 are 1:X
C
        ONDT1=1.0D0*QM(2)/QM(1)
        ONDT2=VP(1)*ONDT1+VP(2)

        PRINT *,'ONDT1,ONDT2',ONDT1,ONDT2

        VFGO=0.48D0
```

Caution! It is very difficult to obtain a well converged solution with the full bimodal kinetic theory. Very small timesteps ($\approx 10^{-5}$) are advised.

A.2.6 Pre- and Postprocessing

In all three packages, the C++ file `meshgen.cc` is included. With this file you can make uniform meshes very easy. To specify the size of the geometry and the amount of meshcells, edit lines 3 through 6 of the file `meshgen.cc`, as shown in Program A.7. The variables `XWID` and `YLEN` indicate the size of the geometry in meters in the X and Y direction, respectively. The variables `NI` and `NJ` are the amount of meshcells in the X and Y direction respectively.

Postprocessing is done in MatLab with the file `cfdtijd.m`. This file can read

Program A.7 *Lines 3 through 6 of the file* `meshgen.cc`

```
#define NI 400
#define NJ 20
#define XWID 1.00
#define YLEN 0.10
```

any variable have specified in the file `USRTRN.F` during the execution of CFX. You can also specify in `USRTRN.F` how often the solution is written to disk.

A.3 Animations of simulations

This section described some AVI animations of simulations performed for this work. The animations van be found in the directory Movies. This directory contains four directories with movies:

- Euler This directory contains animations of simulations freely bubbling or slugging fluidized beds. The specifications regarding the superficial gas velocity and the particle properties can be found in the file index.dat.
- Inject This directory contains animations of simulations of a gas jet penetrating into a minimum fluidized bed. The specifications regarding the jet velocity and the particle properties van be found in the file index.dat.
- Lagrangian This directory contains animations of simulations of the Lagrangian-Eulerian model. Particle and gas properties are given in the file index.dat. Also, video animations of the actual experiment are present.
- Shearing This directory contains some animations of particles subject to an external shear or compression. These are animations of current work, and have not been published yet.

Bibliography

Alder, B.J. and Wainwright, T.E. (1960). Studies in molecular dynamics. II. behaviour of a small number of elastic spheres. *J. Chem. Phys.*, 33:1439–1451.

Allen, M.P. and Tildesley, D.J. (1980). *Computer Simulation of Liquids*. Oxford University Press, Oxford.

Anderson, J.D. (1995). *Computational Fluid Dynamics: The basics with applications*. Mechanical Engineering Series. McGraw-Hill, New York.

Anderson, T.B. and Jackson, R. (1967). A fluid mechanical description of fluidized beds. *Ind. Engng. Chem. Fundam.*, 6(4):527–539.

Arnarson, B.O. and Willits, J.T. (1998). Thermal diffusion in binary mixtures of smooth, nearly elastic spheres with and without gravity. *Phys. Fluids*, 10:1324–1328.

Balzer, G. and Simonin, O. (1993). Extention of eulerian gas-solid flow modelling to dense fluidized bed. In Viollet, P.L., editor, *Proc. 5th Int. Symp. on Refined Flow Modelling and Turbulence Measurements*, pages 417–424. Paris.

Balzer, G. and Simonin, O. (1996). Private Communication.

Barthod, D., Pozo, M. Del, and Mirgain, C. (1999). CFD-aided design improves FCC performance. *Oil & Gas J.*, Apr. 5:66–69.

Baskakov, A.P., Tuponogov, V.G., and Filippovsky, N.F. (1986). A study of pressure fluctuations in a bubbling fluidized bed. *Powder Technol.*, 45:113–117.

Bird, R.B., Stewart, W.E., and Lightfoot, E.N. (1960). *Transport Phenomena*. John Wiley & Sons, USA.

Boemer, A., Qi, H., and Renz, U. (1997). Eulerian simulation of bubble formation at a jet in a two dimensional fluidized bed. *Int. J. Multiphase Flow*, 23:927–944.

Boemer, A., Qi, H., Renz, U., Vasquez, S., and Boysan, F. (1995). Eulerian computation of fluidized bed hydrodynamics - a comparison of physical models. In *Proceedings of the 13th Int. Conf on FBC*, pages 775–786, Orlando, USA.

Carnahan, N.F. and Starling, K.E. (1969). Equations of state for non-attracting rigid spheres. *J. Chem. Phys.*, 51:635–636.

Chapman, S. and Cowling, T.G. (1970). *The Mathematical Theory of Non-Uniform Gases.* Cambridge University Press, 3d edition.

Coulomb, C.A. (1776). Essai sur une application des règles de maximis et minimis à quelques problèmes de statique, relatifs à l'architecture. *Acad. R. Sci. Mém. Math, Phys. par Divers Savants*, 7:343–382.

Dalla Valle, J.M. (1948). *Micromeritics.* Pitman, London.

Darton, R.C., LaNauze, R.D., Davidson, J.F., and Harrison, D. (1977). Bubble growth due to coalescence in fluidised beds. *Trans IChemE*, 55:274–280.

Davidson, J.F. and Harrison, D. (1963). *Fluidized Particles.* Cambridge Univ. Press.

Daw, C.S. and Halow, J.S. (1991). Characterization of voidage and pressure signals from fluidized beds using deterministic chaos theory. In Anthony, E.J., editor, *Proceedings of the 11th International Conference on Fluidized Bed Combustion*, pages 777–786. ASME.

Ding, J. and Gidaspow, D. (1990). A bubbling fluidization model using theory of granular flow. *AIChE J.*, 36(4):523–538.

Ding, J. and Tam, S.W. (1994). Asymptotic power spectrum analysis of chaotic behaviour in fluidized beds. *Int. J. Bifurcation and Chaos*, 4(2):327–341.

Enwald, H., Peirano, E., and Almstedt, A.E. (1996). Eulerian two-phase flow theory applied to fluidization. *Int. J. Multiphase Flow*, 22:21–66.

Ergun, S. (1952). Fluid flow through packed columns. *Chem. Engng Prog.*, 48:89–94.

Ferschneider, G. and Mege, P. (1996). Eulerian simulation of dense phase fluidized beds. *Revue de l'I.F.P.*, 51(2).

Garside, J. and Al-Dibouini, M.R. (1977). Velocity-voidage relationship for fluidization and sedimentation. *I&EC Proc. Des. Dev.*, 16:206–214.

Garside, J. and Al-Dibouni, M.R. (1977). Velocity-voidage relationship for fluidization and sedimentation. *I&EC Proc. Des. Dev.*, 16:206–214.

Gaspard, P. and Wang, X.J. (1993). Noise, chaos, and (ϵ, τ)-entropy per unit time. *Physics Reports*, 235:291–343.

Geldart, D. (1973). Types of gas fluidization. *Powder Technol.*, 7:285.

Gidaspow, D. (1994). *Multiphase Flow and Fluidization*. Academic Press, San Diego, first edition.

Gidaspow, D., Bezburuah, R., and Ding, J. (1992). Hydrodynamics of circulating fluidized beds; kinetic theory approach. *Fluidization VII, Proceedings of the 7th Engineering Foundation Conference on Fluidization*, pages 75–82.

Glowinski, R., Pan, T.-W., Hesla, T.I., and Jospeh, D.D. (1999). A distributed lagrange multiplier/fictitious domain method for particulate flows. *Int. J. Multiphase Flow*, 25:755–794.

Grace, J.R. (1990). High-velocity fluidized bed reactors. *Chem. Eng. Sci.*, 45:1953–1966.

Grace, J.R. and Sun, G. (1991). Influence of particle size distribution on the performance of fluidized bed reactors. *Can. J. Chem. Eng.*, 69:1126–1134.

Grad, H. (1963). Asymptotic theory of the boltzmann equation. *Phys. Fluids*, 6.

Groot, J.H. De (1967). In Drinkenberg, A.H.H., editor, *Proc. Intern. Symp. Fluidization*, page 348. Netherlands University Press, Amsterdam.

Hilligardt, K. and Werther, J. (1986). Local bubble gas hold-up and expansion of gas/solid fluidized beds. *German Chem. Eng.*, 9:215–221.

Hirsch, C. (1988). *Numerical Computation of Internal and External Flows, Volume 1: Fundamentals of Numerical Discretization*. John Wiley and Sons Ltd., Chichester.

Hoomans, B.P.B., Kuipers, J.A.M., Briels, W.J., and van Swaaij, W.P.M. (1996). Discrete particle simulation of bubble and slug formation in a two-dimensional gas-fluidised bed: A hard-sphere approach. *Chem. Eng. Sci.*, 51(1):99–118.

Hrenya, C.M. and Sinclair, J.L. (1997). Effects of particle-phase turbulence in gas-solid flows. *AIChE J.*, 43:853–869.

Hsiau, S.S. and Hunt, M.L. (1996). Granular thermal diffusion in flows of binary-sized mixtures. *Acta Mech.*, 114:121–137.

Hu, H.H. (1996). Direct simulation of flows of solid-liquid mixtures. *Int. J. Multiphase Flow*, 22(2):335–352.

Ishii, M. (1975). *Thermo-Fluid dynamic theory of Two-Phase Flow*. Direction des Etudes et Recherches d'Electricité de France. Eyrolles, Paris, France.

Ishii, M. and Mishima, K. (1984). Two-fluid model and hydrodynamic constitutive relations. *Nuclear Eng. Des.*, 82:107–126.

Jackson, R. (1983). Some mathematical and physical aspects of continuum models for the motion of granular materials. In Meyer, R.E., editor, *Theory of Dispersed Multiphase Flow*, pages 291–338. Academic Press, USA.

Jackson, R. (1985). In Davidson, J.F., Clift, R., and Harrison, D., editors, *Fluidization*, page 47. Academic Press, New York, 2nd edition.

Jackson, R. (1997). Locally averaged equations of motion for a mixture of identical spherical particles and a newtonian fluid. *Chem. Eng. Sci.*, 52:2457–2469.

Jackson, R. (1998). Erratum. *Chem. Eng. Sci.*, 53:1955.

Jenkins, J.T. and Mancini, F. (1987). Balance laws and constitutive relations for plane flows of a dense, binary mixture of smooth, nearly elastic, circular disks. *J. App. Mech.*, 54:27–34.

Jenkins, J.T. and Mancini, F. (1989). Kinetic theory for binary mixtures of smooth, nearly elastic spheres. *Phys. Fluids A*, 1(12):2050–2057.

Jenkins, J.T. and Savage, S.B. (1983). A theory for the rapid flow of identical, smooth, nearly elastic, spherical particles. *J. Fluid Mech.*, 130:187–202.

Johnson, P.C. and Jackson, R. (1987). Frictional-collisional constitutive relations for granular materials, with application to plane shearing. *J. Fluid Mech.*, 176:67–93.

Johnson, P.C., Nott, P., and Jackson, R. (1990). Frictional-collisional equations of motion for particulate flows and their application to chutes. *J. Fluid Mech.*, 210:501–535.

Kehoe, P.W.K. and Davidson, J.F. (1971). Continuously slugging fluidised beds. *Inst. Chem. Eng. Symp. Ser.*, 33:97–116.

Kincaid, J.M., Cohen, E.G.D., and de Haro, M. Lopez (1987). The enskog theory for multicomponent mixtures. iv. thermal diffusion. *J. Chem. Phys.*, 86:963–975.

Koch, D.L. (1990). Kinetic theory for a monodisperse gas-solid suspension. *Phys. Fluids A*, 2:1711–1723.

Kuipers, J.A. (1990). *A Two-Fluid Micro Balance Model of Fluidized Beds.* PhD thesis, University of Twente, The Netherlands.

Kuipers, J.A.M., Prins, W., and van Swaaij, W.P.M. (1991). Theoretical and experimental bubble formation at a single orifice in a two-dimensional gas-fluidized bed. *Chem. Eng. Sci.*, 46(11):2881–2894.

Kunii, D. and Levenspiel, O. (1991). *Fluidization Engineering.* Butterworth-Heinenmann, second edition.

Lopez de Haro, M. and Cohen, E.G.D. (1984). The enskog theory for multicomponent mixtures. iii. transport properties of dense binary mixtures with one tracer component. *J. Chem. Phys.*, 80:408–415.

Lopez de Haro, M., Cohen, E.G.D., and Kincaid, J.M. (1983). The enskog theory for multicomponent mixtures. I. linear transport theory. *J. Chem. Phys.*, 78:2746–2759.

Louge, M.Y. (1994). Computer simulations of rapid granular flows of spheres interacting with a flat, frictional boundary. *Phys. Fluids*, 6:2253–2269.

Louge, M.Y., Mastorakos, E., and Jenkins, J.T. (1991). The role of particle collisions in pneumatic transport. *J. Fluid Mech.*, 231:345–359.

Lun, C.K.K. and Savage, S.B. (1986). The effects of an impact velocity dependent coefficient of restitution on stresses developed by sheared granular materials. *Acta Mechanica*, 63:15–44.

Lun, C.K.K., Savage, S.B., Jefferey, D.J., and Chepurniy, N. (1984). Kinetic theories for granular flow : inelastic particles in couette flow and slightly inelastic particles in a general flowfield. *J. Fluid Mech.*, 140:223–256.

Mansoori, G.A., Carnahan, N.F., Starling, K.E., and Leland, T.W.Jr (1971). Equilibrium thermodynamic properties of the mixture of hard spheres. *J. Chem. Phys.*, 54:1523–1525.

Maw, N., Barber, J.R., and Fawcett, J.N. (1976). The oblique impact of elastic spheres. *Wear*, 38:101–114.

Molerus, O. (1982). Interpretation of geldart's type a,b,c,d powders. *Powder Technol.*, 33:81–87.

Nadim, A. and Stone, H.A. (1991). The motion of small particles and droplets in quadratic flows. *Stud. Appl. Mech.*, 85:53–73.

Ocone, R., Sundaresan, S., and Jackson, R. (1993). Gas-particle flow in a duct of arbitrary inclination with particle-particle interactions. *AIChE J.*, 39:1261–1271.

Patankar, S.V. (1980). *Numerical Heat Transfer and Fluid Flow.* Hemisphere Publising Corporation.

Pirog, T.W. (1998). *Dynamics of destabilization of food emulsions. Measurement and simulation of gravity driven particle velocities in polydisperse dispersions.* PhD thesis, Purdue University.

Pritchett, J.W., Blake, T.R., and Garg, S.K. (1978). A numerical model of gas fluidized beds. *AIChE Symposium Series,* 74(176):134–148.

Pyle, D.L. and Harrison, D. (1967). *Chem. Eng. Sci.*, 22:531.

Reed, T.M. and Gubbins, K.E. (1973). *Applied Statistical Mechanics.* McGraw-Hill, New York.

Rhie, C.M. and Chow, W.L. (1983). Numerical study of the turbulent flow past an airfoil with trailing edge separation. *AIAA J1,* 21:1527–1532.

Richardson, J.F. and Zaki, W.N. (1954). Sedimentation and fluidisation: Part I. *Trans. Inst. Chem. Eng.*, 32:35–52.

Rowe, P.N. (1961). Drag forces in a hydraulic model of a fluidized bed, part II. *Trans Inst Chem. Engs.*, 39:175–180.

Roy, R., Davidson, J.F., and Tuponogov, V.G. (1990). The velocity of sound in fluidised beds. *Chem. Eng. Sci.*, 45(11):3233–3245.

Schaeffer, D.G. (1987). Instability in the evolution equations describing incompressible granular flow. *J. Differential Equations,* 66:19–50.

Schouten, J.C. and van den Bleek, C.M. (1992). Chaotic hydrodynamics of fluidization: Consequences for scaling and modeling of fluid bed reactors. *AIChE Symp. Ser.*, 289:780–784.

Schouten, J.C., van der Stappen, M.L.M., and van den Bleek, C.M. (1996). Scale-up of chaotic fluidized bed hydrodynamics. *Chem. Eng. Sci.*, 51:1991–2000.

Shauly, A., Wachs, A., and Nir, A. (1998). Shear-induced particle migration in a polydisperse concentrated suspension. *J. Rheol.*, 42:1329–1348.

Sinclair, J.L. and Jackson, R. (1989). Gas-particle flow in a vertical pipe with particle-particle interactions. *AIChE J.*, 35:1473.

Sokolichin, A., Eigenberger, G., Lapin, G., and Lübbert, A. (1997). Direct numerical simulation of gas-liquid two-phase flows. Euler/Euler versus Euler/Lagrange. *Chem. Eng. Sci.*, 52:611–626.

Sokolovski, V.V. (1965). *Statistics of Granular Media.* Pergamon Press.

Sundaresan, S. (1999). Private Communication.

Syamlal, M., Rogers, W., and O'Brien, T.J. (1993). Mfix documentation theory guide. *U.S. Dept of Energy, Office of Fossil Energy*, DOE/METC-94/1004(DE94000087). Technical note.

Tsuji, Y., Kawaguchi, T., and Tanaka, T. (1993). Discrete particle simulation of two-dimensional fluidized bed. *Powder Technology*, 77:79–87.

van den Bleek, C.M. and Schouten, J.C. (1993). Deterministic chaos: A new tool in fluidized bed design and operation. *Chem. Eng. J.*, 53:75–87.

van Der Schaaf, J., Schouten, J.C., and van den Bleek, C.M. (1998). Origin, propagation and attenuation of pressure waves in gas-solid fluidized beds. *Powder Technol.*, 95:220–233.

van Der Stappen, M.L.M. (1996). *Chaotic Hydrodynamics of Fluidized Beds*. PhD thesis, Delft University of Technology.

van Ommen, J.R., Schouten, J.C., vander Stappen, M.L.M., and van den Bleek, C.M (1999). Response characteristics of probe-transducer systems for pressure measurements in gas-solid fluidized beds: How to prevent pitfalls in dynamic pressure measurements. *Powder Technol.*, 106:199–218.

van Wachem, B.G.M., Bakker, A.F., Schouten, J.C., Heemels, M.W., and de Leeuw, S.W. (1997). Simulation of fluidized beds with lattice gas cellular automata. *J. Comp. Phys.*, 135:1–7.

van Wachem, B.G.M., Schouten, J.C., Krishna, R., and den Bleek, C.M. Van (1998). Eulerian simulations of bubbling behaviour in gas-solid fluidised beds. *Computers Chem. Engng*, 22:s299–s306.

van Wachem, B.G.M., Schouten, J.C., Krishna, R., and den Bleek, C.M. Van (1999). Validation of the Eulerian simulated dyanmic behaviour of gas-solid fluidised beds. *Chem. Eng. Sci.*, 54:2141–2149.

van Wachem, B.G.M., Schouten, J.C., Krishna, R., den Bleek, C.M. Van, and Sinclair, J.L. (2000). Comparative analysis of CFD models of dense gas-solid systems. *Submitted to AIChE Journal*.

Wen, C.Y. and Yu, Y.H. (1966). Mechanics of fluidization. *Chem. Eng. Progr. Symp. Ser.*, 62:100–111.

Werther, J. (1974). Bubbles in gas fluidised beds-part i. *Trans. Inst. Chem. Eng.*, 52:149–159.

Werther, J. and Molerus, O. (1973). The local structure of gas fluidized beds i. a statistically based measuring system. *Int. J. of Multiphase Flow*, 1:103–122.

Wolfram, S. (1988). *Mathematica*. Addison-Wesley Publishing Company, USA.

Wu, S.Y. and Baeyens, J. (1998). Segregation by size difference in gas fluidized beds. *Powder Technol.*, 98:139–150.

Xu, B.H. and Yu, A.B. (1997). Numerical simulation of the gas-solid flow in a fluidized bed by combining discrete particle method with computational fluid dynamics. *Chem. Eng. Sci.*, 52(16):2785–2809.

Yates, J.G. (1996). Effects of temperature and pressure on gas-solid fluidization. *Chem. Eng. Sci.*, 51(2):167–205.

Zamankhan, P. (1995). Kinetic theory of multicomponent dense mixtures of slightly inelastic spherical particles. *Phys. Rev. E*, 52:4877–4891.

Zamankhan, P. (1997). Comment and authors' reply on "granular thermal diffusion in flows of binary-sized mixtures". *Acta Mech.*, 123:235–237.

Zhang, D.Z. and Prosperetti, A. (1994). Averaged equations for inviscid disperse two-phase flow. *J. Fluid Mech.*, 267:185–219.

Zhang, D.Z. and Rauenzahn, R.M. (1997). A viscoelastic model for dense granular flows. *J. Rheol.*, 41:1275–1298.

Nawoord/ Epilogue

Naast mijzelf zijn vele anderen, direct of indirect, verantwoordelijk voor de totstandkoming van dit proefschrift. Hiervoor wil ik allereerst mijn promotoren Cock van den Bleek, Prof. R. Krishna, en Jaap Schouten bedanken, die mij in staat hebben gesteld dit promotieonderzoek te doen. Cock en Jaap, ik wil jullie hartelijk bedanken voor de uitstekende leiding, de stimulerende manier van werken, en de visie op wetenschappelijk werk, die ik altijd zeer heb gewaardeerd.

Mijn collega's, zowel in Delft als in Amsterdam: Adriaan, Bastiaan, Bouke, Bron, Cees, Coen, Danny, Frank, Germaine, Geuch, Henk, Henrike, HP, Ioana, Johan, John, Koen, Laura, Marc-Olivier, Martijn, Monique, Onno, Otto, Rembrandt, Remko, Robert-Jan, Rob, Ruud, Sander, Sjoerd, Wijnand, en Yi wil ik hartelijk bedanken voor de discussies en de zeer plezierige werksfeer. Huub, jouw kennis, ervaring en ideeën zijn voor mij erg leerzaam geweest en ik hoop dat ik daar in de toekomst van kan blijven profiteren. Albert, met jouw grondige basiskennis stel je altijd de juiste vragen en heb je discussies met mij gevoerd die voor mij zeer leerzaam waren. Sander, dank voor de prettige discussies tijdens mijn tijd in Amsterdam. Geuch, als mijn kamer- en later bureaugenoot, wil ik je hartelijk bedanken voor de vele discussies en de goede sfeer.

I would like to thank Prof. J.L. Sinclair for making my stay at Purdue a very fruitful and pleasant one. I have learnt a great deal by our numerous discussions and I hope to have much more of them in the future. Caner, Nick, Steve, and Gavin, thanks for making me feel at home and giving me some insight in the American culture. I would like to thank Ian Jones and the rest of the CFX staff for their support and discussions. I would also like to thank Andreas Boemer, Prof. O. Simonin, and Georges Balzer for their initial help and discussions.

Anton, Arno en Els, jullie waren erg belangrijk voor de juiste randvoorwaarden voor mijn financiële, computergerelateerde en administratieve vraagstukken. Mijn dank daarvoor is groot. Ton, kleine klussen had jij af voordat ik ze in de gaten had. Nicole, bedankt voor de catering en je relativerende kijk op het leven. Ik dank mijn afstudeerstudenten Ritsaert, Joris, en Simone voor hun bijdrage aan dit werk. Hester, bedankt voor het delen van jouw CFD kennis. Willem Vermin en de rest van de ondersteuning bij SARA wil ik hartelijk bedanken voor hun zeer snelle en effectieve respons.

Mijn vrienden en familie zijn onmisbaar geweest in al de voorgaande jaren en hen wil ik hier ook hartelijk bedanken. Mijn ouders ben ik erkentelijk dat ze mij altijd alle mogelijkheden hebben gegeven om mijzelf te ontwikkelen. Evelien, na mijn vertrek uit Amsterdam zijn we gezellig thee met elkaar blijven drinken en ben je me zeer dierbaar geworden.

Bedankt allemaal!

Berend

About the Author

Berend van Wachem was born on June 5, 1972 in Amsterdam. In 1990 he obtained is "VWO" highschool certificate at the "Commenius College" in Hilversum. He then started his university studies at Delft University of Technology where he earned an M.Sc. degree in Applied Physics October 1995, on the topic of computer simulations employing lattice gas cellular automata in the group of Prof. S.W. de Leeuw. During his studies, he has actively rowed and has competed on many international regatta's. In November 1995 he started his Ph.D. research in a combined project of the University of Amsterdam and Delft University of Technology under the guidance of Prof. C.M. van den Bleek, Prof. R. Krishna, and Prof. J.C. Schouten, of which the results are presented in this thesis. In 1998 he visited Purdue University for a period of 8 months and worked under the guidance of Prof. J.L. Sinclair. Since Febuary 2000, he is working at Eindhoven University of Technology as a Research Associate on the modeling of three-phase reactive flows.

Index

2D versus 3D, 144

animations, 189

balances
  continuity, 43, 78, 97, 118
  continuity(mass), 14
  fluctuating velocities, 14
  granular energy, 44, 79
    bimodal, 120
  momentum, 14, 43, 78, 97, 118
bimodal mixture, 30, 116
  bed expansion, 129
Boltzmann
  equation of, 11
  solving of, 20
    bimodal mixture, 30
    discrete method, 20
    Enskog approach, 24
    Grad's approximation, 29
    Monte-Carlo, 20
    second order Enskog approach, 25
    steady state, 21
boundary conditions, 57, 85, 129
bubble
  rise velocity, 61, 87
  size, 61, 86

chaos analysis
  fluidized bed, 99
  Kolmogorov entropy, 99, 109
  reorientation effect, 107
chemical potential, 123, 138
closure relations, 44

delayed bubbling, 3
detailed balancing, 21
diffusion
  force, 123
  velocity, 120
dominant frequency, 102
dynamic behavior
  fluidized bed, 95

Enskog
  equation of, 13
  revised theory, 119
  simplified equation, 14
  solving of, *see* Boltzmann, solving of
Enskog approach, *see* solving of, Boltzmann
Eulerian, 5, 37, 140
experiments, 148
  measurements, 149

fines, 116
fluctuation rise velocity, 98
fluidization, 2
fluidized bed
  advantages, 3
  bimodal mixture, 116
  bubble injection, 63
  chaos analysis, 99
  disadvantages, 3
  dynamic behavior, 95
  freely bubbling, 59
  general description, 2
  slugging, 62
flux of fluctuating energy, 16

frictional stress, 51, 81, 118, 125

governing equations, 37
  Ishii approach, 40
  Jackson approach, 37
granular
  bimodal particle mixture, 119
  bulk viscosity, 45, 80, 97
    bimodal, 122
  energy, 44
    balance, 44, 79
    bimodal, 120
    conductivity, 48
    dissipation, 50, 79
    simplified balance, 44, 81, 97
  mixture temperature, 120
  pressure, 79, 80, 97
  shear viscosity, 45, 80, 97
  stress tensor, 45
  temperature, 44, 79

initial conditions, 58
interphase momentum transfer, 53, 82, 97
inversion, 117, 132

kinetic theory, 10, 44
  binary particle mixture, 119

Lagrangian, 5, 36, 78, 96, **140**

Maxwellian distribution, 22
mean free path, 45
mean point properties, 38
minimum fluidization, 2
mixing, 117
molecular chaos assumption, 23

natural period, 102
number density, 11

pair PDF, 18
particles
  clusters, 146
  collisions, 16, 142, 147
  flow of properties, 15
  flux-vector, 16
  motion, 141
  number-flow, 16
PDF, **10**
power law decay, 104
pressure waves, 101
probability density function, 10

radial distribution function, 23, 50, 81
  bimodal, 123
research objectives, 5

segregation, 117
settling velocity, 119
slug
  rise velocity, 62
software
  eulerian, 181
  Lagrangian, 171
solids, *see* granular
Sonine polynomials, 27
steady state results, 76
stress tensor, 16
  granular, 45
summational invariants, 21

two-fluid model, 37, 78

voidage waves, 102

weighting function, 38